Final Report for Project 13-4791

DOE Award Number: DE-NE0000722

Recipient: Oregon State University

Project title: (Project 13-4791) New Mechanistic Models of Creep-Fatigue Crack Growth Interactions for Advanced High Temperature Reactor Components

Principal investigator: Professor Jamie Kruzic, Oregon State University
jamie.kruzic@oregonstate.edu
541-908-5178

Team Members: Professor Thomas Siegmund, Purdue University
siegmund@purdue.edu
765-494-9766

Professor Vikas Tomar, Purdue University
tomar@purdue.edu
765-494-3423

Project period: 1/13/14 – 12/20/18

Report submission date: 3/20/18

Reporting period: 1/13/14 – 12/20/17

Table of Contents

List of Figures

List of Tables

1. Executive Summary

This project developed and validated a novel, multi-scale, mechanism-based model to quantitatively predict creep-fatigue crack growth and failure for Ni-based Alloy 617 at 800°C. Alloy 617 is a target material for intermediate heat exchangers in Generation IV very high temperature reactor designs, and it is envisioned that this model will aid in the design of safe, long lasting nuclear power plants. The technical effectiveness of the model was shown by demonstrating that experimentally observed crack growth rates can be predicted under both steady state and overload crack growth conditions. Feasibility was considered by incorporating our model into a commercially available finite element method code, ABAQUS, that is commonly used by design engineers. While the focus of the project was specifically on an alloy targeted for Generation IV nuclear reactors, the benefits to the public are expected to be wide reaching. Indeed, creep-fatigue failure is a design consideration for a wide range of high temperature mechanical systems that rely on Ni-based alloys, including industrial gas power turbines, advanced ultra-super critical steam turbines, and aerospace turbine engines. It is envisioned that this new model can be adapted to a wide range of engineering applications.

2. Project Accomplishments and Summary of Activities

This is the final report submitted for this project. The scope of this project was to create and validate a robust, multi-scale, mechanism-based model that quantitatively predicts creep-fatigue crack growth (CFCG) and failure in the Ni-based Alloy 617 at 800°C. The project ended on December 20, 2017 after a a no-cost extension was requested and granted because of delays that were incurred due to Michelle Jennings (graduate student at OSU) leaving the project mid-2015, and Philipp Seiler (postdoc at Purdue) leaving the project mid-2016. We hired new graduate students, Dylan Addison at OSU in September 2015 and Joshua Pribe at Purdue in August 2016.

Table 1 summarizes the status of the project milestone objectives for the final report. The table is followed by a discussion of the project accomplishments and activities. The report will describe the experimental data that was collected for determining inputs for the model, the data that was collected for validation of the model, and finally a description of the model development and validation.

Table 1. Summary of the status of the milestone report objectives

Milestone Objective	Status
Crack growth model modification and refinement will be complete and the model will be validated by agreement with experiments.	Complete
Model parameter sensitivity has been determined.	Complete

2.1. Material - Alloy 617

The material selected for this project was Alloy 617, which is of interest for components in future Very High Temperature Reactor designs. The temperature of interest selected for this project is 800°C. Based on discussions with Richard Wright at Idaho National Laboratory (INL), at higher temperatures the failure mechanism for Alloy 617 shifts away from the propagation of a dominant

crack and becomes controlled by diffuse creep damage. This initial assumption was consistent with our own observations during the project. Since the objective of this project is to model crack propagation, 800°C represents the upper end of the temperature range when crack propagation is an important failure mechanism.

Plates of Alloy 617 were received from Richard Wright at INL on January 31st, 2014. The supplied plate (heat 314626) was fabricated by ThyssenKrupp VDM for the NGNP R&D program. The chemical composition and mechanical properties of this heat of the alloy are given in Table 2 and Table 3 respectively.

Table 2. Chemical Composition of Alloy 617 (in wt%).

	Ni	Cr	Co	Mo	Fe	Mn	Al	C	Cu	Si	S	Ti	B
Min	44.5	20.0	10.0	8.0	—	—	0.8	0.05	—	—	—	—	—
Max	—	24.0	15.0	10.0	3.0	1.0	1.5	0.15	0.5	1.0	0.015	0.6	0.006
Heat 314626	54.1	22.2	11.6	8.6	1.6	0.1	1.1	0.05	0.04	0.1	<0.002	0.4	<0.001

Table 3. Tensile properties of heat 314626.

Temperature	YS (MPa)	UTS (MPa)	% Elongation	%RA
~20°C	768	302	65	32
800°C	189	290	95	80

The first round of sample machining was completed in May, 2014 including compact tension samples for crack growth experiments, tensile samples, and samples for indentation experiments that were shipped to Purdue. Subsequent test samples have been machined from the same plate as needed during the project. Microstructure data was obtained from Richard Wright at INL, as shown in Fig. 1 and Table 4.

Fig. 2 shows a micrograph of the microstructure taken from the literature [1]. Richard Wright shared uniaxial tensile data for Alloy 617 at 800°C, which is shown in Fig. 3 and Table 3. Finally, Richard Wright also shared creep data for Alloy 617 at 800°C from 60 MPa to 126 MPa (

Fig. 4 & Fig. 5) to help define the model creep parameters.

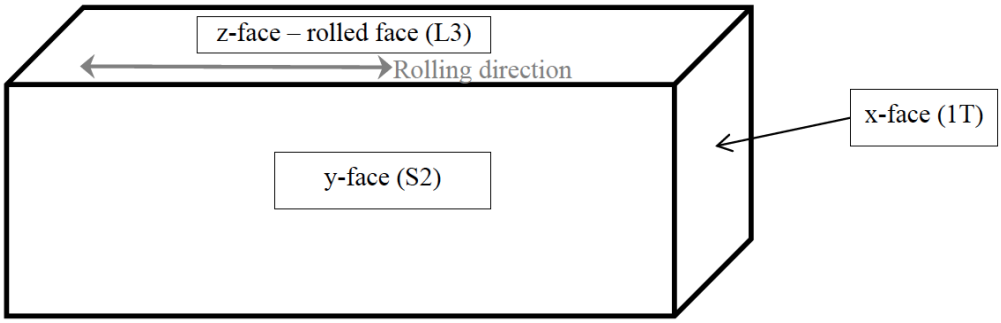

Fig. 1. Schematic illustration of the three faces of the rolled Alloy 617 plate that were analyzed for grain size.

Table 4. Average grain size for each plate face

Analysis Face	Average Grain Diameter*		Average ASTM Grain Size	
	Number Average	Area-Weighted Average	Number Average	Area-Weighted Average
X	85 ±4	190 ±8	5.4	2.6
Y	56 ±3	179 ±8	6.5	3.0
Z	82 ±5	235 ±12	5.7	2.1
All faces	73 ±2	204 ±5	5.9	2.6

*Error range indicates 95% confidence interval.

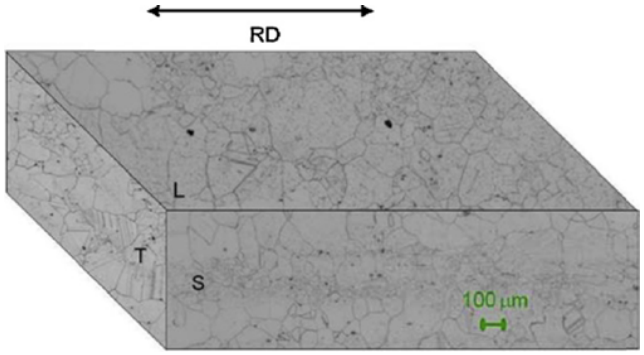

Fig. 2. Alloy 617 micrograph from [1].

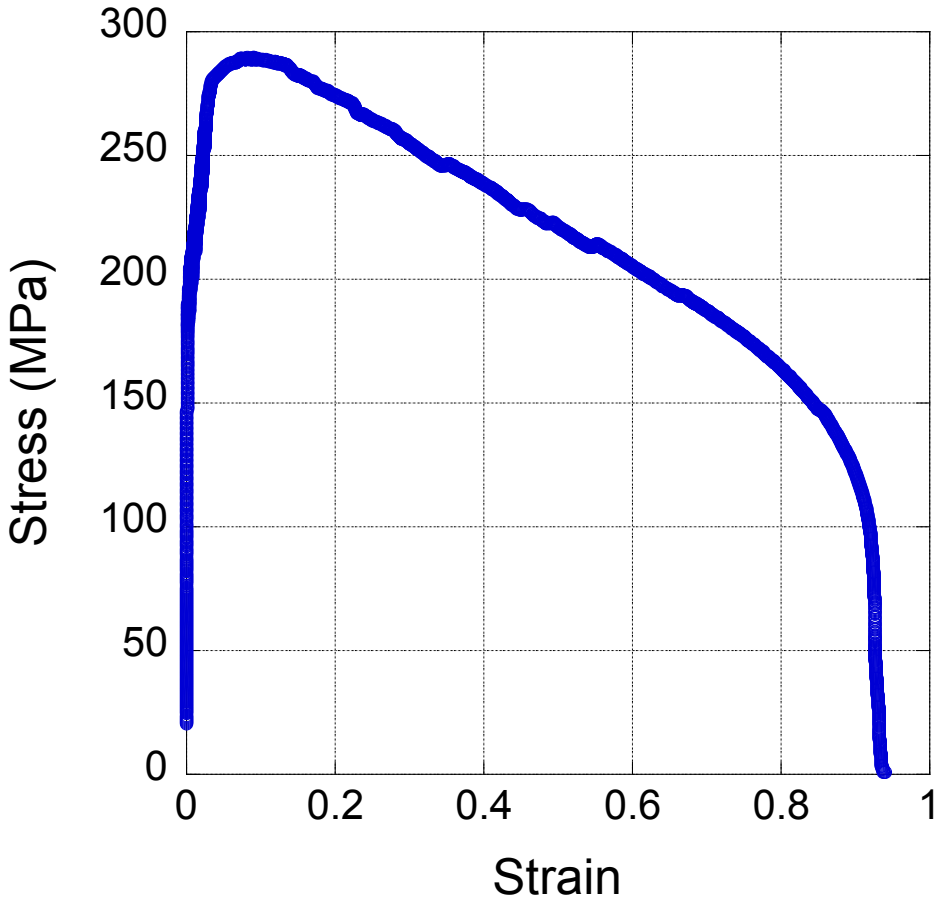

Fig. 3. Stress-strain curve for Alloy 617 at 800°C

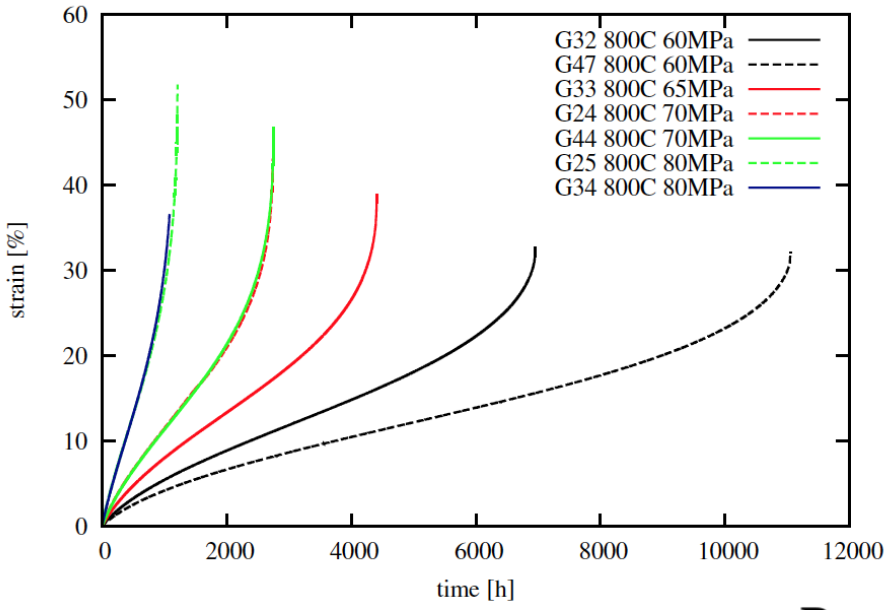

Fig. 4. Creep rupture data for Alloy 617 at 800°C and stress levels from 60 – 80 MPa.

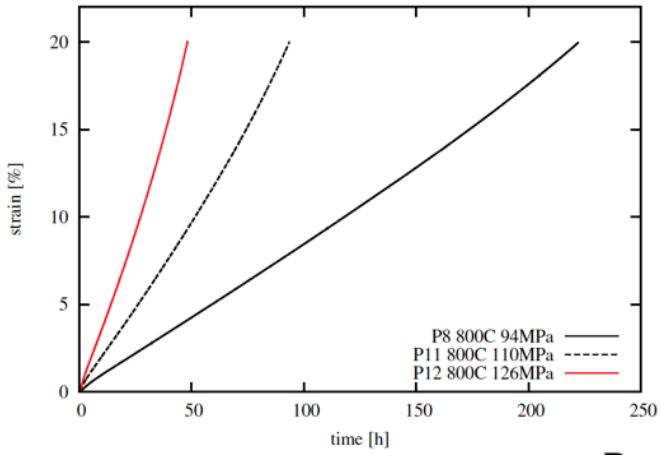

Fig. 5. Creep data out to 20% strain for Alloy 617 at 800°C and stress levels from 94 – 126 MPa.

The tension creep data from INL (

Fig. 4) does not show a traditional shape with a well-defined secondary creep regime [2,3]. In Alloy 617, the minimum creep rate is found as an inflection point. Benz et al. [2] used a minimum creep rate approach to fit a power law creep law using an additional threshold stress at 750°C. For fitting the creep law above 800°C, additional threshold stresses can be neglected:

$$\dot{\varepsilon} = A\sigma^m = A_0\sigma^m \exp\left(\frac{-Q}{RT}\right).$$

Eq. 1

The creep data from INL consider a hold time much longer than a typical creep-fatigue experiment. To model the material data of interest, short times must be fitted. As a first approximation, the minimum creep rate and also the initial creep rate was fitted (see Table 5). A Zener-Hollomon plot as shown in Fig. 6(b) was used to collapse the minimum creep rates at different temperatures. As shown in Fig. 6(a), for short time data a power law approach fits the experimental data reasonably well. At long holding times the data deviates significantly from the used power law fit. The fit of the minimum and initial creep rate and the data fitting by Benz et al. [2] will be used in the subsequent simulations.

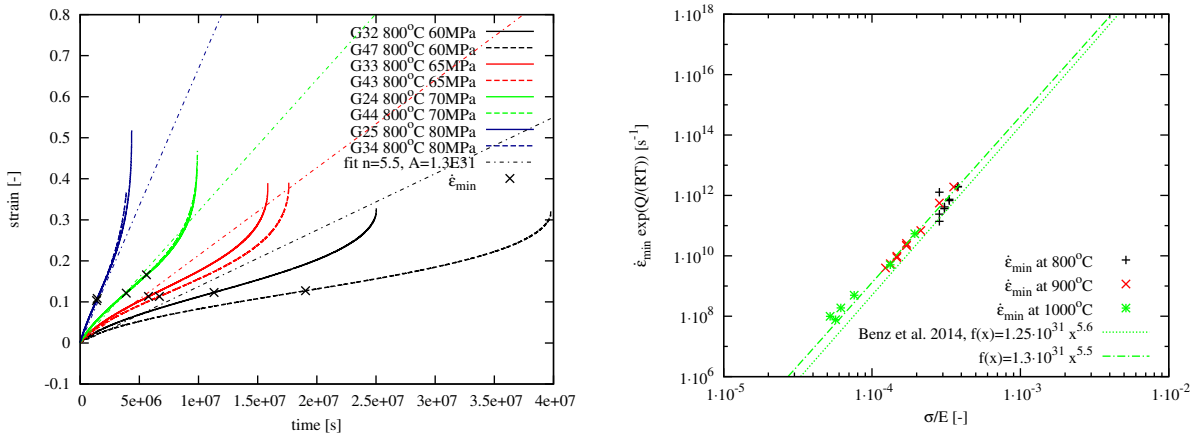

Fig. 6 Fitting of a power law creep law by min. creep rate. (a) Creep data from INL and fitted power law. (b) Zener-Hollomon plot of min. creep rate.

Additionally, to cover the initial shape of the creep data, a Norton-Miller law was used:

$$\dot{\varepsilon}^{vp} = C\sigma^n t^m \exp\frac{-Q}{RT} \qquad \text{Eq. 2}$$

which gives a reasonable fit of the creep data below the minimum creep rate. The Norton-Miller parameters can also be found in Table 5.

Table 5. Fit parameter of different creep laws.

Min. creep rate	**Initial creep rate**	**Norton-Miller**
A_0 = 1.30E31 m = 5.5	A_0 = 1.03E31 m = 5.7	C = 4.89E42 n = 6.16 m = -2.13

Low cycle fatigue testing at 800°C was used to determine the cyclic hardening behavior of alloy 617 for the visco-plastic model. Laura Carroll at INL shared some initial low cycle fatigue (LCF) data from INL at 800°C on alloy 617. Samples had a nominal 7.5 mm diameter and 12 mm gauge length. Fully reversed strain ranges used were ± 0.13%, ± 0.15%, and ± 0.50% with a strain rate of 0.1 %/s. Example curves are shown in Fig. 7 and Fig. 8.

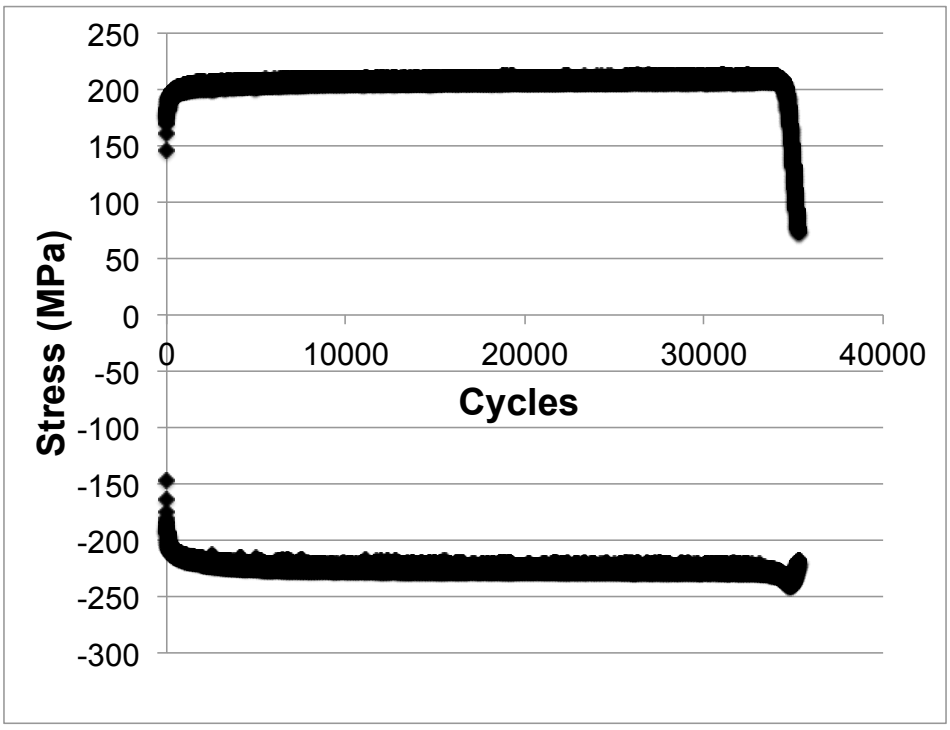

Fig. 7. Cyclic hardening behavior for alloy 617 at 800°C at ± 0.15% strain.

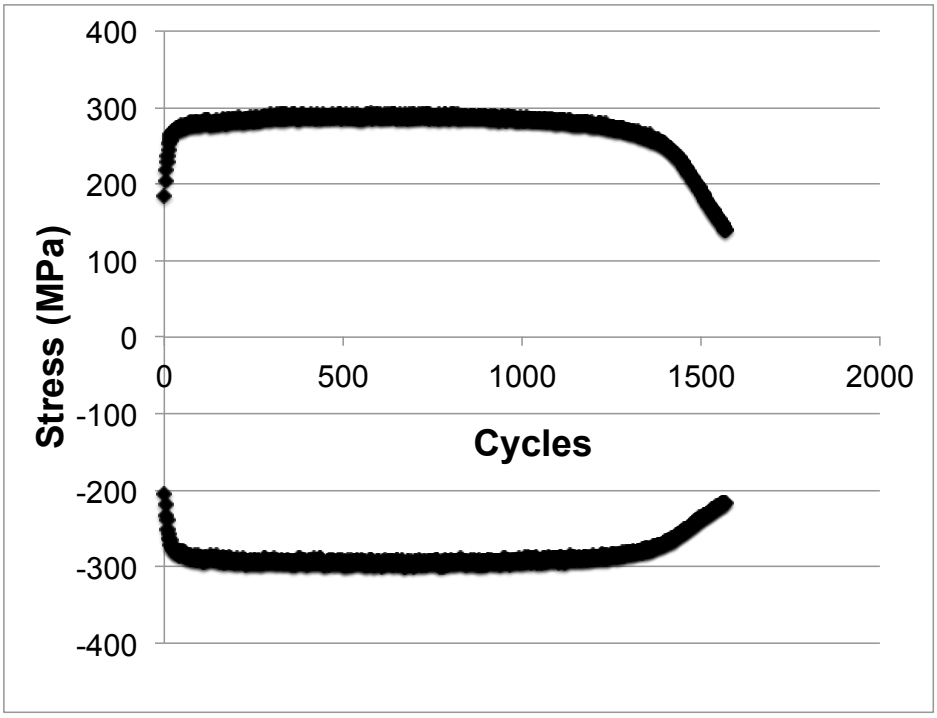

Fig. 8. Cyclic hardening behavior for alloy 617 at 800°C at ± 0.50% strain

2.2. Nano-indentation experiments

Nano-indentation experiments were performed for this project over a range of temperatures up to 800°C to understand 1) the strain gradient material length scale by examining the indentation size

effect, 2) the creep behavior under high strain gradients and short time scales, and 3) the effect of microstructure heterogeneities on the local mechanical properties.

2.2.1. Sample Preparation

For the nanoindentation tests, the as-received Alloy 617 block was cut into two different dimensioned samples. For room temperature and high temperature indentation tests, the as-received Alloy 617 block was cut into 8 mm by 8 mm by 2 mm (thickness) blocks. For specific area (nitride particles) indentations, the small dimensions of 2 mm by 2 mm by 1 mm (thickness) were selected because it was much easier to locate the indent marks and analyze the area through scanning electron microscopy (SEM). In order to reveal the microstructure for optical microscopy and to remove the effect of hardening due to mechanical polishing, electrolytic polishing and etching techniques were used. After cutting into the desired dimensions, the Alloy 617 samples were polished first by grinding to 400, 600 and 800 grit SiC papers one by one and then by mechanical polishing using 6 μm and 3 μm diamond grits successively. After mechanical polishing, the Alloy 617 samples were electrolytically polished and etched using a perchloric acid based electrolyte solution.

2.2.2. Experimental Procedure

2.2.2.1. Experimental Setup

Nanoindentation is a standard experimental method to find the modulus and hardness of materials at the micro and nano scale. All tests were performed using a multi-module mechanical tester (Micro Materials Ltd., UK) shown in Fig. 9. Fig. 9(a) is the real photo image of the overall experimental setup for nano-indentation. Fig. 9(b) depicts the setup illustrating the approach for performing high temperature indentation. The load that can be applied by this platform ranges from 0.1 mN to 500 mN, with the accuracy of better than 0.1 mN.

At high temperature, both the sample and the indenter tip were heated to the required testing temperature which was closely monitored using thermocouples. After reaching the desired temperature the set-up was kept inactive for 8 hours in order to achieve thermal stability. The remaining parts of setup are separated by a heat shield in order to maintain them at room temperature. The tests were performed at different temperatures ranging from room temperature to 800 ^{o}C. A Berkovich diamond indenter with tip radius of 20 nm was used for nanoindentation at room temperature and 400 ^{o}C, and a cBN (cubic boron nitride) indenter was used at 800 ^{o}C. During the tests, the samples were firmly mounted on the indentation hot stage using high temperature using super glue to avoid any movement during the experiments. After both the indenter and stage reached the desired temperature, the setup was kept inactive for one hour per hundred degree of temperature increase in order to achieve thermal stability. The indenter approached the sample in its thickness direction. Indentation locations were selected randomly on the sample surfaces.

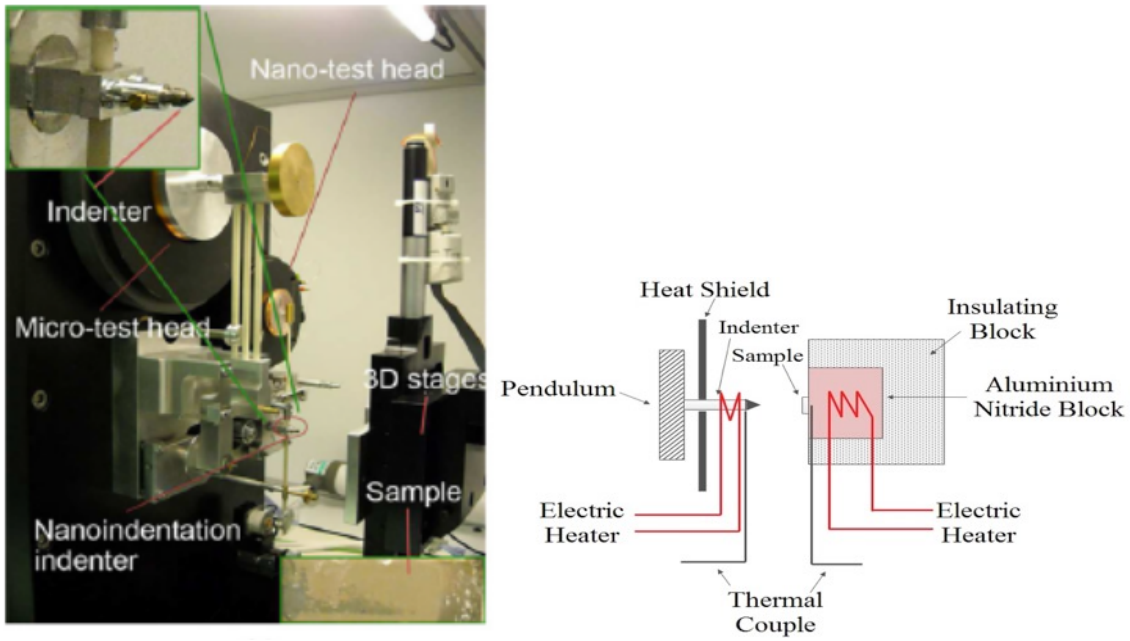

(a) (b)

Fig. 9. Experimental Set-up (a) Micro and Nano indentation Setup, (b) Schematic for high temperature indentation approach

For each reported data point, the results were averaged from 10 different indentation spots. The indentation depths and maximum indentation load were chosen to minimize the effect of measurement drift that usually occurs in indentation tests if the depth is too small. The depth calibration and the area function computation was done for each temperature using Tungsten and fused silica as reference sample in case of micro-indentation & nanoindentation, respectively. Sample were first loaded from zero to a maximum loading, the maximum load was held for 5 or 500 seconds, and then unloading was done. The reduced modulus of the material was calculated from the slope of the unloading curve. Creep characterization data was collected from the dwell period by observing the change in depth at constant load. Depending on the dwell period, the creep properties change as the system undergoes a transient to steady state creep transition. It was determined that 500 seconds was long enough to achieve steady state creep and yields quite good prediction of the material behavior. During unloading, when the load reached 10% of the maximum load, the load was kept constant for another 500 seconds in order to estimate thermal drift correction and compute the actual creep displacement. The temperature levels chosen for the experiments were 25 ^{o}C (room temperature), 400 ^{o}C and 800 ^{o}C. The high load range to explore the size effect was applied as 200 mN, 300 mN and 400 mN. The load and unload rate were chosen to be 10 mN/s, 15 mN/s and 20 mN/s, respectively.

2.2.2.2. Indentation Theory

The experimental process involves indenting the surface of the tested material by increasing the load force with certain loading rate. During the period of unloading only elastic recovery happens in the material, so the data of this part is used for the modeling the contact mechanics [4-6]. A

typical indentation loading-unloading curve is shown in Fig. 11(a) which can be described by the Oliver–Pharr method with a power law [4,5] as:

$$P = A(\mathrm{h} - h_f)^m. \qquad \text{Eq. 3}$$

In the above equation, parameters of A and m are empirically determined material constants. Parameter h is the displacement of the indenter, and h_f is the indentation depth after completing the unloading process. The contact depth h_c at the peak load $P_{\max}$ that corresponds to the total indentation depth $h_{\max}$ is given as

$$h_c = h_{\max} - \varepsilon \frac{P_{\max}}{S}. \qquad \text{Eq. 4}$$

Here, the parameter ε is a correction factor for the specific indenter, $\varepsilon = 1$ for a spherical tip and $\varepsilon = 0.75$ for a Berkovich tip. The parameter S is the stiffness which is calculated as:

$$S = \left.\frac{dp}{dh}\right|_{h=h_{\max}} = Am(\mathrm{h} - \mathrm{h}_f)^{m-1}. \qquad \text{Eq. 5}$$

In this case, stiffness is the initial unloading stiffness, near when the depth is at the maximum value. During the experiment the peak load $P_{\max}$ and the maximum area of indentation A is measured. The hardness of the material is given by the formula:

$$H = \frac{P_{\max}}{A}. \qquad \text{Eq. 6}$$

For the Berkovich indenter, the area of contact is calculated as a function of contact depth h_c:

$$A = 3\sqrt{3}h_c^2 \tan^2 65.3^o \approx 24.5h_c^2. \qquad \text{Eq. 7}$$

In the current research, the specific area function of the indenters is calculated from the indents on the reference quartz sample as

$$A = 18.72h_c^2(\mathrm{nm}^2) + 11542.71h_c(\mathrm{nm}^2). \qquad \text{Eq. 8}$$

The hardness of the material is calculated by:

$$H = \frac{P_{\max}}{24.5h_c^2}. \qquad \text{Eq. 9}$$

The reduced Young's modulus E_r is related to the slope of the upper part of the unloading curve by the equation from Sneddon's solution [7]:

$$E_r = \frac{\sqrt{\pi}}{2}\frac{S}{\sqrt{A}}. \qquad \text{Eq. 10}$$

The Young's modulus value of the material can be calculated from the reduced modulus by the formula:

$$\frac{1}{E_r} = \frac{1-\nu^2}{E} + \frac{1-\nu_i^2}{E_i}. \qquad \text{Eq. 11}$$

Here, E and ν are the Young's Modulus and Poisson's ratio of the material. E_i and ν_i are Young's modulus and Poisson's ratio of the indenter. For the diamond indenter, the values used were E_i = 1141 GPa and ν_i = 0.07. For the cubic boron nitride indenter, the values used were E_i = 800 GPa and ν_i = 0.12.

2.2.2.3. Machine Compliance Correction

According to Eq. 10, reduced modulus is proportional to the stiffness S. The overall stiffness includes the material stiffness and machine stiffness. Without the correction of machine compliance, the properties of material will not be calculated correctly, especially at high temperature. The machine compliance c can be calculated using the measured stiffness S and corrected stiffness S' based on the literature value of the reference samples (sapphire and quartz) as:

$$c = 1/S - 1/S'. \qquad \text{Eq. 12}$$

The corrected total depth h_t' is calculated considering the machine compliance as:

$$h_t' = h_t - P \cdot c. \qquad \text{Eq. 13}$$

The corrected contact depth h_c' is given using Eq. 4 as:

$$\begin{aligned} h_c' &= h_t' - e \cdot \frac{P}{S'} = h_t - P \cdot c - e \cdot \frac{P}{S'} \\ &= h_c + e \cdot \frac{P}{S} - P \cdot c - e \cdot \frac{P}{S'} = h_c + e \cdot \frac{P}{S} - P \cdot \left(\frac{1}{S} - \frac{1}{S'}\right) - e \cdot \frac{P}{S'} \\ &= h_c + P\left(\frac{1}{S} - \frac{1}{S'}\right)(e-1). \end{aligned} \qquad \text{Eq. 14}$$

For Berkovich indenter tip which was used in the current research, $e = 0.75$, so the corrected contact depth is:

$$h_c' = h_c - 0.25P\left(\frac{1}{S} - \frac{1}{S'}\right) = h_c - \frac{1}{4}P \cdot c. \qquad \text{Eq. 15}$$

Combining Eq. 10, Eq. 12, and Eq. 15, the machine compliance is expressed as:

$$c = \frac{1}{S} - \frac{1}{S'} = \frac{\sqrt{\pi}}{2E_r\sqrt{A}} - \frac{\sqrt{\pi}}{2E_r'\sqrt{A'}}$$
$$= \frac{\sqrt{\pi}}{2E_r\sqrt{ah_c^2 + bh_c}} - \frac{\sqrt{\pi}}{2E_r'\sqrt{ah_c'^2 + bh_c'}}$$
$$= \frac{\sqrt{\pi}}{2}\left[\frac{1}{E_r\sqrt{ah_c^2 + bh_c}} - \frac{1}{E_r'\sqrt{a(h_c - P\cdot c/4)^2 + b(h_c - P\cdot c/4)}}\right]. \quad \text{Eq. 16}$$

In this equation, E_r, h_c and P are measured values and E_r' is the corrected value. Parameters of a and b are constants for area function. For ideal function a=24.5 and b=0, and for the actual function, a=18.74 and b= 11542.71. Only one parameter c is unknown here, which can be calculated using Eq. 15. Solving the equation using MATLAB gives the value as 0.42958 nm/mN. For the maximum load 400 mN,

$$h_c - h_c' = \frac{1}{4}P\cdot c = 42.958nm \quad \text{Eq. 17}$$

which is much lower than the contact depth with the range of thousands of nanometers. Thus, it can be ignored.

2.2.2.4. Contact Area Calibration

In the Oliver-Pharr methodology, contact area is directed related to indentation depth. The indentation depth measurement is highly affected by factors such as thermal expansion at high temperatures, surface finish, and relative deformation of the indenter tip with respect to the reference sample as a function of material type. In this work, actual measurements of contact area under SEM were performed for all the indents under different temperature and different loads. One typical illustration for each data point is shown in Fig. 10(a). The comparison of SEM measured contact area and function calculated contact area is shown in Fig. 10(b). The SEM measured area values were used in predicted material properties.

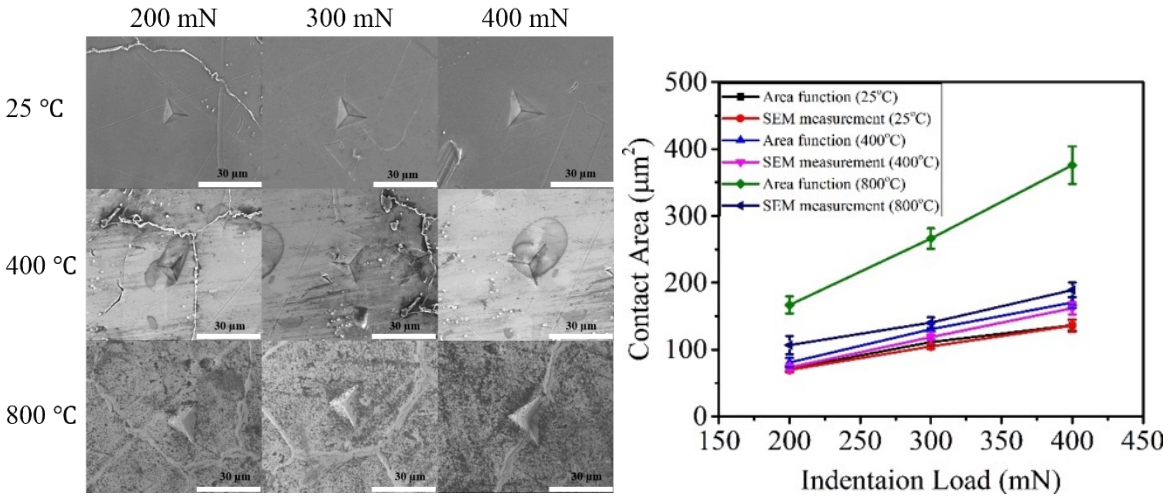

(a) (b)

Fig. 10. (a) SEM measurements of contact area under different temperature and loads, (b) comparison of SEM measured contact area and function calculated contact area

2.2.2.5.Indentation Creep Measurements

During depth sensing indentation with a self-similar indenter, the strain rate $\dot{\varepsilon}$, stress σ, and instantaneous indentation depth h, are related based on the analyses for a power law creeping solid [8] as:

$$\dot{\varepsilon} \sim \frac{\dot{h}}{h}, \qquad \text{Eq. 18}$$

and

$$\sigma \propto \frac{P}{h^2} \qquad \text{Eq. 19}$$

P is indentation load and $\dot{h} = dh/dt$, where t is time. The relations assume that in the case of indentation by a conical punch the ratio of h and radius of contact zone depends only on the stress exponent n. The derivation of the strain rate requires differentiation of the $h(t)$ curve. As shown in Fig. 11(b), the $h(t)$ data is scattered around a trend line. A commonly used fitting function for $h(t)$ developed by Li and Ngan [9] is given as

$$h(\mathrm{t}) = \mathrm{h}_i + a(\mathrm{t} + \mathrm{t}_i)^b + \mathrm{kt}. \qquad \text{Eq. 20}$$

In this equation, h_i is the initial depth during the creep period, t_i is the time-related parameter, f, d and k are constants. The above equation was used by Cao et al. [10] to investigate the creep behavior of thin Ta film and by Ma et al. [11] in investigating the creep behavior of thin Ni film. A slightly modified form was used in our analysis for reduced fitting error, [12], as:

$$h(\mathrm{t}) = \mathrm{h}_i + at^b + \mathrm{kt}.$$

Eq. 21

Using the $h(t)$ curve, the stress exponent and creep strain rate may be calculated. In the subsequent section, the elastic moduli, stress exponent trend, and creep rate (strain rate) are investigated as a function of temperature, length scale, and maximum indentation load.

Three different analytic approaches are available to calculate creep stress exponent: depth sensing constant load (h-CL) method [13], the continuous stiffness constant load (SCL) method [14], and the exponential load (EL) method [15]. The two constant load methods use data from a load hold at the maximum load. In our experiments, the h-CL method was selected as the most reliable. During indentation, because the contact area will increase during the holding period if creep occurs, the hardness will subsequently decrease with the corresponding decrease in the indentation strain rate. Tabulation of a series of pairs of the strain rate and stress based on the measured data is used to calculate stress exponent. For the scaling of strain rate and stress to be correct, the indentation tip must be self-similar. In order to ensure this, the indentation depth must not be influenced by the tip head curvature. Thus, the tip depth was maintained to be more than 500 nm, which is greater than 5 times the tip radius.

2.2.3. Indentation Results

2.2.3.1. Indentation Curves

Fig. 11(a) represents the typical load displacement curve for an indentation experiment done at room temperature with 400 mN maximum load. In this case, the sample is loaded up to the maximum load, the maximum load is hold for around 500 seconds and then unloading is carried out. The reduced Young's modulus in this case is computed from the slope of the unloading curve. Creep data is abstracted from the maximum load holding period. Fig. 11(b) shows the extracted creep curve. Fig. 11(c) shows the thermal drift data collection. Thermal drift is observed to be higher at higher temperature. This data is used to correct the data collected from the indentation and the corrected data is used for the reduced modulus and hardness calculations.

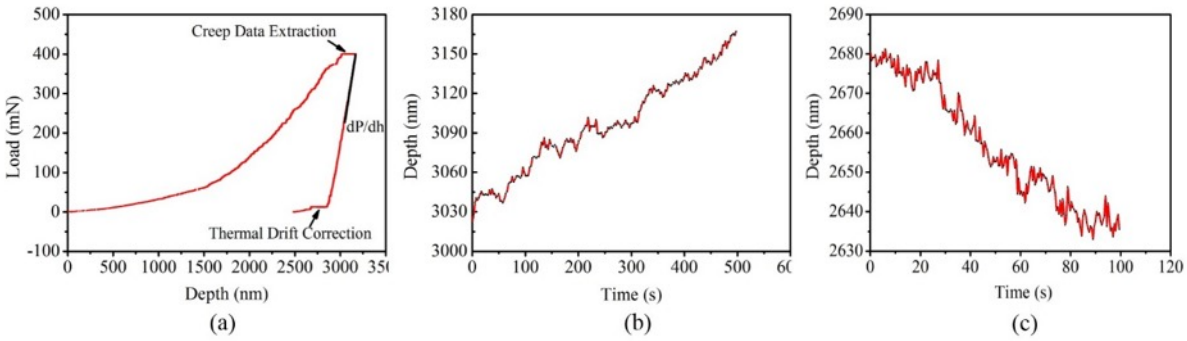

Fig. 11 (a) Typical Indentation Curve, (b) Creep Data Extraction, (c) Thermal Drift Data. These example curves were collected at room temperature.

2.2.3.2. Reduced Modulus and Hardness as a Function of Different Loads

After correction for the depth using thermal drift and creep data and calibration of contact area using actual SEM measurements, the reduced elastic modulus and indentation hardness values of

Alloy 617 samples as a function of temperature are plotted in Fig. 12. Both hardness and reduced modulus show a decreasing trend with the increase of temperature. The reduction of indentation hardness and reduced modulus are mainly due to the effect of strain softening and pile up of material around the indented position.

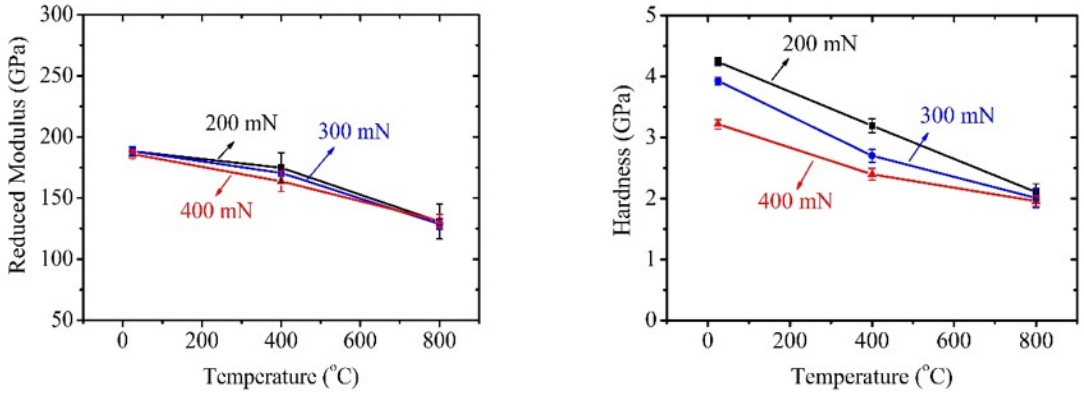

(a) (b)

Fig. 12. Reduced modulus and hardness of the Alloy 617 samples as a function of temperature under different loads. (a) Reduced modulus, (b) hardness.

2.2.3.3. Indentation Size Effect (ISE)

The phenomenon of different properties under different indentation depth is called indentation size effect which is also observed in previous research [16-18]. Reduced modulus values of Alloy 617 samples under different ranges of indentation depth at different temperatures are shown in the Fig. 13(a). Reduced modulus shows stable properties with increase of indentation depth.

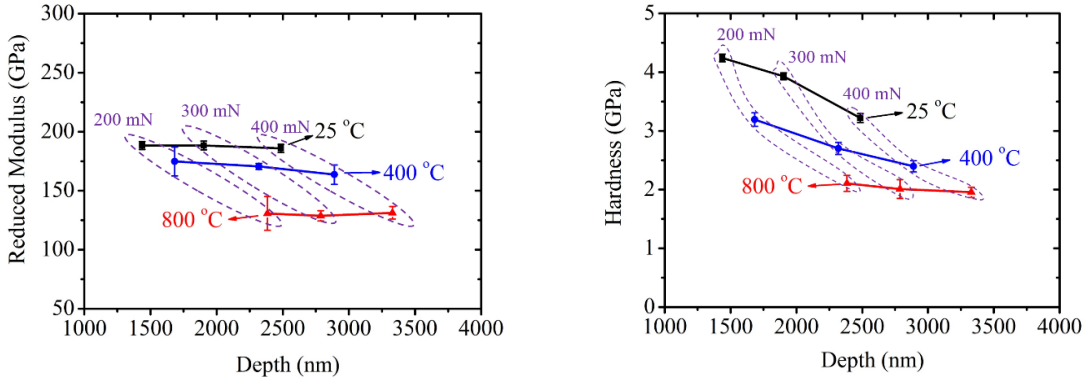

(a) (b)

Fig. 13 Reduced modulus and hardness of the Alloy 617 samples as a function of depth under different temperature. (a) Reduced modulus, (b) hardness

Indentation hardness values of the Alloy 617 samples under different ranges of indentation depth at different temperatures are shown in the Fig. 13(b). As shown, indentation hardness values

decrease with increase of depth. According to the Nix-Gao relation, the indentation size effect can be expressed as [19]:

$$\frac{H}{H_0} = \sqrt{1 + \frac{h^*}{h}},$$

Eq. 22

where H is the hardness for a given depth of indentation h, H_0 is the hardness at the infinite indentation depth and h^* is a characteristic length parameter which is not only related to material properties [20] and H_0,but also possibly on the geometry of the indenter. The material intrinsic length scale parameter related to h^* is a very important parameter of a material. Without it, constitutive equations cannot predict the size effect of material in the theory of gradient plasticity [21-26]. Eq. 22 can be rearranged as:

$$H^2 = H_0^2 + H_0^2 h^* / h.$$

Eq. 23

The values of H and h can be determined from the experimental results and the values of H_0 and h^* can be determined by a curve fit.

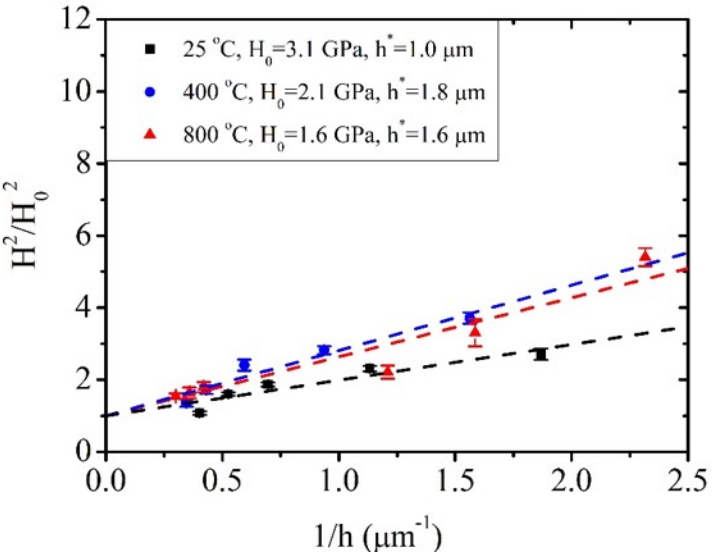

Fig. 14. Curve fitting for indentation size effect according to Nix-Gao relation under different temperature

Fig. 14 represents the variation of $\frac{H^2}{H_0^2}$ with $\frac{1}{h}$ using Nix-Gao relation from the experimental results. From the linear curve fitting hardness at infinite depth (H_0) is found to be 3.1 GPa, 2.1 GPa and 1.6 GPa at 25 °C, 400 °C and 800 °C, respectively. The length scale related parameter h^* values are 1.0 μm, 1.8 μm and 1.6 μm, respectively.

2.2.3.4. High Temperature Creep Properties

At high temperature, creep effects are non-negligible. Fig. 15(a) plots creep depth as a function of dwell period at 800 °C at the peak load of 200 mN to show the creep effect of Alloy 617. Creep

data is normalized by subtracting the initial depth of each creep test. For consistency, the plots show the thermal drift corrected data and results. The creep function was determined by fitting the corrected data using Eq. 21. The creep depth vs. time plot reached steady state within first 100 s of plotting in all cases. The creep rate was calculated by linear curve fitting in the steady period. Effect of load is to increase the creep rate, which is shown in the Fig. 16(a).

As shown in the Fig. 15(b), the stress exponent was also calculated in the steady state of the double-log plots of creep strain rate and stress by linear curve fitting. Fig. 16(b) plots stress exponent as a function peak indentation load at the nanoscale. These values within the range of 5 to 6 are consistent with the value reported by Benz et al. for a minimum creep rate power law for Alloy 617 [2], and is also similar to our own fitting of the initial part of the creep curves from INL (Table 5).

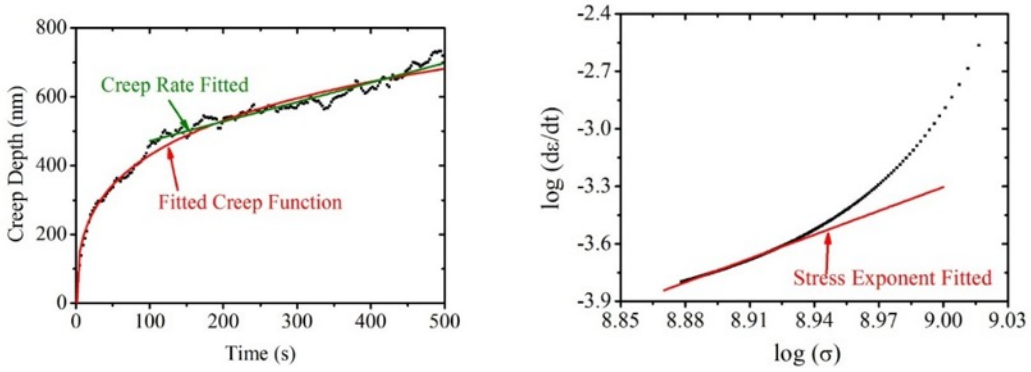

Fig. 15: Illustration of stress exponent calculation. (a) The creep raw data file was and fitted and creep rate linear fitting; and (b) The equivalent strain rate and stress based on the fitted data. The linear fitting is used to calculate steady state stress exponent.

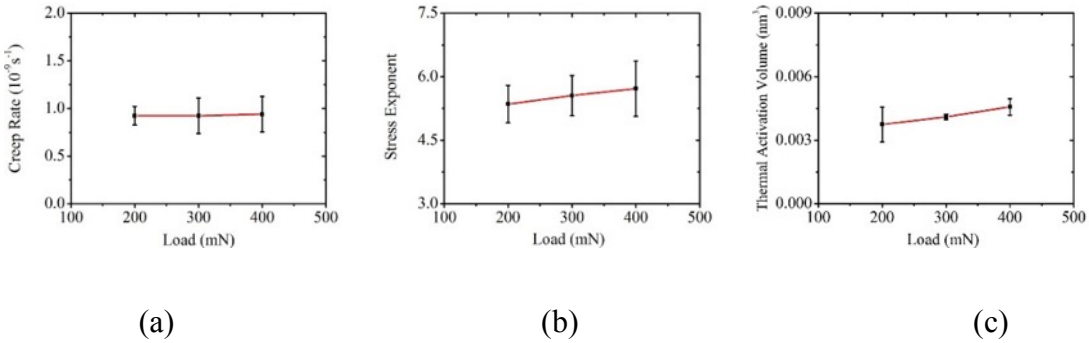

Fig. 16: Creep properties of Alloy 617 sample at 800 ℃. (a) Creep rate, (b) stress exponent, (c) thermal activation volume

The extent of the dislocation climb mechanism determining deformation is governed by the availability of excess free volume which is related to thermal activation volume and also the

average change in volume of the flow unit. In the present work, the thermal activation volume V^* is approximated as [12],

$$V^* = \kappa_B T \frac{\partial \ln \dot{\varepsilon}}{\partial \sigma} |_{\varepsilon,T}. \quad \text{Eq. 24}$$

In the above equation, $\dot{\varepsilon}$ is the strain rate that varies with the dwell time, σ is the stress for the creep period, κ_B is Boltzmann's constant and T is temperature in Kelvin. The derivatives are taken at fixed strain at each temperature to constrain the influence of structure change due to work hardening and softening. Fig. 16(c) plots the thermal activation volume calculated in this case as a function of peak indentation load also at 800 °C. As shown, thermal activation volume increases with increase in peak load and also the length scale of measurements. Since, the thermal activation volume is directly correlated to the deformation energy, the trend implies a significantly higher deformation work is required at the high load in comparison to the low load.

2.2.3.5. Effect of Oxidation

As the properties of the samples are measured at high temperature in air, the surface of the samples become oxidized. As a result, it is necessary to study the effect of the oxidized layer to understand the indentation size effect of Alloy 617 at high temperature.

To make an oxidized sample that reflects the indentation experiment, the Alloy 617 sample was heated to 800 ^oC gradually over 10 hours and then held for 8 more hours before finally decreasing the temperature gradually again over 10 hours. As it is difficult to measure the exact thickness of the oxidized layer at the surface of sample, different loads that can make different depth have been applied to the sample to measure the property of the sample at room temperature. By comparing to the properties of the polished samples without the oxidized layer, the thickness of the layer can be approximated and the indentation size effect can be determined at high temperature. Fig. 17 shows the comparison of the indentation size effect of oxidized sampled to the polished samples with the Nix-Gao relation. The data points of hardness of oxidized sample are above the trend line of original sample which indicates that the hardness of oxidized layer is higher than the polished sample. Based on these results, the thickness of the oxidized layer was estimated at around 400 nm.

The oxidized layer of the Alloy 617 is mainly made of Cr_2O_3 mixed minor amounts of $MnCr_2O_4$. Al-Hatab et al. [27] measured the parabolic rate constant κ_p of Alloy 617 in $g^2m^{-4}h^{-1}$ (in respect to mass) at the temperature of 750, 850 and 950 ^oC. Through the method of interpolation, the parabolic rate constant κ_p is approximated as $1.5\times10^{-2} g^2 m^{-4} h^{-1}$ at 800 ^oC. The parabolic rate constant $\kappa_p^{'}$ in $m^2\ h^{-1}$ (in respect to the area) is calculated by

$$\kappa_p^{'} = \kappa_p (\frac{Mo_x}{\rho o_x \cdot b \cdot Mo})^2, \quad \text{Eq. 25}$$

Where Mo_x is the molar mass of Cr_2O_3 ($152 g/mol$), Mo is the molar mass of oxygen (16g/mol), ρo_x is the density of Cr_2O_3 ($5.22\times10^6 g/m^3$) and b is the number of oxygen atoms in M_aO_b (b =

3). As a result, $\kappa_p^{'}$ is calculated as $5.5\times10^{-15} m^2 h^{-1}$. The thickness of the oxidized layer can be calculated by:

$$s = \sqrt{\kappa_p^{'} t}. \qquad \text{Eq. 26}$$

As a result, the estimated thickness of the oxidized layer of Alloy 617 at 800 °C after about 31 hours (equivalent time which includes 8 hours heating, 8 hours stabilizing and 15 hours experimental time) heating is about 413 nm, which is in agreement with SEM measurements of the approximate values of oxidized layer thickness, as shown in Fig. 18.

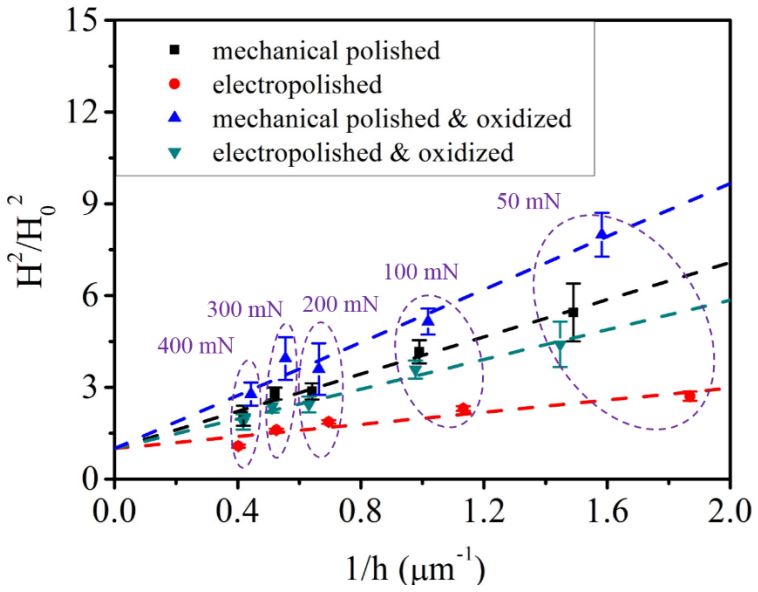

Fig. 17. Comparison of hardness of oxidized sample and original sample

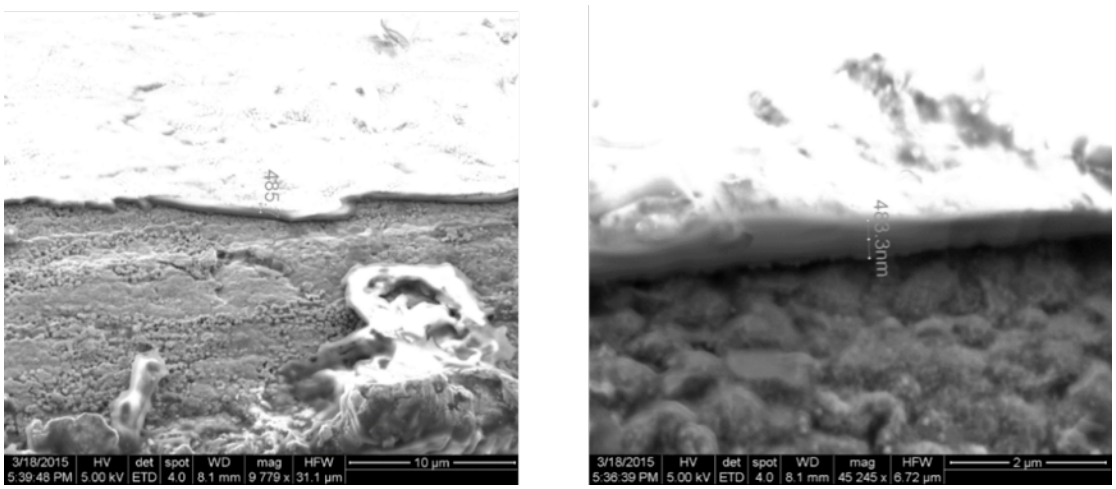

Fig. 18 Oxidized layer and thickness measurement under SEM

2.2.3.6. Effect of Precipitates

One challenge in developing constitutive laws using indentation is local material heterogeneities. Based on published reports [3], there are both nitride particles (gold) and bands of carbide precipitates in alloy 617 shown in Fig. 19(a). We evaluated the heterogeneity of the mechanical response of alloy 617 in the regions of these particles.

Nitride particles on the surface of Alloy 617 are shown in the Fig. 19(a) from the literature [3] and the Fig. 19(b) from the optical microscope of the nanoindentation platform. The dimension of the nitride particles are around 10 μm.

To explore the different properties in nitride areas, nanoindentation experiments at room temperature have been performed. The loads are 50 mN and 100 mN. The loading and unloading rate are 2.5 mN/s, and 5.0 mN/s. For the selection of the experimental load, since low load will not make visible marks under the microscope and high load will produce high depth which exceeds the nitride area, loads of 50 mN and 100 mN were selected.

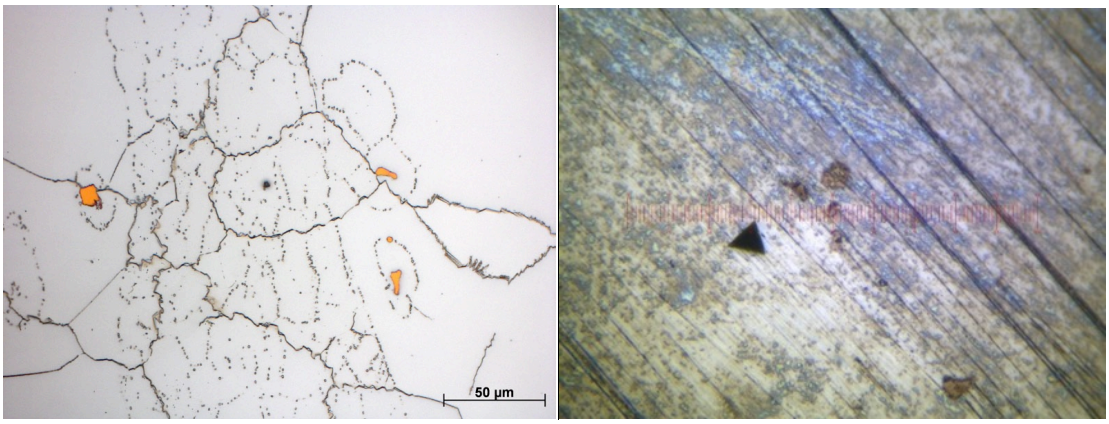

Fig. 19. Nitride particles on the surface of the Alloy 617 (a) from the literature [3] (b) from indentation platform microscope

The experimental results of hardness of nitride area at room temperature are shown in Fig. 20(a). There is an obvious effect of the nitride particles at room temperature under this load range. Through the Fig. 20(a), the values of hardness of nitride particles has distributed in the 3 different ranges. The first range is 6-7 GPa, which is close to the values of overall hardness of Alloy 617 (4-5 GPa). The second range is 10-14 GPa, which covers the most nitride particles. The third range is 18-21 GPa, which is the largest value range of hardness of nitride particles. To analysis the difference of the hardness of different area in the nitride particles, further SEM and EDX analysis will be performed. The element composition at the indented point/area was measured and compared. It shows that hardness value increases with the weight percentage of Ti and N. A linear fitting is used to estimate the relation between the hardness and weight percentage of Ti and N, which is also shown in the Fig. 20(b).

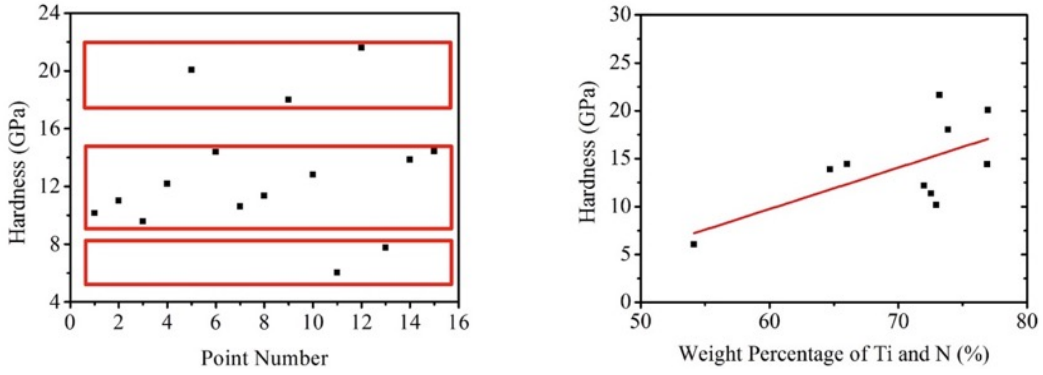

(a) (b)

Fig. 20. (a) Hardness and reduced modulus of different nitride areas at room temperature and (b) the relation between hardness and weight percentage Ti and N.

2.3. Crack growth testing at 800°C

The effect of varying loading frequency and the application of a hold-time were studied for Alloy 617 at 800 °C. Fatigue crack growth experiments were done in general accordance with ASTM standard E647 [28]. Direct current potential drop methodology was used to monitor crack length at 800 °C. Additionally, several tests were performed to measure the crack growth response to cyclic overloads.

2.3.1. Experimental Procedures

2.3.1.1. Specimen Design

Compact tension, C(T), specimens were machined from the as-received Alloy 617 in the L-T orientation. Nominal specimen width of $W = 25.4$ mm and nominal thickness of $B = 6.4$ mm were used for the first set of specimens, with a subsequent redesign of $W = 40$ mm and $B = 4.2$ mm for the purpose of achieving higher stress intensity ranges (ΔK) during testing while also conforming to the uncracked ligament requirement of ASTM standard E647 section A1.2.6.1 [28]. Machined notches were a minimum length of $0.2W$. Side grooving was used on many samples in the first set of specimens to reduce surface effects and reduce the necessary loads for crack growth, and was used on all of the second set of specimens. Side grooving reduced the effective thickness to $B_n = 5.9$ mm and $B_n = 3.76$ mm for the first and second sample sets, respectively. Current leads were attached by spot welding onto top and bottom faces of the sample along the load line as recommended in ASTM E647 [28]. Voltage leads were spot welded onto the front face above and below the notch on opposite sides of the sample as recommended in ASTM E647 (Fig. 21) [28]. Dimensioned drawings of C(T) specimens are given in Fig. 22 and Fig. 23 for the two C(T) sample geometries used in this work.

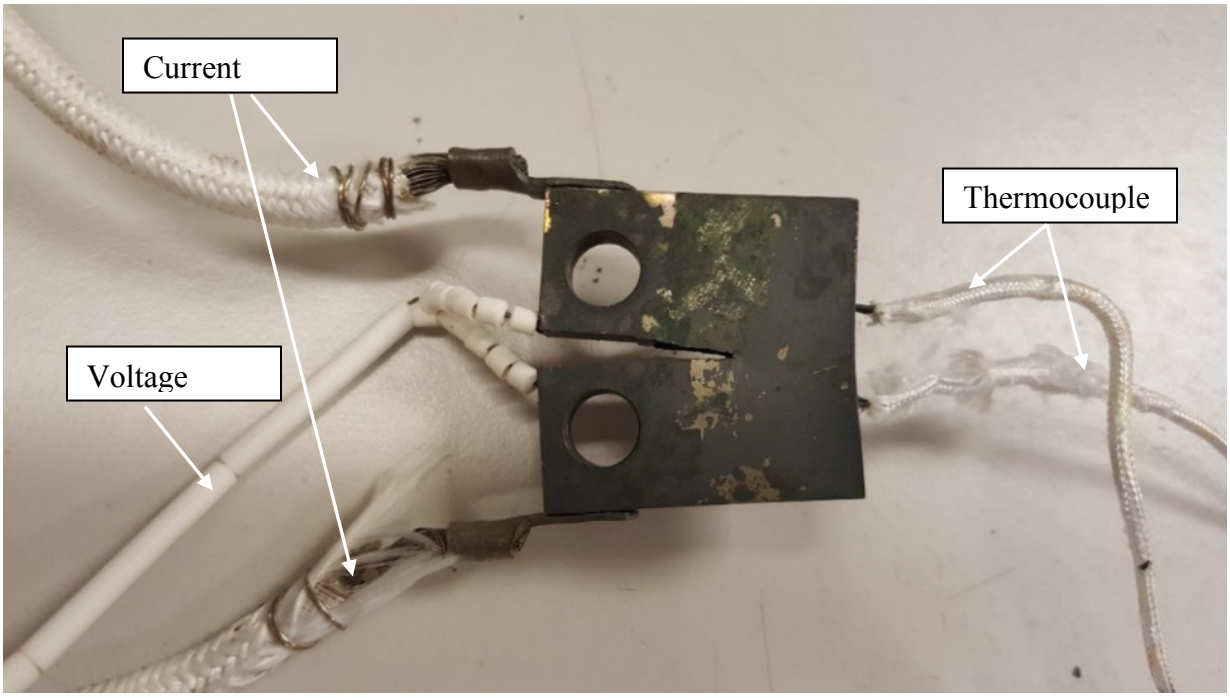

Fig. 21. A typical sample used for testing at 800°C.

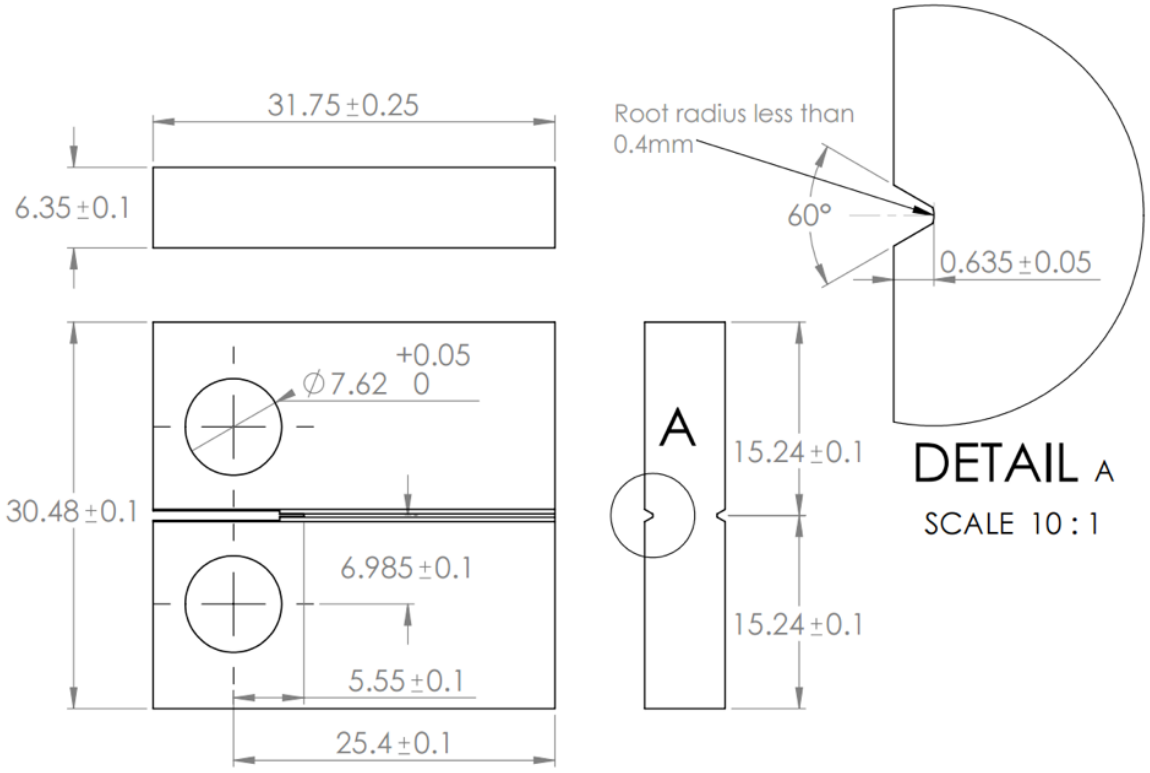

Fig. 22. C(T) specimen geometry of samples 08-20. All dimensions in mm.

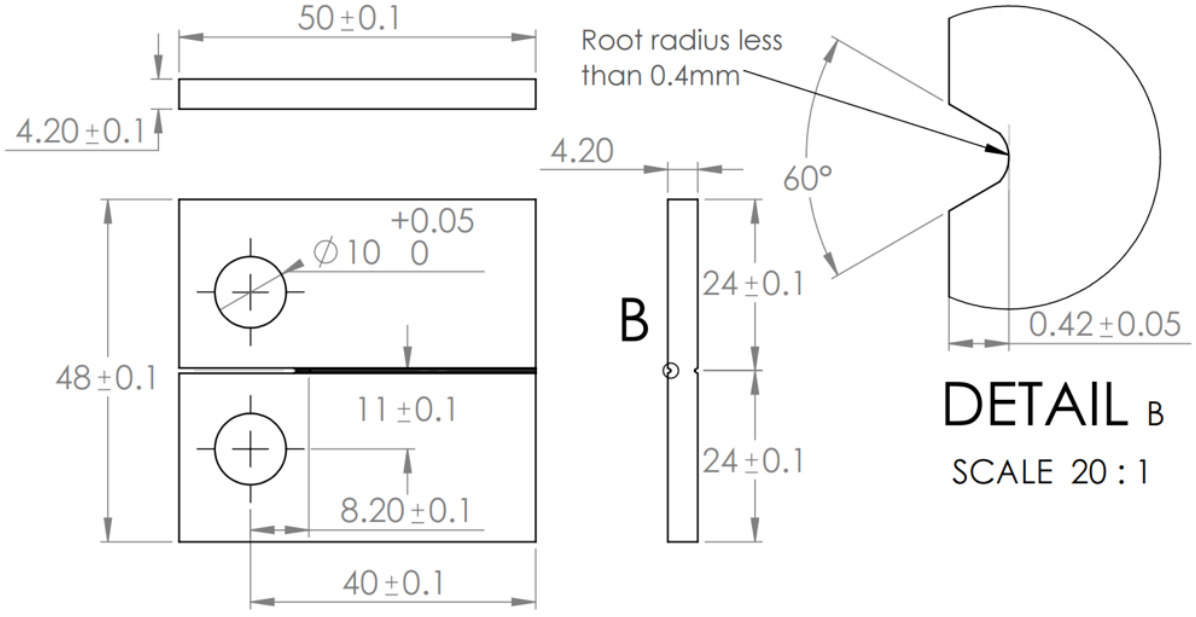

Fig. 23. C(T) specimen geometry of samples 21-28. All dimensions in mm.

2.3.1.2. Experimental Setup

A 250 kN capacity computer controlled servo-hydraulic MTS load frame was used with a 25 kN load cell for load controlled testing. Heating was accomplished via an induction furnace in

laboratory air and loading was achieved using water cooled clevises. Type-K thermocouples were spot welded to the rear face of the C(T) samples away from stress zones for monitoring and controlling the temperature at 800°C. The full experimental setup is shown in Fig. 26.

Fatigue tests were performed at 800°C under constant force amplitude, increasing ΔK conditions, in laboratory air using three different triangular loading waveforms: 5Hz, 0.33Hz, and 0.05Hz. Additionally, a trapezoidal (hold-time) waveform was employed to test the creep-fatigue crack growth response. The hold-time waveform had an identical ramp rate to the 0.33Hz triangle wave, and an identical period to the 0.05Hz triangle wave. the selected ratio of minimum to maximum load, $R = P_{min}/P_{max}$, was 0.5 to avoid any effects of crack closure. Fig. 24 shows the loading waveforms used in this work. Finally, the response to cyclic overloads was tested using a 0.33Hz waveform, shown schematically in Fig. 25

.

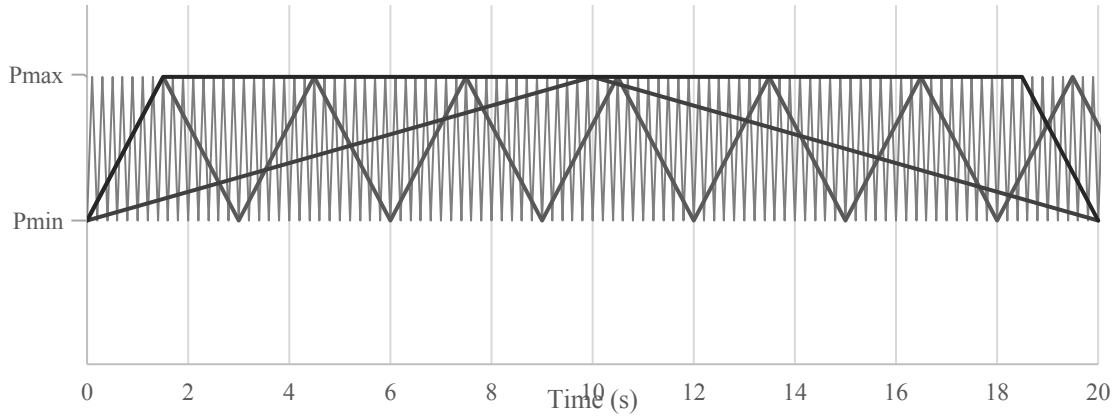

Fig. 24. Loading waveforms used for fatigue and creep-fatigue testing. A load ratio (Pmin/Pmax) of 0.5 was used in all tests.

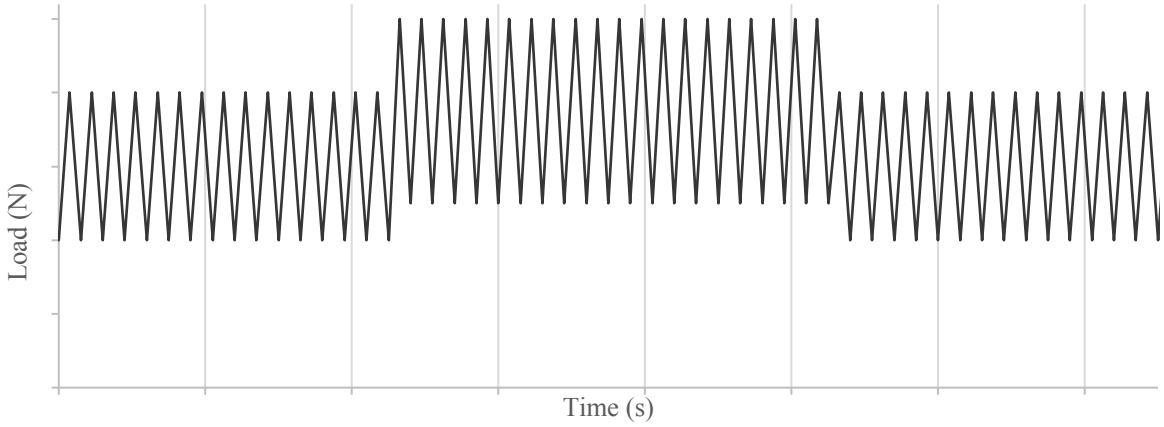

Fig. 25. Schematic of 0.33Hz waveform used to test the response to cyclic overloads.

In early tests, both side grooved and non-side grooved C(T) samples were used to determine what impact, if any, side grooving would have on the resulting crack propagation behavior. The lower required loads for a given stress intensity, K, level was beneficial for side grooved samples given

the persistent danger of deforming the clevises and/or loading pins during testing at 800°C. As an identifier, a "G" was added to all side grooved sample names.

Multiple thermocouples were used to control and monitor temperature. Large plastic deformation was observed in all samples tested at this temperature, making large portions of the data collected invalid under section 10.5 of E2760 for Creep-Fatigue Crack Growth Testing [29].

Heating was accomplished via an induction furnace in laboratory air and loading was achieved using water cooled clevises. Type-K thermocouples were spot welded to the rear face of the C(T) samples away from stress zones for monitoring and controlling the temperature at 800°C. The full experimental setup is shown in Fig. 26.

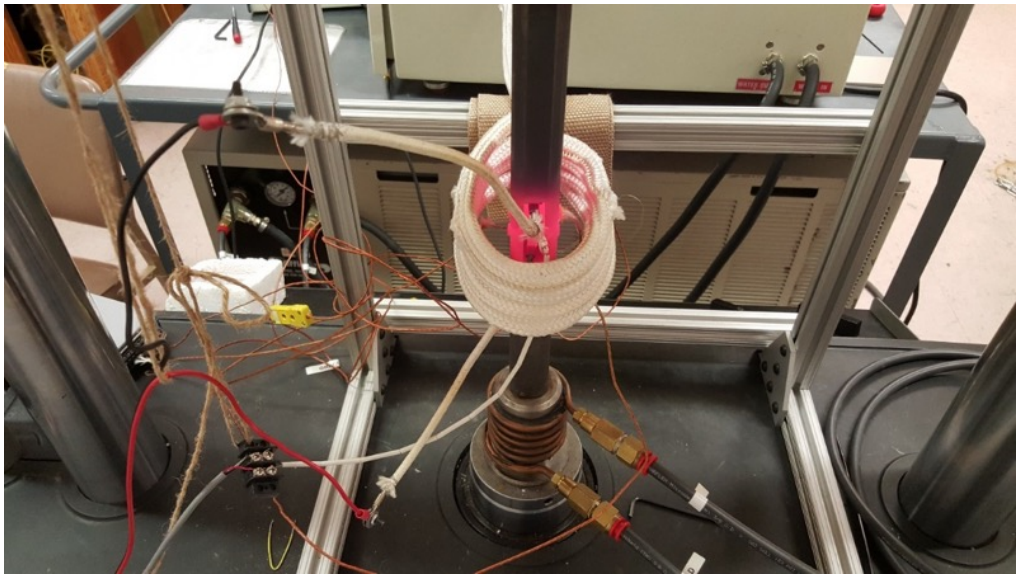

Fig. 26. Photo of the experimental setup running at 800 °C.

2.3.1.3. Crack Growth Test Procedures

Before testing, samples were precracked at room temperature with a load ratio (P_{max}/P_{min}) of 0.1 and loading frequencies between 15 and 40hz. A decreasing ΔK was used and care was taken to ensure that the final K_{max} during precracking did not exceed the initial K_{max} for which test data were obtained. Precracks were a minimum of $a/W = 0.48$ for the first set of samples and 0.27 for the second set.

For the first set of samples, a custom crack length calibration for EPD was developed to allow a greater range of crack length monitoring ($0.2 \leq a/W \leq 0.8$) than the ASTM standard calibration permits. This calibration is shown below (V is the measured voltage and Vr is the reference voltage).

$$V/V_r = 0.5089 + 2.3047\left(a/W\right) - 1.3901\left(a/W\right)^2 + 1.9854\left(a/W\right)^3 \qquad \text{Eq. 27}$$

$$a/W = -0.3979 + 0.7401\left(V/V_r\right) - 0.1099\left(V/V_r\right)^2 + 0.0024\left(V/V_r\right)^3 \qquad \text{Eq. 28}$$

For the second sample geometry, the calibration from E647 section A1.5.3.1 was used, which is applicable from $0.24 \leq a/W \leq 0.7$ [28].

A 10A current source was passed through all samples, with the nanovoltmeter having been balanced after heating to 800 ± 2°C to eliminate thermoelectric effects. The temperature was maintained at 800 ± 2°C for all tests, except where low temperature excursions were noted due to extreme deformation which altered the position of the sample within the induction coil significantly. A moving average was applied to voltage readings to smooth out the noise caused by operation at 800°C. A linear crack length correction was applied after examining the fracture surface according to E399. Initial transients in the EPD data were excluded, and the corrected precrack length was matched with the onset of stable EPD readings. The EPD data was then fit to the corrected crack lengths using a linear interpolation. An average error of +/-10% was observed in the EPD crack length data, compared to the fracture surface measurments, regardless of the calibration used. The secant method described in section X1.1 of E647 was used to compute crack growth rates at 0.25mm intervals throughout each test [28]. Crack growth rates observed in the first 0.25mm of crack growth were discarded and assumed to be an artifact of initial transient effects. The first few tests we conducted had large noise in the EPD signal and were reduced to a single average crack growth rate and average ΔK value based on fracture surface measurements.

2.3.1.4. Force Line Displacement Rate

An Epsilon 3648 high temperature extensometer was mounted to the test frame and used to approximate the force line displacement rate, which can be used to approximate relevant time dependent parameters, such as the transition time of the material. While a clip gauge that could take the measurement directly on the sample, it would have interfered with current and voltage leads used for EPD measurements. Instead, the extensometer's ceramic knife edges were made to contact the upper and lower clevises through the induction coil. After each millimeter of displacement during a test, the knife edges were disengaged and reengaged with the clevises in order to avoid contact with the induction coil (see Fig. 27). Data was later combined and compared had considerably less noise than the actuator data collected by the Instron, see Fig. 28.

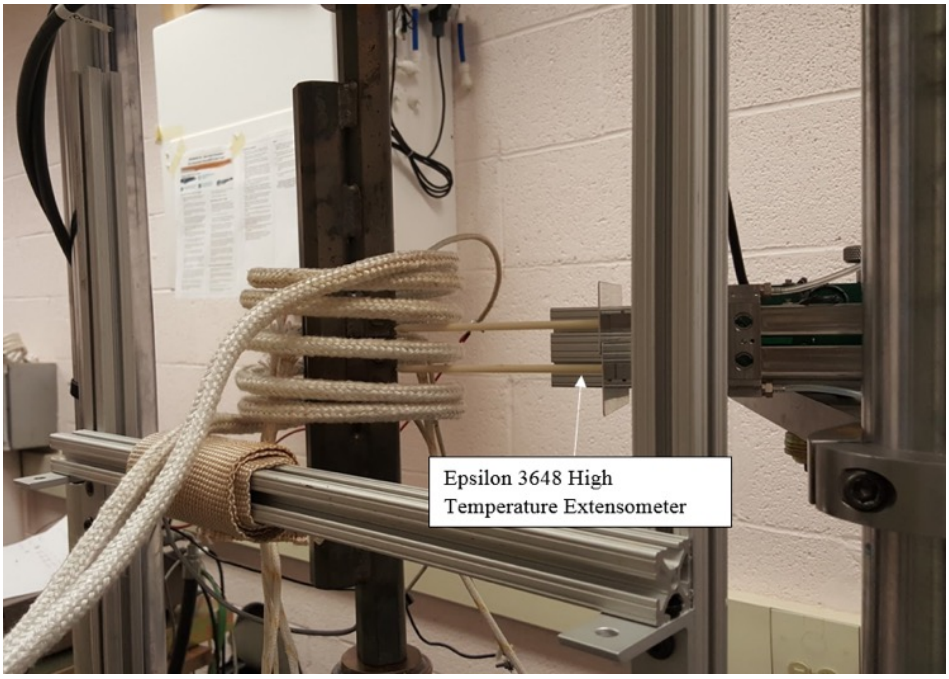

Fig. 27. High temperature extensometer used to approximate force line displacement throughout 1.5s-17s-1.5s hold-time testing of sample 27G.

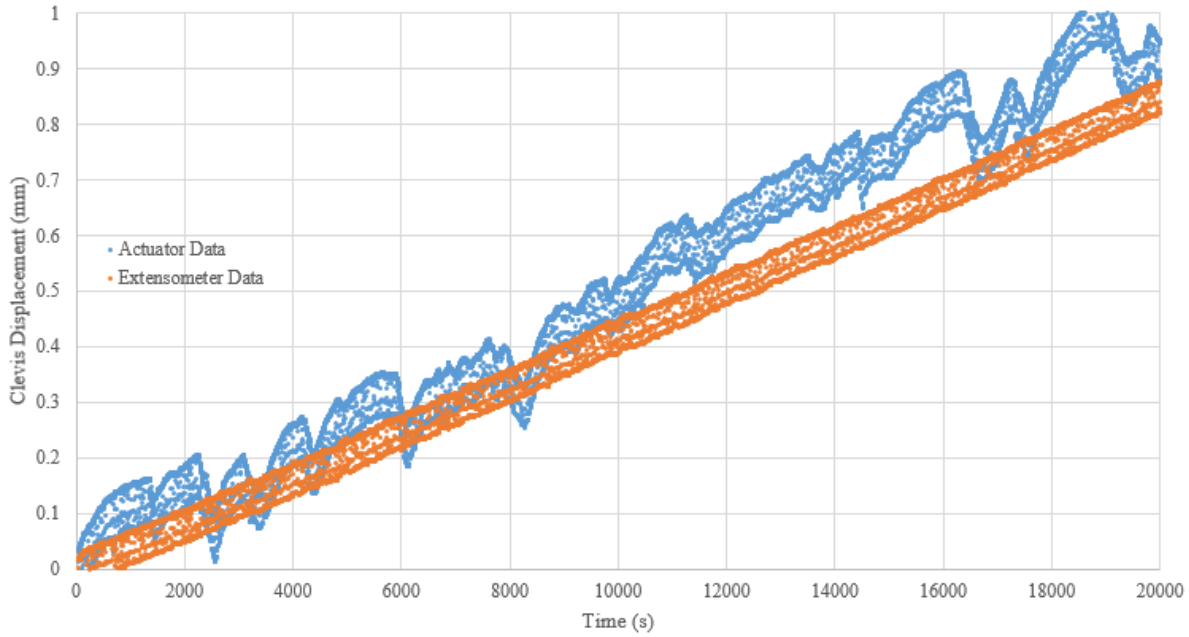

Fig. 28. Instron actuator and extensometer data comparison for sample 617-27G. A relevant force line displacement rate (per hold-time cycle) approximation can be made from the extensometer signal.

2.3.1.5. Fracture Surface and Crack Profile Analysis

Electrical discharge machining (EDM) was used to split some samples in half after each test, so that both the profile of the crack near the center of the sample and the fracture surface could be imaged using a Quanta 600 scanning electron microscope (SEM) equipped with energy dispersive

x-ray spectroscopy (EDS). The interior profile of the split sample was polished to a 0.05 μm finish with sandpaper, followed by a 1 μm and 0.05 μm polish with diamond suspension in order to image the crack profile near the center of the sample. EDS was used to perform line scans across crack tip profiles to explore the influence of oxygen. Additionally, the profiles of two samples were etched using Kalling's reagent, applied for 30 seconds with a swab then washed off with DI water.

The other half of the samples were fatigue cycled at room temperature to fracture the sample and reveal the fracture surface. Samples that weren't split were simply fatigued to fracture at room temperature and the fracture surface was examined.

2.3.2. Crack Growth Results at 800°C

2.3.2.1. Summary of Experiments

Table 6 provides an overview of the conditions used for each test. Samples 617-01 through 617-07 were used to gain experience with the capabilities of the experimental setup in terms of its capacity for handling high loads and/or long hold times, but produced no useable data. Samples 617-10 and 617-21G also produced no useable data due to deformation of the clevises and uneven heating, respectively. Samples 617-11G and 617-12 were used to test the creep crack growth response and the response to a 10s-60s-10s hold-time waveform, respectively, but both resulted in blunted crack tips and no crack growth. Data from 617-09G and 617-14G are not reported due to an inconclusive final crack length after fracture surface analysis was conducted. Finally, 617-30G, was used to test sustained load crack growth, but the test was halted after only 0.1 mm of growth because an EPD lead had detached from the sample. Due to its similarity to 610-10, 617-30G was not sectioned for profile analysis. As a result, no data is reported for 617-30G.

Table 6. Experimental matrix for C(T) samples used in this work. All experiments were performed at 800°C with a load ratio R=0.5.

Sample ID	P min (N)	P max (N)	Min ΔK or K (MPa√m)	Max ΔK or K (MPa √m)	Freq.	a/w (precrack)	a/w (final)	Length of test (hrs)	Total cycles	Final Force Line Disp. (mm)
617-08	778	1562	8.3	12.2	0.05	0.512	0.644	66.2	11910	2.9
617-10	n/a	1560	15.6	15.9	(creep)	0.523	0.528	33.4	(creep)	2.3
617-11G	n/a	748	17.0	18.3	(creep)	0.679	0.693	64.9	(creep)	5.8
617-12	650	1300	11.8	13.2	0.0125*	0.672	0.694	6.1	275	8.7
617-13GO	730	1460	8.6	8.8	0.33	0.5431	0.550	44.3	53200	0
617-15GO	730	1460	7.2	24.9	0.33	0.483	0.766	20.1	24140	7.2
617-16GO	730	1460	8.0	23.3	0.33	0.520	0.757	14.5	17420	5.8
617-17GO	730	1460	9.5	15.5	0.33	0.542	0.692	9.1	10910	1.4
617-18G	730	1460	8.3	9.0	0.05*	0.531	0.560	20.4	3670	1.3
617-19G	730	1460	8.3	10.9	0.05*	0.531	0.605	47.2	8500	4.0
617-20G	730	1460	7.9	22.8	5	0.511	0.751	1.7	30645	1.8
617-22G	1125	2250	7.8	12.8	0.33	0.271	0.458	23.2	27860	1.6
617-23G	1125	2250	7.9	23.9	5	0.272	0.640	3.5	63805	2.7
Sample ID	**P min (N)**	**P max (N)**	**Min ΔK or K (MPa√m)**	**Max ΔK or K (MPa √m)**	**Freq.**	**a/w (precrack)**	**a/w (final)**	**Length of test (hrs)**	**Total cycles**	**Final Force Line Displacement (mm)**
617-24G	875	1750	8.1	11.0	0.05*	0.394	0.488	75.1	13520	7.8
617-25G	875	1750	7.2	7.6	0.05	0.333	0.357	93.2	16770	1.0

617-26G**	800	1600	7.9	9.5	0.05	0.400	0.491	142.8	25700	4.7
617-27G	750	1500	9.2	13.6	0.05*	0.483	0.599	57.1	10280	10.7
617-28GO	750	1500	7.9	19.3	0.33	0.431	0.680	28.0	33600	5.8
617-29G	750	1500	9.1	11.8	0.05	0.475	0.572	62.2	11190	5.5
617-31G	750	1500	11.0	15.9	0.05	0.547	0.643	34.6	6220	9.3
617-32G	750	1500	12.2	17.6	0.05*	0.552	0.654	20.0	3600	12.6
617-33G	-	1500	23.0	30.2	(creep)	0.553	0.627	19.7	(creep)	11.3

*Denotes samples used to test a 0.05 Hz hold time equivalent waveform.

**Low temperature excursions of approximately 10°C occurred near the end of the test due to an insufficient drive signal from the induction furnace's PID controller.

2.3.2.2. Crack growth rates

Crack growth rates per cycle were compared to stress intensity ranges for all waveforms. Because of large amounts of noise in their EPD datasets, samples 617-08, 617-09G, 617-18G and 617-19G were all reduced to single points based on their fracture surface measurements for the beginning and ending of the experiments. Fig. 29 shows data from every other fatigue and hold time test. Initial transient data (high crack growth rates at the beginning of each experiment) are excluded. Fig. 30 shows the same data plotted as a function of time vs. Kmax, with the addition of sustained load crack growth data from 617-33G.

Fig. 29 shows that an unambiguous increase in crack growth rate was observed from 5 Hz to 0.33 Hz, but further reduction in frequency (0.05 Hz triangular or trapezoidal loading) failed to produce higher crack growth rates than the 0.33 Hz waveform, up to about 11.5 MPa$\sqrt{}$m. In fact, the 0.05 Hz triangular waveform appears to produce crack growth rates per cycle closer to 5 Hz than 0.33 Hz for the smallest ΔK levels in the dataset. At stress intensity ranges higher than 11.5 MPa$\sqrt{}$m, both the 0.05 Hz triangle and trapezoidal waveforms appear to cause an increase in crack growth rate per cycle above those obtained for the 0.33 Hz triangle waveform.

Fig. 31 shows the results obtained with sample 617-33G for sustained load crack growth. Crack growth per unit time is correlated with the C* parameter and shows good agreement with the power law fit reported by Rödig et al., but may be construed as resulting in slightly lower rates [30].

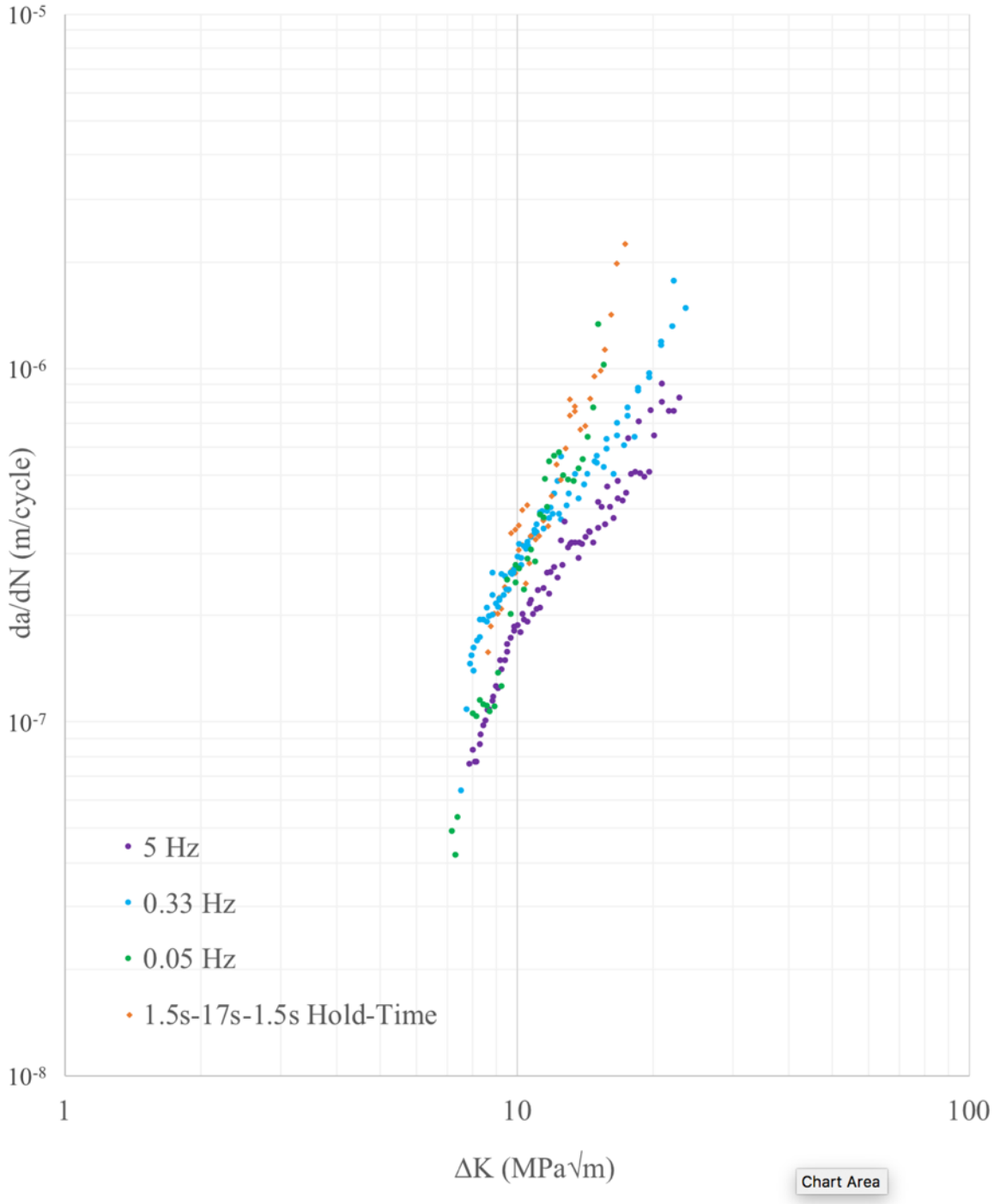

Fig. 29. Cyclic crack growth rates vs stress intensity ranges.

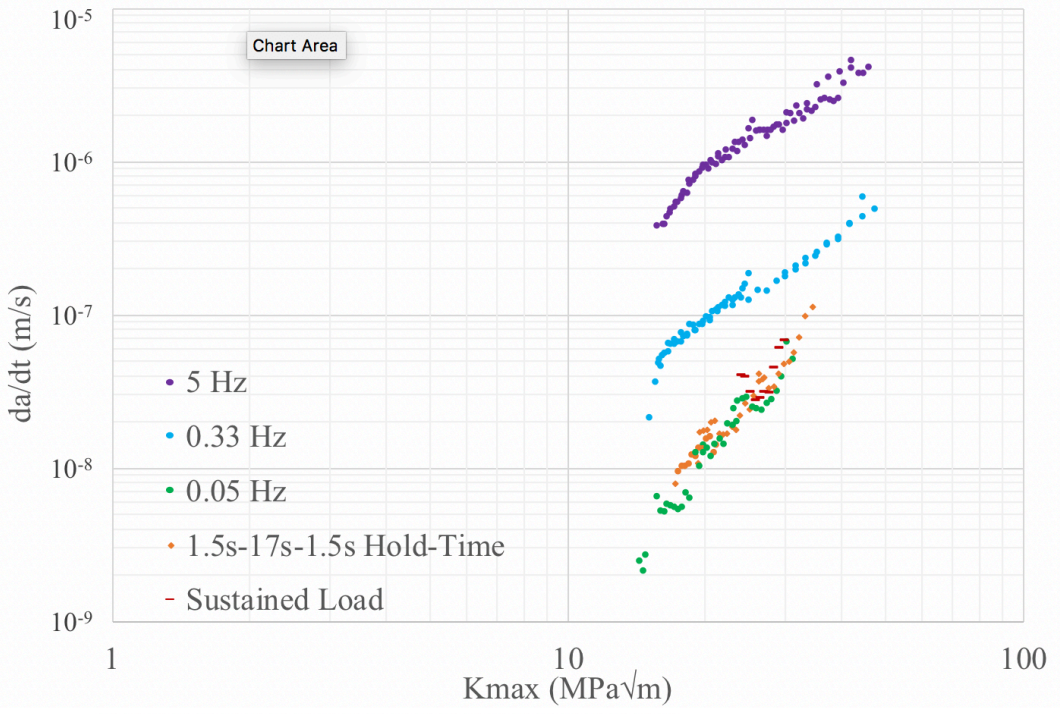

Fig. 30. Crack growth rates vs stress intensity ranges.

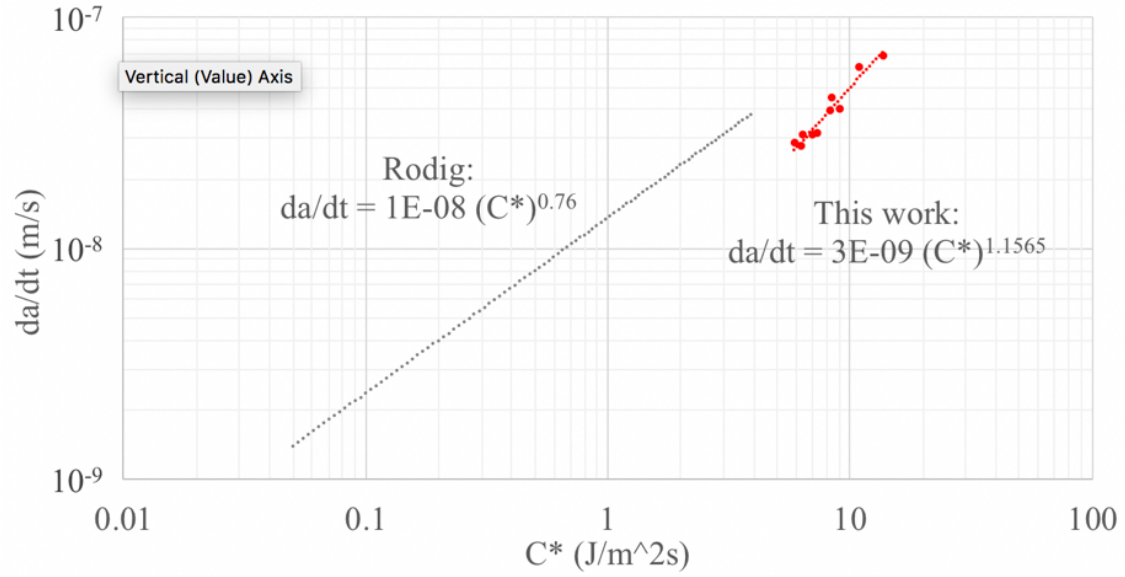

Fig. 31. Sustained load crack growth data for sample 617-33G compared with power law fit for the C* parameter reported by Rödig *et al.* [30].

For the first set of samples, data collected for ΔK levels at and above 11 MPa√m are in violation of section A1.2.6.1 of ASTM Standard E647, which specifies that the uncracked ligament at the end of a test have the following relationship to K_{max}:

$$W - a \geq (4/\pi) * (Kmax/\sigma_{flow})^2 \quad \text{Eq. 29}$$

where σ_{flow} is the flow stress determined at the same temperature at which the tests are conducted. For the second set of samples, valid data by Eq. 29 was collected up to ΔK=13.5 MPa√m. However, almost all of the data for both sample sets are in violation of section 10.5 of ASTM Standard E2760, which states that force line displacement is not to exceed 0.05W, which translates to 1.27 and 2.0mm for the first and second sample sets, respectively. Force line displacement was as much as 11mm by the end of hold-time tests.

2.3.2.3. Fractography

Fracture surfaces are shown and compared on the millimeter scale in Fig. 32 through Fig. 37, with the beginning and ending of each increasing stress intensity test marked with its corresponding stress intensity range. The direction of crack propagation is from left to right. In Fig. 32 and Fig. 35 samples tested with the same waveform but different specimen geometries are aligned and scaled to contrast the effects of sample thickness and ΔK on the fracture surface character. Samples 617-08 through 617-20G have the dimensions specified in Fig. 22, while all other samples have the dimensions specified in Fig. 23. The thicker (but smaller in length and width) samples were scaled up in order to map their beginning and ending ΔK levels onto the thinner (but larger in length and width) samples. This allows for a direct visual comparison of fracture surface character. For the sake of clarity, "thick" will be used to describe the specimen geometry in Fig. 22, while "thin" will refer to the geometry in Fig. 23.

All loading waveforms resulted in transgranular cracking at the lowest stress intensities tested. The 5 Hz waveform samples shown in Fig. 32 display slight fracture surface roughness only at the highest ΔK levels tested for both specimen geometries. Likewise, for the 0.33 Hz waveform, although there may be a slight difference in the stress intensity that produces this roughness in the two specimen geometries. In Fig. 33, two thick 0.33 Hz samples display the reproducibility of rough features starting around 15.5 MPa√m. In Fig. 34, two thin 0.33 Hz samples show the reproducibility of rough features starting around ΔK = 12.8 MPa√m, regardless of load amplitude. It should be noted that in Fig. 34, sample 617-28GO was used for a cyclic overload test, but given the small effect the overload blocks had on crack growth, the fracture surface is considered comparable to sample 617-22G.

Similarly, for the 0.05 Hz triangular loading waveform, Fig. 35 shows the impact of specimen geometry at the same stress intensity ranges and almost identical load amplitudes for samples 617-08 and 617-26G. The thinner sample shows significantly more roughness. Also shown in Fig. 35 is the fracture surface of 617-25G, which displayed crack growth that appears to be near the fatigue threshold, evidenced in Fig. 29 by the sharp increase in 0.05 Hz growth rates from ΔK ~ 7 to 9 MPa√m. Similar crack growth data near the fatigue threshold was collected for sample 617-15G at 0.33 Hz. Fig. 36 shows samples 617-29G and 617-31G. Like 617-26G, 617-29G appears to have more surface roughness than 617-08 for comparable ΔK values. The roughness also appears to be more pronounced near the surface of the sample than in the center. Finally, at the highest stress intensities applied, sample 617-31G displays a significant increase in roughness after ΔK ~ 12 MPa√m. It should be noted that at the highest stress intensities investigated in this work, samples were highly compliant, as shown by the depressed surface of 617-31G. It is also clear that the crack is longest at the surface (the sidegroove) of 617-31G.

Fig. 37 shows the fracture surface of 617-33G, a sustained load crack growth test, whose rough features began almost immediately after starting the experiment. These features are comparable to the features observed at the end of the hold time tests for 617-24G, 617-27G, and 617-32G, and the end of the 0.05 Hz triangle wave test for 617-31G. Finally, for the transgranular portions of samples tested at 0.33 Hz and 5 Hz, fatigue striations were visible, as shown in Fig. 38 and Fig. 39, while no striations were detectable for the transgranular portions of 0.05 Hz samples. Overall, at 5 Hz and 0.33 Hz, while some roughness developed the crackpartht remained transgranualr with striation formation, while for 0.05 Hz and hold times tests, there was a transition at higher ΔK to rough features akin to sustained load creep crack growth.

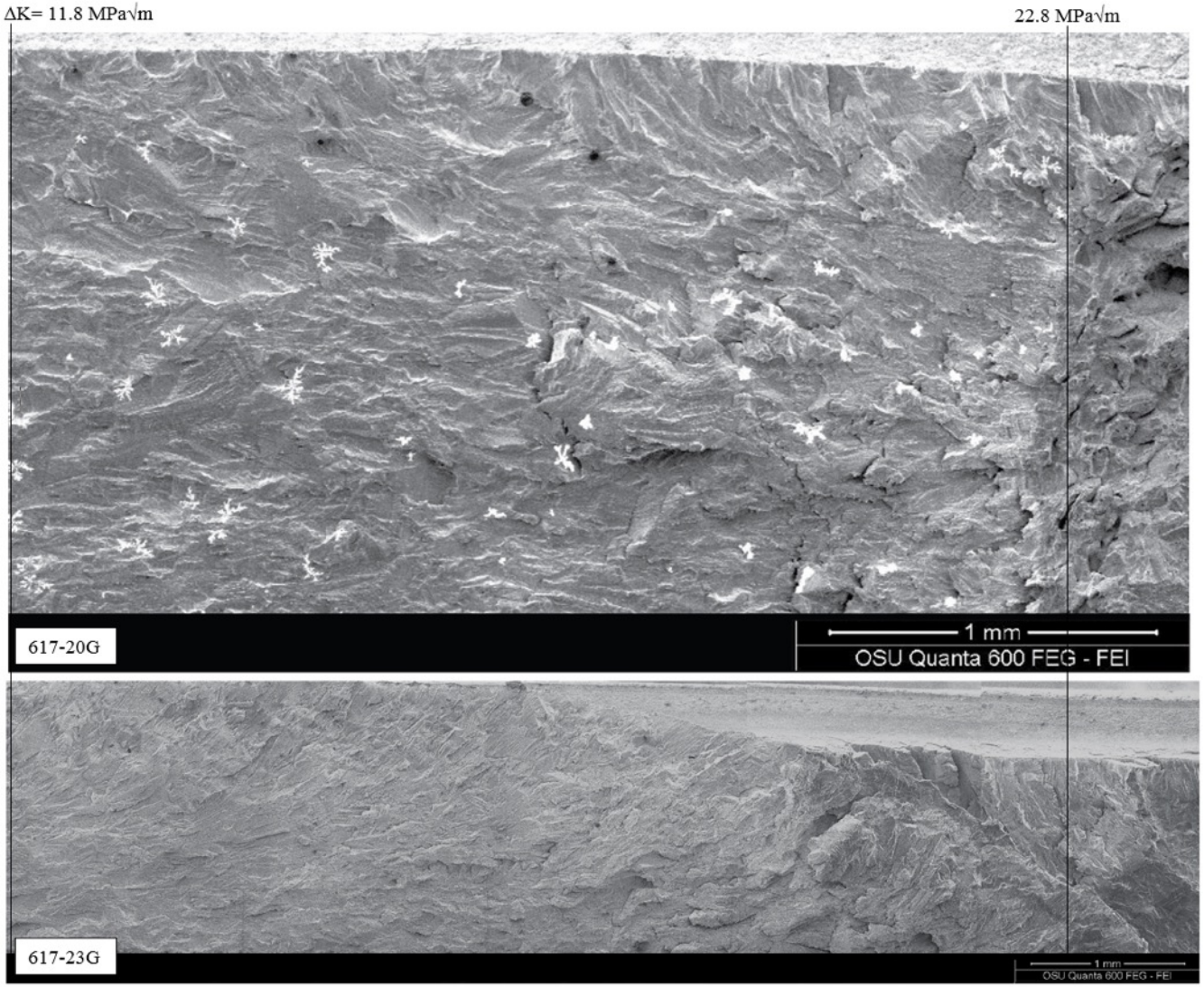

Fig. 32. Fracture surface comparison of samples 617-20G and 617-23G with ΔK levels superimposed. Crack propagation is from left to right.

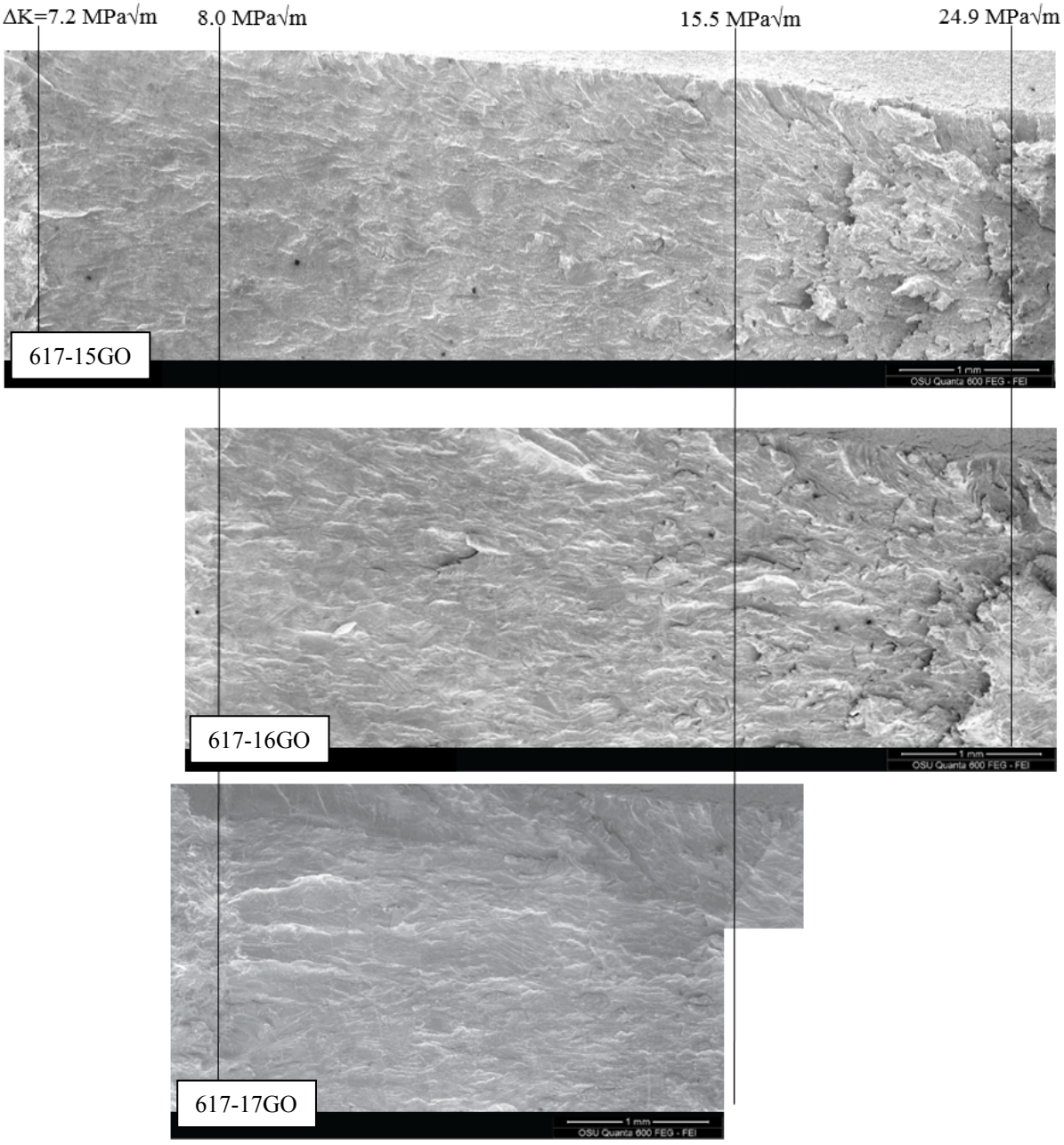

Fig. 33. Fracture surface comparison of samples 617-15G, 617-16GO and 617-17GO with ΔK levels superimposed. Crack propagation is from left to right.

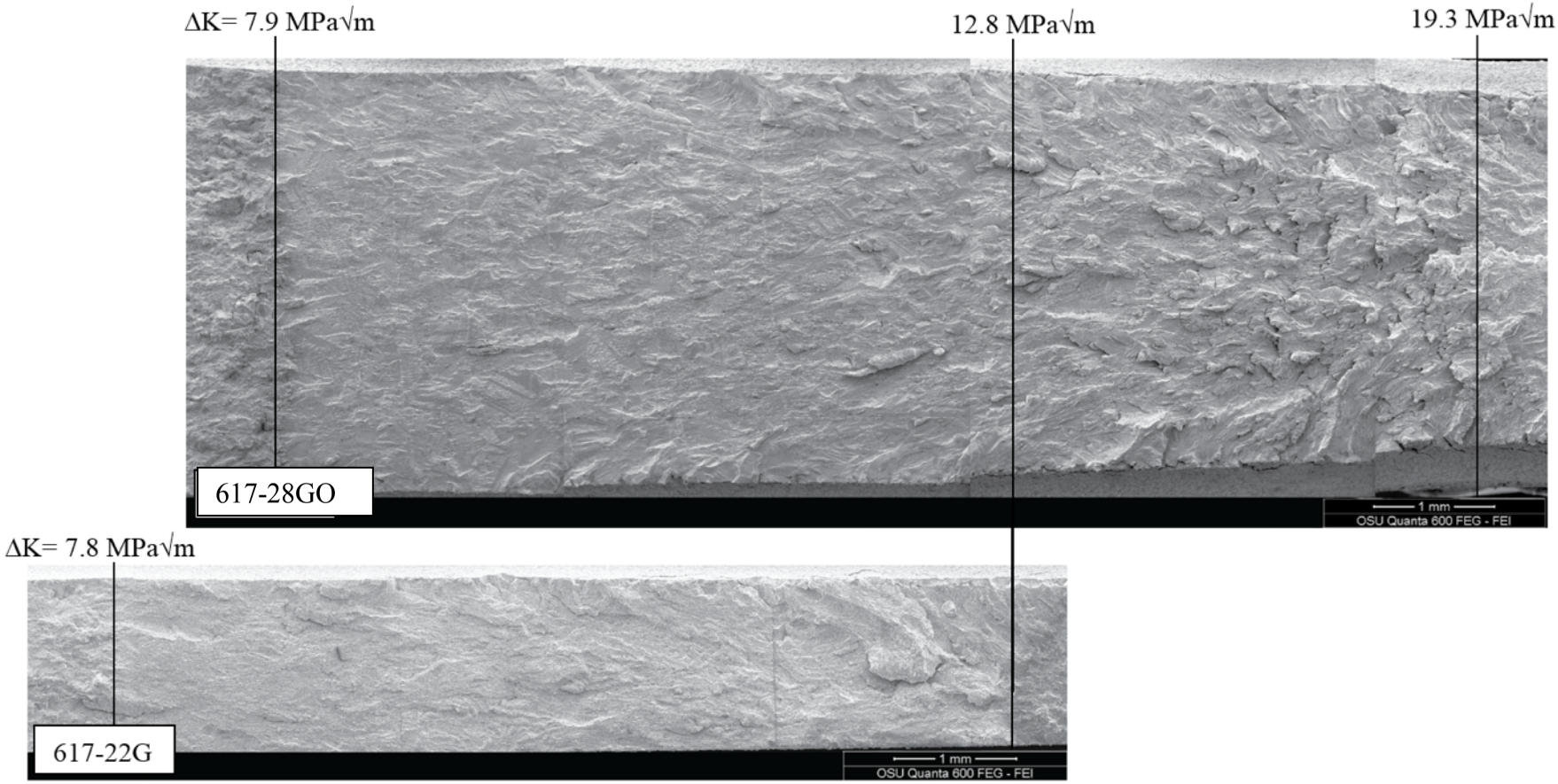

Fig. 34. Fracture surface comparison of 617-22G and 617-28G with ΔK levels superimposed. Crack propagation is from left to right.

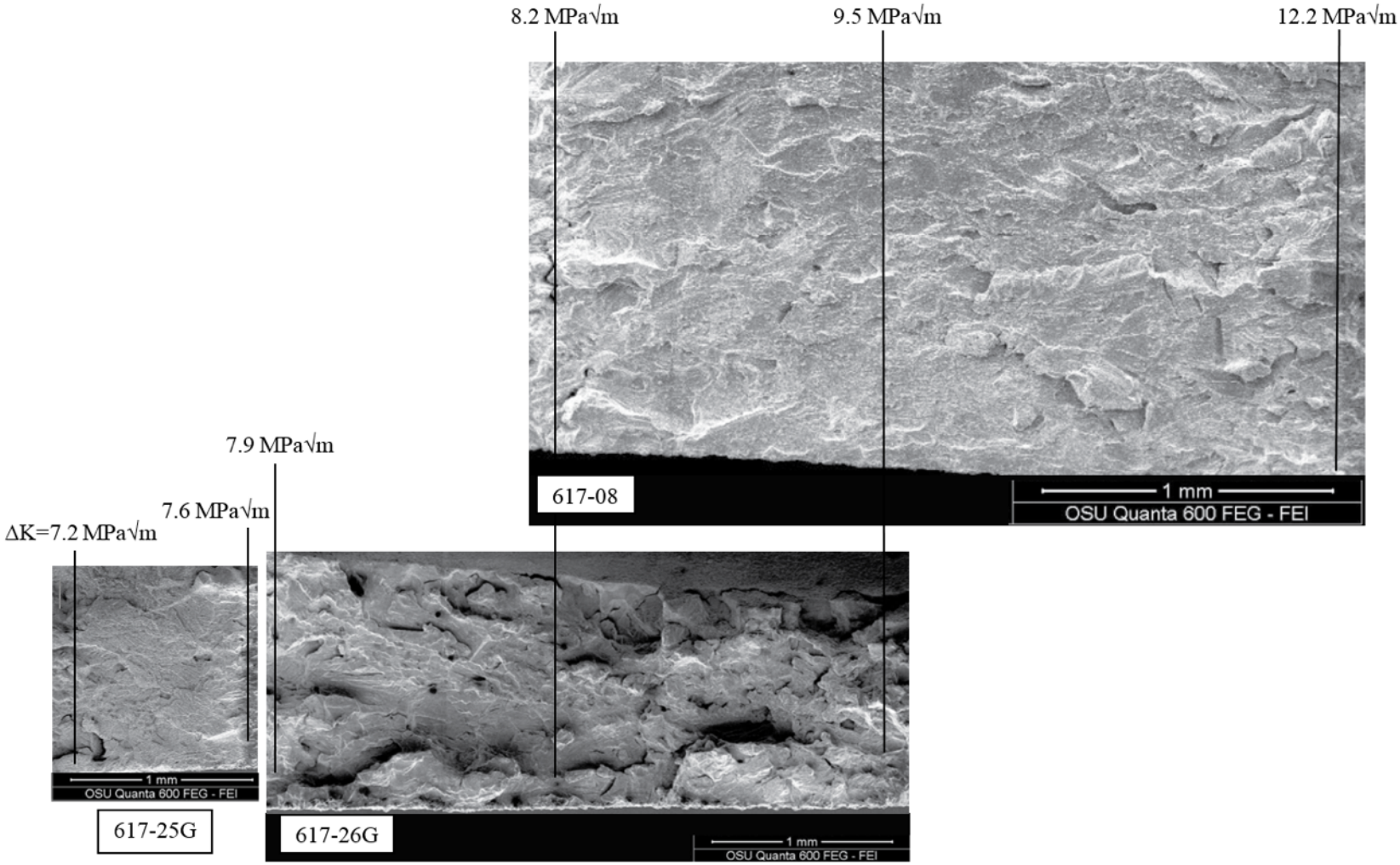

Fig. 35. Fracture surface comparison of samples 617-08, 617-25G and 617-26G with ΔK levels superimposed. Crack propagation is from left to right.

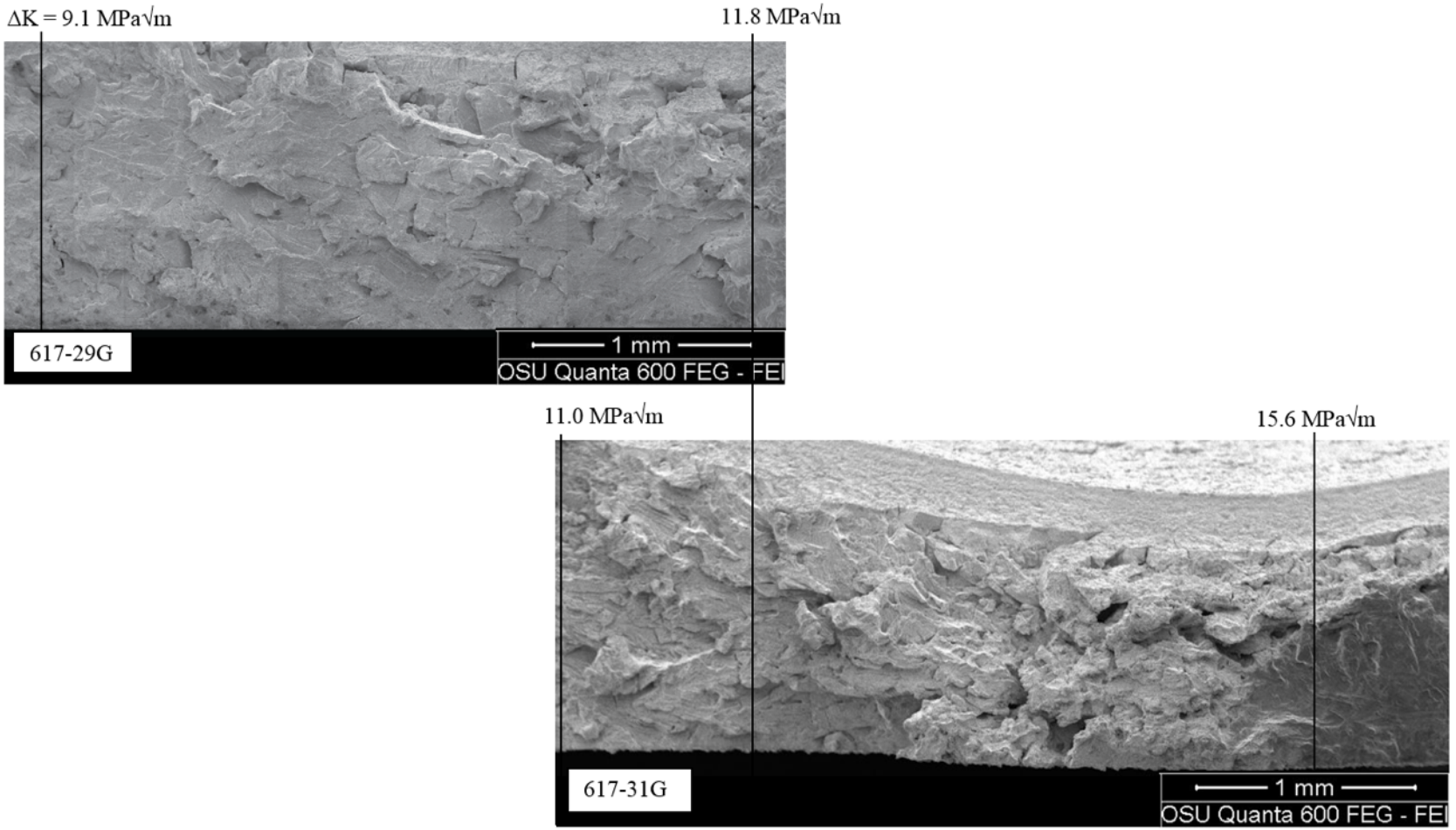

Fig. 36. Fracture surface comparison of samples 617-29G and 617-31G with ΔK levels superimposed. Crack propagation is from left to right.

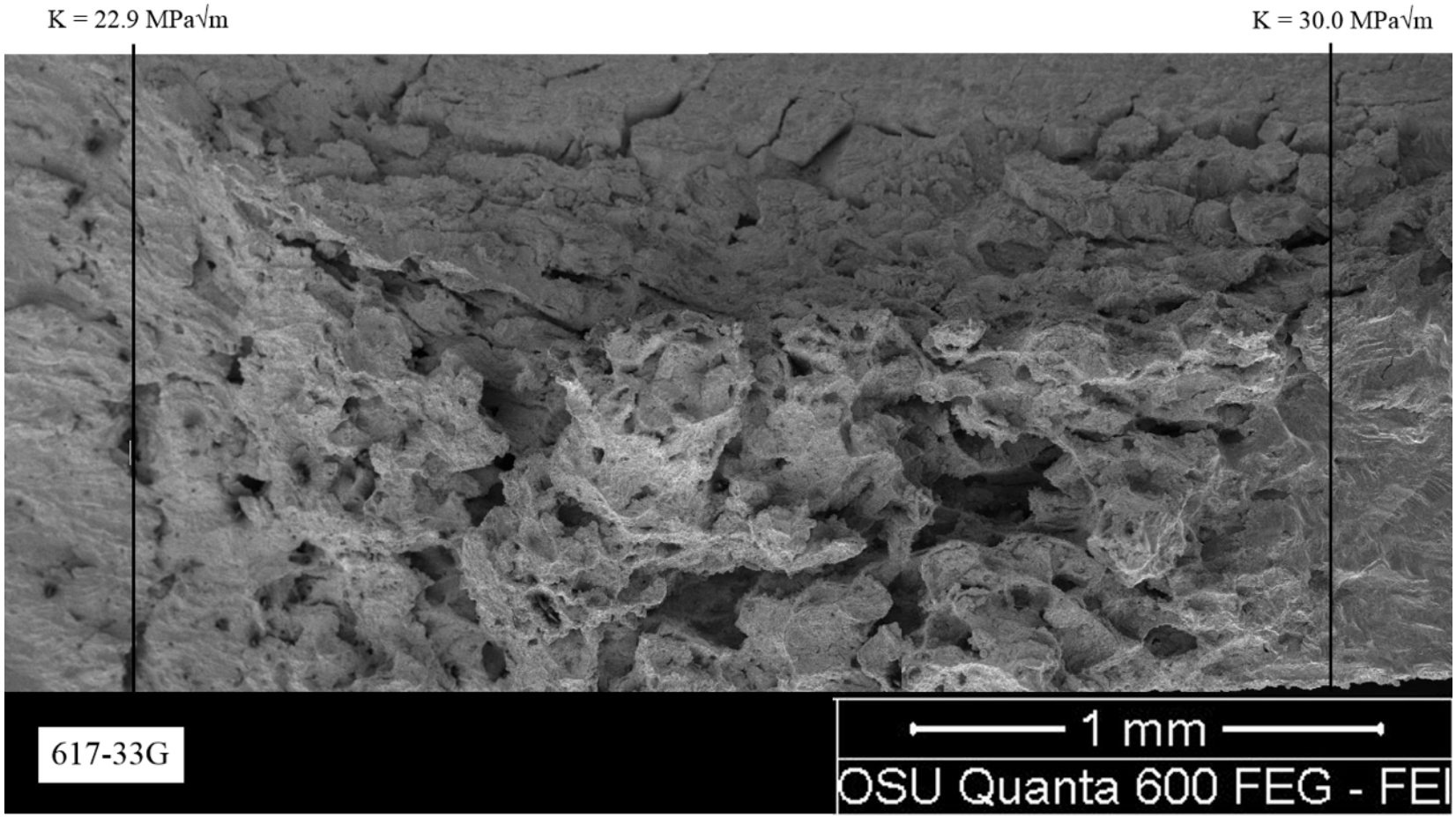

Fig. 37. Fracture surface of 617-33G with K levels superimposed. Crack propagation is from left to right.

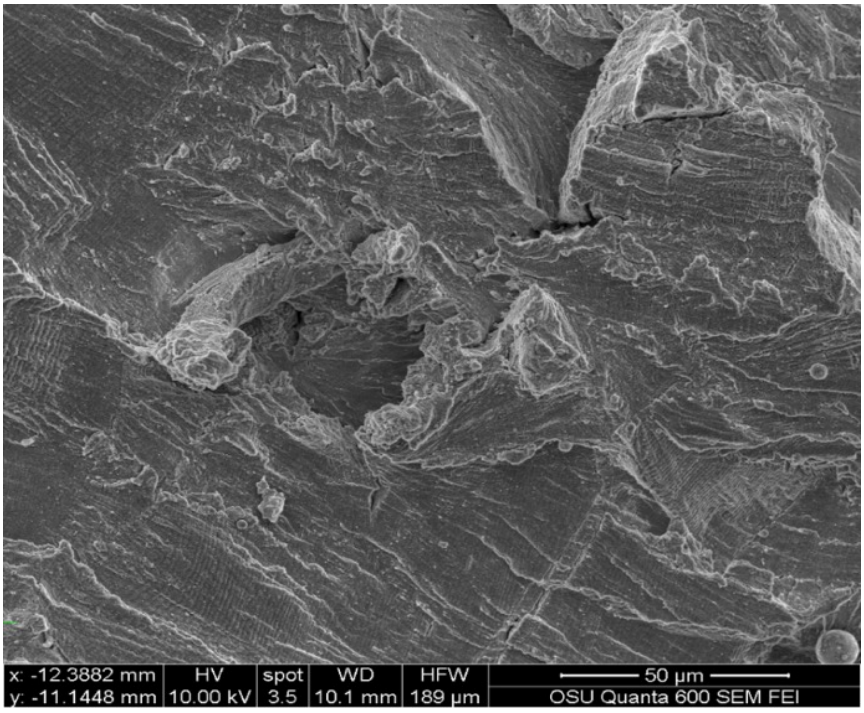

Fig. 38. Striations on the fracture surface of 617-15GO, tested at 0.33 Hz. Crack propagation is from left to right.

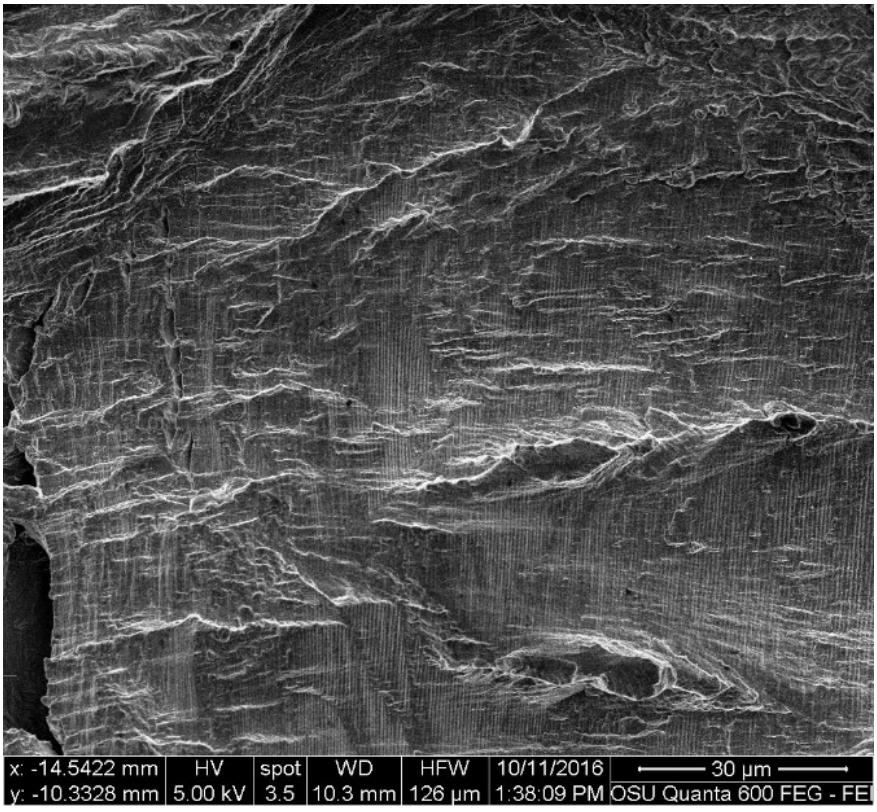

Fig. 39. Striations on the fracture surface of 617-20G, tested at 5 Hz. Crack propagation is from left to right.

2.3.2.4. Crack Tip Profiles

Crack tip profiles were examined at several scales and compared to fracture surfaces to study crack growth mechanisms. EDS line scans were performed to quantify the extent of oxygen's interaction at the crack tip under different loading conditions. Fig. 40 - Fig. 44 show crack tip profiles for samples 617-19G, 617-08, 617-16GO, 617-17GO, and 617-20G, and the corresponding oxygen concentrations in the crack tips at multiple locations. It should be noted that the wt% oxygen detected is not absolute, but can be used to compare the relative interaction of oxygen under different loading conditions.

It is important to consider the effect may have on the micromechanism at play in each crack tip profile. Comparisons can be made to fractographs for this purpose. The hold-time waveform resulted in the highly branched profile when viewed on a 500μm scale, shown in Fig. 40b, and a highly oxidized crack tip, shown in Fig. 40c. 617-19G's fracture surface (not shown) is predominantly transgranular in character, but displays more roughness than the corresponding 0.05 Hz triangular waveform. Fig. 41 shows that the 0.05 Hz triangular waveform produced a similar oxygen concentration in the crack wake but much less so at the crack tip itself. The 0.05 Hz triangular waveform sample in Fig. 41 was subjected to a higher ΔK, but resulted in less branching than the trapezoidal sample in Fig. 40.

The amount of branching appears to be directly related to the fracture surface roughness. Samples 617-16GO and 617-17GO in Fig. 42 and Fig. 43, respectively, bear this out. Both samples were tested at 0.33 Hz. 617-16GO shows branching at a high ΔK, corresponding to the rough fracture surface in Fig. 33. 617-17GO displayed no surface roughness – the test was stopped just before the prerequisite ΔK level (~ 16.2 MPa$\sqrt{m}$) for roughness observed in 617-15G and 617-16GO. The interaction of oxygen at the crack tip appears stronger in the sharp tip shown in Fig. 43(b) than in the bifurcated tip shown in Fig. 42(b).

The 5 Hz sample in Fig. 44 shows similar oxygen concentrations to those in the 0.33 Hz sample in Fig. 42. The tests ended at similar ΔK levels. At lower magnifications, excursions were noted on the crack wake of 617-20G (not shown), which may have evolved to bear resemblance to the branched tip of 617-16GO if given more time, but as shown in Fig. 30, the 5 Hz waveform results in a much faster growth rate per unit time, and as a result, a smaller force line displacement.

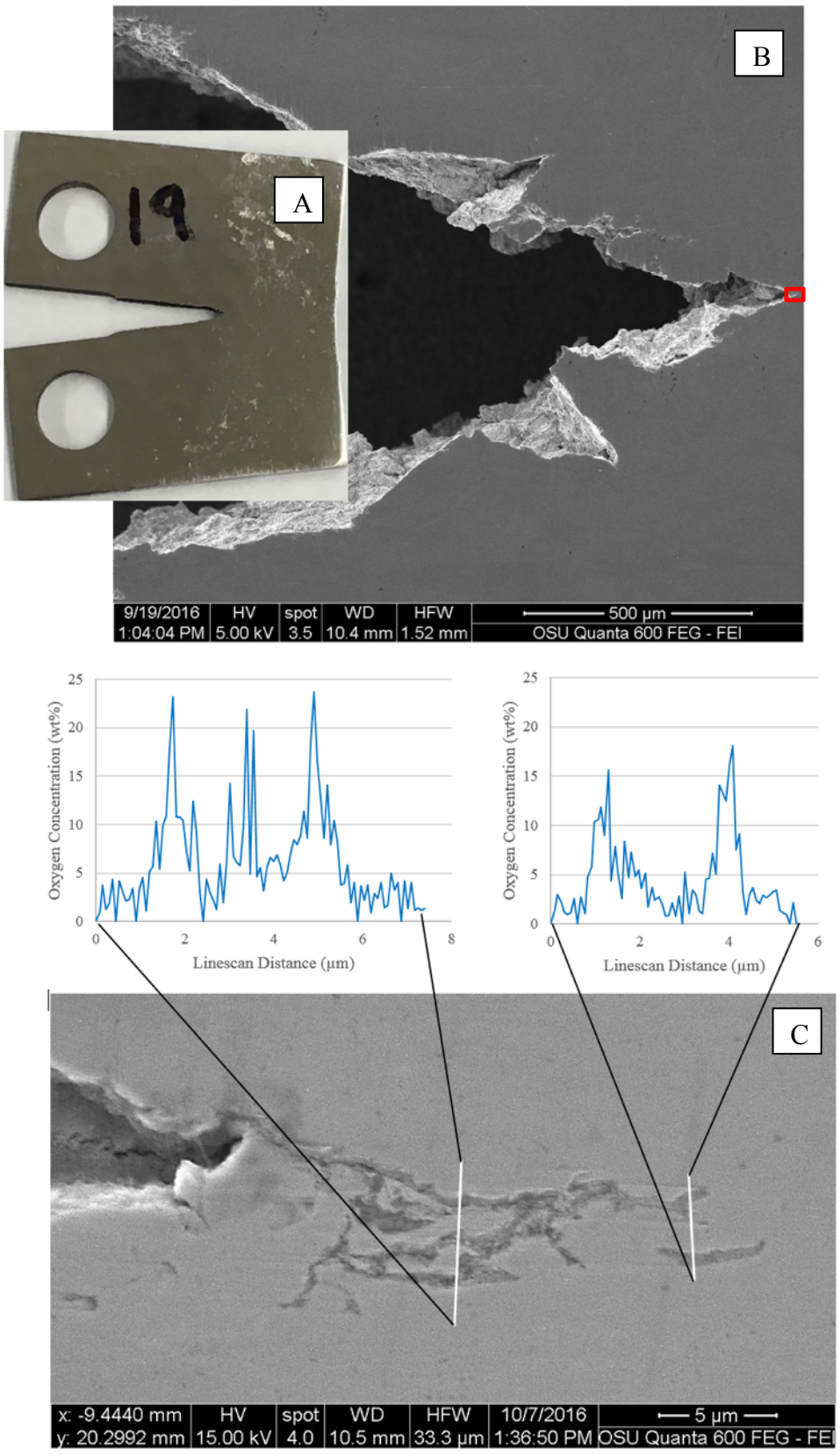

Fig. 40. (A) 617-19G post experiment, tested with a hold-time waveform with final ΔK=10.9 MPa√m, (B) SEM micrograph of crack tip, (C) Enlarged crack tip region with oxidation quantified by EDS line scans.

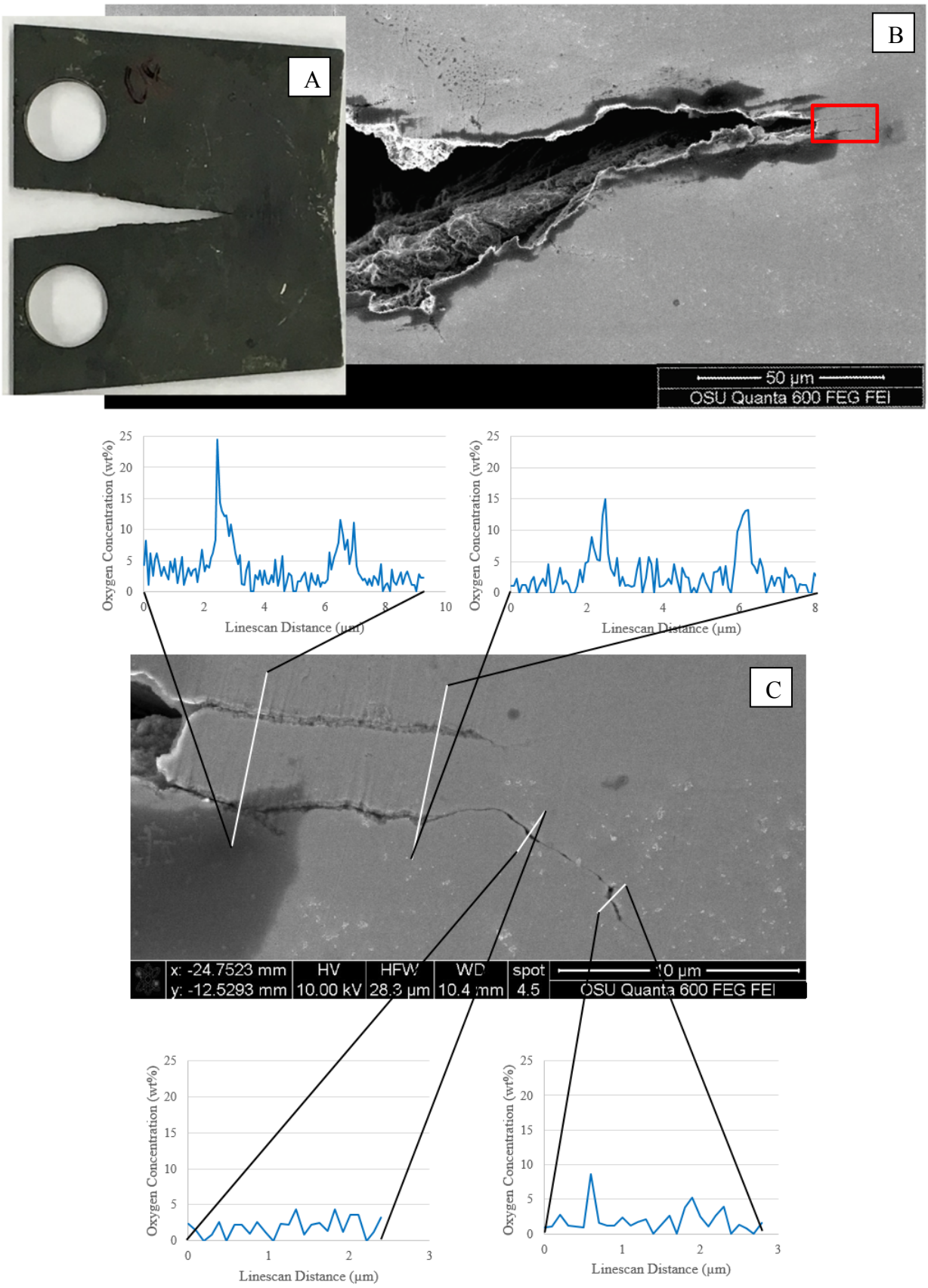

Fig. 41. (A) 617-08 post experiment, tested at 0.05Hz with final ΔK=12.2 MPa√m, (B) SEM micrograph of crack tip, (C) Enlarged crack tip region with oxidation quantified by EDS line scans.

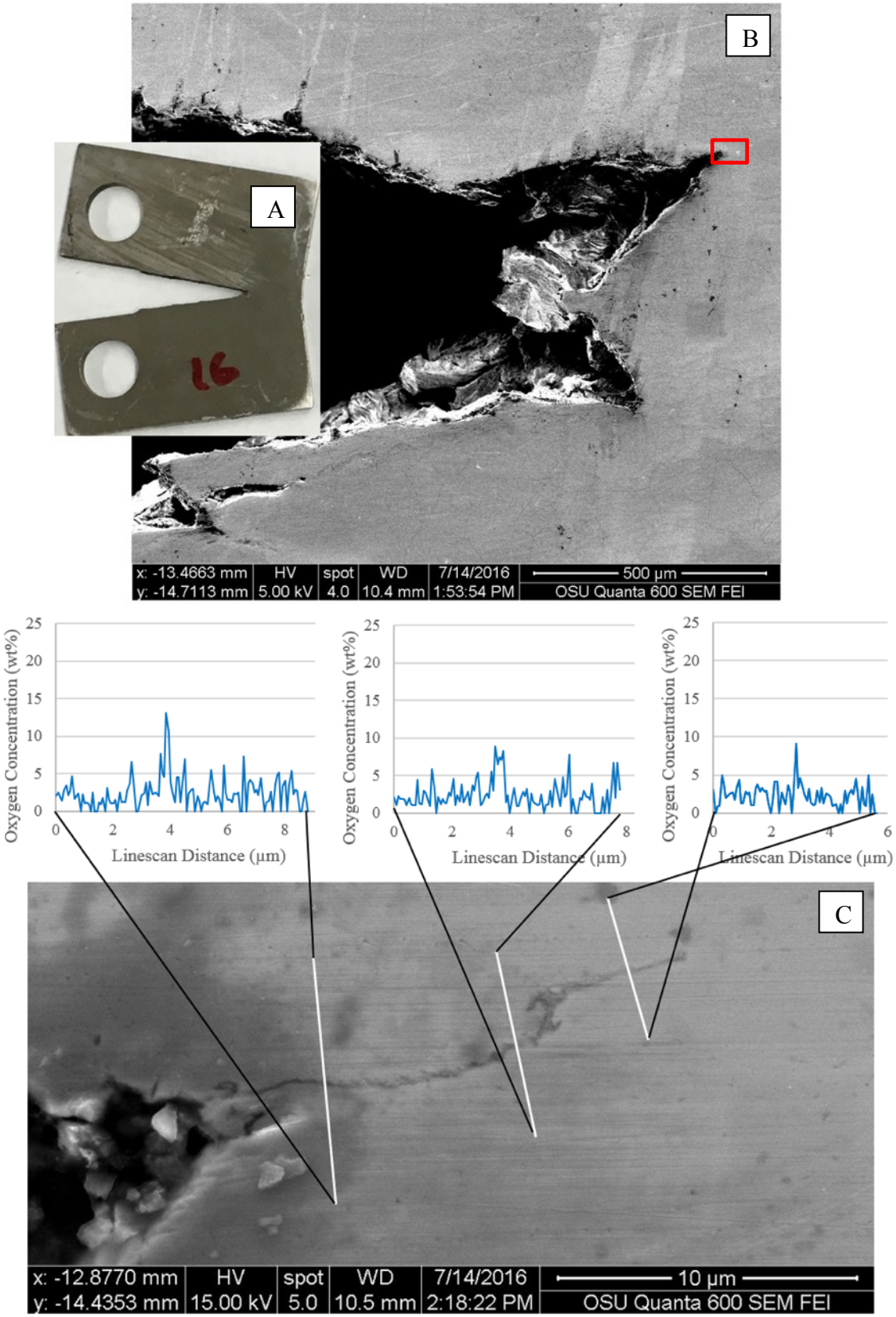

Fig. 42. (A) 617-16G post experiment, tested at 0.33Hz, with final ΔK=23.3 MPa√m (B) SEM micrograph of crack tip, (C) Enlarged crack tip region with oxidation quantified by EDS line scans.

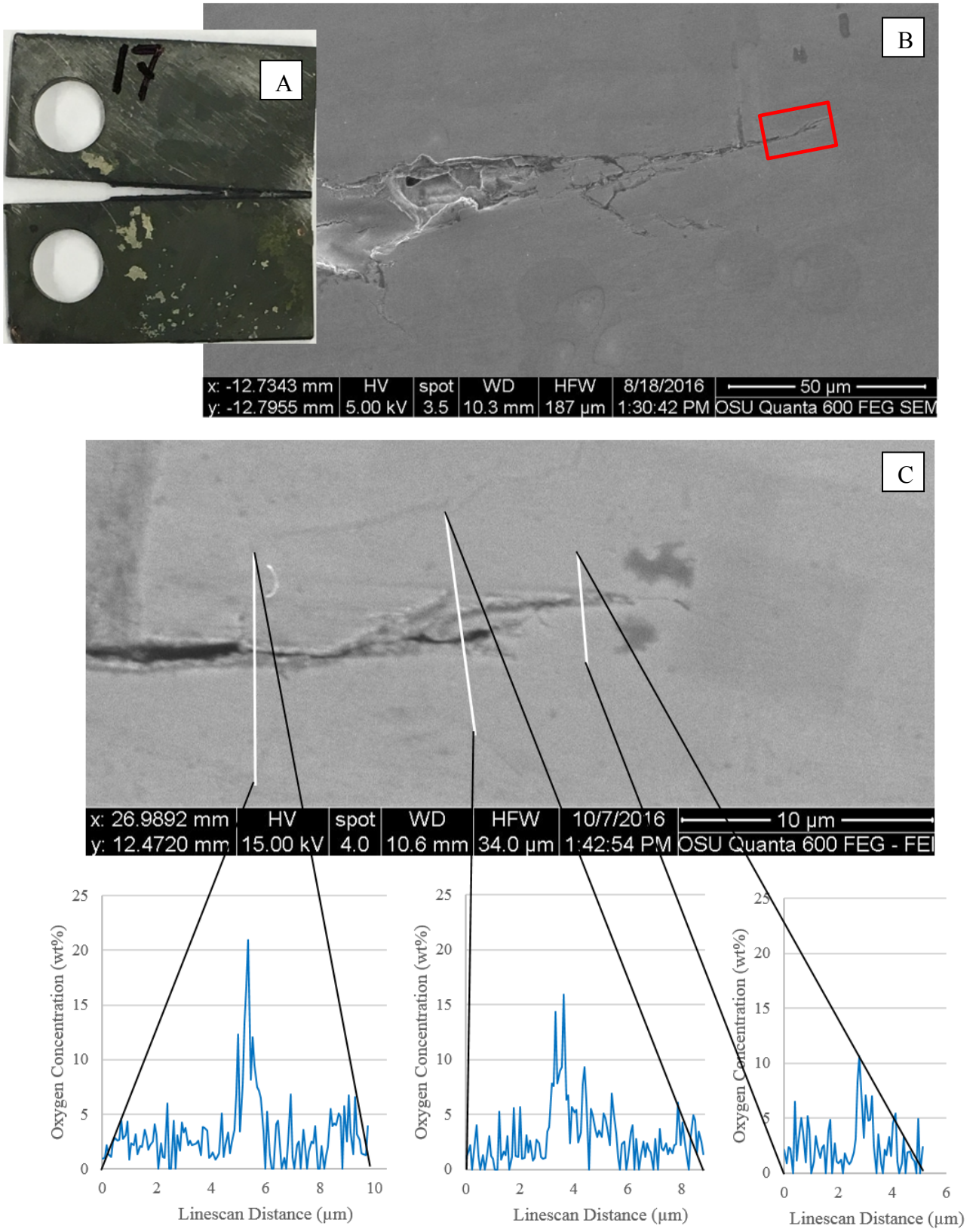

Fig. 43. (A) 617-17GO post experiment, tested at 0.33Hz with final ΔK=16.2 MPa√m, (B) SEM micrograph of crack tip, (C) Enlarged crack tip region with oxidation quantified by EDS line scans.

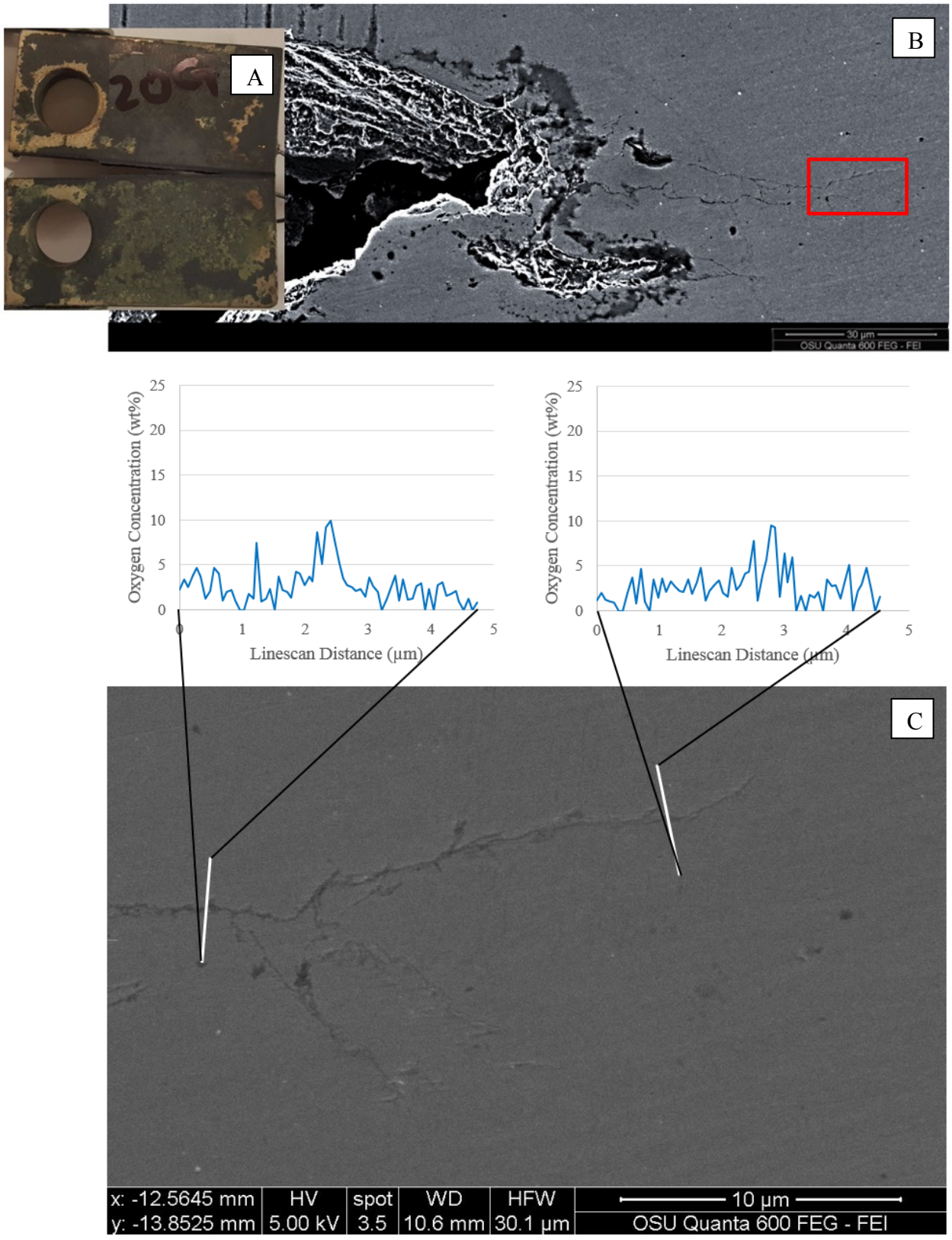

Fig. 44. (A) 617-20G post experiment, tested at 5Hz with final ΔK=22.8 MPa√m (B) SEM micrograph of crack tip, (C) Enlarged crack tip region with oxidation quantified by EDS linescans.

Fig. 45 through Fig. 62 show profiles which were etched in order to reveal grain boundaries surrounding the crack path. The profiles of samples 617-08, 617-19G, 617-17GO and 617-16GO were shipped to collaborators for further testing before etching took place. All other profiles were etched and examined with a Leica optical microscope at multiple magnifications. Sample 617-15GO ended at a similar ΔK as 617-16GO, and fair comparisons can be made between the two samples. 617-18G ended at a lower ΔK than 617-19G, and its fracture surface (not shown) was significantly smoother than that of 617-19G, and the profile of 617-19G was more heavily branched, implying that the line scans performed on 617-19G should not be compared to the etch of 617-18G.

Fig. 45 and Fig. 46 show excursions (small branches) on the crack wake of the 5 Hz samples 617-20G and 617-23G, respectively. Both etched profiles contain evidence of void growth, which is particularly prominent in Fig. 46b. Fig. 47 and shows the heavily branched profile of 617-15GO, tested at 0.33 Hz, in which each branch appears to be propagating transgranularly. Voids are present ahead of the growing branches. Fig. 48 shows the crack tip of 617-22G, another 0.33 Hz sample, which has no excursions along its wake and no visible voids remote from the crack tip.

Fig. 49 through Fig. 52 show samples tested at 0.05 Hz, arranged by increasing stress intensity at the time the experiment was stopped and the profile examined. 617-25G was tested at what appears to be the crack growth threshold, displays an unbranched crack tip and does not show evidence for void formation remote from the crack tip. Fig. 50 shows 617-26G, which displays both voids remote from the crack tip and more branching than 617-25G off its transgranular crack path. Fig. 51 shows 617-29G, which was tested at 0.05 Hz and halted at $\Delta K = 11.8$ MPa$\sqrt{m}$. 617-29G displays very different character than the profiles at lower stress intensities. The branching at the crack tip is extensive and they appear to be growing transgranularly into voids which had formed previously. Finally, Fig. 52 shows 617-31G, which ended at $\Delta K = 15.9$ MPa$\sqrt{m}$. In Fig. 52, evidence of the same transgranular branching behavior as 617-29G is present in the crack wake, which gave way to one dominant branch that grew in a more intergranular fashion, connecting to voids ahead of its path.

Fig. 53 through Fig. 55 show samples tested with a 0.05 Hz hold time waveform, again arranged by ascending stress intensity. In Fig. 53, 617-18G displays a transgranular a crack path with an extensive network of voids forming in the smaller grains above the crack tip. The crack appears to be on the verge of branching in a similar manner as 617-29G. Fig. 54 shows 617-24G, which is the only sample in this study that unambiguously displays intergranular cracking at the leading crack tip of a steadily growing crack, as shown in Fig. 54b. The leading 1mm of the crack is jagged as a result of growing through a series of voids. As described previously, the conditions to which 617-24G were subjected (thermal cycling and an 8 hour hold at zero load in the middle of the test) make it somewhat unique relative to the other samples in this study. Fig. 55 shows 617-32G, which demonstrates the same crack growth mechanism as 617-24G and 617-31G (void coalescence) with its jagged profile and visible voids ahead of the crack tip.

Fig. 56 through Fig. 62 show the time dependent behavior of samples 617-10, 617-11G, 617-12 and 617-33G. In Fig. 56, 617-10 displays voids ahead of a blunted crack tip, which is beginning to form an intergranular branch (Fig. 57a), perhaps as a result of void formation. The transgranular tip in Fig. 57b is likely the original precrack. Fig. 58 shows 617-11G, another heavily blunted sustained load sample which was subjected to a higher stress intensity than 617-10. In 617-11G, the formation of voids just ahead of the crack tip suggest the threshold for

sustained load crack growth had nearly been reached. Although 617-12 was subjected to a 10s-60s-10s hold time waveform, the same character as 617-10 and 617-11G was displayed, suggesting that at this or longer hold times, the crack tip is dominated by time dependent mechanisms, rather than fatigue. The K_{max} experienced by 617-12 in Fig. 59 and Fig. 60 was 23.6 MPa√m. This appears to have caused voids to coalesce just ahead of the crack tip, suggesting that this K_{max} value is even closer to, or even above, the sustained crack growth threshold. Finally, Fig. 61 and Fig. 62 show sample 617-33G, a sustained load experiment which resulted in stable crack propagation beginning with K = 23 MPa√m, confirming this value as the threshold for time dependent void coalescence in Alloy 617 at 800°C.

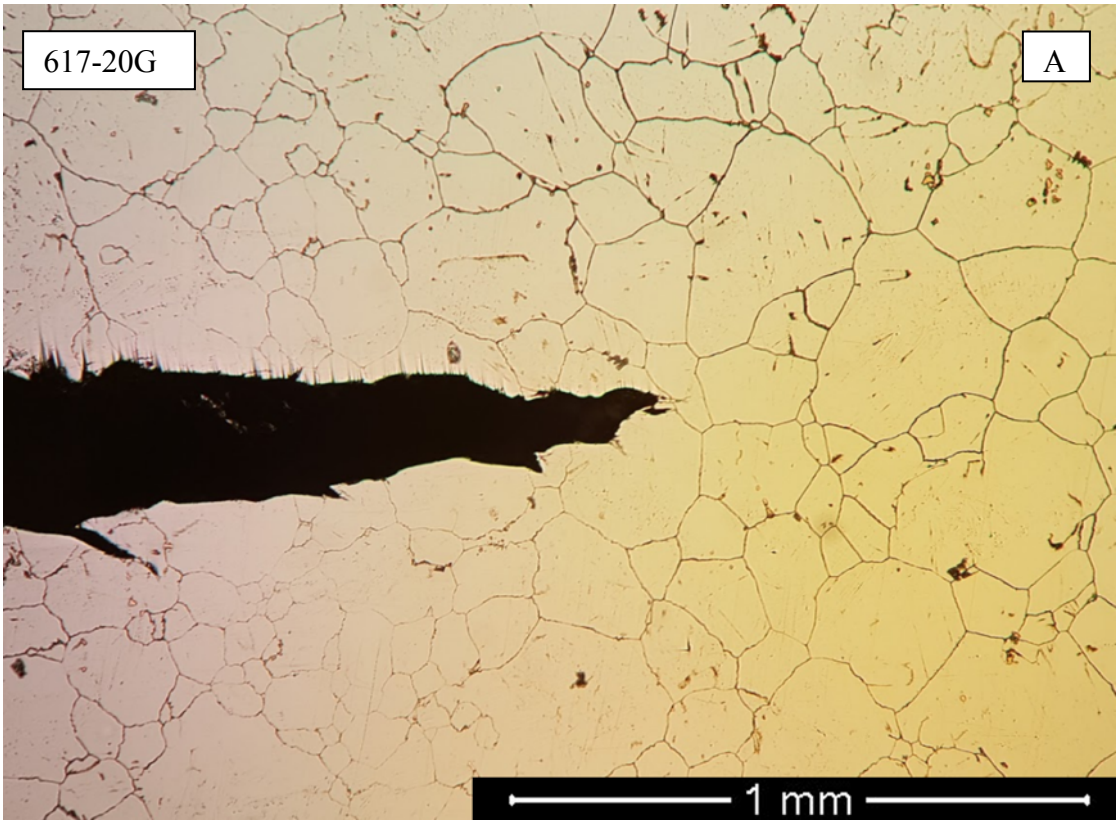

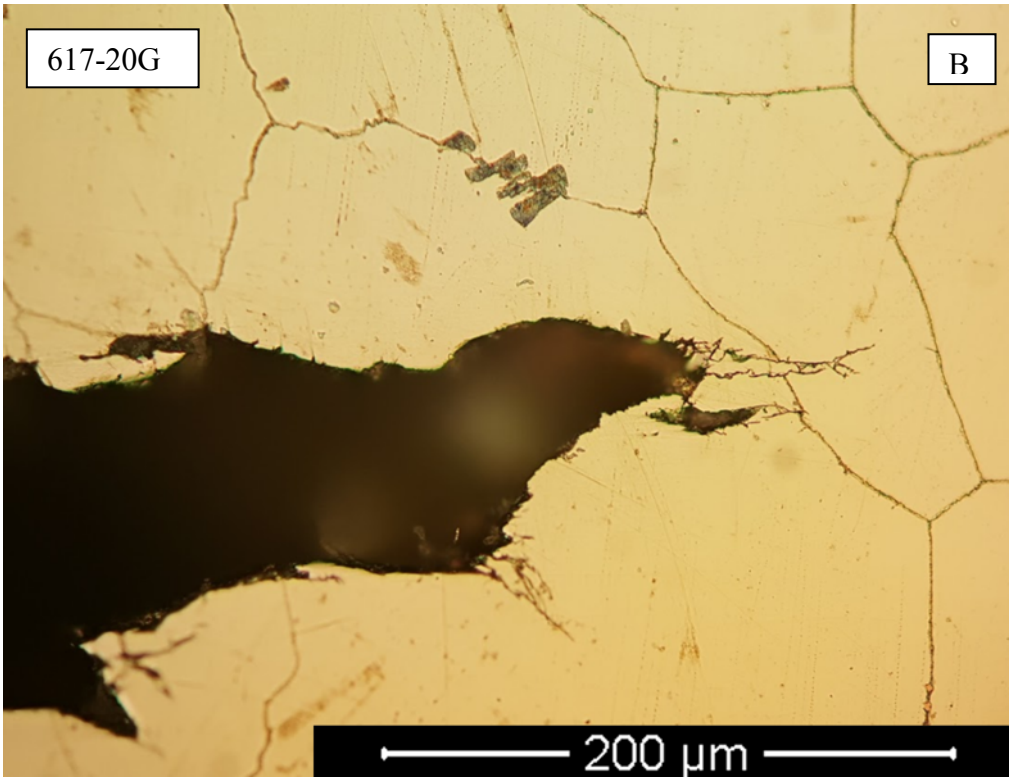

Fig. 45. Optical micrographs of etched profile of 617-20G tested at 5 Hz with final $\Delta K = 22.8$ MPa$\sqrt{m}$. (A) 10x (B) 50x.

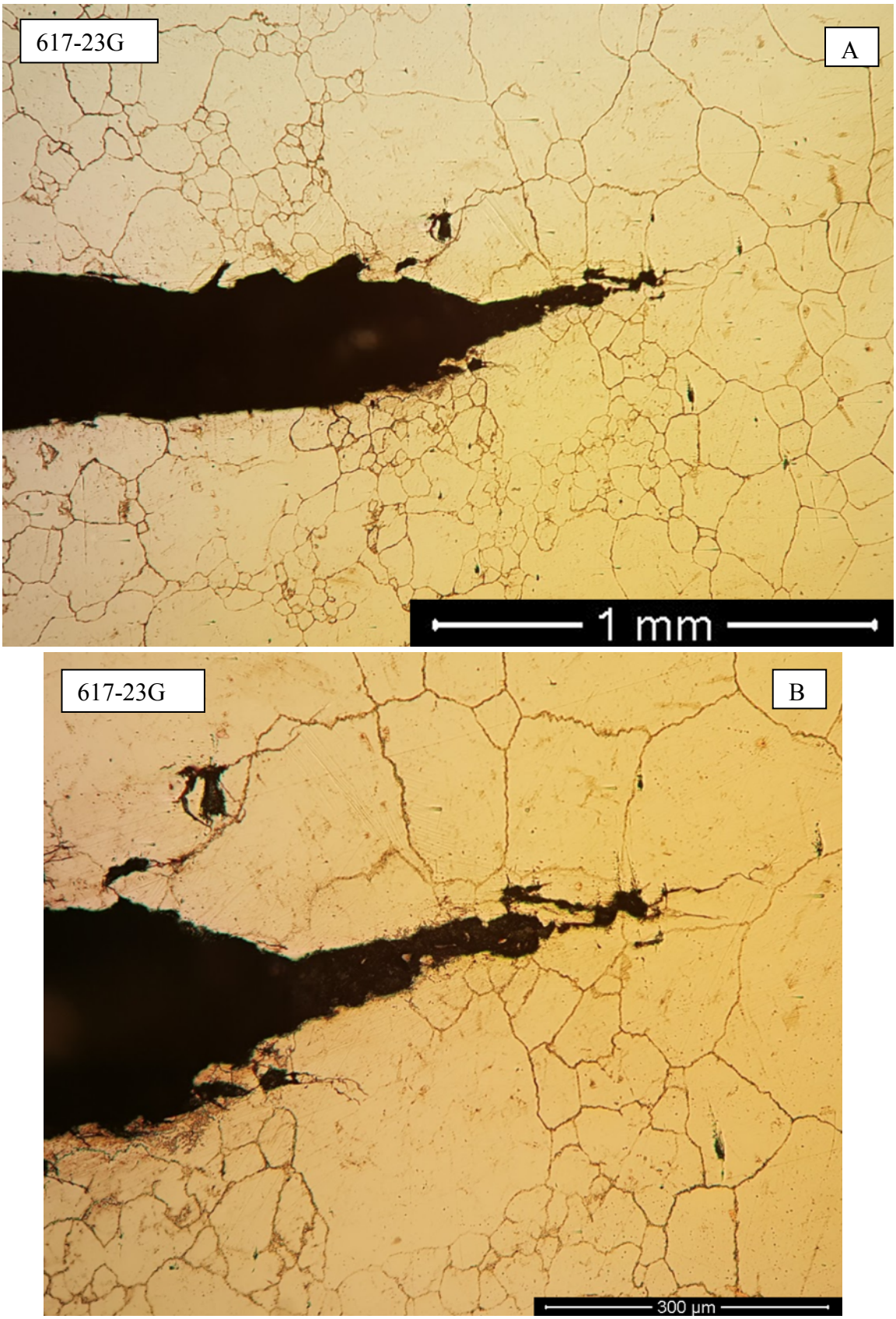

Fig. 46. Optical micrographs of etched profile of 617-23G tested at 5 Hz with final $\Delta K = 23.9$ MPa$\sqrt{m}$. (A) 10x (B) 20x.

Fig. 47. 20x optical micrograph of etched profile of 617-15GO tested at 0.33 Hz with final ΔK = 24.9 MPa$\sqrt{m}$.

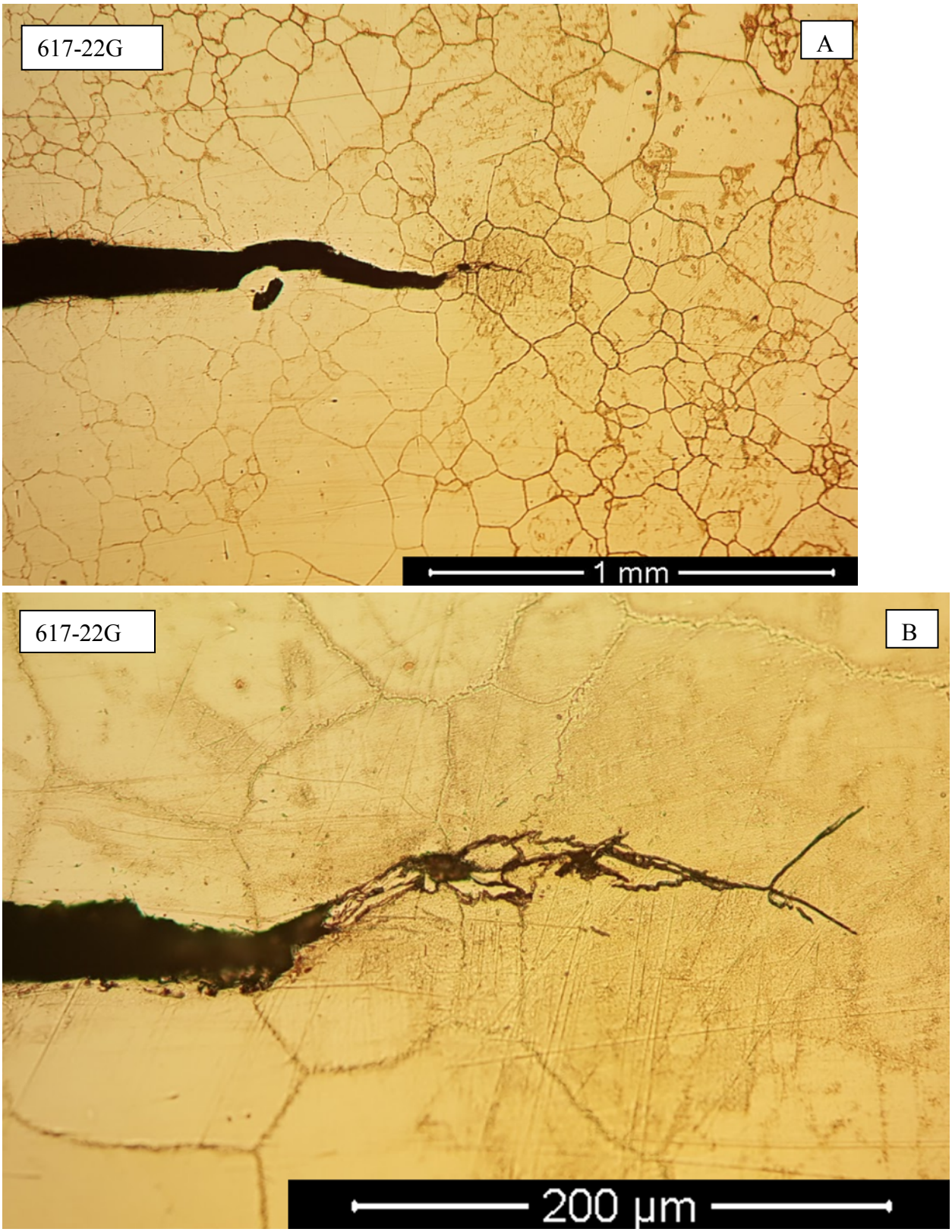

Fig. 48. Optical micrographs of etched profile of 617-22G tested at 0.33 Hz with final $\Delta K = 12.8$ MPa$\sqrt{m}$. (A) 10x (B) 50x.

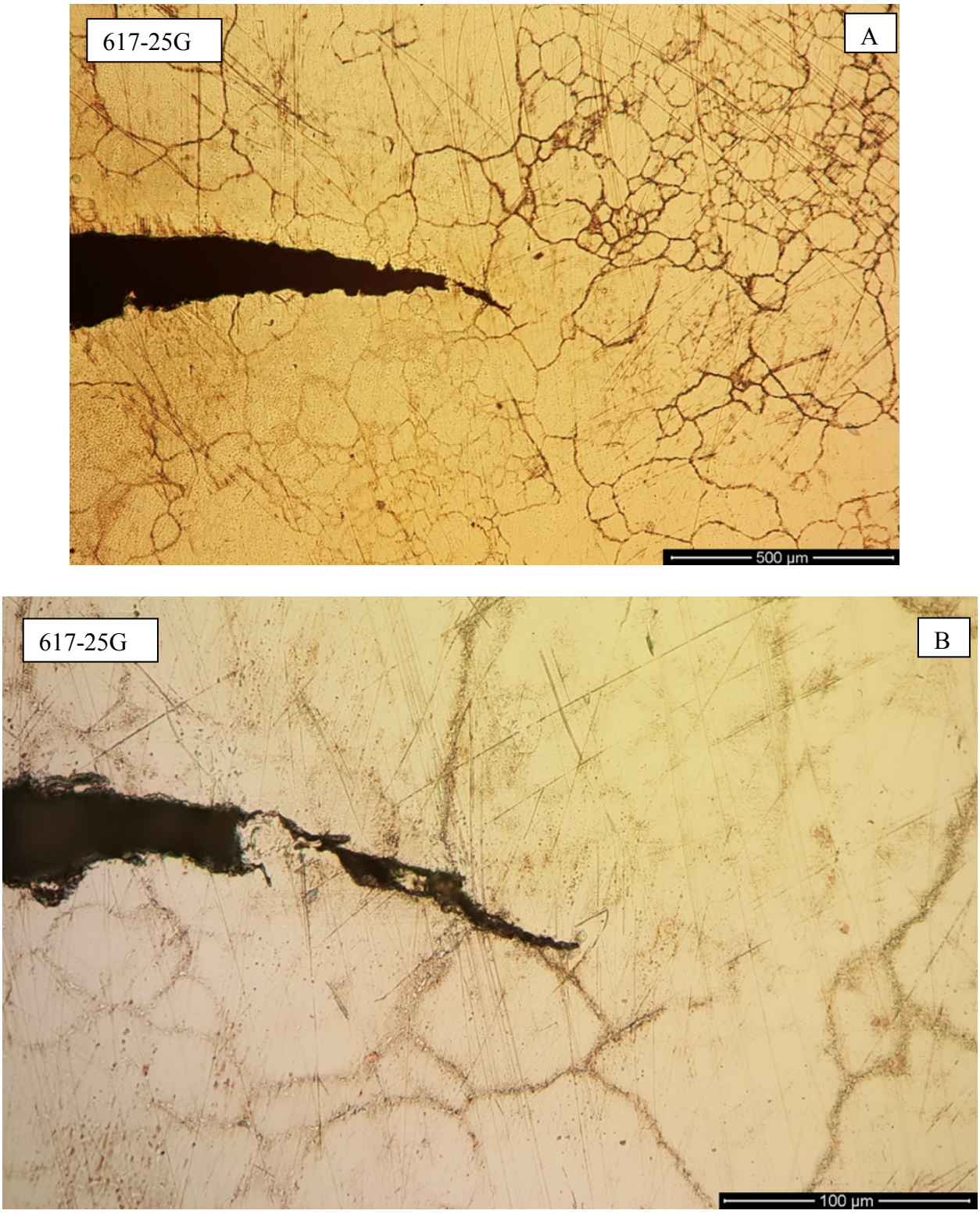

Fig. 49. Optical micrographs of etched profile of 617-25G tested at 0.05 Hz with final $\Delta K = 7.6$ MPa$\sqrt{m}$. (A) 10x (B) 50x.

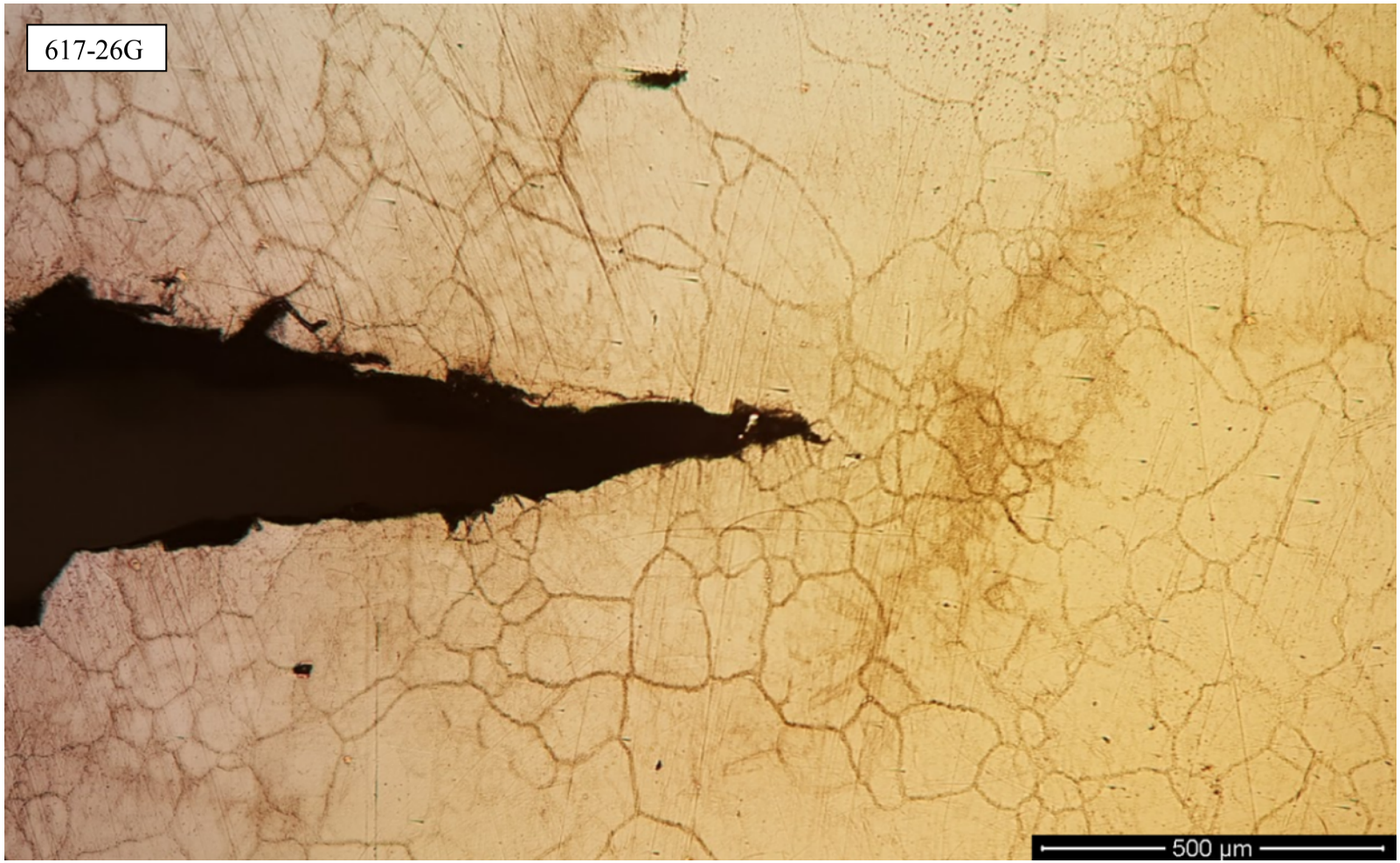

Fig. 50. 10x optical micrograph of etched profile of 617-26G tested at 0.05 Hz with final $\Delta K = 9.5$ MPa$\sqrt{m}$.

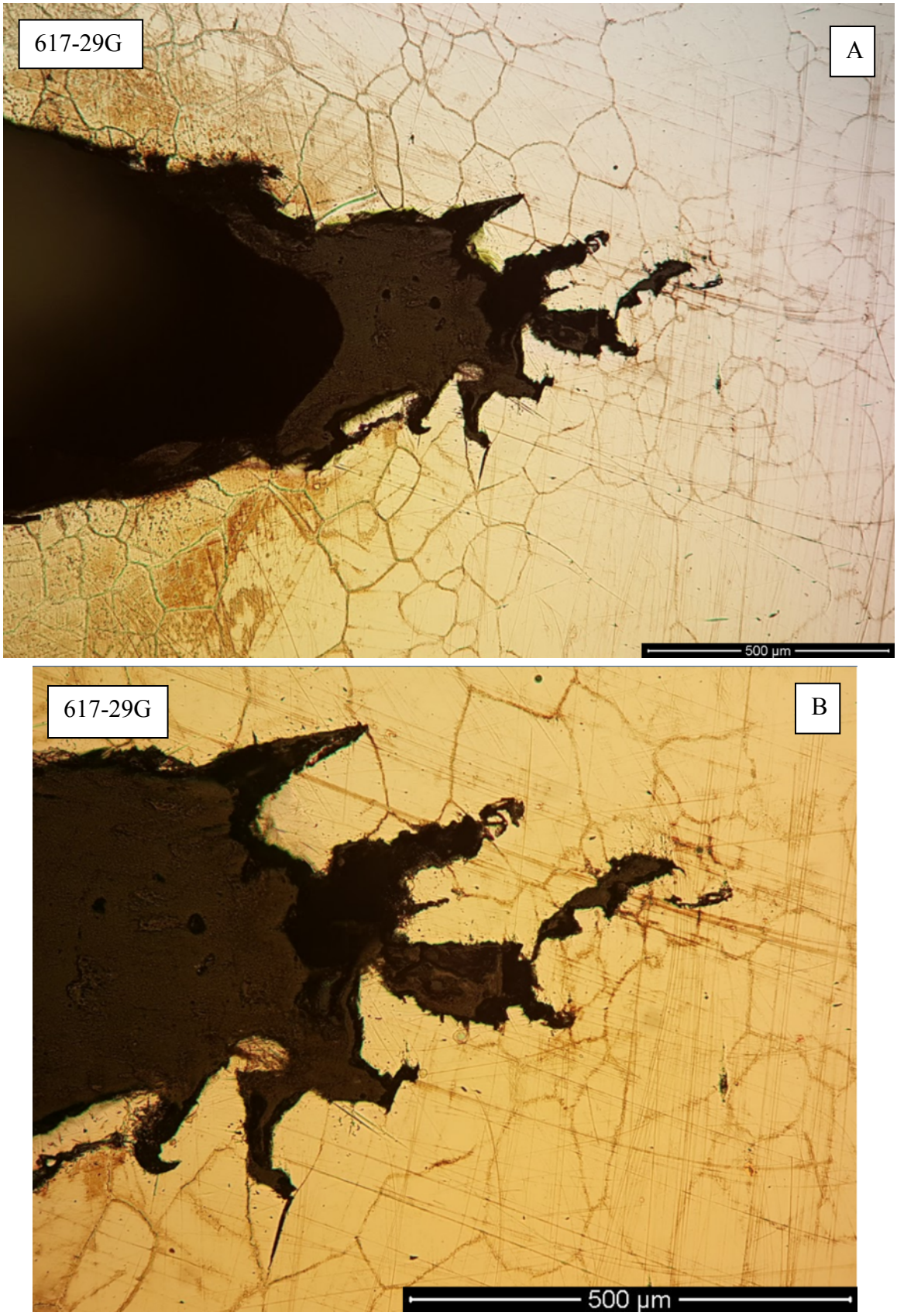

Fig. 51. Optical micrographs of etched profile of 617-29G tested at 0.05 Hz with final ΔK = 11.8 MPa$\sqrt{m}$. (A) 10x (B) 20x.

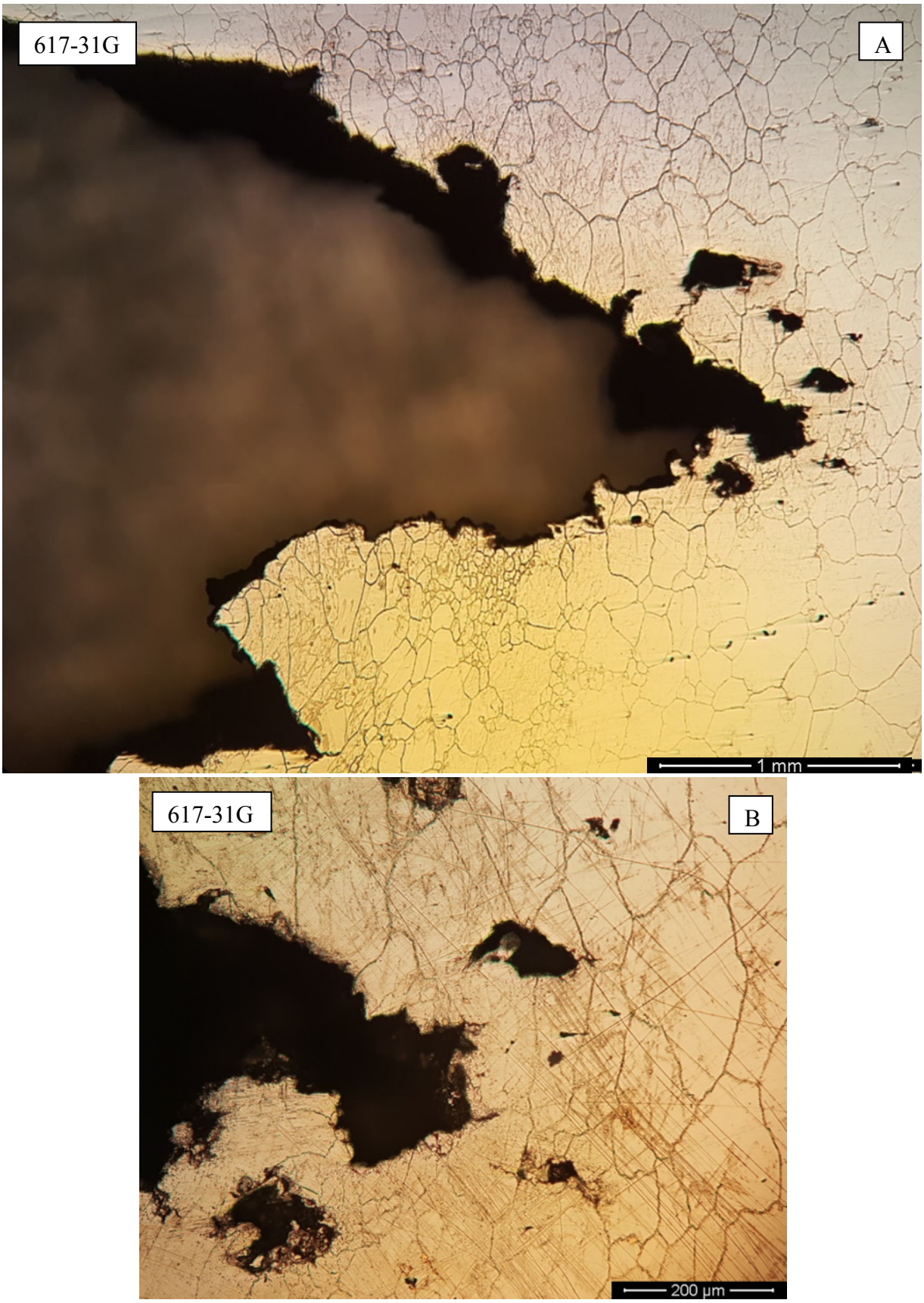

Fig. 52. Optical micrographs of etched profile of 617-31G tested at 0.05 Hz with final $\Delta K = 15.9$ MPa$\sqrt{m}$. (A) 5x (B) 20x.

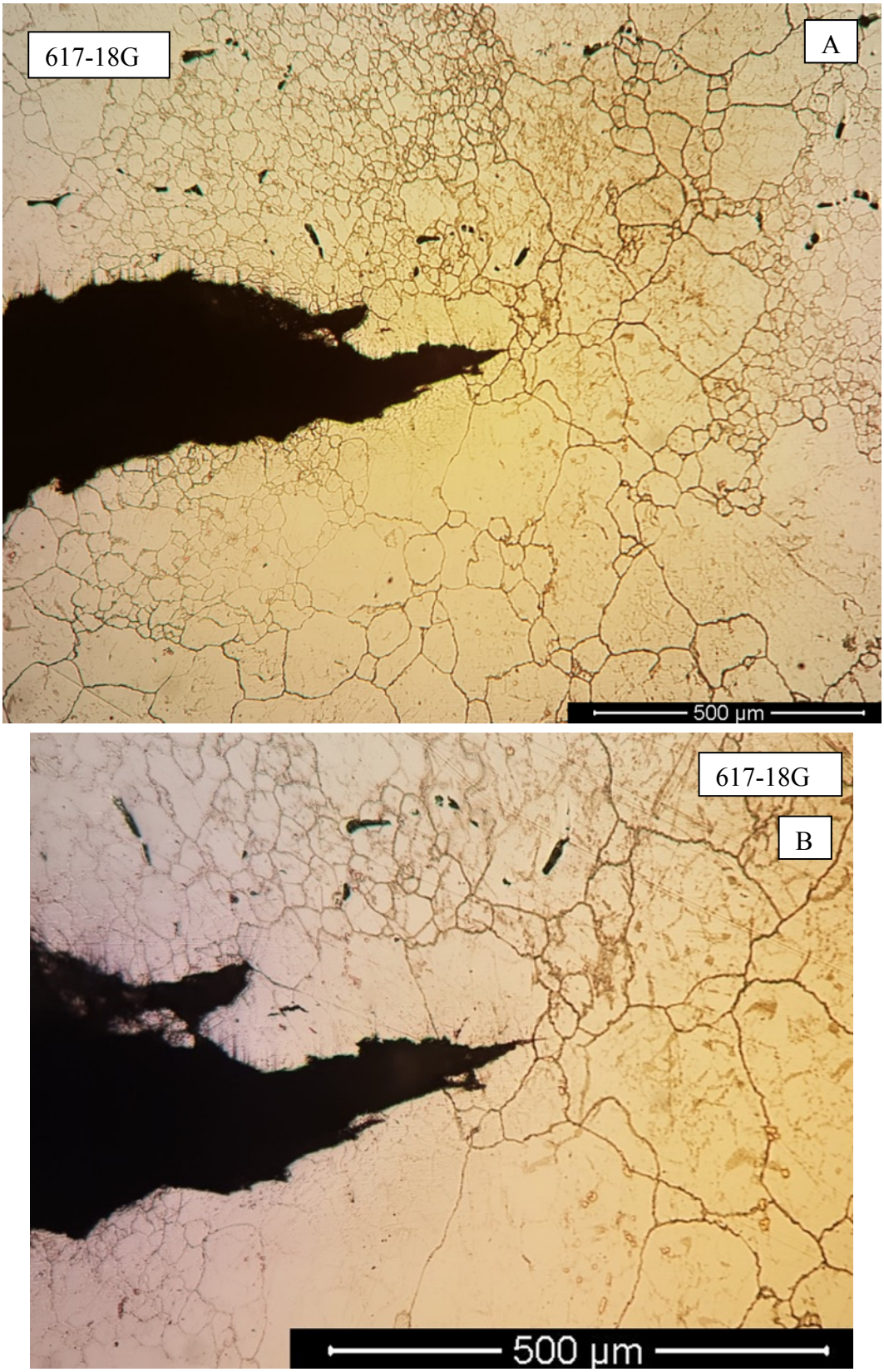

Fig. 53. Optical micrographs of etched profile of 617-18G tested with a hold time waveform with final $\Delta K = 9.0$ MPa$\sqrt{m}$. (A) 10x (B) 20x.

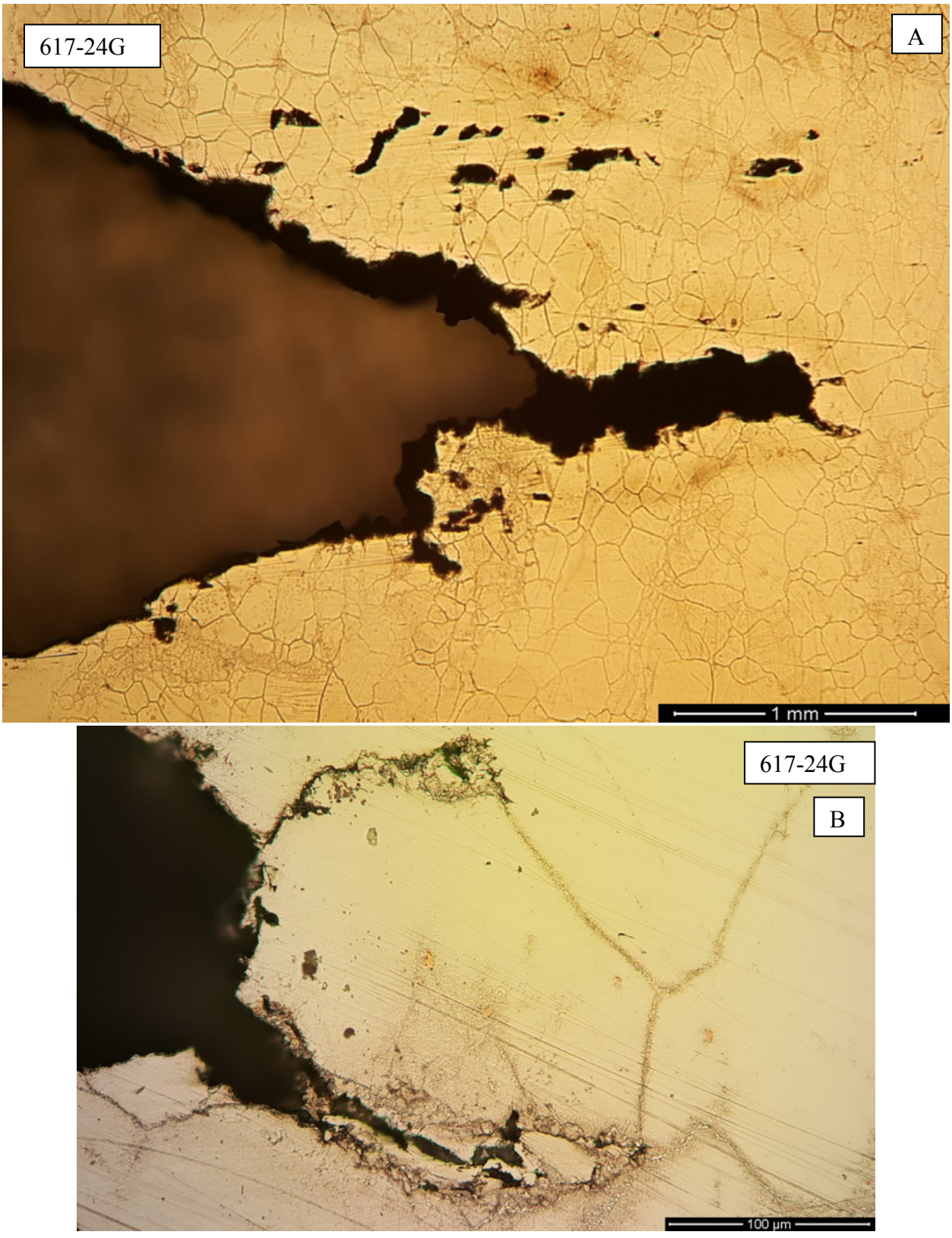

Fig. 54. Optical micrographs of etched profile of 617-24G tested with a hold time waveform with final ΔK = 11.0 MPa√m. (A) 5x (B) 50x.

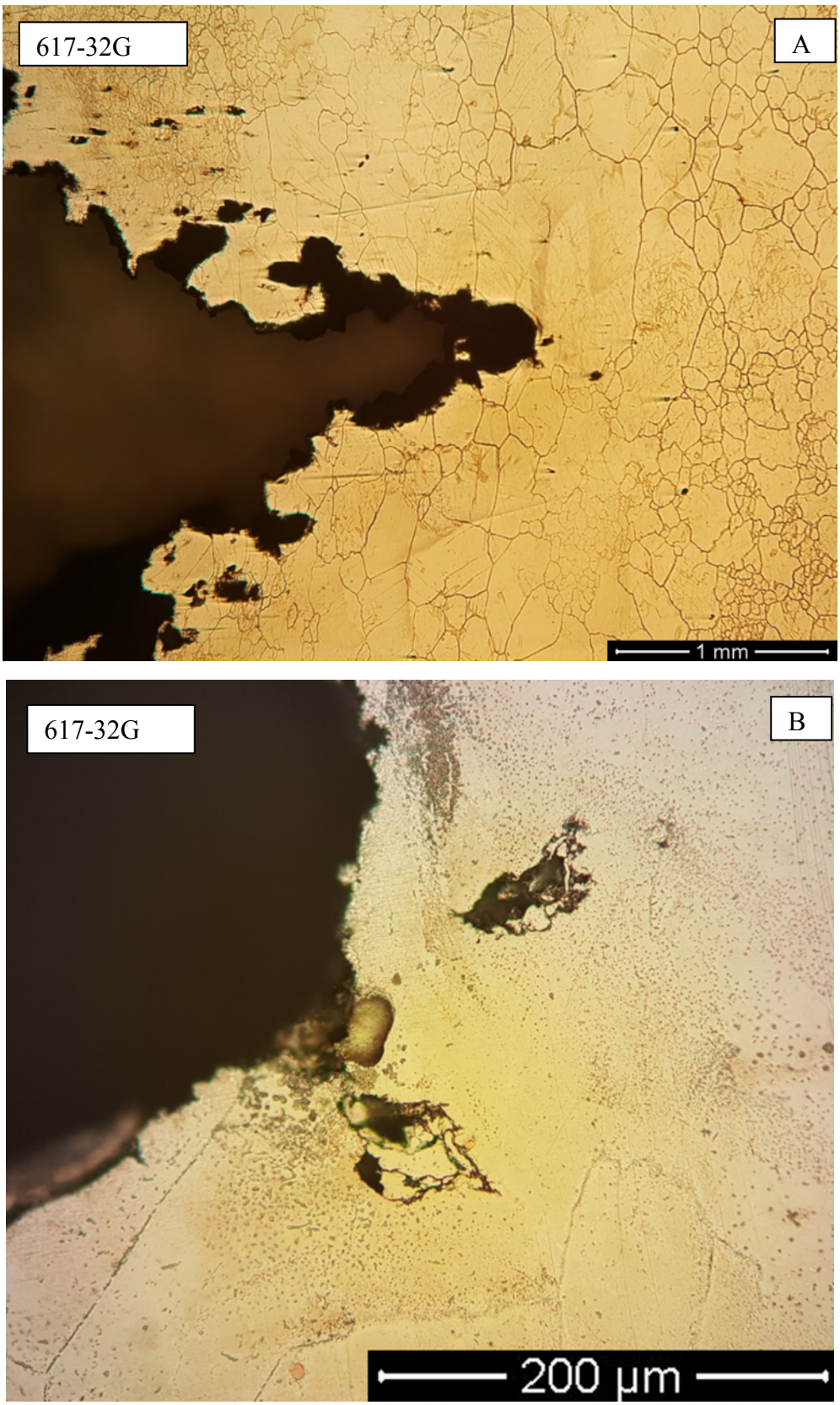

Fig. 55. Optical micrographs of etched profile of 617-32G tested with a hold time waveform with final ΔK = 17.6 MPa$\sqrt{m}$. (A) 5x (B) 50x.

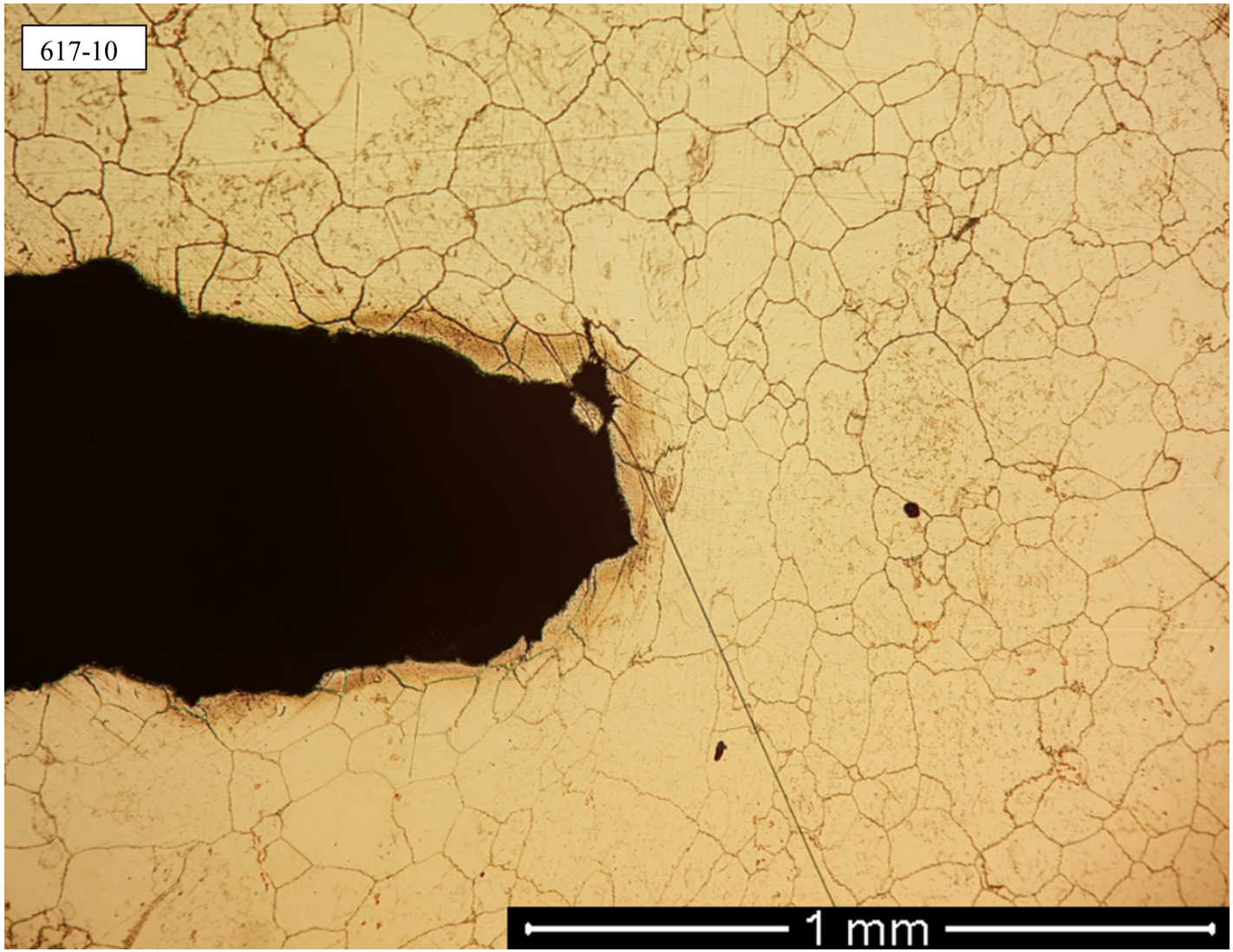

Fig. 56. Optical micrograph of etched profile of 617-10 tested with a sustained load with final K = 15.9 MPa√m.

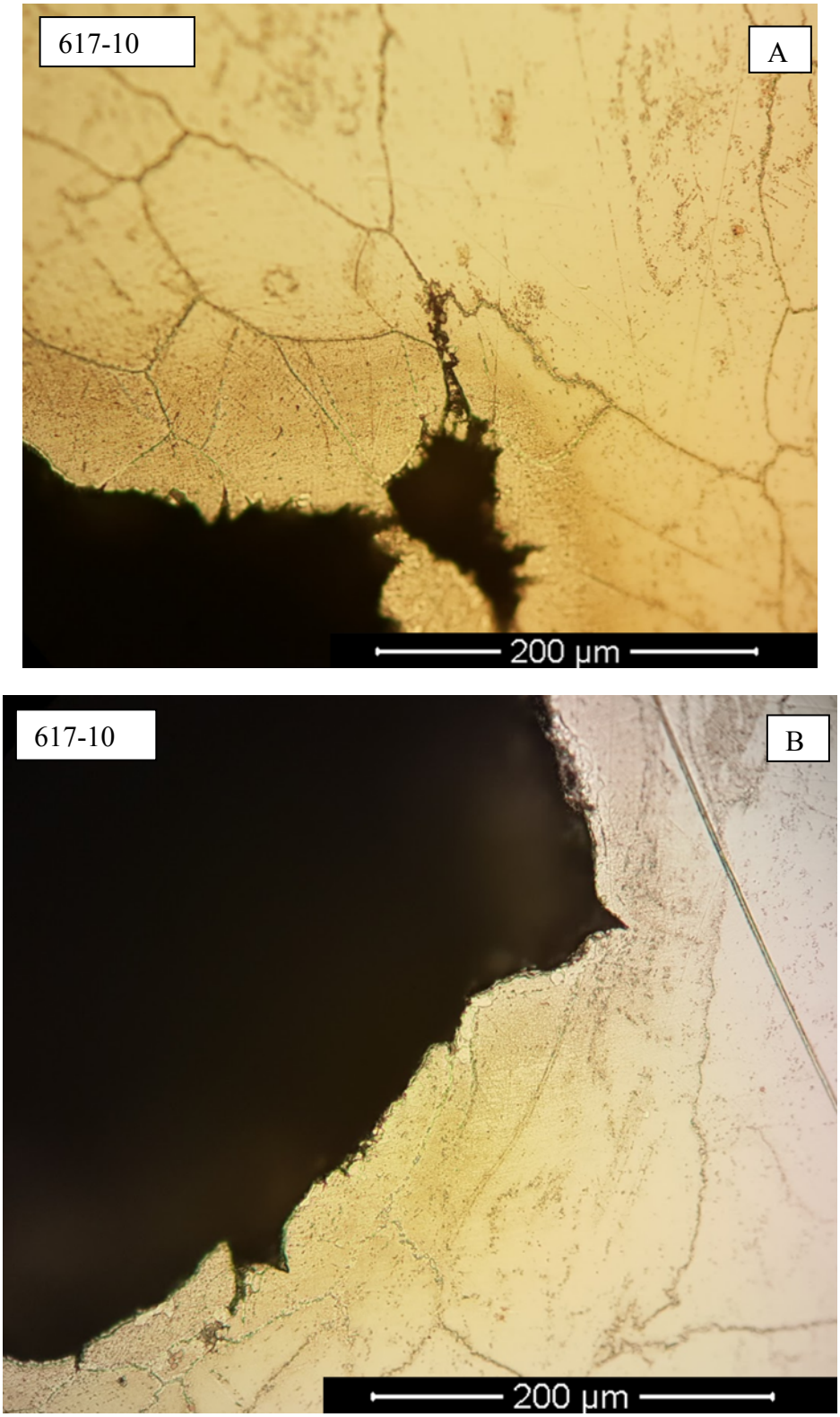

Fig. 57. 50x optical micrographs of etched profile of 617-10 tested with a sustained load with final K = 15.9 MPa√m. (A) Top half of blunted crack (B) Bottom half of blunted crack.

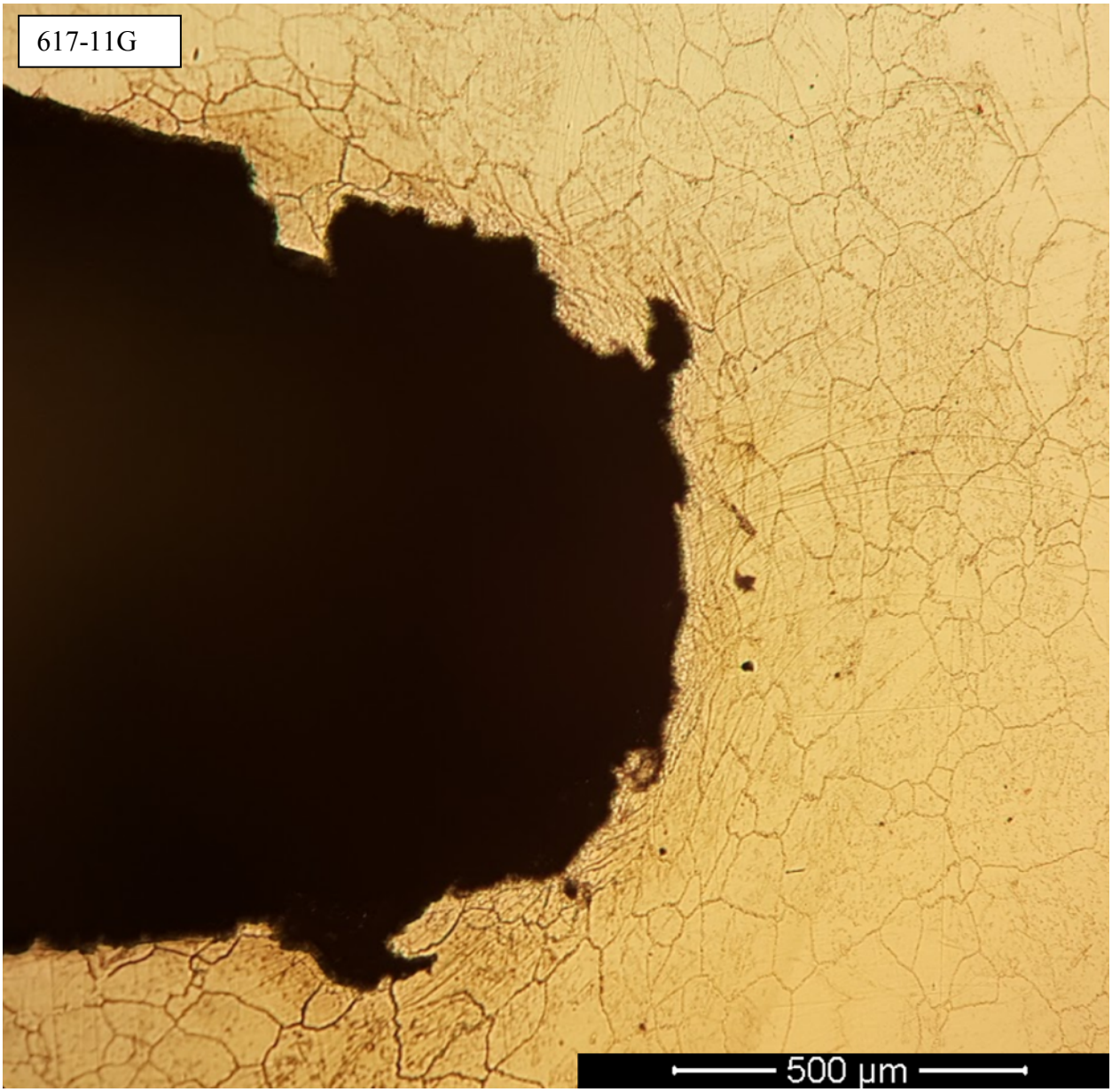

Fig. 58. 5x optical micrograph of etched profile of 617-11G tested with a sustained load with final K = 18.3 MPa√m.

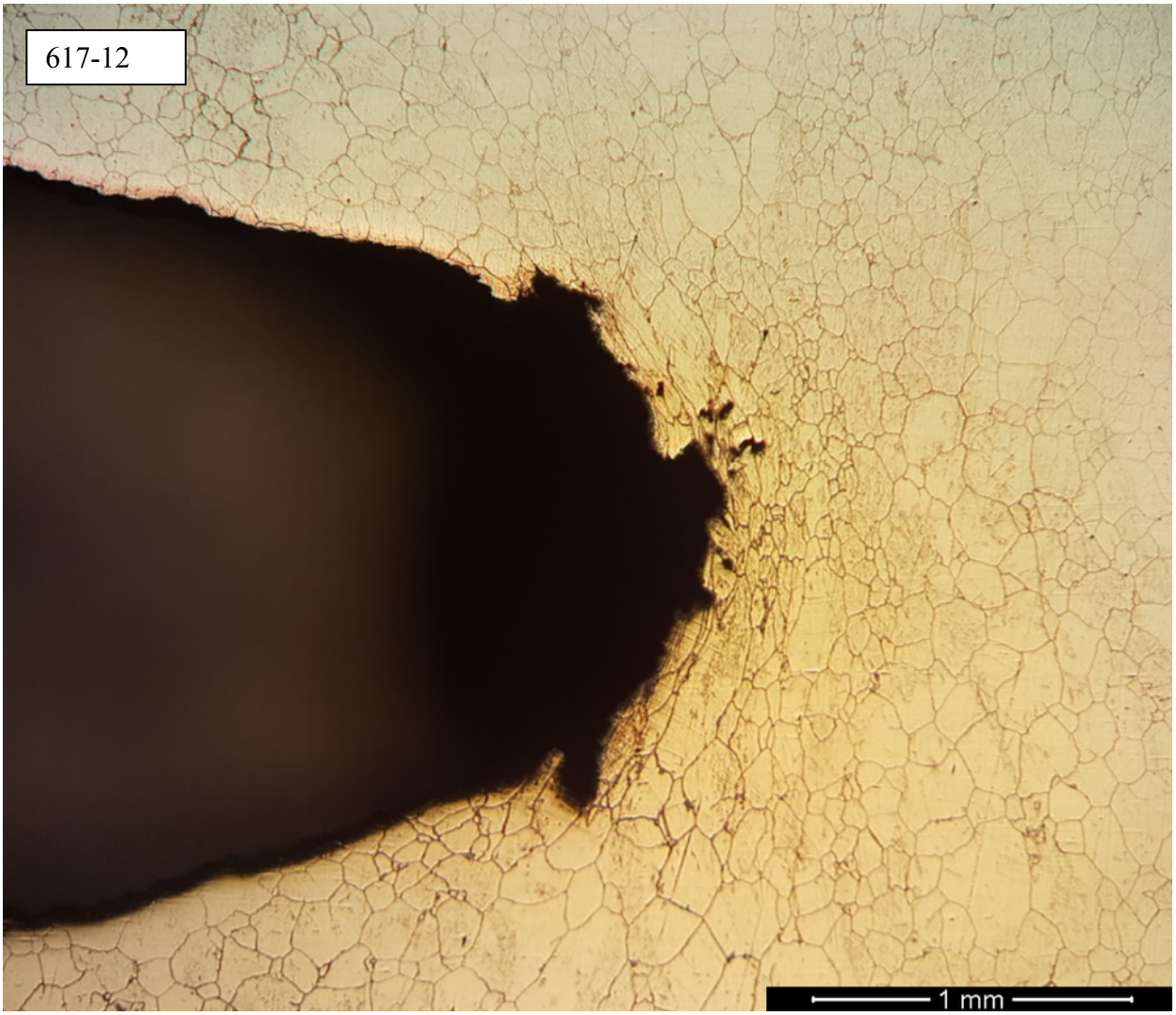

Fig. 59. 5x optical micrograph of etched profile of 617-12 tested with a 10s-60s-10s hold time waveform with final $\Delta K = 13.2$ MPa$\sqrt{m}$.

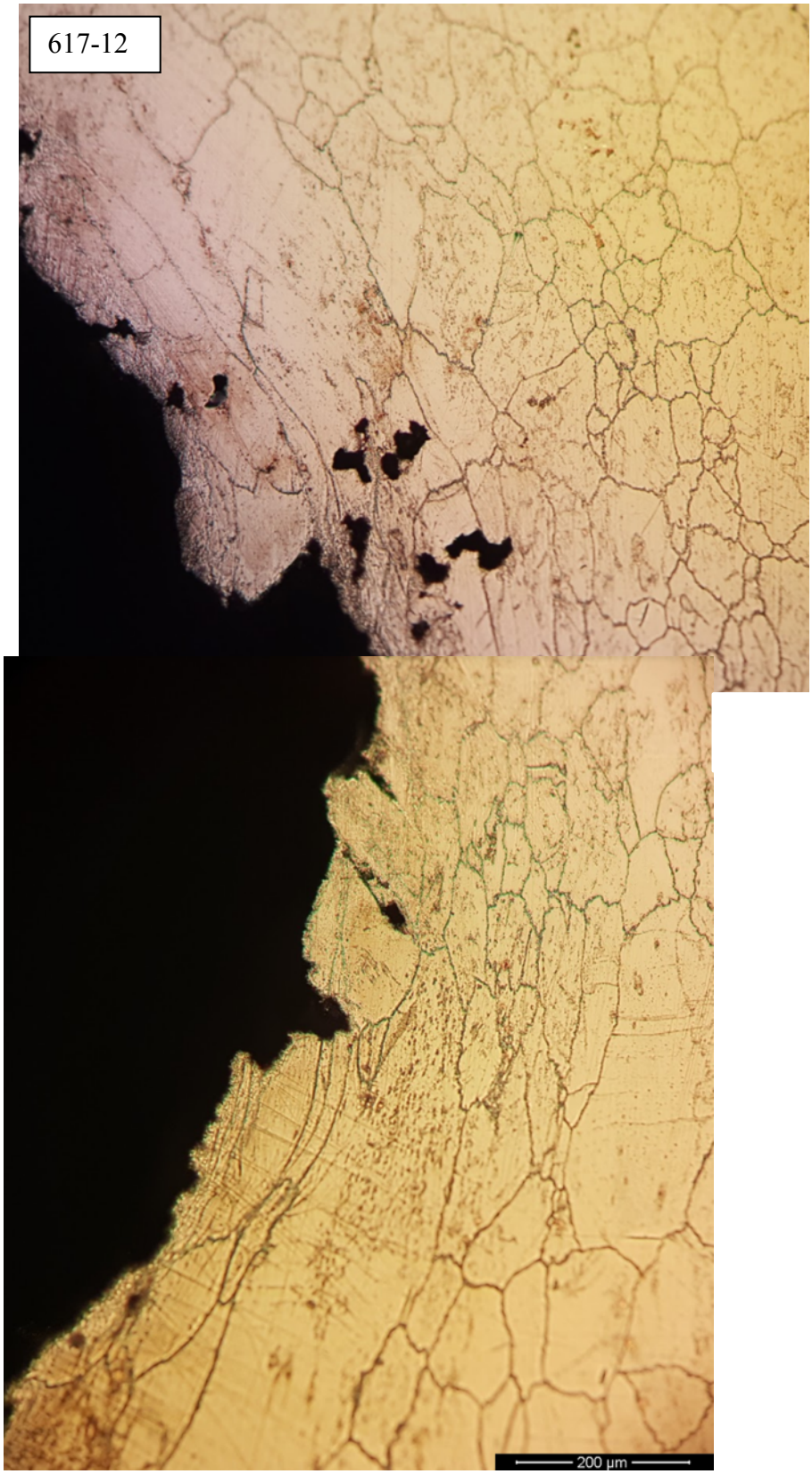

Fig. 60. 20x optical micrograph of etched profile of 617-12 tested with a 10s-60s-10s hold time waveform with final $\Delta K = 13.2$ MPa$\sqrt{m}$.

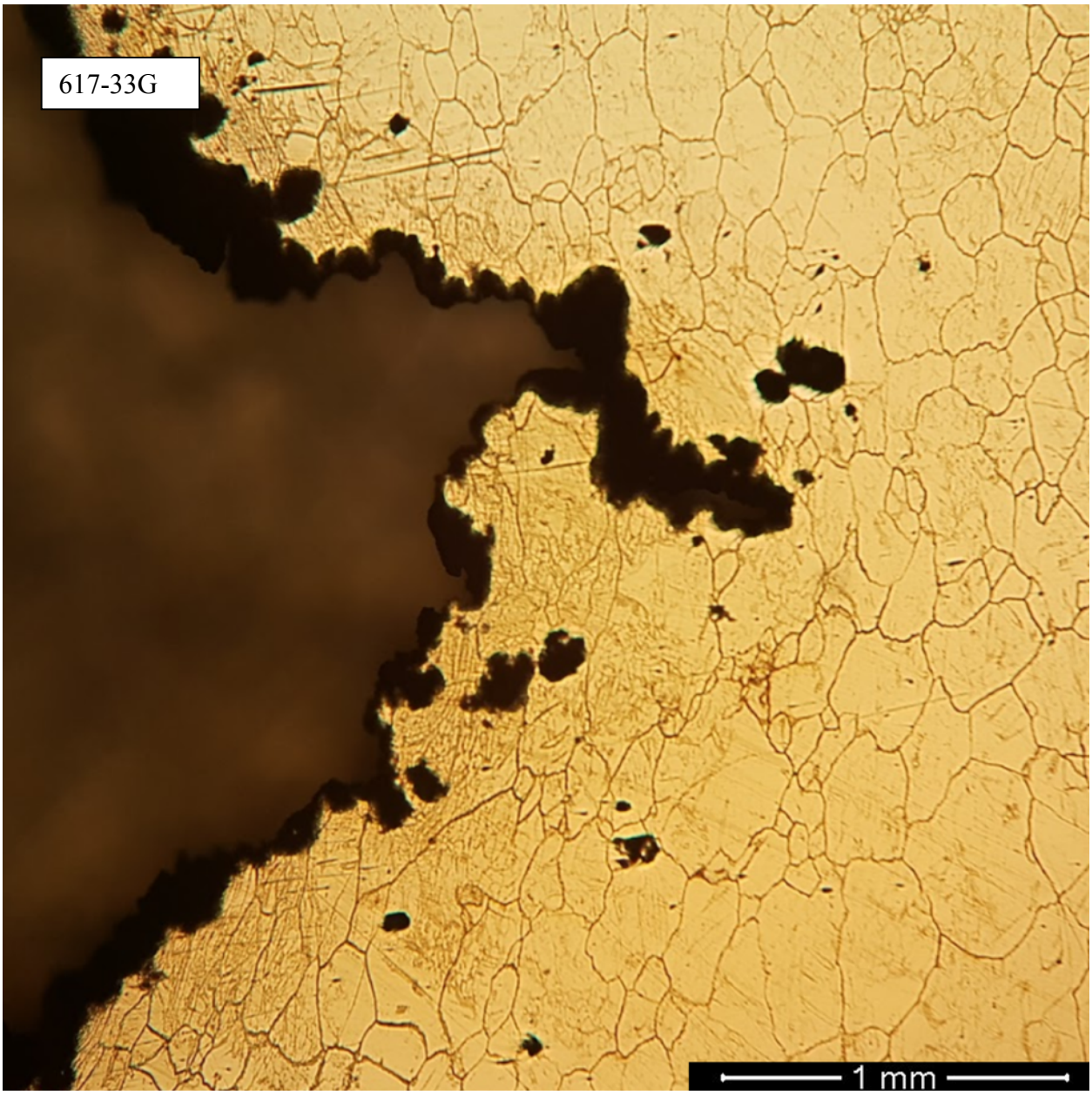

Fig. 61. 5x optical micrograph of etched profile of 617-33G tested with a sustained load with final K = 30.2 MPa√m.

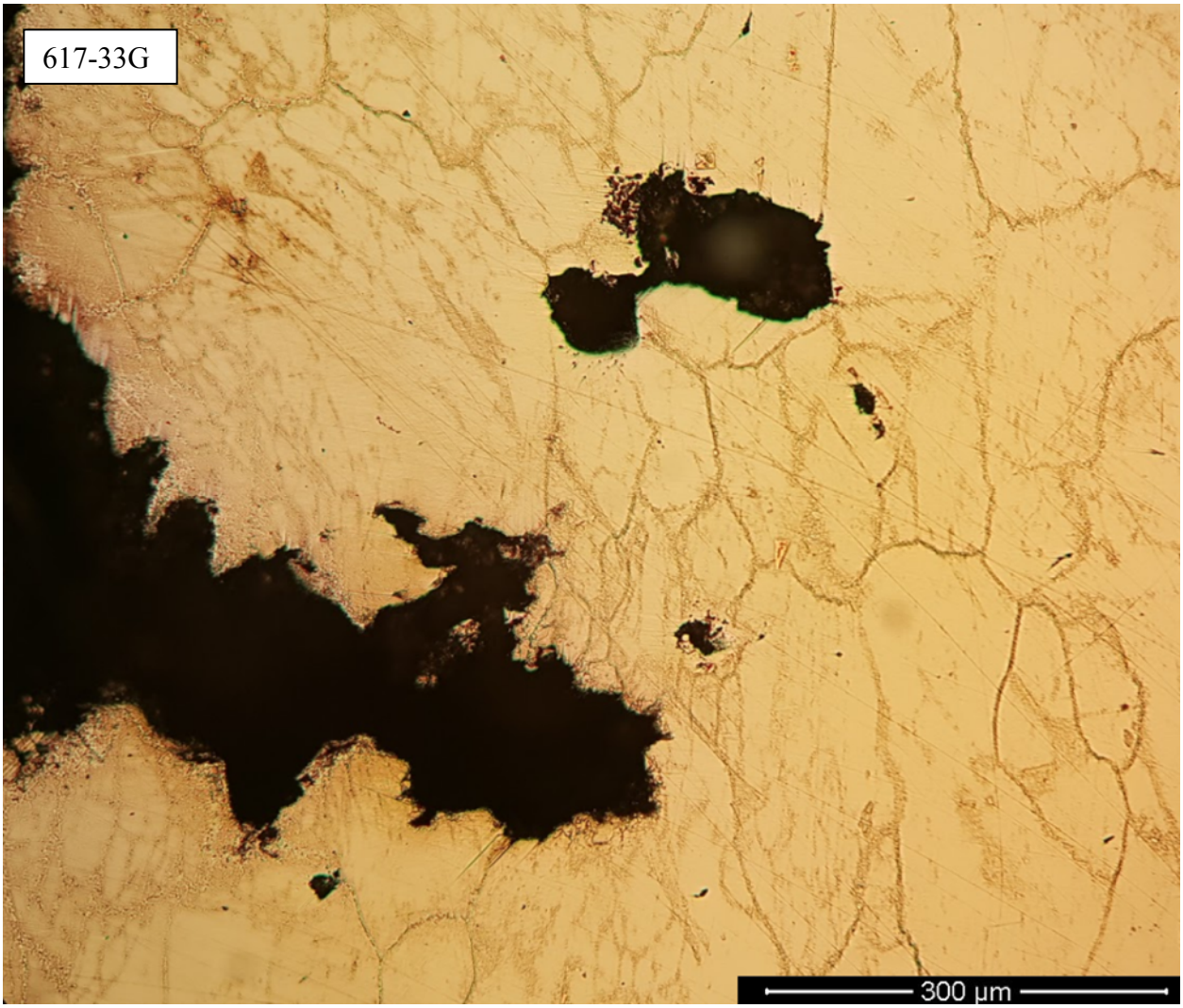

Fig. 62. 20x optical micrograph of etched profile of 617-33G tested with a sustained load with final K = 30.2 MPa√m.

2.3.2.5. Transition Time Calculation

An estimate of the transition time between small scale and extensive creep conditions was performed using data from samples 617-27G and 617-32G. Knowing the transition time between will aid in the design of future experiments. The transition time between small scale creep and extensive creep was described by Riedel and Rice in 1980, and is given by [31]:

$$t_T = \frac{K^2(1-v^2)}{E(n+1)C^*} \qquad \text{Eq. 30}$$

Where K is the stress intensity factor (K_{max} during the hold-time), v is Poisson's ratio, E is Young's modulus, n is the secondary creep exponant. Because Alloy 617 does not display classical steady state creep, the secondary creep constant n has been approximated with a power law fit to the minimum creep rate. C^* is given by:

$$C^* = \frac{P\dot{\Delta}^{FLD}}{B_N(W-a)} H^{FLD}\eta^{FLD} \qquad \text{Eq. 31}$$

Where P is the load, $\dot{\Delta}^{FLD}$ is the force-line displacement rate, and H^{FLD} and η^{FLD} have been calculated numerically. All variables were readily accessible except the force line displacement rate. Fig. 63 shows sample extensometer data used to estimate the force line displacement rate.

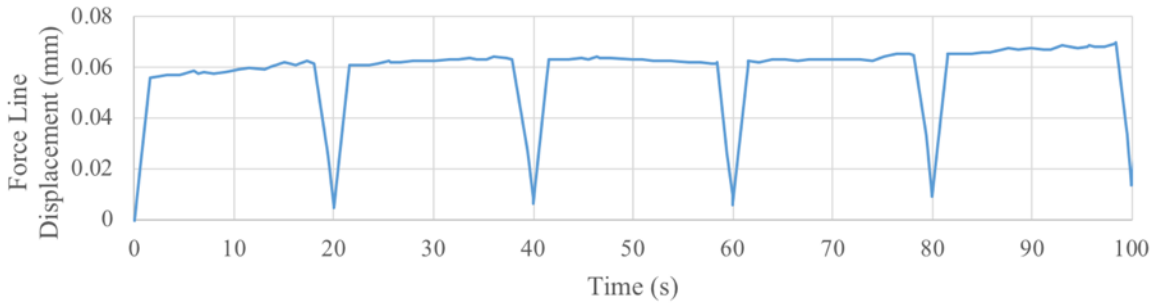

Fig. 63. Five cycles of extensometer data from sample 617-27G. Variations in force line displacement were averaged over 300 cycles for each estimation of the transition time.

The slope of the data during the hold times is equal to the force line displacement rate. Experimental scatter caused negative force line displacement rates throughout the dataset, such as the cycle pictured in Fig. 63 between 40 and 60s. Such cycles were discarded. A 300-cycle moving average was applied to the displacement rate of remaining non-negative cycles. The rate is plotted against cycle count in Fig. 64. Data from sample 617-32G was aligned based on ΔK experienced by the sample, and plotted with data from 617-27G in Fig. 64, showing good agreement in the area of overlap between the two datasets.

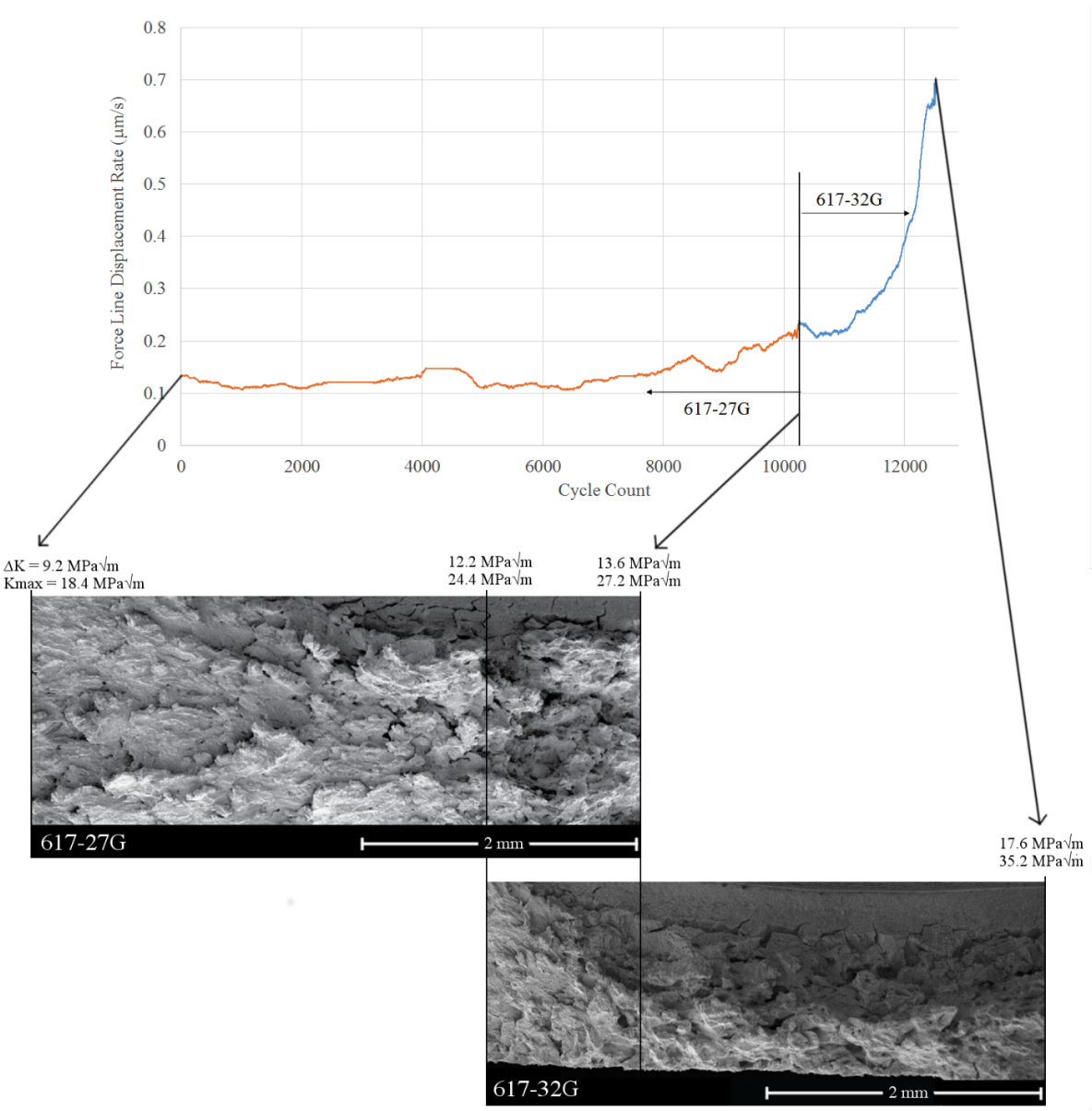

Fig. 64. Force line displacement rate data for sample 617-27G. Discontinuities were caused by extensometer data collected outside of the calibrated range of the instrument.

Based on these data, estimations of the transition time were made throughout each test. From the lowest ΔK experienced by sample 617-27G to the highest ΔK experienced by sample 617-32G, the transition time was found to be approximately 80 s.

According to E2760 for creep-fatigue crack growth testing [29], the stress intensity factor should not be used to characterize crack growth under the following condition:

$$\frac{1}{F} \leq \frac{t_T}{10} \qquad \text{Eq. 32}$$

Where F is the frequency of the hold-time cycle. As a result of this estimation, the data presented in Fig. 29 and Fig. 30 for 0.05 Hz triangle and trapezoidal waveforms must be flagged and treated

with care, because they do not meet the criteria set forth in Eq. 32 for correlating crack growth rates in a creep-ductile material with ΔK. However, because the transition time is 2-4 times larger than the waveform period tested (rather than a full order of magnitude as dictated by E2760), the data presented in Fig. 29 and Fig. 30 likely represents the transition between the correlating parameters ΔK and $(C_t)_{avg}$, where each have some utility.

2.3.2.6. Transition from cycle dependent fatigue to time dependent fatigue crack growth

Fig. 65 shows four etched crack profiles of 0.05 Hz triangular wave samples where the cracks were arrested at different stress intensity levels. Those micrographs show that a transition from transgranular to intergranular cracking occurs between K_{max} = 19 MPa√m and 23 MPa√m. This is also seen in the fatigue crack data as a breakaway acceleration in growth rates for both the 0.05 Hz and hold time specimens (Fig. 65). Despite the obvious grain boundary oxidation that occurs (Fig. 40 - Fig. 44), voids form ahead of the oxidized grain boundaries and coalesce to link with the main crack. Thus, stress assisted grain boundary oxidation (SAGBO) does not appear to be the time dependent crack growth mechanism under these test conditions. Rather, time dpenedent creep crack growth occurs by a classic void formatin mechanism. Fig. 64 also captures the transition from transgranular cracking to intergranular void coalescence observed in this study. The knee in the force line displacement rate curve at the onset of void coalescence is notable, as is the high level of compliance in the samples (i.e. thinner effective section thickness) at higher stress intensities.

A model recently proposed by Chan [32] can be used to predict the creep crack growth threshold for the SAGBO mechanism in nickel based alloys as:

$$K_{th} = K_{ox} + 2\, sgn(\varepsilon_{tr})[\frac{E_{ox}\sigma_{ys}|\varepsilon_{tr}|t_{ox}}{2(1-\nu^2)}]^{1/2} \qquad \text{Eq. 33}$$

In Eq. 33, K_{th} is the threshold stress intensity governing the transition to stress assisted oxidation of grain boundaries and subsequent cracking, K_{ox} is the fracture toughness of the oxide, sgn is a function giving 1 if the transformation strain associated with oxide formation, ε_{tr}, is positive, and -1 if ε_{tr} is negative, E_{ox} is the elastic modulus of the oxide species, σ_{ys} is the yield stress of the alloy; t_{ox} is the thickness of the oxide at the crack tip, and ν is Poisson's ratio of the oxide. The oxide thickness, t_{ox}, was estimated as ~1 μm from EDS line scans (Fig. 66) of a crack tested at the lower bound of the mechanistic transition (K_{max} = 19 MPa√m) while the yield stress, σ_{ys}, of Alloy 617 at 800 °C was taken as 189 MPa [1]. Each of the other parameters were taken from Chan [32]: K_{ox} of Cr_2O_3 was taken as 3.6 MPa√m, ε_{tr} as 5.96, E_{ox} as 143.6 GPa, and ν as 0.33. These values predict a threshold stress intensity, K_{th}, for SAGBO crack propagation of approximately 23 MPa√m. This demonstrates the threshold for void growth is only slightly lower than that for SAGBO, and these mechanisms are in competition. This is supported by our own observations of oxidized, non-propgating grain boundaries and this could also explain why a study by Ma et al. concluded that a SAGBOE mechanism was active in Alloy 617 at 800 °C in air when a sustained load of K = 27.75 MPa√m was held.

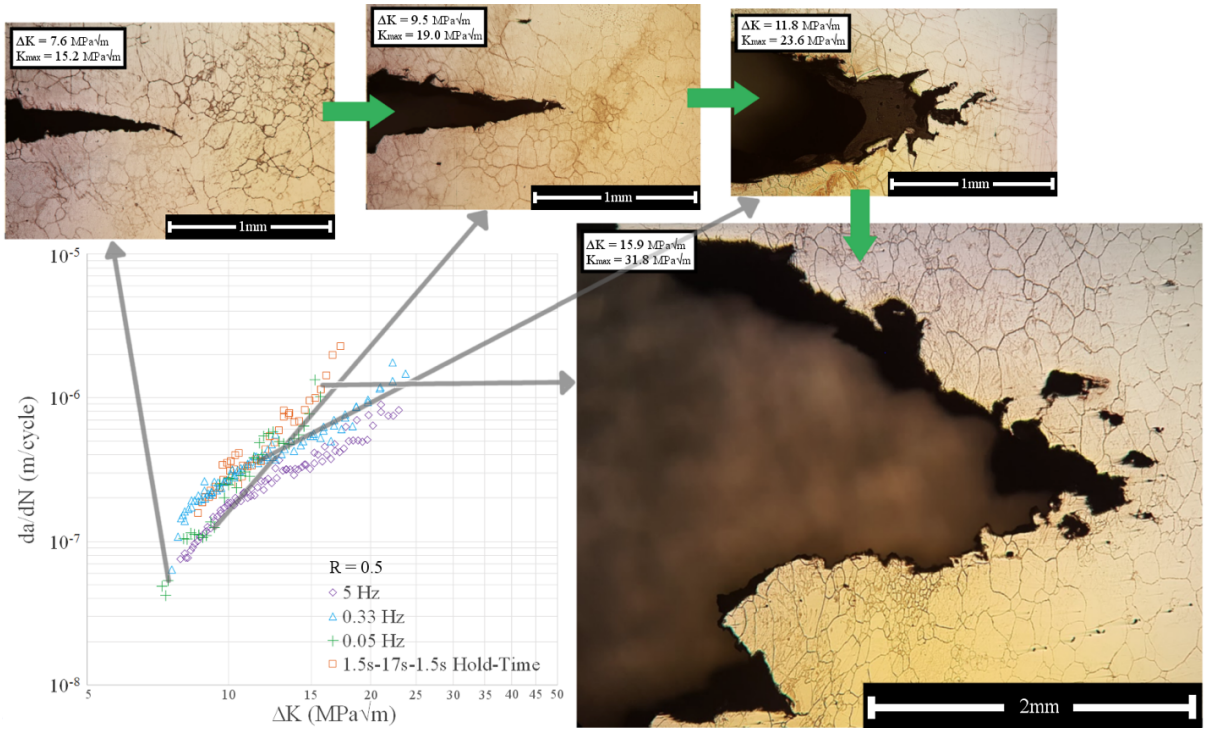

Fig. 65. The transition from transgranular crack growth to void coalescence, displayed in the sectioned profiles of four 0.05 Hz samples.

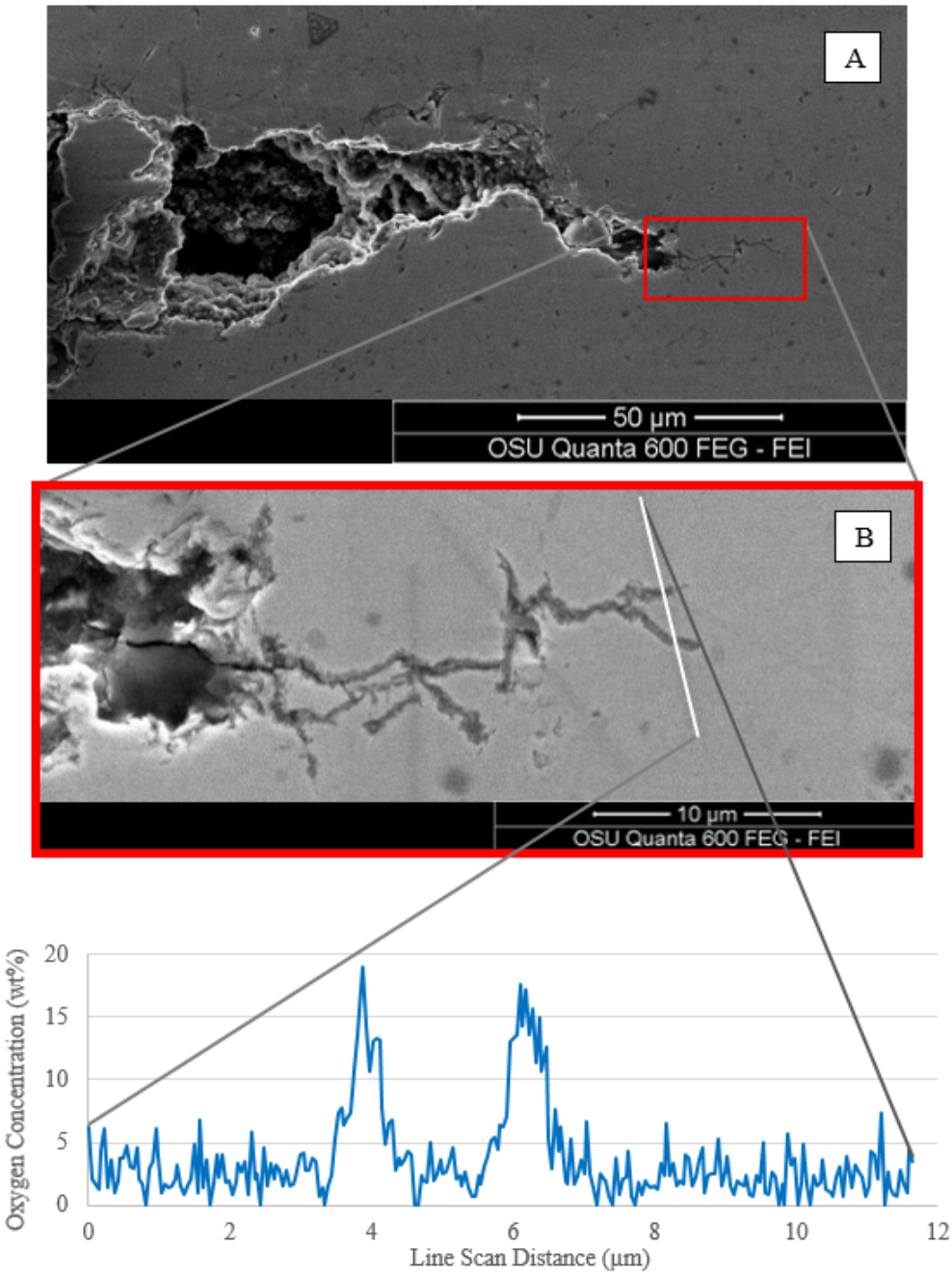

Fig. 66. Crack tip profile of 0.05 Hz sample 617-26G, with final ΔK=9.5 MPa√m and Kmax = 19 MPa√m. (A) SEM micrograph of crack tip, (B) Enlarged crack tip region with oxidation quantified by an EDS line scan.

2.3.3. Overload Crack Growth Experiments at 800 °C

The response to cyclic overloads was studied using both sample geometries at a frequency of 0.33 Hz. Samples 617-15GO, 617-16GO, 617-17GO and 617-28GO were used for this purpose.

For sample 617-15GO at $\Delta K \sim 8.3$, a single 125% overload was applied and the response was recorded upon a return to normal cycling. Under these conditions, no discernable crack growth retardation effect was detected. Likewise, no discernable traces of the single overload were found on the fracture surface.

Samples 617-16GO, 617-17GO and 617-28GO were subjected to blocks of cyclic overloads in order to enhance the crack growth rate retardation effect. Each block was 20 cycles long, as shown schematically in Fig. 25. For 617-16GO and 617-17GO, K_{max} of the overload cycles was equal to 125% of K_{max} during normal cycling, and the samples were subjected to two and ten blocks, respectively. Successive overload blocks were separated by at least 1000 cycles. For 617-28GO, K_{max} of the overload cycles was 150% of K_{max} during normal cycling, and the sample was subjected to 5 overload blocks in total. R was maintained at 0.5 during all overload cycles. Fig. 67 and Fig. 68 show the effect of the first and second block of overloads applied to sample 617-16GO, and include a micrograph of the fracture surface at that point. Fig. 69 shows the effect of the first block of overloads applied to sample 617-28GO, and the micrograph of the fracture surface is lower in magnification, emphasizing the overall character of the overload region, which took place within a transgranular cracking mode. In Fig. 67 through Fig. 69, linear regressions of the first 200 normal cycles following an overload, as well as after the overload effect dissipated, were constructed and intersected in order to gauge the length of the deceleration period. Note that there appears to be no discernable deceleration period in Fig. 68 – the linear regressions practically overlap, and it is consistent with an increasing ΔK test regime that the linear regression constructed several hundred cycles after the overload block would be slightly steeper.

The depression in crack growth rates after overloading lessened at higher stress intensities. The ten overload blocks applied to sample 617-17GO were plotted against the crack growth rates predicted by a power law fit of the unimpeded cyclic fatigue data produced at 0.33 Hz. The results are shown in Fig. 70.

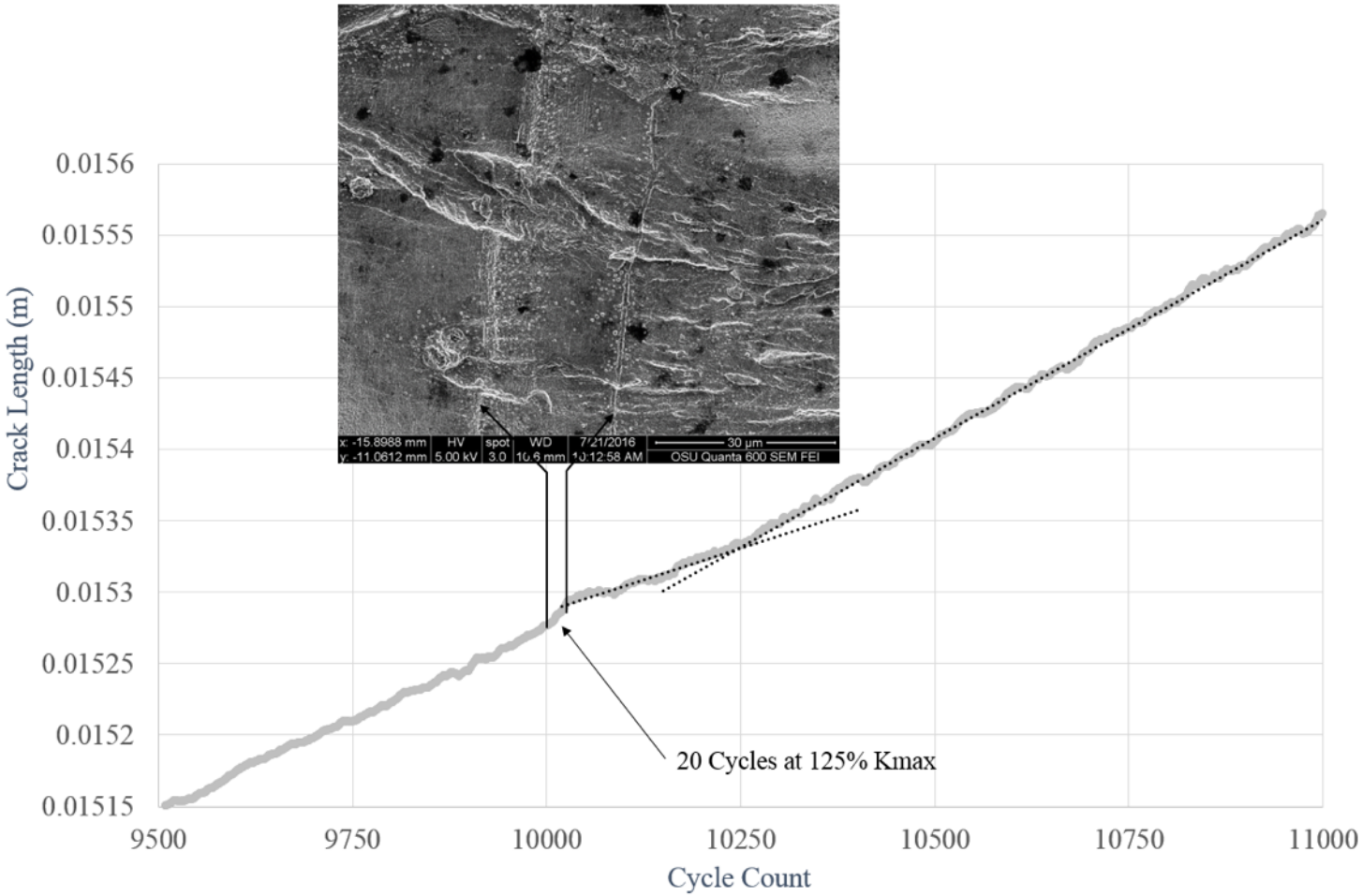

Fig. 67. Crack length vs. cycle count surrounding the first 20 cycle 125% Kmax overload block applied to sample 617-16GO. ΔK measured just prior to the overload block was 10.4 MPa√m. The average ΔK during the overload block was 13.0 MPa√m.

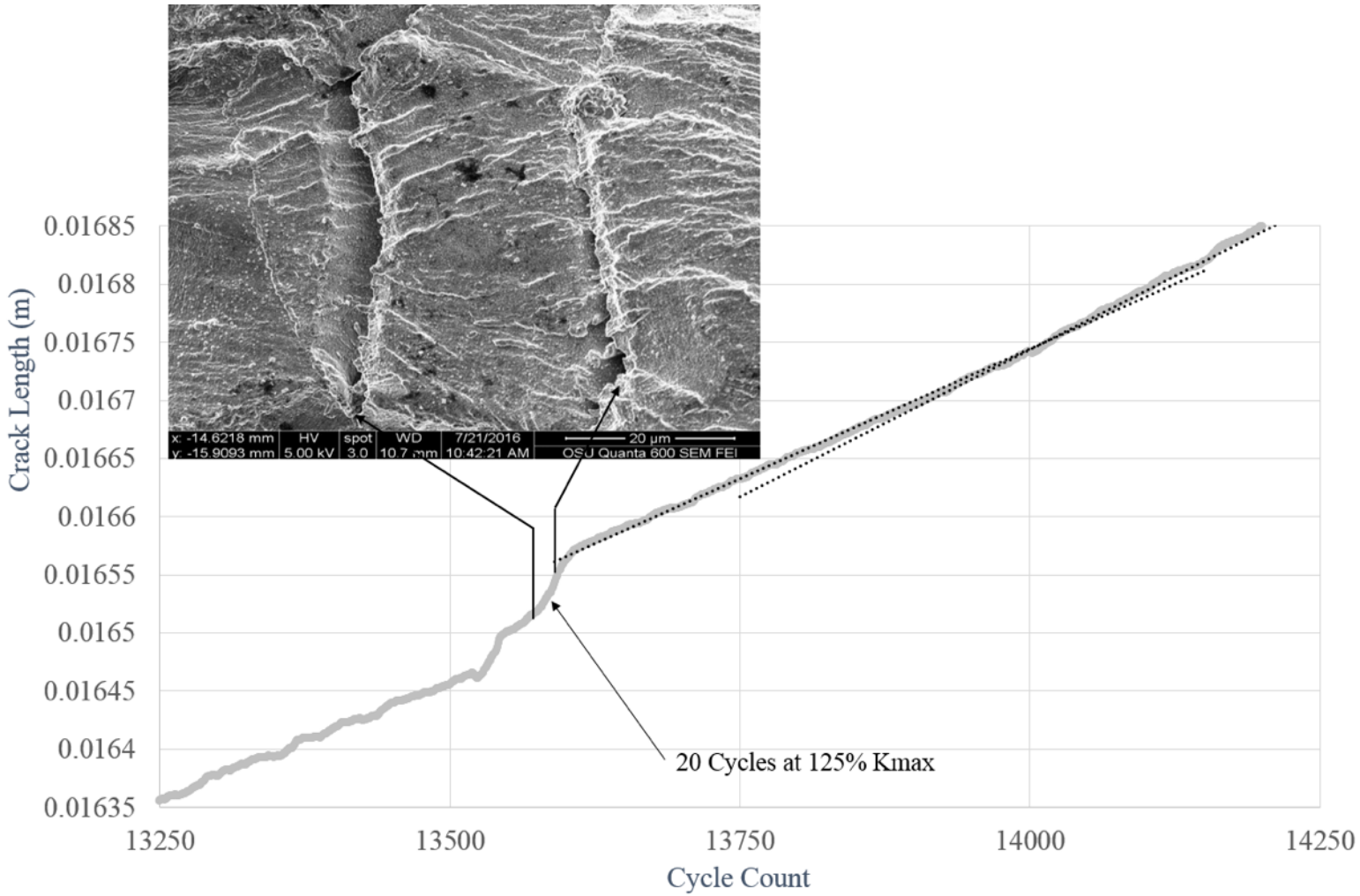

Fig. 68. Crack length vs cycle count surrounding the 2nd 20 cycle 125% Kmax overload block applied to sample 617-16GO. ΔK measured just prior to the overload block was 12.6 MPa√m. The average ΔK during the overload block was 15.9 MPa√m.

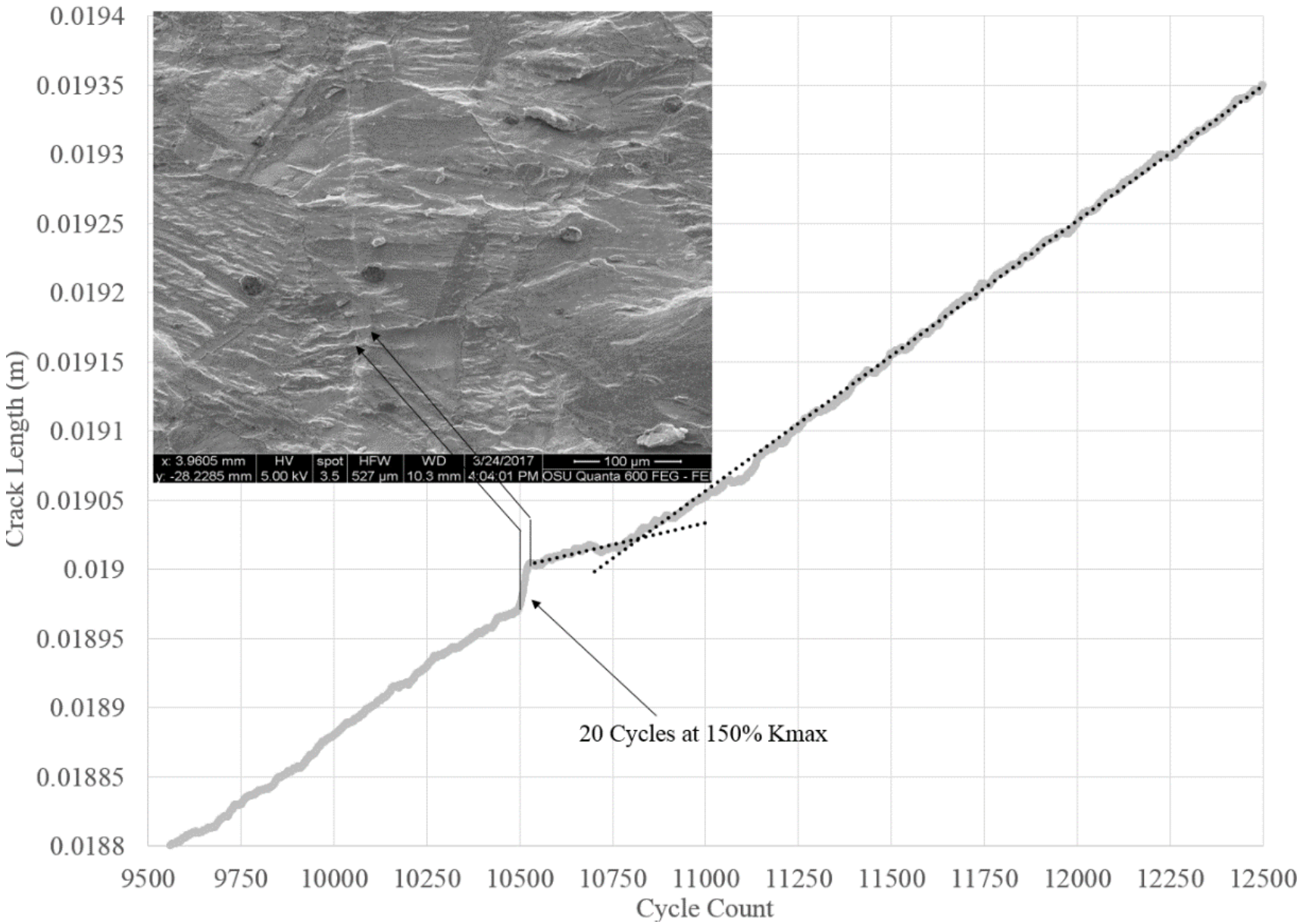

Fig. 69. Crack length vs cycle count surrounding the first 20 cycle 150% Kmax overload block applied to sample 617-28GO. ΔK measured just prior to the overload block was 8.3 MPa√m. The average ΔK during the overload block was 12.6 MPa√m.

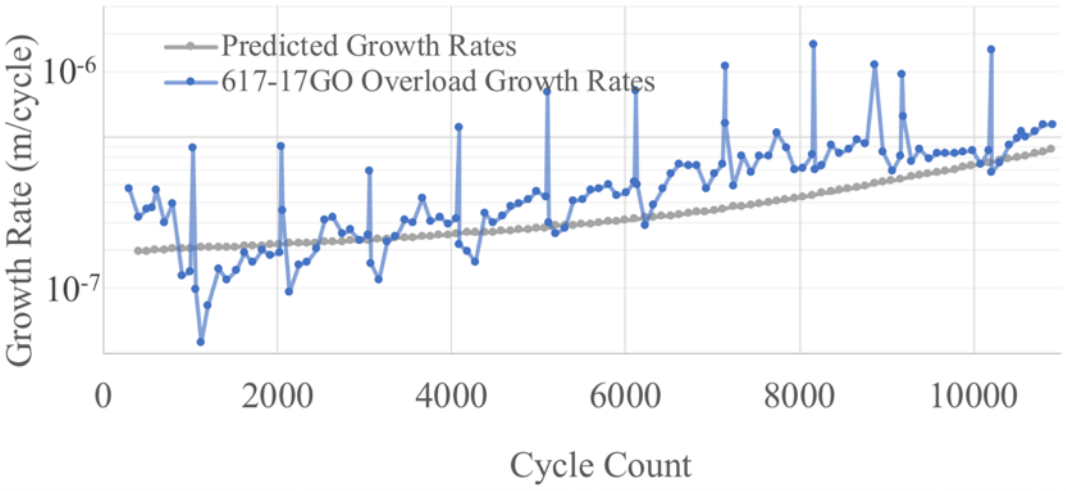

Fig. 70 Crack growth rates calculated for 617-17GO and predicted growth rates for a sample cycled at 0.33 Hz with no overloads.

2.4. Visco-Plastic Strain-Gradient Irreversible Cohesive Zone Formulation

The main goal of this project is to apply a multi-scale, mechanism-based model to predict the creep-fatigue crack growth in Alloy 617 at 800°C. While the previous sections discussed our efforts to measure model parameters and collect data for model validation, the following sections outline the model development.

2.4.1. Background

In a classical formulation of plasticity or visco-plasticity, no lengthscale-effects are included. Here we report on computations with a strain gradient dependent visco-plasticity model. We first use high temperature nanoindentation to determine the creep response. As Phani and Oliver [33] pointed out, it is difficult measuring basic material properties at high temperature by indentation following the Nix and Gao [19] approach. This is due the time-dependency of the extracted values, e. g. the hardness which not only depends on the load but also on the holding-time due to visco-plastic material behavior. Therefore, inverse analysis by finite element (FE) method can be an invaluable tool to identify material parameters. Especially indentation has a great potential for identifying creep parameters even after short holding times due the inhomogeneous stress field underneath the indenter. In contrast to uniaxial creep test, only one experimental setup at a chosen loading would be sufficient to represent the behavior of different stress levels. Beside defining a method to identify indentation creep parameters, the computational model can be used to determine the best indenter geometry and load history to be used in experiments. Examples of such analyses are provided for nanoindentation creep at large loads.

However, a range of micro-scale experiments have shown distinct size effects associated with plasticity [34-37] even at high-temperatures [38,39]. Strain-gradient plasticity theories have been developed to introduce an intrinsic material length parameter [40-43] in order to account for the observed size effects. The intrinsic lengthscale then relates to the scale of deformation at which effects due to plastic strain gradients becomes significant [44]. The response of a mechanical model accounting for plastic strain gradients in the formulation of the constitutive model converges

to that obtained with a conventional plasticity model if the characteristic length of the plastic deformation process is considerably larger than the intrinsic material length l [43]. We currently identify the material length scale without the use of the FE analysis.

In elasto-plastic solids, the local flow stress and strain hardening conditions determine the crack tip fields, and thus also the crack growth resistance through the energy dissipation associated with plastic deformation. The small size of the plastic zone at the crack tip and the large plastic strain gradients can promote a strong size effect associated with cracks [45,46]. In [46-50], it was shown that plastic strain gradient effects increase the stresses at the crack tip significantly. The radius of the influence zone of the strain gradients at the crack tip is on the order of 10 μm which is on the same order of magnitude as intrinsic lengthscales in strain gradient plasticity models. Thus, local mechanisms associated with plastic strain gradients can play an important role on fracture processes.

The seminal work of [51] employing a boundary layer model in combination with cohesive zone elements established important knowledge on to the processes of mode I crack growth in an elasto-plastic solid. The ratio of cohesive strength to yield strength, and the strain hardening exponent N were found to be key parameters determining fracture toughness and crack growth resistance. Using a similar model, [52] demonstrated that once plastic strain gradients are accounted for in the constitutive model, a reduced steady state toughness emerges. In [44], a comparable model was used to study steady-state crack growth, again including plastic strain gradients. These authors found that larger values of the intrinsic length would lead to increased stresses near the crack tip but at the same time results in lower stresses away from the crack tip, all compared to a response based on strain-only plasticity. In additional, accounting for plastic strain gradients lead to an increase of the predicted plastic zone size while at the same time resulting in a decreased crack opening displacement and steady state toughness.

A few authors have considered visco-plastic strain gradient theories. In [53,54], initial visco-plastic strain gradient theories were defined. A small deformation visco-plastic strain gradient theory was proposed in [55], and applied in [56] to the analysis of thin films but rate effects were not considered explicitly for the analysis of this boundary value problem. In [57] a visco-plastic strain gradient formulation based on [58] and [59] was introduced and applied to inclusion and void growth problems. The results demonstrate an increased rate sensitivity when strain gradient effects are accounted for in the visco-plastic formulation. A small and large-deformation visco-plastic strain gradient theory was introduced by [60,61]. Both theories are higher order gradient models accounting for microscopic boundary conditions. The model was applied to several boundary value problems but rate effects were not explored. Recently, in [62] a rate-dependent implementation of the corresponding rate independent models of [63] was presented. Loading rate conditions considered in that study were such that stress relaxation was dominant. Visco-plastic effects were found to be more pronounced for larger (dissipative) lengthscale parameters.

In the context of fracture problems few prior investigations exist that have investigated the effects of visco-plasticity combined with strain gradients effects. In [64] and [65] steady state crack growth in mode I and mixed mode, respectively, was analyzed by combining a steady-state crack growth model with a strain gradient visco-plastic constitutive model. These authors applied a model for cleavage cracking proposed by [66]. It was found that hardening due to plastic strain gradients decreases the macroscopic toughness independent of the crack tip velocities. Strain gradients also alter the stress triaxiality, and visco-plastic effects appear to stabilize this effect. A characteristic velocity delineating domains of increased and decreased toughness with the degree

of visco-plasticity was found to exist not only for the case of a lengthscale independent constitutive formulation but persisted in the case of a gradient theory as well.

The present study considers a visco-plastic strain gradient model for the analysis of transients as these arise in stresses and strains associated with a crack tip. The study employs a finite element representation of a modified boundary layer model and cohesive zone elements for crack growth studies. The parameters of the visco-plastic strain gradient model are varied parametrically covering small and large visco-plastic power exponent, as well as a range of relevant intrinsic material length values. Two scenarios are investigated: (i) a model with a stationary crack and (ii) a model with crack growth under monotonic loading. Both a modified boundary layer model as well as a model of a compact tension specimen is employed.

2.4.2. Visco-plastic strain-gradient formulation

A constitutive model of conventional theory of mechanism-based strain-gradient visco-plasticity (CMSG-vp) is considered in order to model the time and length-scale dependent constitutive response. Both a plane strain and an axisymmetric version are considered. The model is based on the formulation of [43]. An intrinsic material length parameter l which is defined for a face-centered cubic (FCC) crystal:

$$l = 18\alpha^2 \left(\frac{\mu}{\sigma_Y} \right)^2 b \qquad \text{Eq. 34}$$

where b is the magnitude of the Burgers vector, μ is the shear modulus, σ_Y is the yield strength, and α is an empirical prefactor ($0.2<\alpha<0.5$) [41]. Employing summation notation of continuum mechanics, the increment of the effective visco-plastic strain gradient $\dot{\eta}^{vp}$ is calculated as Gao et al. [41]:

$$\dot{\eta}^{vp} = \sqrt{\frac{1}{4}\dot{\eta}^{vp}_{ijk}\dot{\eta}^{vp}_{ijk}} \qquad \text{Eq. 35}$$

where

$$\dot{\eta}^{vp}_{ijk} = \dot{\varepsilon}^{vp}_{ik,j} + \dot{\varepsilon}^{vp}_{kk,i} - \dot{\varepsilon}^{vp}_{ij,k} \qquad \text{Eq. 36}$$

and

$$\eta^{vp} = \int \dot{\eta}^{vp}\, dt \qquad \text{Eq. 37}$$

with the visco-plastic strain rate $\dot{\varepsilon}^{vp}$ A visco-plastic constitutive model is used leading to the visco-plastic strain rate $\dot{\varepsilon}^{vp}$ via a Norton visco-plastic model, Eq. 38:

$$\dot{\varepsilon}^{vp} = A\sigma^m = \frac{\dot{\varepsilon}_0}{\sigma_Y^m}\left[\frac{\sigma_e}{\sqrt{f^2\left(\varepsilon^{vp}\right) + l\eta^{vp}}} \right]^m \qquad \text{Eq. 38}$$

$$\dot{\varepsilon}^p = \dot{\varepsilon}\left[\frac{\sigma_e}{\sigma_Y\sqrt{f^2(\varepsilon^p)+l\eta^p}}\right]^{75} \qquad \text{Eq. 39}$$

where A is the visco-plastic prefactor, m is the visco-plastic exponent, and $\dot{\varepsilon}_0$ is the reference strain rate. The visco-plastic formulation has been modified by Huang et al. [44] to obtain a rate independent formulation of the conventional mechanism strain gradient plasticity model, Eq. 39. Also, a flow stress is defined as $\sigma_{flow} = \sigma_Y f^2(\varepsilon^{vp}) + l\eta^{vp}$. The non-dimensional function $f^2(\varepsilon^{vp})$ in is defined for a power-law hardening solid

$$f\left(\varepsilon^{vp}\right) = \left(1+\frac{E\varepsilon^{vp}}{\sigma_Y}\right)^N \qquad \text{Eq. 40}$$

with the plastic strain hardening exponent N, the Young's modulus $E=2\mu(1+\nu)$, and the Poisson's ratio ν. A basic Norton model can be obtained with $N=0$ and $l=0$ and describes a steady-state secondary creep regime. This model is used as a comparison system and for several of the basic model development studies. Additional strain hardening $N>0$ for $l=0$ corresponds to the conventional primary creep regime [67,68] for short loading times which passes into a steady-state regime in the long term. Strain gradients affect the hardening response of the model if gradients are sufficiently large. All calculations are isothermal and the intrinsic material length is considered as constant during one simulation. The constitutive model was implemented as a UMAT subroutine for the implicit commercial finite element solver ABAQUS STANDARD. The model is based on the rate-independent UMAT created by [43].

The current CMSG user defined material is based on an explicit calculation of the nonlinear material equations. To ensure the stability of the solution, small time increments had to be defined. An additional stability check of the current explicit solution was not performed in the original code. In the current project phase, an additional stability criterion for the explicit solution was defined and implemented. A critical time step Δt_c was defined by

$$\Delta t_c = \frac{cetol}{\dot{\varepsilon}^{vp}\Big|_{t+\Delta t} - \dot{\varepsilon}^{vp}\Big|_t} \qquad \text{Eq. 41}$$

with the creep strain $\dot{\varepsilon}^{cr}$ at two different times t and $t+\Delta t$. If the current time step is bigger than the critical time step Δt, is reduced by a factor of 0.25. *cetol* is an error tolerance which has to be defined by the user. It can be estimated by the Young's modulus E and a characteristic stress increment $\Delta\sigma$ by:

$$cetol \ll \frac{\Delta\sigma}{E} \qquad \text{Eq. 42}$$

Therefore, *cetol* is a small fraction of the ratio of the typical stress increment and the effective elastic modulus of the given problem. This approach is in most chases very conservative and good

solutions can be obtained by larger values of *cetol*. This strategy is used by the built-in viscous STEP in ABAQUS standard.

To test the modified CMSG code, 64 different test cases of the void growth simulation were performed by varying the void size r between 0.1μm, 0.2μm, 0.4μm & 1.0μm, the material length l between 0.0 μm & 4.5 μm, the maximum time step Δt between 0.001s, 0.002s, 0.005s & 0.01s, and the loading time t_{max} between 1s & 10s. The void model is shown in Fig. 71. Especially for a small void radius r and short loading times t_{max} the expected solution is not reached and the solution depends on the maximum time increment Δt as shown in Fig. 72(a). Fig. 72(b) shows the same results using the modified CMSG by defining *cetol*=0.001 which agrees very well with the expected solution. A dependency on Δt cannot be found in the modified code if a sufficient *cetol* is used.

Fig. 73 depicts representative solutions for the void growth problem. In Fig. 73(a) solutions are depicted that were obtained with the material length l=0.0 μm and l=4.5 μm for two small void sizes. These results demonstrate that in such a case the model is rate dependent for l=4.5 μm but not for l=0.0 μm. Both cases they are rate dependent. In Fig. 73(b) solutions are depicted with the material length l=0.0 μm and l=4.5 μm and two large void sizes. Now, the system response is less size dependent but the rate dependence remains.

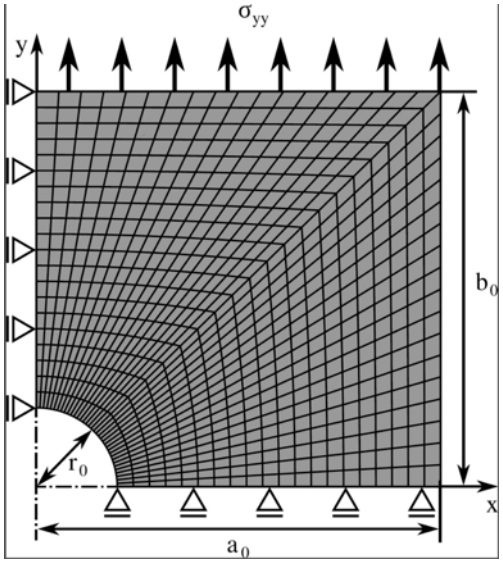

Fig. 71. Void model employed for the verification studies of strain gradient visco-plastic constitutive model.

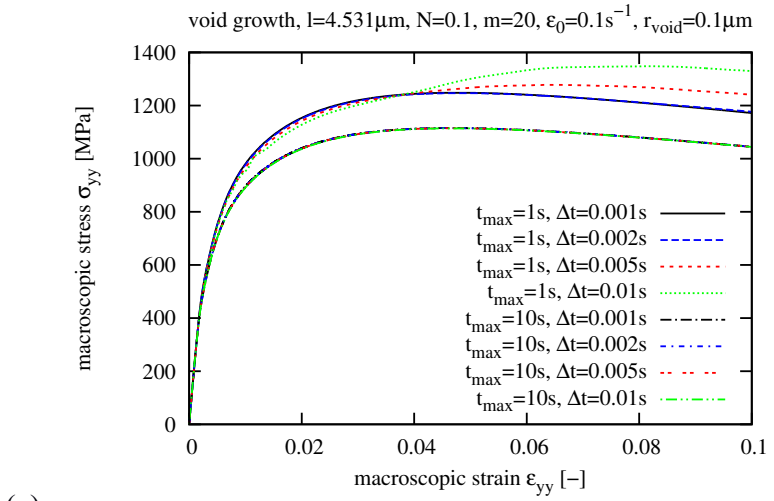

(a)

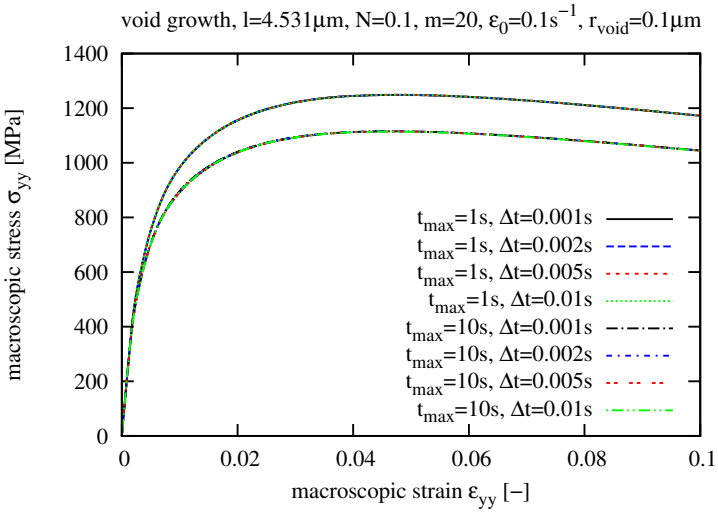

(b)

Fig. 72. Solution of void growth for small void radius (0.1µm) and l=4.5µm applying the modified CMSG (a) without defining an error tolerance *cetol* and (b) with defining an error tolerance *cetol*=0.001.

(a)

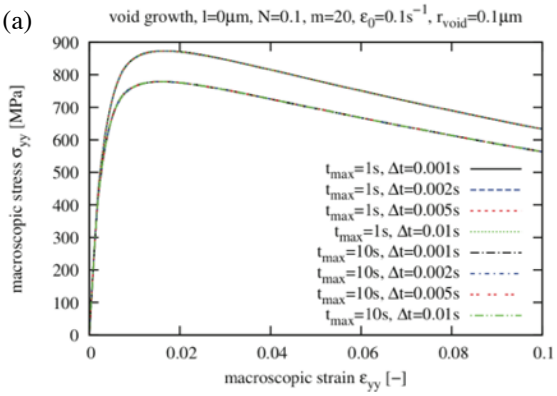
void growth, l=0μm, N=0.1, m=20, ε0=0.1s−1, rvoid=0.1μm
macroscopic stress σyy [MPa]
macroscopic strain εyy [−]
tmax=1s, Δt=0.001s
tmax=1s, Δt=0.002s
tmax=1s, Δt=0.005s
tmax=1s, Δt=0.01s
tmax=10s, Δt=0.001s
tmax=10s, Δt=0.002s
tmax=10s, Δt=0.005s
tmax=10s, Δt=0.01s

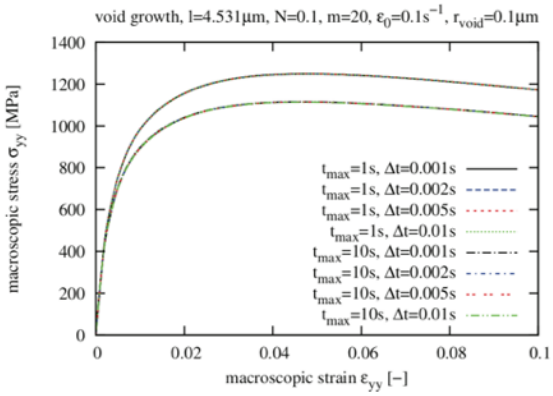
void growth, l=4.531μm, N=0.1, m=20, ε0=0.1s−1, rvoid=0.1μm
macroscopic stress σyy [MPa]
macroscopic strain εyy [−]
tmax=1s, Δt=0.001s
tmax=1s, Δt=0.002s
tmax=1s, Δt=0.005s
tmax=1s, Δt=0.01s
tmax=10s, Δt=0.001s
tmax=10s, Δt=0.002s
tmax=10s, Δt=0.005s
tmax=10s, Δt=0.01s

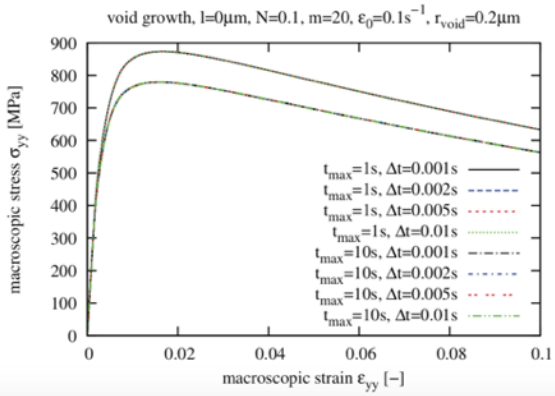
void growth, l=0μm, N=0.1, m=20, ε0=0.1s−1, rvoid=0.2μm
macroscopic stress σyy [MPa]
macroscopic strain εyy [−]
tmax=1s, Δt=0.001s
tmax=1s, Δt=0.002s
tmax=1s, Δt=0.005s
tmax=1s, Δt=0.01s
tmax=10s, Δt=0.001s
tmax=10s, Δt=0.002s
tmax=10s, Δt=0.005s
tmax=10s, Δt=0.01s

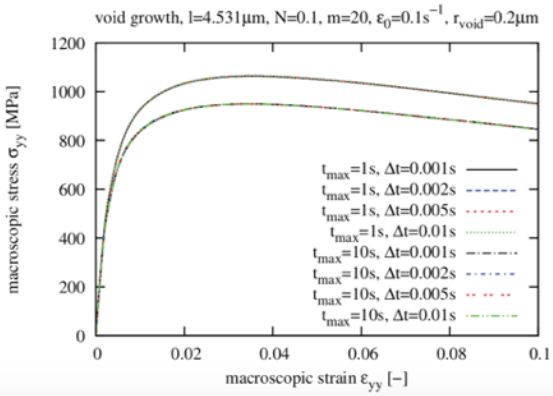
void growth, l=4.531μm, N=0.1, m=20, ε0=0.1s−1, rvoid=0.2μm
macroscopic stress σyy [MPa]
macroscopic strain εyy [−]
tmax=1s, Δt=0.001s
tmax=1s, Δt=0.002s
tmax=1s, Δt=0.005s
tmax=1s, Δt=0.01s
tmax=10s, Δt=0.001s
tmax=10s, Δt=0.002s
tmax=10s, Δt=0.005s
tmax=10s, Δt=0.01s

(b)

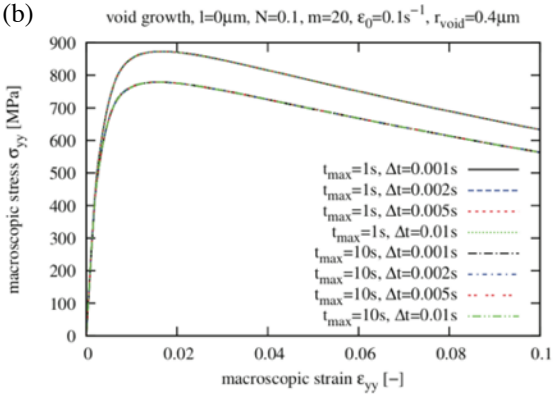
void growth, l=0μm, N=0.1, m=20, ε0=0.1s−1, rvoid=0.4μm
macroscopic stress σyy [MPa]
macroscopic strain εyy [−]
tmax=1s, Δt=0.001s
tmax=1s, Δt=0.002s
tmax=1s, Δt=0.005s
tmax=1s, Δt=0.01s
tmax=10s, Δt=0.001s
tmax=10s, Δt=0.002s
tmax=10s, Δt=0.005s
tmax=10s, Δt=0.01s

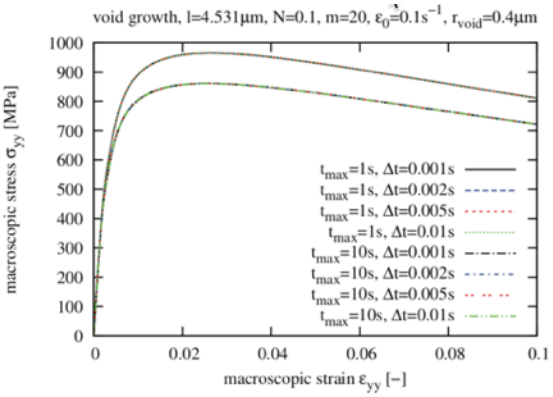
void growth, l=4.531μm, N=0.1, m=20, ε0=0.1s−1, rvoid=0.4μm
macroscopic stress σyy [MPa]
macroscopic strain εyy [−]
tmax=1s, Δt=0.001s
tmax=1s, Δt=0.002s
tmax=1s, Δt=0.005s
tmax=1s, Δt=0.01s
tmax=10s, Δt=0.001s
tmax=10s, Δt=0.002s
tmax=10s, Δt=0.005s
tmax=10s, Δt=0.01s

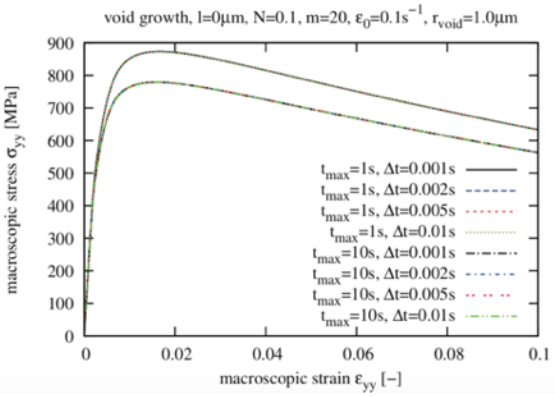
void growth, l=0μm, N=0.1, m=20, ε0=0.1s−1, rvoid=1.0μm
macroscopic stress σyy [MPa]
macroscopic strain εyy [−]
tmax=1s, Δt=0.001s
tmax=1s, Δt=0.002s
tmax=1s, Δt=0.005s
tmax=1s, Δt=0.01s
tmax=10s, Δt=0.001s
tmax=10s, Δt=0.002s
tmax=10s, Δt=0.005s
tmax=10s, Δt=0.01s

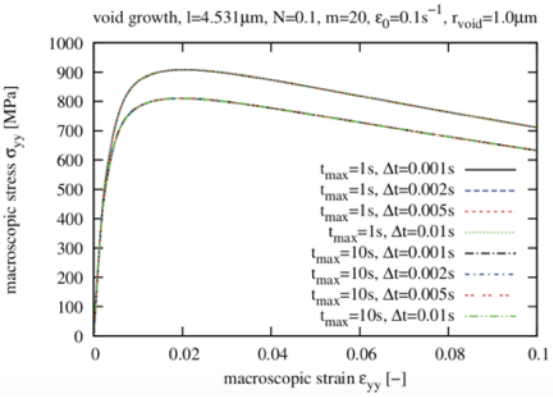
void growth, l=4.531μm, N=0.1, m=20, ε0=0.1s−1, rvoid=1.0μm
macroscopic stress σyy [MPa]
macroscopic strain εyy [−]
tmax=1s, Δt=0.001s
tmax=1s, Δt=0.002s
tmax=1s, Δt=0.005s
tmax=1s, Δt=0.01s
tmax=10s, Δt=0.001s
tmax=10s, Δt=0.002s
tmax=10s, Δt=0.005s
tmax=10s, Δt=0.01s

Fig. 73. Macroscopic stress/strain curves for the void growth problem comparing l=0 μm (no influence of strain gradient) to l=4.5 μm for two different strain rates and incrementations of the solution. (a) Void radii 0.1 and 0.2 μm. (b) Void radii 0.4 and 1.0 μm.

Summary on Computational Modeling: Visco-plastic Strain Gradient Plasticity

(a) Model description: A constitutive model which accounts for both size and rate effects on plastic deformation. The constitutive model accounts for an internal length scale in the plasticity formulation.

(b) Performance criteria: Implementation needs to allow for computation without the need for overly strong constraint in the time increments. This is accomplished by use of automated increment size correction.

(c) Test results demonstrating meeting model performance criteria: Model demonstrates the desired combination of rate and size effects. Size effects are large for small structures, size effects are absent for large structures.

(d) Theory behind the model: The model is a novel combination of the theory of conventional mechanism strain gradient plasticity and the Norton creep model.

(e) Mathematics to be used, formulas and calculation methods: See Eq. 33-38.

(f) Peer review of theory and algorithm, strength and weaknesses: The model has not been peer reviewed. Strength: the model allows for computation of combined rate effects and size effects in plasticity. Weakness: computation of plastic strain gradients require finite element meshes based on equiaxed quadrilateral elements.

(g) Hardware: Executable with a linux environment, requires the ABAQUS finite element code and fortran compiler

(h) Documentation (user guide, model code): Available on request to PI Siegmund (siegmund@purdue.edu)

2.4.3. Analysis of Nano-indentation

2.4.3.1. Methods

Indentation experiments are a convenient way to obtain conduct experiments on material behavior. However, the record of force-depth response does not directly translate into the parameters values needed to populate the material constants in constitutive models. The reason for this is that the stress and strain state associated with an indentation is highly heterogeneous.

An **inverse parameter identification method** has been established to identify material constants (the parameters of creep law and the material length scale). The parameter search uses either a Levenberg-Marquardt algorithm (LMA) or the interior-point alogorithm (FMINCON). The LMA is a robust non-linear least squares fit algorithm, which combines the Gauss-Newton method and the gradient descent method by using an interpolation technique. The LMA approach was used successfully for identification of creep parameters. Alternatively, the FMINCON algorithm in MATLAB is used. This algorithm is a constrained nonlinear multi-variable function with constraints defined by physical meaningful lower and upper bounds for the optimization variables. The algorithm is based on the interior point method which solves nonlinear convex optimization problems. This algorithm is robust, especially near the minimum where the gradient descent tends

to a zig-zag path which is not accessible by the LM algorithm. Far away from the minimum, the gradient descent is used which guaranties fast convergence.

To execute the simulations, the LMA algorithm in the MATLAB Optimization Toolbox was linked to the ABAQUS simulations. Fig. 74 provides an overview over the computational approach.

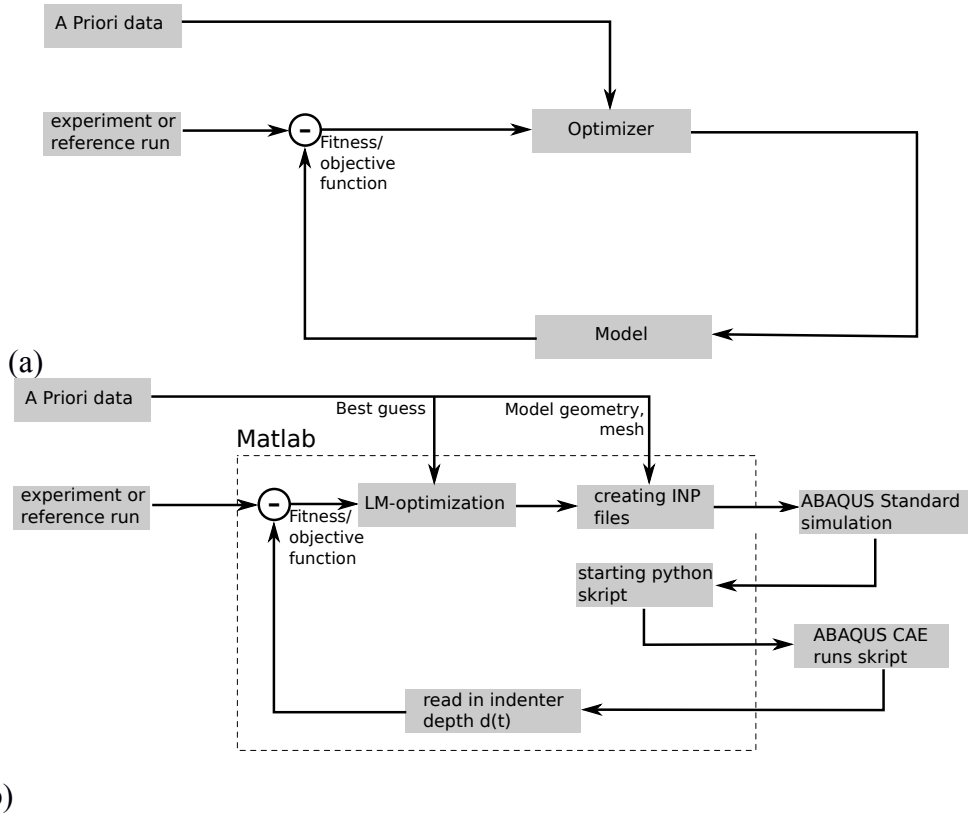

Fig. 74. (a) Overall concept of the inverse parameter identification approach. (b) Details of inverse modeling approach for the computational determination of material model parameters from indentation data. The LM-optimization can be substituted with the FMINCON-optimization if needed.

The fitness or objective function *objf* of a simulation run was defined as the sum of the least squares at all time points *k* as

$$objf = \sum_k \left(d_{k,ref} - d_k \right)^2 \qquad \text{Eq. 43}$$

where the indentation depth of a reference indentation (e.g. the experimental result or a defined reference parameter set) and d_k is the indentation depth of the simulation run. The inverse analysis approach described here was first tested on a linear elastic problem. Then computations were conducted were simulations with an assumed creep law were used to create synthetic reference data, and the algorithm "re-indentifies" the original creep parameters. Subsequently, experimental data were analyzed. For comparing the experimental results with FE simulations, constant number of time points very defined when the indentation depth were evaluated. The number of time points was constant for all simulation: the depth was evaluated 3 times during loading and unloading and 10 times during holding. During loading, holding, and unloading, the time points were chosen

equitemporal. Finally, computations were conducted to determine the material length scale. Again, first a parameter re-identification on synthetic data was conducted and subsequently the model was applied to experimental data.

A computational indentation model was developed to analyze indentation experiments on Alloy 617. These FE models were developed such that a close interaction between the computational mechanics aspects and the experimental work are enabled. The computational model is of axisymmetric geometry. In exploratory work, indentation simulations were performed with several different types of indenter geometries: a circular, a flat-punch, and a conical indenter. This allowed for the determination of the indenter geometry best suited to the investigation of Alloy 617 and high temperature nanoindentation. Similarly, exploratory studies were conducted with a range of different loading histories to determine which loading history one should consider in experiments. The geometries of the indenter and the sample, including the used FE mesh, are parameterized and can be adjusted to the experimental setup. A typical finite element mesh use in the simulation is shown in Fig. 75.

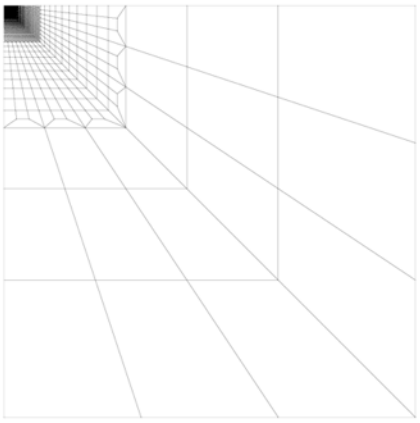

Fig. 75. Model domain for indentation simulation.

Three different indenter geometries are considered: (i) conical indenter, (ii) spherical, and (iii) flat-punch indenter (Fig. 76). Shi et al. [69] showed that a Berkovich indenter can be approximated by a conical indenter shape choosing the same cone angle of 65.3° if strain gradients are considered in the constitutive law. Otherwise an equivalent angle of 70.3° can be calculated. Hard surface-to-surface and frictionless contact is assumed between indenter and specimen. The simulation is load-controlled by specifying the load $P(t)$. The indentation depth $d(t)$ is therefore the output function. Different load scenarios of one step or stepwise increase of $P(t)$ are tested. The maximum load in this study is P_{max}=400 mN which also the maximum load used in the experimental setup. This maximum load results in an indentation depth in the order of micrometers representing the macroscopic behavior of the material at which no local hardening due to a high dislocation density underneath the indenter has to be considered.

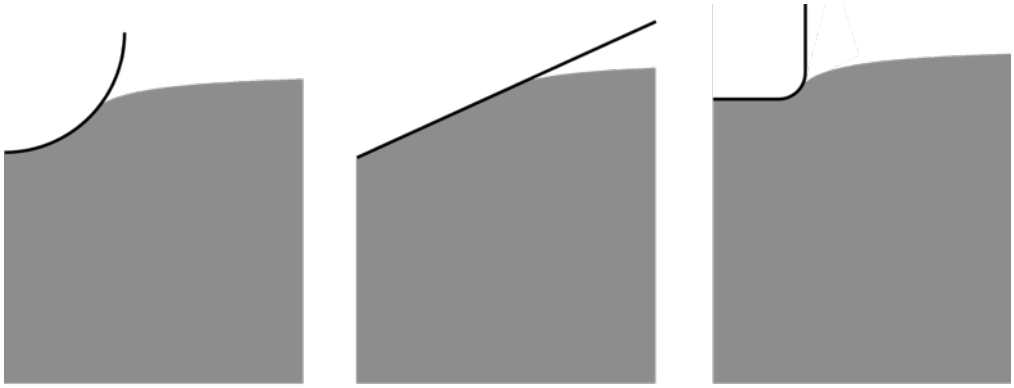

Fig. 76. Sketch of indenter geometries: spherical, conical, and flat.

2.4.3.2. Computational Results on Inverse Analysis of Indentation

First, **verification of the inverse parameter identification** approach was conducted. The approach is initially verified on a linear elastic system. Fig. 77**Error! Reference source not found.** depicts the problem. A plate with a hole (motivated by the micromechanical void growth problem) is considered and the material response is isotropic, homogenous and elastic. The computations demonstrated that the algorithm can successfully identify the material properties of reference computation.

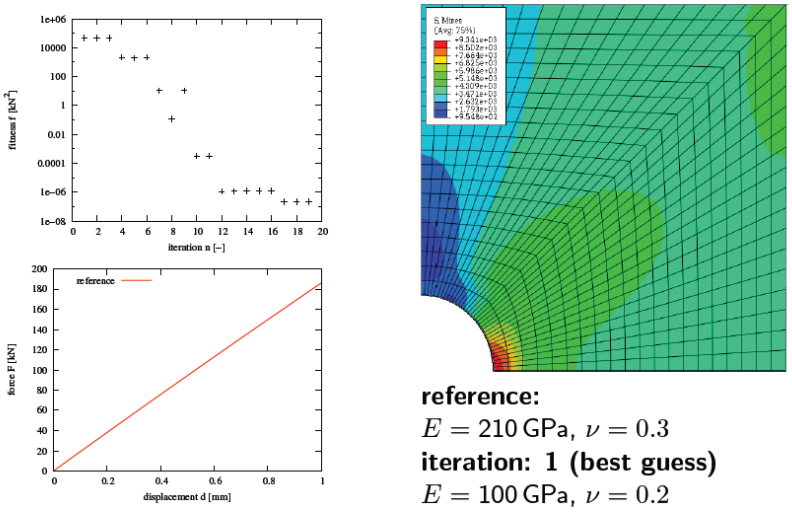

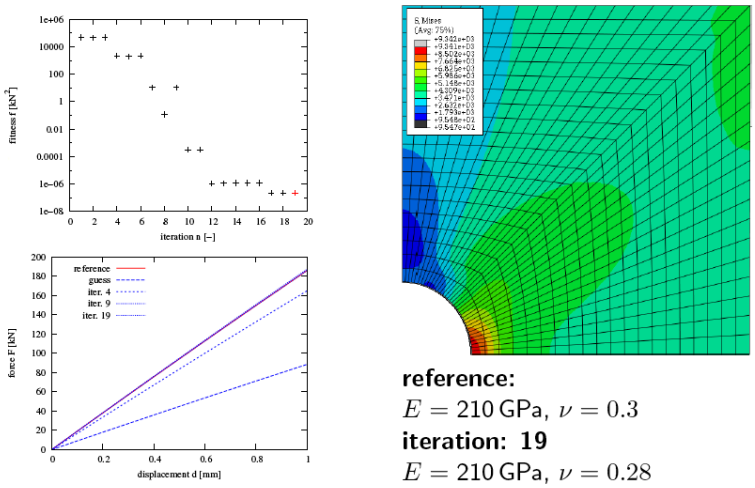

Fig. 77. Example of parameter identification with an elastic system, iteration and iteration 19 of the computation.

Subsequently, the algorithm was applied to the visco-plastic indentation problem. To optimize the experimental procedure of the indentation, a systematic variation of load scenarios were performed. Fig. 78 shows the load scenarios with varied holding time, a single or a stepwise increase of the load by 2 or 4 steps. A stepwise loading might be beneficial to identify the parameters of the creep law because the pre-factor A and the exponent m dominant different parts of the indentation response: For m=1 the pre-factor acts like a scaling factor of the equivalent stress. For $m \gg 1$ areas of high equivalent stress are lead to very high creep rates. The reference parameter set was set to A=5×10^{-21}MPa-ms^{-1} and m=5.6. The reference run represents an objective function with *objf*=0. For every loading scenarios, the creep parameters A and m of a power law creep law were varied within a range of values A=1×10^{-21}MPa-ms^{-1} to A=9×10^{-21} MPa-ms^{-1} and m=5.2 to m=6.0 The objective functions *objf* of every load scenario was calculated for the case of a conical indenter with θ=65.03° with a tip radius of r_{tip}=200 nm (approximating a Berkovich indenter geometry). Fig. 79(a) shows the objective function values computed for the load scenario 1 – 3 and Fig. 79(b) for the load scenarios 4 – 6. Every point of the surfaces grids indicates the fitness of one single indentation simulation (486 FE calculations in total for all considered scenarios) and was compared to the reference simulation run. It is shown, that the highest sensitive of a secondary creep law is achieved if the load is applied in one single step. This is indicated by the steeper slops or the higher values of the objective functions in that cases. A possible explanation for this behavior is that creep is more prominent if the maximum load was applied over a longer time interval. If the loading time is increased up to 1000 s the slope is further increased which confirms this hypothesis. Additional simulations show that the influence of the loading/unloading time on the objective function is negligible. Fig. 80 then depicts a set of similar computations of the objective function value and the sensitivity of the objective function values, but now considers the spherical and flat-punch indenter geometry (two indenter sizes are considered for each case). The computational data indicates that the use of indenter geometries other than the conical (Berkovich) indenter is not useful for the inverse analysis process. No clear minima are observed in the objective function field for these indenters. The subsequent analyzes are therefore conducted solely with the Berkovich (cone) indenter and a single step indentation-hold process.

The **computational identification of creep parameters** is the first step of the computational analysis of nano-indentation data. This analysis uses data from deep indentation such that

indentation size effects are excluded. Fig. 81 shows results from a computation demonstrating the identification of the creep power law using a single load step and 500 s hold time at maximum load. The identification of the creep parameters was successful by approximating the indentation depth over time data more closely with each iteration in the creep data. In summary, the results indicate that one single load step and use of Berkovich indenter can be used to identify a visco-plastic material law. Fig. 82 then demonstrates the use of the inverse analysis approach to identify creep model parameters on IN 617. Experimental indentation curves at large indentation loads and therefore in absence of strain gradient effects were considered. The computations were employed to successfully fit such experimental data using the inverse analysis approach with the FE method. A creep exponent m=5.6 was identified which is in excellent agreement with the value reported by Benz et al. for a minimum creep rate power law for Alloy 617 [2], and is also similar to our own fitting of the initial part of the creep curves from INL (Table 5).

2.4.3.3. Material Length Scale and Indentation on Alloy 617

Once the creep parameters are identified on experimental data with large indentation depth, Fig. 82, one then progresses to the **determination of the material length** using data on shallow indentation. Furthermore, re-identification of the length scale was successful by optimizing only one parameter (material lengthscale l) and keeping the creep parameters A and n constant as determined from the earlier analysis. This approach represents a two-step processes for identification of material constant from experimental nano-indentation data: First, identifying the creep parameters using the high depth/ high force data. Second, the low depth data could be applied identifying the length scale.

Here we demonstrate the length scale determination on synthetic data (i.e. indentation data derived from FE simulations with a non-zero material length scale). Fig. 83 shows the fitness function over iterations during a re-identification process for small indentation depth P_{max}=100 mN. For the generation of the synthetic data, the material length scale was chosen to be l=3.5 μm and the start parameter of 6.5 μm was used in the parameter search. After 11 iterations (representing 49 simulation runs) the optimization run converges. An optimal parameter value for the material length scale of l=3.58 μm was identified with a minimal fitness of 3.88E-6. Fig. 84 shows the indentation depth – time record at different iterations during the optimization process. Therefore, it was shown that the current algorithm is capable of identifying a creep law and the material length scale correctly.

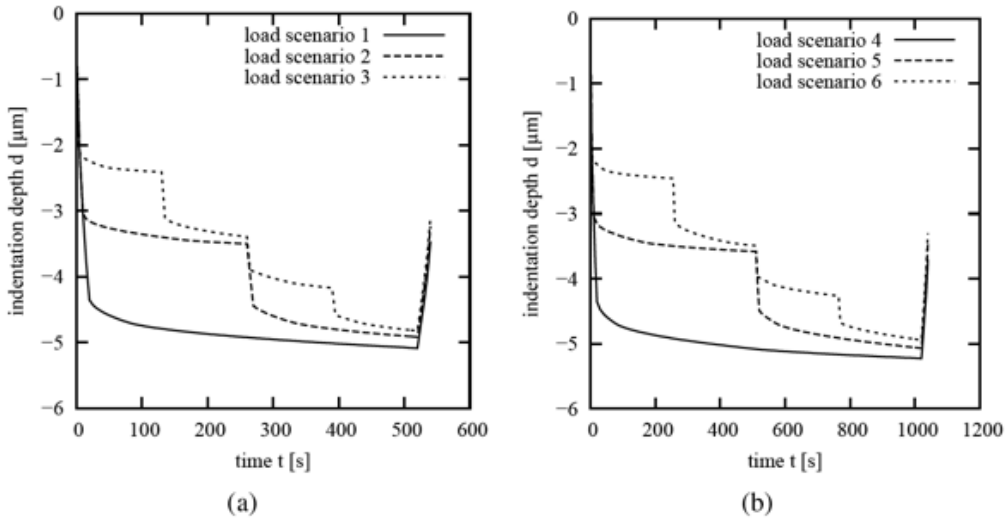

Fig. 78. Indentation depth over time for six loading scenarios, load P=400 mN for creep data A=5×10^{-21} MPa^{-n}s^{-1}, n=5.6. (a) Combined holding time of load scenarios 1–3 is 500 s. (b) Combined holding time of load scenarios 4–6 is 1000 s.

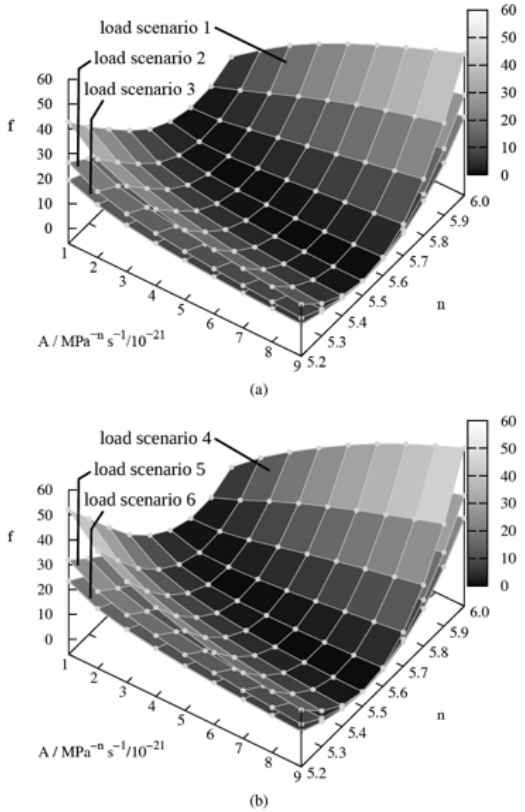

Fig. 79. Computed objective function values *objf* of the six load scenarios (a): 500 s accumulated loading time. (b): 1000 s accumulated loading time

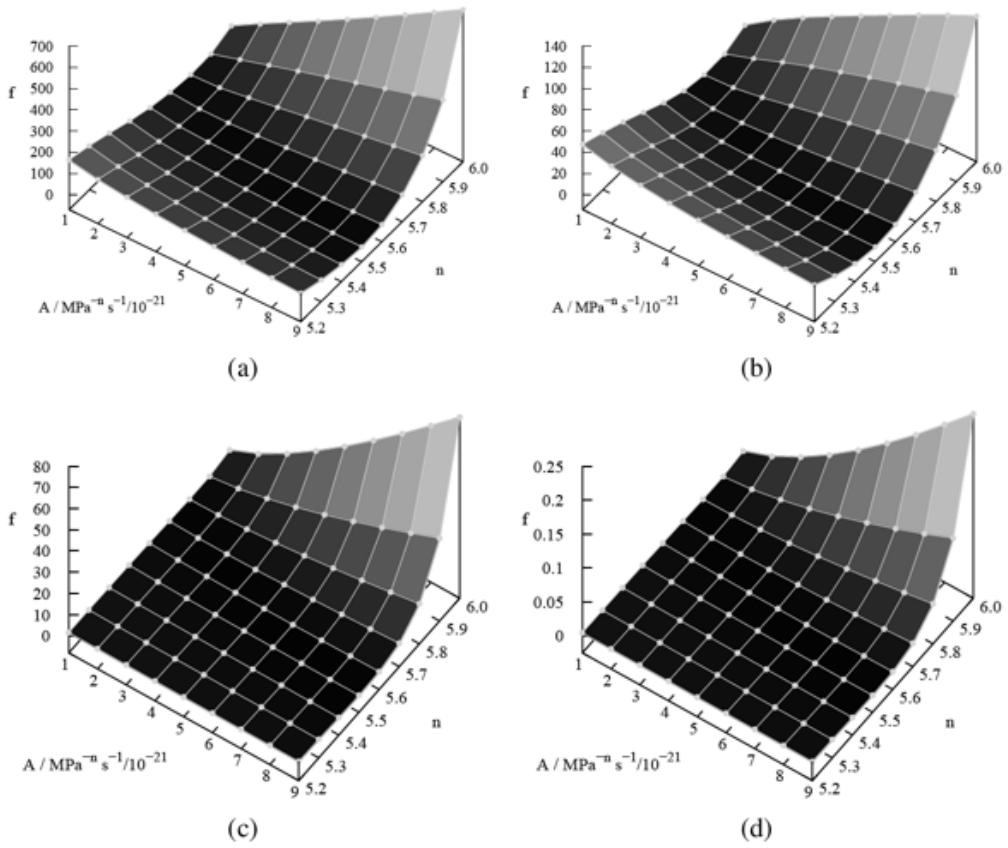

Fig. 80. Computed objective function values *objf* of load scenario #1 with four different indenters (a) Spherical indenter, r=10 micrometer, (b) spherical indenter r=15 micrometer, (c) flat punch indenter, r=10 micrometer, (d)flat punch indenter, r=15 micrometer.

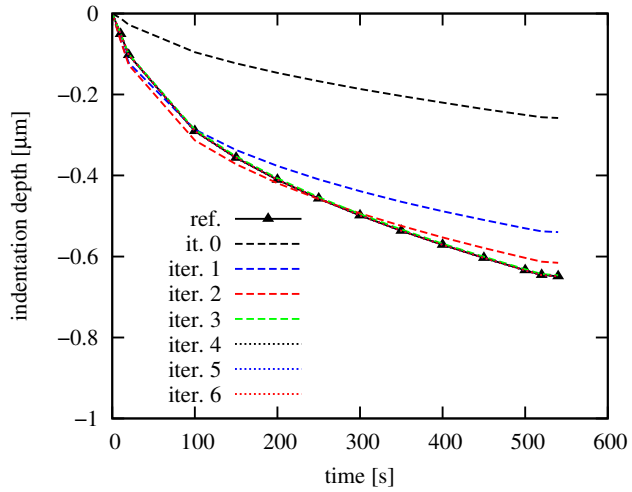

Fig. 81. Identification of power-law creep law (parameters A_0 and m) using 500s holding time after 6 LMA iterations, synthetic data.

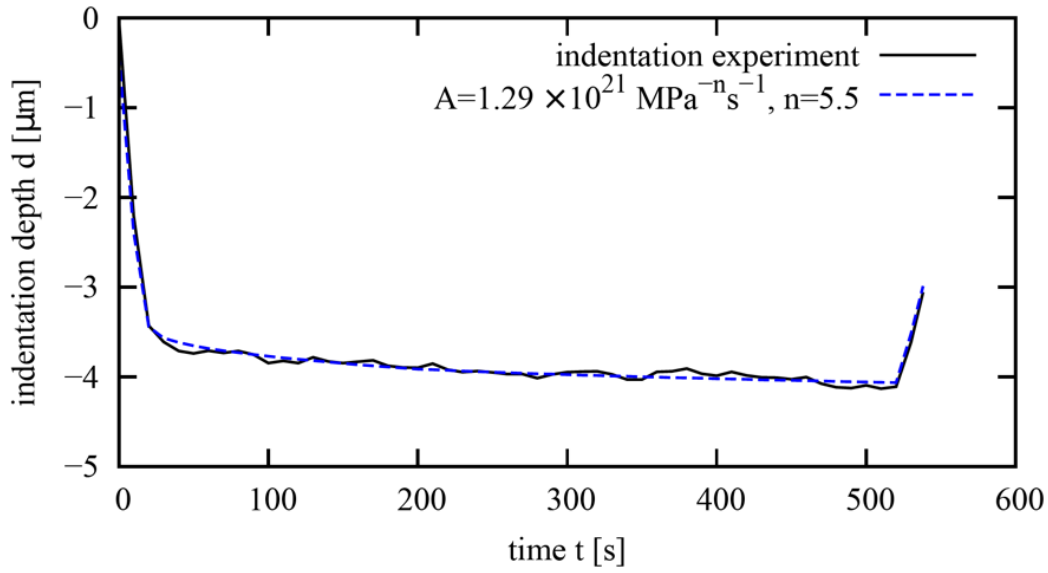

Fig. 82. Identification of creep parameters of Alloy 617 using experimental data and inverse analysis combined with the finite element analysis.

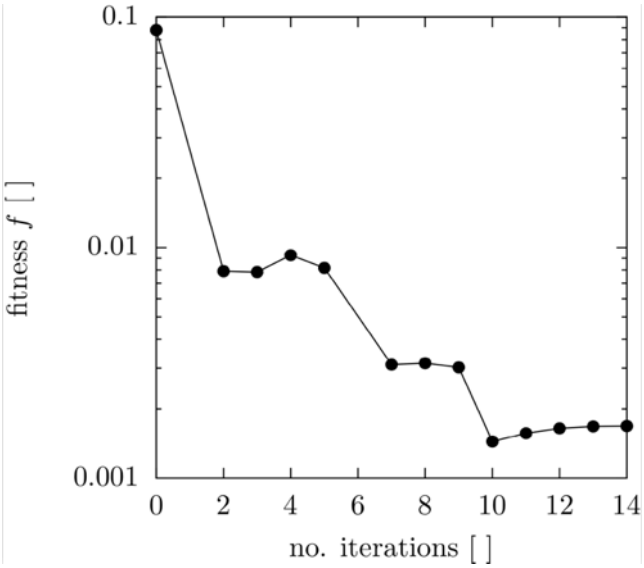

Fig. 83. Evolution of fitness function during search for the material length parameter.

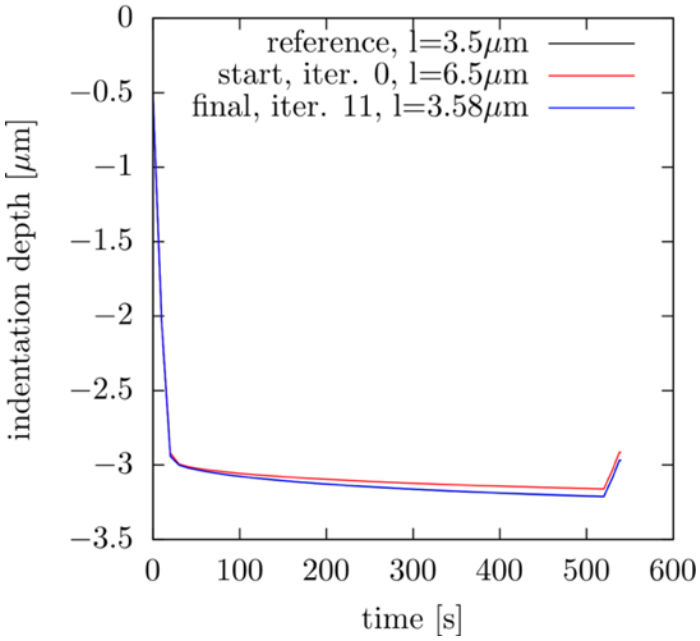

Fig. 84. Identification of material length parameter using synthetic data.

In addition to the inverse parameter identification approach, **a mechanistic approach is taken to obtain estimates for the material length scale** using indentation data in Alloy 617. An expression for the material length scale l is derived using a Taylor dislocation model, as described by Huang et al. [42]:

$$l = M^2 \bar{r} \alpha^2 \left(\frac{\mu}{\sigma_Y} \right)^2 b \approx 18 \alpha^2 \left(\frac{\mu}{\sigma_Y} \right)^2 b \qquad \text{Eq. 44}$$

where M is the Taylor factor (M=3.06 for fcc metals), $\bar{r}$ is the Nye-factor ($\bar{r}$=1.9 for fcc metals), the shear modulus μ, the yield stress σ_Y, the Burgers vector b, and an empirical coefficient α around 0.3. It is further possible to obtain more specific equations relating the material lengths scale to measured hardness data for the conical indenter, Huang et al. [42]:

$$l = \frac{4}{9} \frac{h^* H_0^2}{\sigma_Y^2 \tan^2 \theta} \qquad \text{Eq. 45}$$

Fig. 85 depicts the indentation data for Alloy 617 and denotes the numerical fit parameters for the indentation equations as best-fit parameters to data.

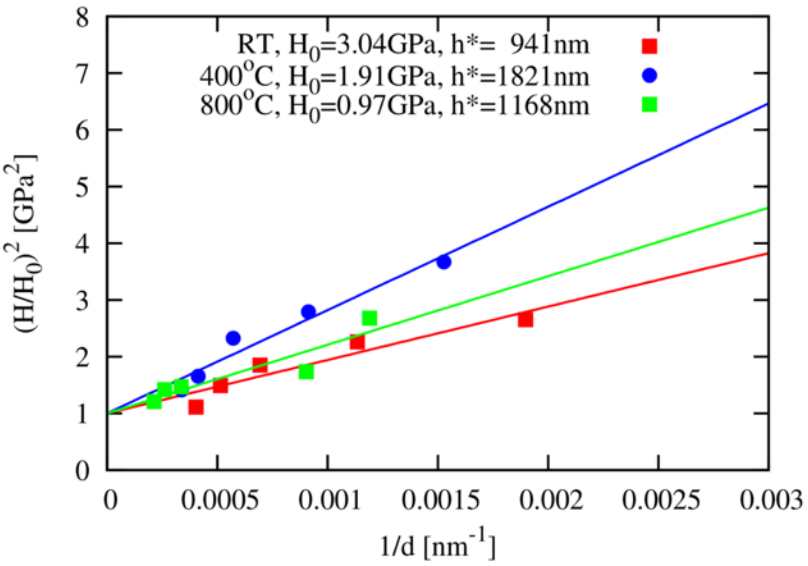

Fig. 85. Interpretation of hardness data across temperatures by use of Eq. 23 to extract a reference hardness H_0 and reference length h^*.

From comparing experimental data to Eq. 23, reference hardness H_0 and length h^* were determined for room temperature, 400 °C and 800 °C, as 3.04, 1.91, 0.97 GPa, respectively and 941, 1821, 1168 nm, respectively. The relevant material length, l, for the strain gradient plasticity model, is determined using Eq. 45. For Alloy 617 l=7.6, 12.0 and 4.8 µm were found for 25°C, 400 °C and 800°C, respectively.

Alternatively, if M, $\bar{r}$, b, and α are considered as temperature independent, the intrinsic material length over temperature $l(T)$ can be extrapolated by known values of l_{RT}, $\sigma_{Y,RT}$ and μ_{RT} at room temperature, and the temperature dependent $\mu(T)$ and $\sigma_Y(T)$ by

$$l(T) = \left[\frac{\sigma_Y(T = RT)\mu(T)}{\mu(T = RT)\sigma_Y(T)}\right]^2 l_{RT} \qquad \text{Eq. 46}$$

Using material parameters from literature (SpecialMetals: www.specialmetals.com/alloys, and summarized in Fig. 86) for RT (μ_{RT}=81 GPa, $\sigma_{Y,RT}$=350 GPa) and 800°C ($\mu_{800°C}$= 61 GPa, $\sigma_{Y,800°C}$=270 MPa), $l_{800°C}$ is about 95% of the material length at room temperature for solution-annealed hot-rolled Alloy 617. Fig. 87 shows the temperature dependency of l. For Alloy 617 the size of l increases from at RT to intermediate temperatures and declines at higher temperatures again. At 800°C the lengthscale is in the same range as at RT due to the combination of decrease in the shear modulus with temperature and the increase of yield strength at elevated temperatures. The finding of the extrapolation from room temperature is good agreement with the material length values obtained directly from data from nanoindentation at elevated temperature.

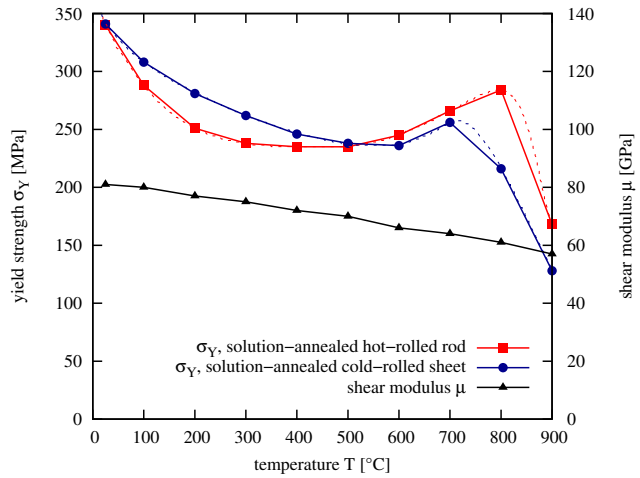

Fig. 86. Temperature dependent material data of Alloy 617 following SpecialMetals published data.

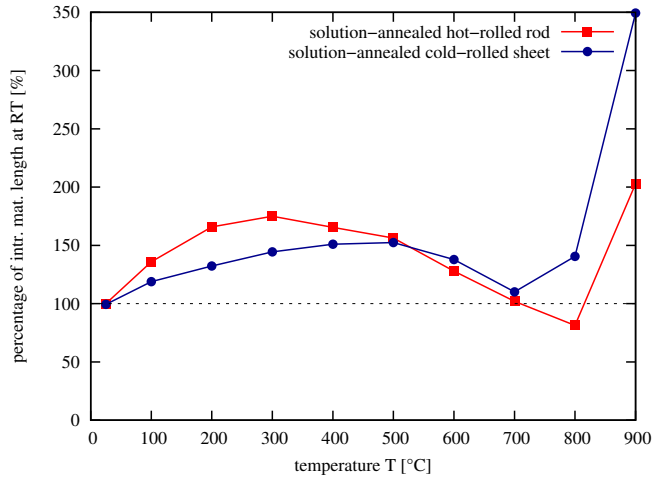

Fig. 87. Predicted change of intrinsic material length *l* over temperature.

Summary on Computational Modeling: Parameter Identification from Nano-indentation

(a) Model description: A parameter search method to determine values of constitutive model constants for the visco-plastic strain gradient model. Combining optimization algorithms with finite element computations leads to a code system for the parameter identification.

(b) Performance criteria: Implementation needs to be successful to identify parameters of synthetic material response.

(c) Test results demonstrating meeting model performance criteria: Test results demonstrate that the model is successful to re-identify material parameters for elastic, visco-plastic, and strain gradient visco-plastic response.

(d) Theory behind the model: The model is a novel combination of the theory of the rate dependent conventional mechanism strain gradient plasticity and optimization algorithms. Specific load cases are executed with a standard nonlinear finite element model.

(e) Mathematics to be used, formulas and calculation methods: See Eq. 33-38 for the constitutive model. LM and FMINCON algorithms are used as implemented in MATLAB.

(f) Peer review of theory and algorithm, strength and weaknesses: The model has not been peer reviewed. Strength: the model allows for effective parameter identification in a nonlinear mechanics problem. Weakness: None noted.
(g) Hardware: Executable with a linux environment, requires the ABAQUS finite element code and fortran compiler, also requires MATLAB and PYTHON.
(h) Documentation (user guide, model code): Available on request to PI Siegmund (siegmund@purdue.edu)

2.4.4. Crack Growth Simulations with the Modified Boundary Layer Model

2.4.4.1. Methods

A modified boundary layer (MBL) model is applied [49-51,64,65,70,71]. Plane strain conditions are assumed. The MBL model contains the crack tip inside a circular zone, with the crack tip near domain meshed by a regular quadrilateral mesh. Considering isotropic, linear elasticity, the asymptotic crack tip solution is applied at the outer circular boundary by an imposed time-dependent displacement $u(t)$ in x- and y-directions. Under these conditions, an elastic zone at the boundary constrains the small creep zone at the crack tip, [31]. A solution for the displacements can be obtained by the Williams-expansion under mode I [72,73]. The first order terms of the displacements u_x and u_y as a function of the radial and angular coordinates r and θ are

$$u_x(t) = K_I(t)\sqrt{\frac{r}{2\pi}}\frac{1}{2\mu}cos\left(\frac{\theta}{2}\right)\left(3-4\nu-cos\theta\right)$$
$$u_y(t) = K_I(t)\sqrt{\frac{r}{2\pi}}\frac{1}{2\mu}sin\left(\frac{\theta}{2}\right)\left(3-4\nu-cos\theta\right)$$

Eq. 47

where $K_I(t)$ is the prescribed time dependent stress intensity factor. The prescribed displacements due to a given remote K_I are applied as boundary conditions to every node on the outer boundary of the MBL model. The boundary conditions are implemented by applying the DISP user subroutine in ABAQUS STANDARD.

Fig. 88 shows the global FE mesh and the mesh refinement near the crack tip. Only a half-model is considered due to symmetry under mode I loading. The model consists of 3892 plane strain elements and 123 cohesive zone elements, both being linear elements. The cohesive elements are defined along the symmetry line starting at the crack tip in the direction of x in Fig. 88. The nodes of the cohesive elements coincidental with the symmetry line of the model are restricted to move only in x-direction. Symmetry conditions also dictate that the the ux displacement of the nodes of the cohesive elements are pairwise tied to each other. The maximum crack advance is much smaller than R_{MBL}. The initial crack was modeled with a sharp crack tip. This mesh geometry is justified by the results of [50] which shows comparable response of a plastic strain gradient formulation including an initially blunted crack. A mesh geometry including a sharp crack tip is ideal for crack propagation problems as is considered here in the monotonic loading case. The MBL model is an approximation of the conditions near the crack tip. For example, if the geometry of a compact tension, C(T), specimen is analyzed, higher order terms have an influence on the stress field near the crack tip which have to be considered. T-stresses can change the shape of the visco-plastic zone

[71] which influences the fracture toughness [74]. In addition, the time-dependent deformation of the circular boundary during loading (predominantly for a prolonged hold time) has not taken into account in the MBL model.

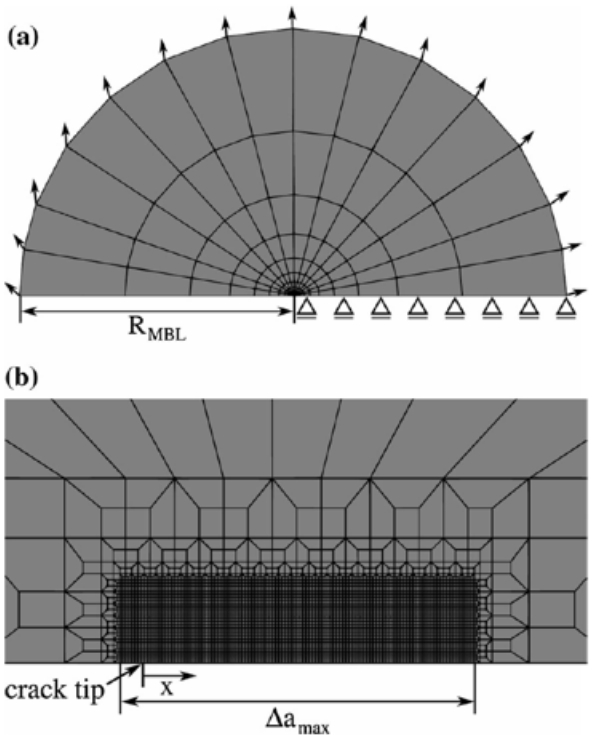

Fig. 88. Global (a) and refined finite element mesh (b) near the crack tip of the modified boundary layer model. The applied displacement u(t) calculated by Eq. 47 at the circular outer boundary is illustrated by arrows.

Cohesive-zone (CZ) elements with a traction-separation relationship as motivated by [75,76] are applied on the plane ahead of the crack tip. The relationship between the cohesive traction in the normal direction T and the associated material separation δ is defined as

$$T\left(\delta\right) = \sigma_{max} e \, exp\left(-\frac{\delta}{\delta_0}\right)\left(\frac{\delta}{\delta_0}\right) \qquad T(\delta) = k\delta \quad \delta < 0 \qquad \text{Eq. 48}$$

with the cohesive strength σ_{max}, the cohesive length δ_0, and e=exp(1), Fig. 89. Only the normal traction has to be considered due to symmetric conditions. For crack surfaces in contact the tractions are computed from a linear contact-overclosure relation with a contact stiffness parameter k, Eq. 48. The parameter δ_0 equals the material separation under normal loading necessary to reach cohesive strength. The CZ elements are considered as failed if the critical normal separation $\delta=5\delta_0$ is reached. This defines the location of the crack tip. Crack advance Δa is related to the undeformed mesh.

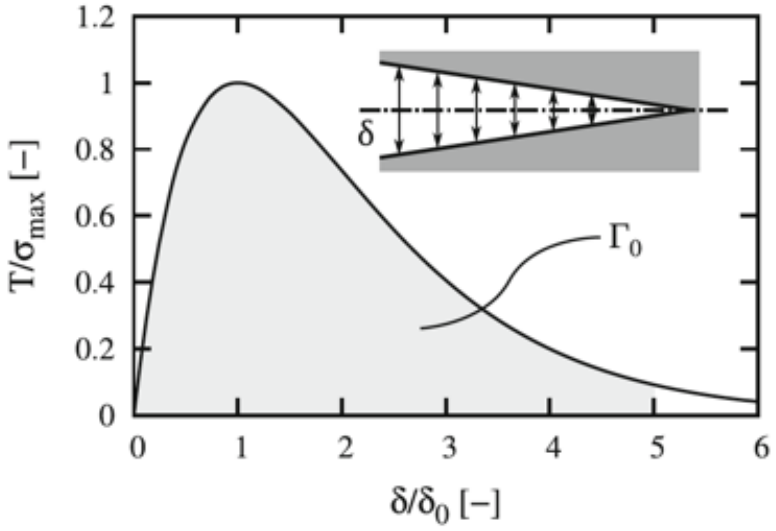

Fig. 89. Traction-separation relationship and definition of the normal crack opening displacement δ .

The cohesive energy Γ_0 is calculated as the integral over the traction–separation response from δ=0 to δ=5δ_0 as Γ_0=ζ e$\sigma_{max}\delta_0$ and ζ=0.98 for the selected crack tip definition δ=5δ_0. Following arguments on the relationship between stress intensity factor and energy release rate under plane strain condition a reference stress intensity factor K_0 is introduced [74]:

$$K_0 = \left(\frac{E\Gamma_0}{1-\nu^2} \right)^{1/2} \qquad \text{Eq. 49}$$

Then, following from the reference stress intensity factor a reference plastic zone size is given:

$$R_{p,0} = \frac{1}{3\pi} \frac{K_0^2}{\sigma_Y^2} \qquad \text{Eq. 50}$$

The constitutive parameters of the visco-plastic strain gradient formulation are μ, σ_Y , ν, N, A, m, and l. The study considers μ/σ_Y=214. Three levels of visco-plastic response are employed m=5.0, 5.6, 6.0, and the strain hardening parameters N is varied from N=0 (Norton model response) to N=0.15. Several levels of strain gradient hardening are considered and compared to results with a conventional visco-plastic constitutive theory (l=0).

For simulations under subcritical cyclic loading the formulation of the cohesive zone model is expanded. The approach followed is that of Roe and Siegmund [77], whereby the cohesive strength of the cohesive interaction is degraded following a damage accumulation law. This approach is rate independent. Damage is computed from the subcritical evolution of damage in cyclic loading through the relationship:

$$\Delta D_f = \frac{[\Delta\delta]}{\delta_\Sigma} \left[\frac{T}{\sigma_{\max}} - C_f \right] \qquad \text{Eq. 51}$$

Thereby, the cohesive zone parameters are δ_Σ which sets the rate of material degradation relative to the material separation δ, but damage then depends on the traction level at which the material separation occurs through the ratio T / σ_{max} and modified by an endurance limit factor C_f. The increment in damage needs to be positive, so that a fatigue threshold would occur at low load levels. Then, the current cohesive strength σ_{max} is related to the initial cohesive strength of the undamaged solid $\sigma_{max,0}$ through Eq. 50 where $D_{fatigue}$ is the accumulated damage:

$$\sigma_{\max} = \sigma_{\max,0}(1 - D_{fatigue}) \qquad \text{Eq. 52}$$

While loading occurs along the traction-separation law equation for material separation, unloading occurs along a path connecting the traction-separation state at the load reversal to the origin of the traction-separation space. In compression, the two opposing cohesive surfaces interact through a contact-overclosure relationship with high contact stiffness. In order to account for the time dependent processes of material separation a second damage process is introduced. This follows the Katchanov-Robotonov damage model for creep and the implementation of Bouvard et al. [84]:

$$\Delta D_c = \left[(1 - D)^{-p} \left(\frac{|T| - T_c}{C_c} \right)^r \right] \Delta t \qquad \text{Eq. 53}$$

Then, the total damage increment is the sum of the damage increments from fatigue and creep. In the creep part of the cohesive damage evolution p and r are model exponents, T_c is a threshold traction and C_c a reference traction.

Parameters for the models for the **stationary crack** and for crack growth under **monotonic loading** were assumed to take the following values. The cohesive strength is set to $\sigma_{\max}=3.5\sigma_Y$. For such a value of $\sigma_{\max}/\sigma_Y$ substantive visco-plastic deformation occurs at the crack tip [78]. The values of the ratio of the intrinsic material length scale to the cohesive length are in the range $l/\delta_0=0$ to 1000. The cohesive length also sets a size of the reference plastic zone, here $R_{p,0}/\delta_0=581$. Consequently, the values of the ratio of intrinsic material length scale to reference plastic zone size ($l/R_{p,0}$) is between 0.0 and 1.7. This order of values for $l/R_{p,0}$ was also considered in [44]. At the maximum value of the applied stress intensity factor, $K_{I,\max=}2.5K_0$ the values of the ratio of intrinsic length scale to the corresponding plastic zone size ($l/R_{P,0}$) are in the range from 0.0 to 0.28, again of the order of values in [44]. The smallest element length near the crack tip is $2.5\delta_0$. The radius of the outer perimeter of the MBL model is $R_{\mathrm{MBL}}/R_{p,0=}42$. The maximum crack advance $\Delta a_{\max}$ is limited to the structures meshed region in the center of the MBL ($\Delta a_{\max}=288\delta_0$). At the maximum applied stress intensity factor $K_{I,\max}=2.5K_0$ the size of the plastic zone remains contained in the MBL model, $R_{\mathrm{MBL}}/R_{p,0}=6$. The load is ramped for 5 s until $K_{I,\max=}2.5K_0$ is reached, followed by a hold step of $t_{\mathrm{hold}}=100$ s. In order to gain insight into the interaction of visco-plastic deformation and plastic strain gradient hardening, identical load and hold times were considered for all computations. The hoop stress values $\sigma_{\theta\theta}$ are evaluated ahead of the crack tip for $\theta=0°$. Two cases are examined: a conventional Norton model ($l=0$, $N=0$) and the strain gradient constitutive model with $l/R_{p,0}$, m, and N varied.

Parameters for the models considering crack growth under cyclic loading were assumed to take the following values. The ratio between yield strength and initial cohesive strength is $\sigma_{max,0}/\sigma_Y$=4, δ_0=7.36 μm, δ_Σ=4 δ_0, C_f=0.25. Compared to monotonic loading cases the cohesive strength to yield strength ratio is higher since for values below $\sigma_{max,0}/\sigma_Y$=4 no significant plastic deformation occurs. No strain hardening is considered and the power in the Norton model is m=5.6. The intrinsic material length is either l=0.0 or l=5.0 μm. Then the characteristic size of elements near the crack tip, and thus the size of the cohesive elements is X_{mesh}=2.5 δ_0. The cohesive contact stiffness is k=10 $\sigma_{max,0}/\delta_0$. The parameter values for the creep damage model are r=5.0, p=6.0, C_C=1000 MPa, T_C=100 MPa, motivated by [85]. Both the rate independent as well as the rate dependent model were executed.

2.4.4.2. Stationary Crack: Results and Discussion

First, results for the **stationary crack and the MBL** are presented. Fig. 90 depicts the hoop-stress values $\sigma_{\theta\theta}$ normalized by σ_Y ahead of the crack tip over the distance r in front of the crack tip for computations considering a range of $l/R_{p,0}$ and m values. Solid lines correspond to the stresses after ramp loading is complete and dashed lines correspond to stresses after the subsequent hold step. Overall, the highest values of $\sigma_{\theta\theta}$ were found for m=5.0 caused by the limited visco-plastic deformation in the case of low visco-plastic powers. For the Norton model (l=0, N=0) the highest $\sigma_{\theta\theta}$ stresses are reached slightly ahead of the crack tip. This breakdown of the singularity type solution of the stress field around the crack tip is due to crack blunting [79-81]. The distance between the location of the maximum stress and the crack tip equals approximately two times the crack tip opening displacement [79].For $l/R_{p,0}$>0, the presence of hardening due to the plastic strain gradients alters the crack tip fields. Now, the location of the maximum stress is shifted towards the crack tip. This change in crack tip fields occurs already for small values of $l/R_{p,0}$. Near the crack tip (e. g. for r/δ_0<10 in Fig. 90(a)) the level of the hoop stresses predicted by use of a strain gradient formulation at the crack tip is 2 – 3.5 times higher compared to the Norton model case (l=0, N=0), and that increase increases with $l/R_{p,0}$. This finding is comparable with data from rate-independent formulation by [49]. The maximum stress level on the order of $10\sigma_Y$, similar to what was found in [44,46]. During the hold time, stresses decrease due to stress relaxation. Stress relaxation is caused by constraining the visco-plastic deformation by the surrounding elastic domain [31,80]. A higher visco-plastic exponent m increases the stress relaxation rate. It is found that the influence zone of the plastic strain gradients grows over time. This change in the stress fields can be explained by higher visco-plastic strain rates caused by the initial higher crack tip stresses in cases with l>0 which then cause more pronounced relaxation processes, similar to what was found even for l=0 in [80]. Further away from the crack tip (e. g. for r/δ_0>10 in Fig. 90(a)) hoop stresses for cases $l/R_{p,0}$>0 are slightly below the hoop stresses of the Norton model case. This is due to the necessary force equilibrium which has to be maintained also in the case of higher hoop stresses at the crack tip for $l/R_{p,0}$ >0. This was also found in rate independent solids by [44]. During hold, stress levels decay as well in this region. As expected, far away from the crack tip for r/δ_0 >> 0 the stresses of the strain gradient model equal the stresses of the Norton model case. In this domain, the influence of the plastic strain gradients is negligible and the response of the strain gradient formulation passes into a conventionally Norton model.

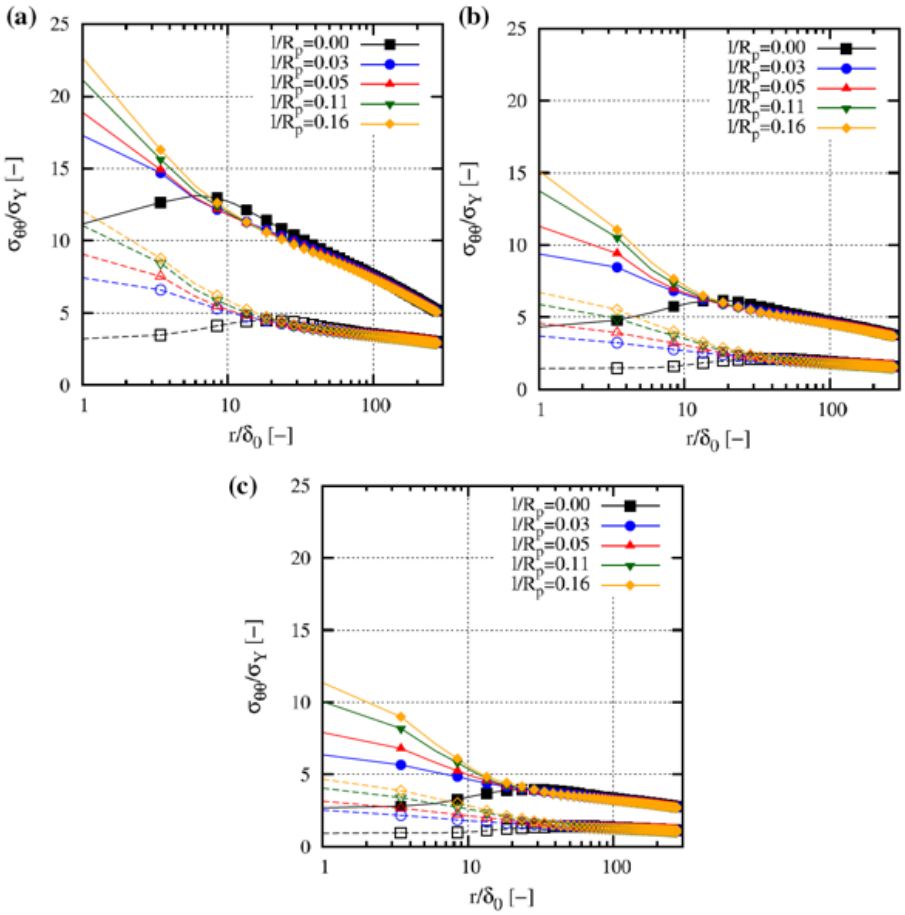

Fig. 90. Normalized hoop-stresses $\sigma_{\theta\theta}/\sigma_Y$ versus the normalized distance r/δ_0 for stationary cracks ahead of the crack tip after loading (t_{hold}=0 s, solid lines) and after (t_{hold}=100 s, dashed lines) for N=0.0, several values of the ratio of intrinsic material length to plastic zone size $l/R_{p,0}$, and visco-plastic exponents: (a) m=5.0, (b) m=5.6, and (c) m=6.0.

To quantify the area influenced by strain gradients, we calculate a distance r_{SGP} from the crack tip where the computed hoop-stresses from plastic strain gradient formulation are significantly higher than the stresses predicted in a strain-only plasticity model. The distance r_{SGVP} (normalized by δ_0) defines the size of the domain in which the hoop-stresses $\sigma_{\theta\theta}$ following for the visco-plastic strain gradient model are significantly higher than the stresses predicted by use of the conventional Norton model, (σ_{SGVP}=1.5σ_{Norton}, Fig. 91).

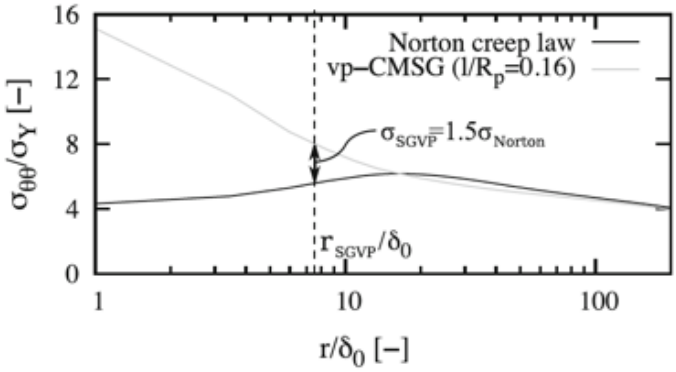

Fig. 91. Definition of r_{SGVP}/δ_0 to quantify the area affected by the visco-plastic strain gradient plasticity in comparison to the Norton visco-plastic model.

Fig. 92 depicts r_{SGVP}/δ_0 over hold time t_{hold} for computations considering three visco-plastic exponents and N=0. A steady-state [80] was not fully reached over the hold time considered here. Still, relevant conclusions can be drawn. As expected, for all cases r_{SGVP}/δ_0 increases with hold time. In [82] the growth of the visco-plastic zone near the crack tip with time was demonstrated. Here, not only does the visco-plastic zone grow during hold, but the domain of influence of the plastic strain gradient expands as well. By comparing parameter sets with different visco-plastic exponents m it can be seen that r_{SGVP}/δ_0 is larger for cases with large visco-plastic power (Fig. 92(c)) and is larger compared to cases with small visco-plastic power (Fig. 92(b)). The plastic strain gradients also affect s $r_{SGVP}/\delta 0$, and it is found to increase for increasing values of the ratio intrinsic material length to plastic zone size. A larger growth of r_{SGVP}/δ_0 with increase in $l/R_{p,0}$ is due to higher stresses near the crack tip causing a more pronounced relaxation. As a result, the effect of the plastic strain gradients is increasing with $l/R_{p,0}$ and plastic strain gradients affect r_{SGVP}/δ_0 more strongly for larger visco-plastic powers. The rate $\dot{r}_{SGVP}/\delta_0$ was found to increase with increasing $l/R_{p,0}$. The relaxation of the crack tip stresses leads to a decreasing $\dot{r}_{SGVP}/\delta_0$ with hold time until a near steady-state stress distribution is reached at long hold times. The rate $\dot{r}_{SGVP}/\delta_0$ also increases with increasing m for large $l/R_{p,0}$ (the increase of r_{SGVP}/δ_0 with hold time at m=6.0 is about twice as large as at m=5.0) but can be considered as constant for $l/R_{p,0}$=0.03. Next, computations with N=0 and N>0 are considered. Fig. 93 shows r_{SGVP} at the end of the hold time in dependence of the hardening exponent N varied in the region $0 \leq N \leq 0.15$ for m=5.0, 5.6, 6.0 and four values of $l/R_{p,0}$. The higher the strain hardening degree the lower the influence of the size effect in a visco-plastic strain gradient formulation for all $l/R_{p,0}$. An increasing N results in an increase of the non-dimensional function $f(\varepsilon vp)$ and therefore in an increase of the flow stress σ_{flow}. A higher flow stress implies smaller values of visco-plastic strains, and thus a smaller influence of plastic strain gradients. This behavior was also found by [49] in a rate-independent strain gradient model. Results on computations employing conventional Norton model agree well with the results obtained using a visco-plastic strain gradient formulation far away from crack tip. In this area, no influence of local hardening effects due to strain gradient plasticity can be found. When approaching the crack tip, significant difference are predicted in the stresses between the computation with the conventional Norton model and the strain-gradient visco-plastic model. The results in the model with the stationary crack show that size of the zone influence by visco-plastic strain gradients, r_{SGVP}, expands with time. This domain was found to be larger for larger values of $l/R_{p,0}$. Furthermore, r_{SGVP}/δ_0 increases with the visco-plastic exponent m, irrespectively of $l/R_{p,0}$.

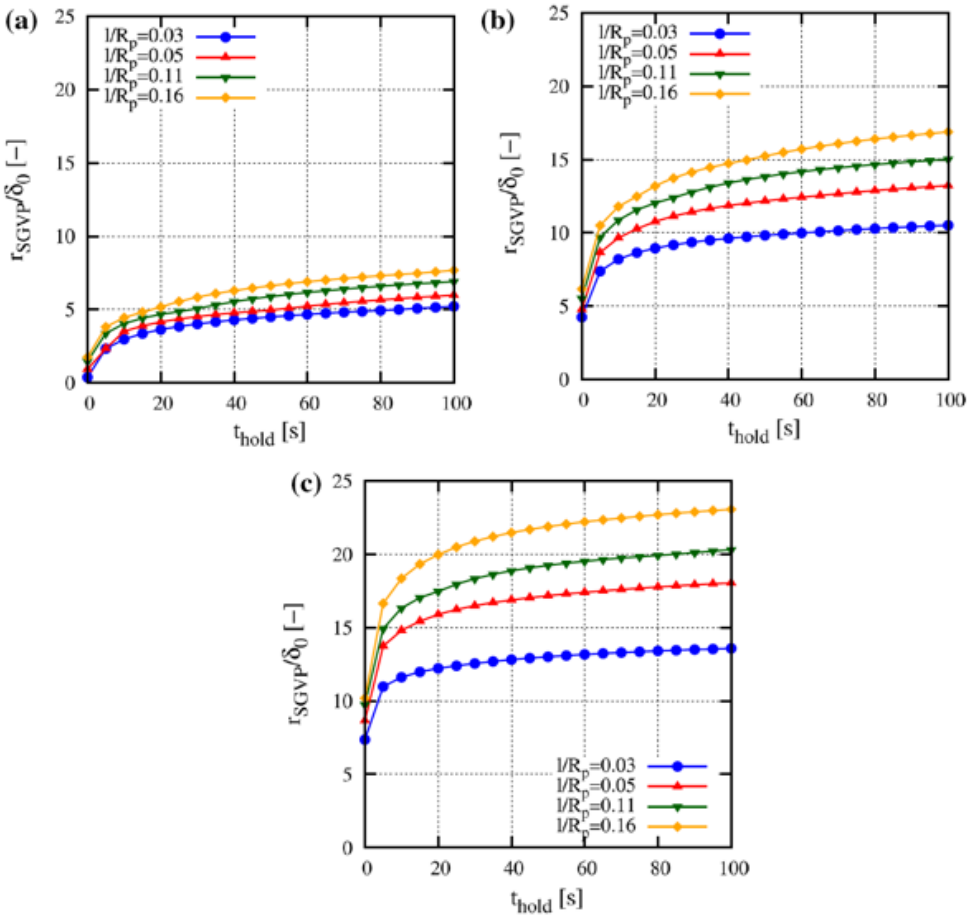

Fig. 92. Distance effected by plastic strain gradients r_{SGVP}/δ_0 for stationary cracks versus hold time t_{hold} for N=0.0, several values of ratio of intrinsic material length to plastic zone size $l/R_{p,0}$, and visco-plastic exponents: (a) m=5.0, (b) m=5.6, (c) m=6.0.

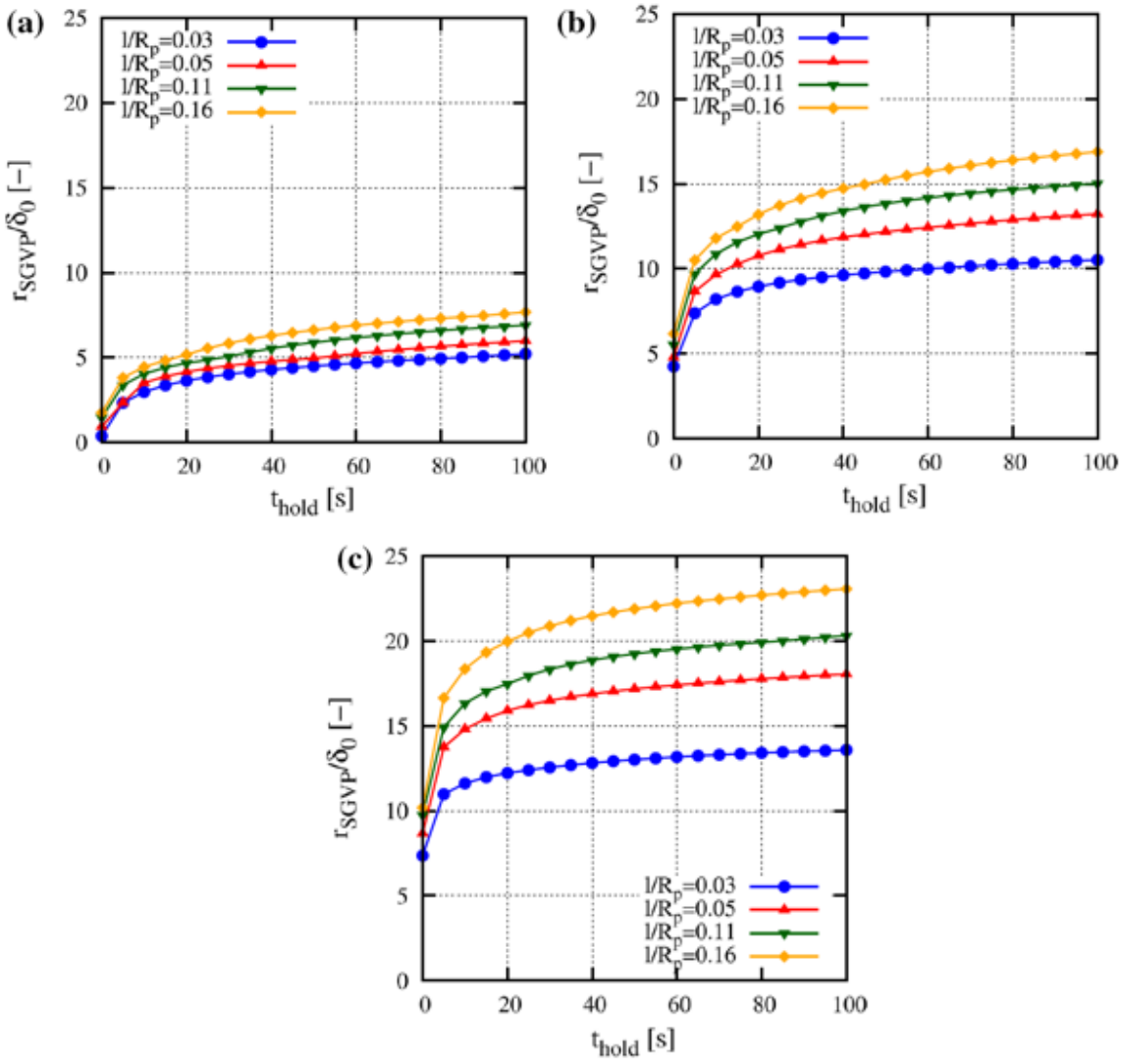

Fig. 93. Distance effected by plastic strain gradients r_{SGVP} for stationary cracks versus hardening exponent N at t_{hold}=100 s for several values of visco-plastic exponents m and ratio of intrinsic material length to plastic zone size: (a) $l/R_{p,0}$= 0.03, (b) $l/R_{p,0}$= 0.06, (c) $l/R_{p,0}$= 0.11, and (d) $l/R_{p,0}$= 0.16.

2.4.4.3. Crack Growth under Monotonic Loading: Results and Discussion

Simulations of crack growth under monotonic loading consider the cohesive zone model to capture crack advance. Two set of computations are conducted: (i) with a fixed $\dot{K}_I=2.5\times10^{-3}K_0/s$ increase load until $K_{I,max}=2.5K_0$, thereby vary the parameter values of $l/R_{p,0}$, m, and N to establish their influence on crack growth, and (ii) for a subset of m and $l/R_{p,0}$ values, all with N=0 consider various load rates $\dot{K}_I$ to establish the rate sensitivity of crack growth. For all cases, the initiation toughness and the tearing modulus are evaluated. Details of the crack tip fields are evaluated. Fig. 94 shows the computed (normalized) crack growth resistance curves, K_I/K_0 vs. $\Delta a/\delta_0$, for various combinations of $l/R_{p,0}$, N, and m, all for $\dot{K}_I=2.5\times10^{-3}K_0/s$. For the limiting elastic case, the crack initiates at K_0 and propagates unstable instantly. If visco-plasticity is considered, crack growth initiation occurs at $K_I/K_0>1$ and that increase over the elastic case increases depends on the magnitude of the parameters m, N, and $l/R_{p,0}$. Similarly, the subsequent crack growth resistance

increases with increasing Δa and that increase over the initiation toughness depends again on the magnitude of m, N, and $l/R_{p,0}$.

The overall resistance to crack growth was found to increase with the magnitude of the visco-plastic power. At low value of m it is found that $l/R_{p,0}$ has little effect on toughness and crack growth resistance and only N influences crack growth. For larger values of m both $l/R_{p,0}$ and N are relevant. Fig. 95 summarizes the predicted initiation toughness values and the normalized tearing moduli as a function of the intrinsic lengthscale ratio $l/R_{p,0}$, for three values of the visco-plastic power m and two values of N. It is found that initiation toughness values $K_{I,\text{init}}/K_0$ predicted by computations accounting for plastic strain gradients and $l>0$ are in all considered cases smaller than those predicted by the corresponding model with $l=0$, Fig. 95(a). A similar influence of the effects of plastic strain gradients on crack growth was described in [64]. For crack initiation, this effect is particularly pronounced for the case with $m=6.0$ where for $l=0$ no crack initiation takes place, but crack growth initiates for $l>0$. The dependence of the initiation toughness on $l/R_{p,0}$ is strongest at small values of $l/R_{p,0}$ and saturates for large $l/R_{p,0}$. The dependence of $K_{I,\text{init}}$ on $l/R_{p,0}$ is more pronounced for cases with large value of m and low N. The decrease of $K_{I,\text{init}}$ with increasing $l/R_{p,0}$ is due to higher stresses near the crack tip as a result of strain gradient hardening, see also Fig. 90. This allows to overcome the cohesive strength of the first CZ element more readily. The highest levels of stress near the crack tip are expected for cases with a small visco-plastic power (here $m=5.0$), and indeed the lowest values of $K_{I,\text{init}}$ can be found there. Since, failure of the cohesive elements is faster than the possible evolution of visco-plastic strain, the magnitude of plastic strain is small only a minor influence of $l/R_{p,0}$ on the initiation toughness can be found. On the other hand, in case of a large visco-plastic powers (here $m=5.6$ and 6.0) a distinct influence of $l/R_{p,0}$ on initiation toughness is present. For small values of $l/R_{p,0}$, additional strain hardening ($N>0$) further reduces the initiation toughness. However, for large $l/R_{p,0}$ the initiation toughness is not effected by N, or even slightly higher for $N>1$ compared to $N=0.0$. Fig. 95(b) shows the computed normalized tearing modulus $(K_I/\Delta a)/(K_0/\delta_0)$. The tearing modulus represents the slope of the curves presented in Fig. 94 at crack initiation. For a small visco-plastic power ($m=5.0$) the tearing modulus is small, independent of all other parameters. For larger visco-plastic powers ($m=5.6$ and 6.0) higher tearing moduli are observed for the dependence of $(K_I/\Delta a)/(K_0/\delta_0)$ on $l/R_{p,0}$ is most pronounced at small values of $l/R_{p,0}$ and saturates as $l/R_{p,0}$ increases.

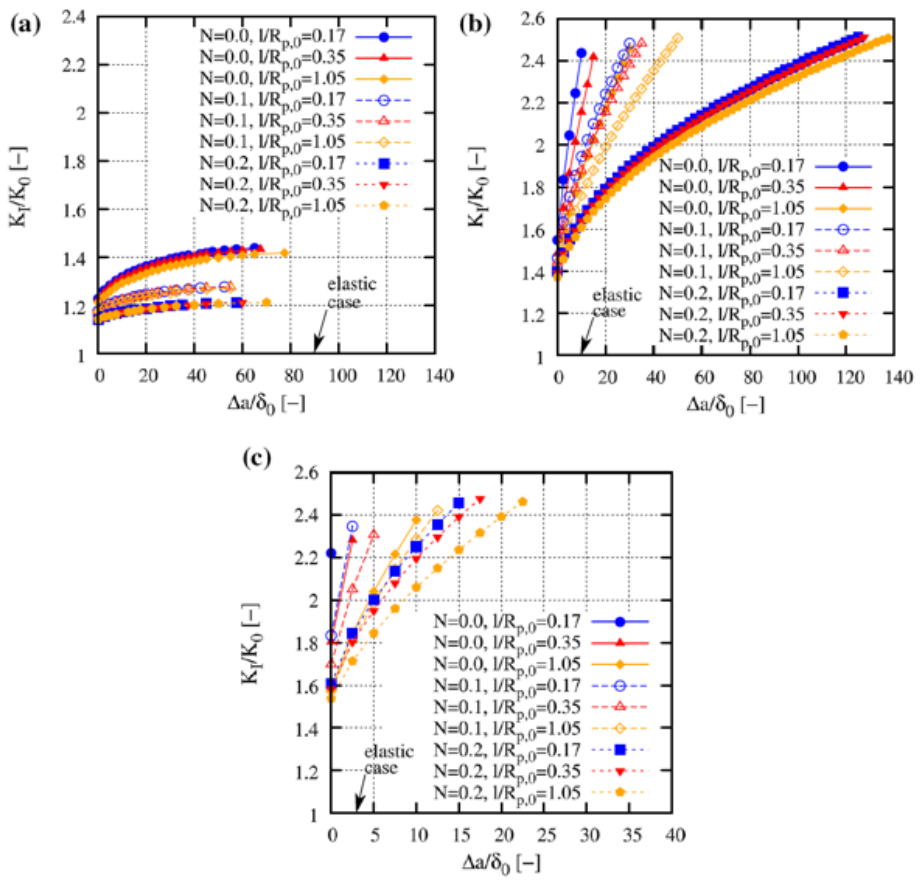

Fig. 94. Normalized crack advance $\Delta a/\delta_0$ versus the loading K_I/K_0 under monotonic loading for several visco-plastic exponents: (a) m=5.0, (b) m=5.6, and (c) m=6.0.

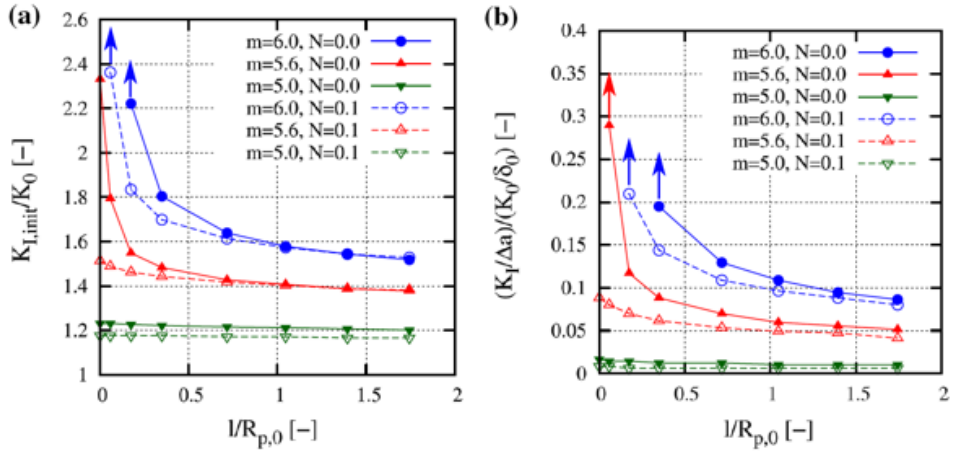

Fig. 95. (a) Normalized initiation toughness $K_{I,\text{init}}/K_0$ (arrows indicating data point representing the smallest $l/R_{p,0}$ value for crack initiation) and (b) normalized tearing modulus $(K_I/\Delta a)/(K_0/\delta_0)$ (arrows indicating data point represents the smallest $l/R_{p,0}$value for crack growth past crack initiation) as a function of the intrinsic material length to reference plastic zone size $l/R_{p,0}$ for constant loading rate.

In particular, for small $l/R_{p,0}$ and high values of m, computations predict crack initiation but no subsequent crack growth. For large values of $l/R_{p,0}$ the dependence of $(K_I/\Delta a)/(K_0/\delta_0)$ on $l/R_{p,0}$

saturates. In all cases, additional strain hardening (N=0.1) further lowers the tearing modulus, similar to results in [51]. This effect is more prominent for low $l/R_{p,0}$. The reduced influence of N with an increase in $l/R_{p,0}$ can be explained by the growing influence of the plastic strain gradients acting in front of the current crack tip: higher stresses in this area make it easier to overcome the traction of the CZ elements.

Fig. 96 shows the predicted initiation toughness and tearing modulus values in dependence of the loading rate $\dot{K}_I/K_0$. The dependence of both initiation toughness and tearing modulus on loading rate is stronger for small values of $l/R_{p,0}$ than for larger values of $l/R_{p,0}$. At low loading rates a distinct influence of $l/R_{p,0}$ on initiation toughness and tearing modulus is present, but as the loading rate is increased the amount of visco-plastic deformation is reduced and the dependence on $l/R_{p,0}$ subsides at high loading rates.

To further understand the influence of intrinsic lengthscales on crack growth, visco-plastic strain ε^{vp} and plastic strain gradients η^{vp} are analyzed. The values of $\dot{\varepsilon}^{vp}$ and $\dot{\eta}^{vp}$ were evaluated along the row of elements right above the crack path. Fig. 97 shows the position of the maximum values of $\dot{\varepsilon}^{vp}$, $\dot{\eta}^{vp}$, respectively, together with the crack tip position in dependence of the applied load for m =5.6 and 6.0, both for N=0 and 0.1. For cases in which there is substantive crack extension, e.g. Fig. 97(b), the position of the maximum in $\dot{\eta}^{vp}$ is in front of the current crack tip, and the position of $\dot{\varepsilon}^{vp}$ is behind the current crack tip. However, if the magnitude of crack extension is small and crack tip blunting is substantial, e.g. Fig. 97(d) then the location of maximum of $\dot{\varepsilon}^{vp}$ and $\dot{\varepsilon}^{vp}$ moves closer together, and both are positioned ahead of the current crack tip. This shift occurs gradually, depending on the relative influence of the material parameters considered, Fig. 97(a).

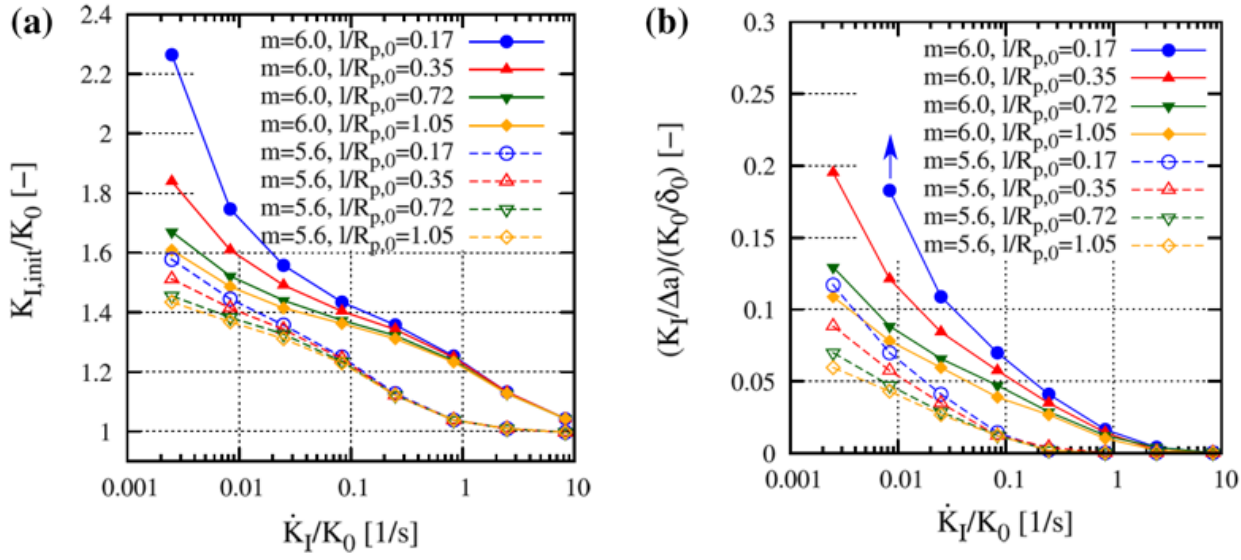

Fig. 96. Normalized initiation toughness $K_{I,\text{init}}/K_0$ (a) and tearing modulus $K_I/\Delta a$ (b) as a function of the loading rate $\dot{K}_I/K_0$ for N=0.0.

In Fig. 96 it was shown that initiation toughness and tearing modulus depend little on N for large values of $l/R_{p,0}$. In such instances the crack growth resistance is overall low and a substantive amount of crack growth occurs. In such cases, the maximum plastic strain rate occurs behind the

current crack tip. Consequently, a change in the crack tip fields due to a change in N has only a minor influence on the deformation processes associated with overcoming the cohesive strength. If, on the other hand $l/R_{p,0}$ is small, and the location of the maximum of the plastic strain rate moves closer to that of the maximum of the plastic strain gradient rate, both the intrinsic lengthscale and strain hardening affect the crack growth resistance. Furthermore, contour plots in Fig. 98 show the crack tip fields ε^{vp} and η^{vp} after failure of the first CZ element for m=6.0. For high l, $\dot{\eta}^{vp}$ is always ahead the crack tip. Also, $\dot{\varepsilon}^{vp}$ is ahead or at the crack tip following $\dot{\eta}^{vp}$. The contour plots show the distinct influence of l on the shape of the ε^{vp} field: For high values of l, Fig. 98(c), less blunting of the crack is observed because strain gradients increase the resistance to plastic deformation due to larger stresses. The field of strain gradients are now slightly shifted ahead of the maximum ε^{vp} towards the crack tip. The hardening mechanics of the strain gradients are acting at the crack tip which leads to earlier failure of the CZ elements in this region. The crack growth rate is therefore increasing with l. Additionally, strain gradients suppress the amount of plastic strain. A low l leads to large blunting of the crack tip, Fig. 98(a) and high amount of ε^{vp}. The maximum strain gradients are behind the crack tip. The hardening mechanics of strain gradients are now acting behind the crack tip and the next CZ elements in this region are not affected leading to a higher tearing modulus. This behavior is more severe for larger m, Fig. 98(c). Therefore, in soft materials with a large visco-plastic power m crack tip blunting prevents decohesion of the material.

From the results presented in the previous section it was found that in most cases additional strain hardening of N=0.1 reduces $K_{I,init}$. The contour plots in Fig. 98 show the influence of strain hardening for N=0.1: for low values of l, (b), strain hardening acts in the area of high strain and therefore it has a distinct influence by lowering the visco-plastic strain level. For large values of l, Fig. 98 (d), hardening due to the strain gradients is dominating because of the already discussed shift of $\dot{\eta}^{vp}$ ahead of the crack tip. Therefore, N has only a minor influence on the strain field.

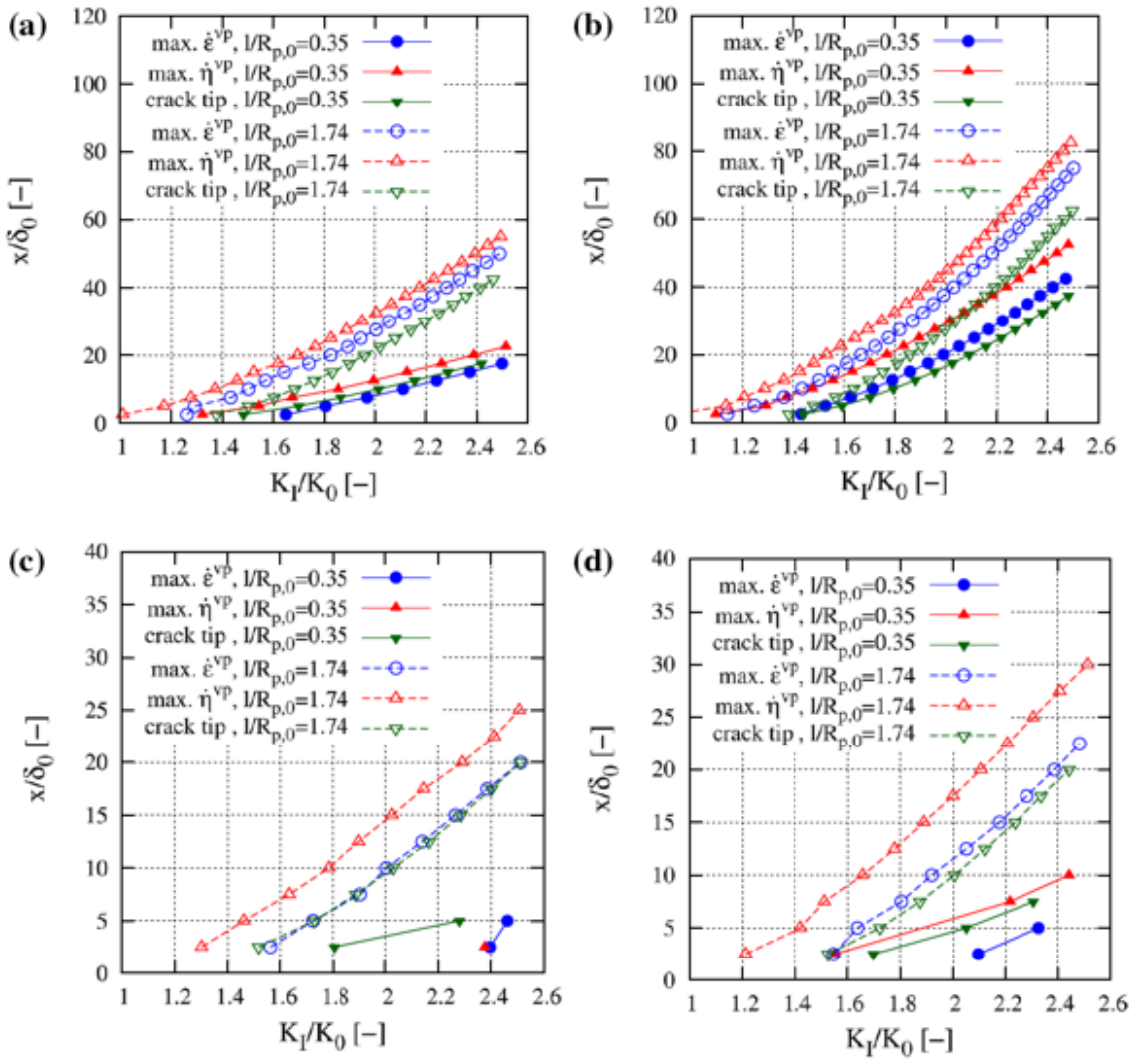

Fig. 97. Position of the maxima of $\dot{\varepsilon}^{vp}$ and $\dot{\eta}^{vp}$ together with the position of the crack tip versus K_I/K_0 for several visco-plastic exponents m and strain hardening exponents N: (a) m=5.6, N=0.0; (b) m=5.6, N=0.1; (c) m=6.0, N=0.0; (d) m=6.0, N=0.1.

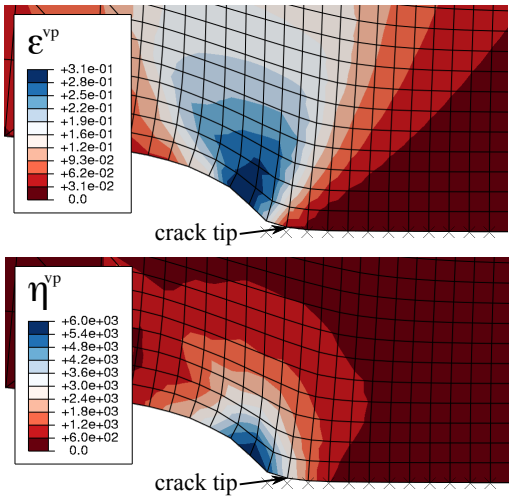

(a) l=1.50μm, N=0.0, K_I/K_0=1.8.

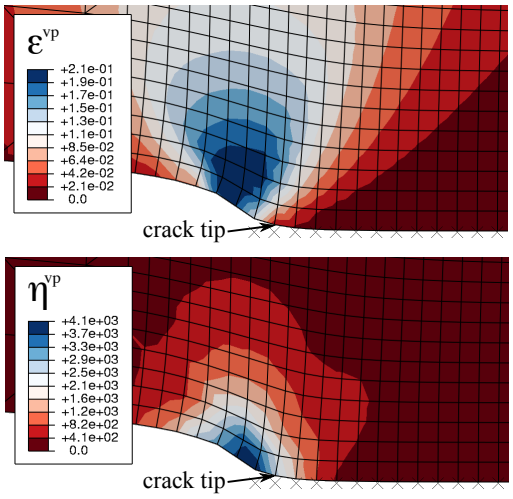

(b) l=1.50μm, N=0.1, K_I/K_0=1.7.

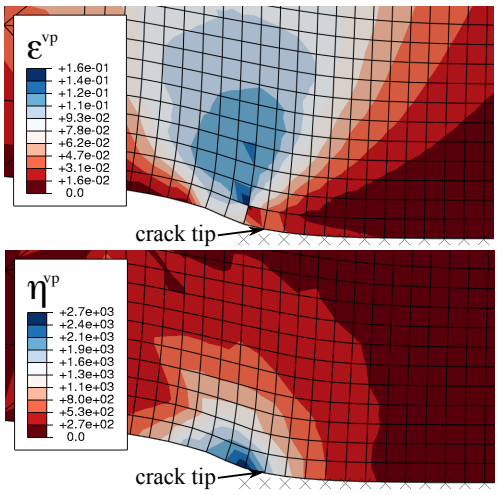

(c) l=7.50μm, N=0.0, K_I/K_0=1.5.

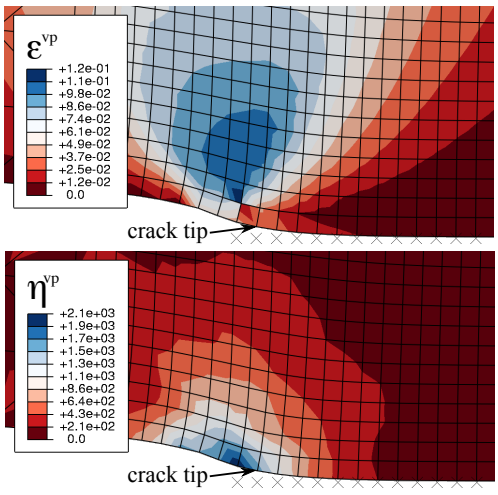

(d) l=7.50μm, N=0.1, K_I/K_0=1.5.

Fig. 98. Contour plots of the visco-plastic strain ε^{vp} and the strain gradients $\dot{\eta}^{vp}$ at the crack tip for m=6.0 after failure of the first CZ element for different intrinsic material lengths l and strain hardening exponents N: (a) l=1.50μm, N=0.0; (b) l=1.5μm, N=0.1; (c) l=7.50μm, N=0.0; (d) l=7.50μm, N=0.1. The nodes of CZ elements are marked as black crosses.

2.4.4.4. Simulations of Crack Growth under Cyclic Loading: Results and Discussion

The MBL model was use for **fatigue crack growth computations**. Fig. 99 depicts predicted crack extension data for computations with the MBL where loading is subcritical $K_{\max} < K_0$ and cyclic with $K = K(t)$. Three different frequencies are considered, Fig. 99(a), and two length scale values are compared, Fig. 99(b). In all simulations, there is an incubation time for crack growth to start, then a steady growth stage is reached. The focus is on the crack growth rates in the steady state regime. The results predict that the fatigue crack growth rate increases with an increase in loading

frequency. Lower frequencies allow for stronger effects of stress relaxation and higher frequencies, therefor leading to a reduction in the stresses at the crack tip, and thus reducing the subcritical damage evolution. The effect of the strain gradient is most pronounced at the lowest loading frequency where also the largest amount of visco-plastic deformation takes place. If the strain gradient effect is considered, the crack growth rates are larger than for the cases where the strain gradient effect is not accounted for. The finding that the loading frequency increases the crack growth rate is in contradiction with the findings from experiments on Alloy 617.

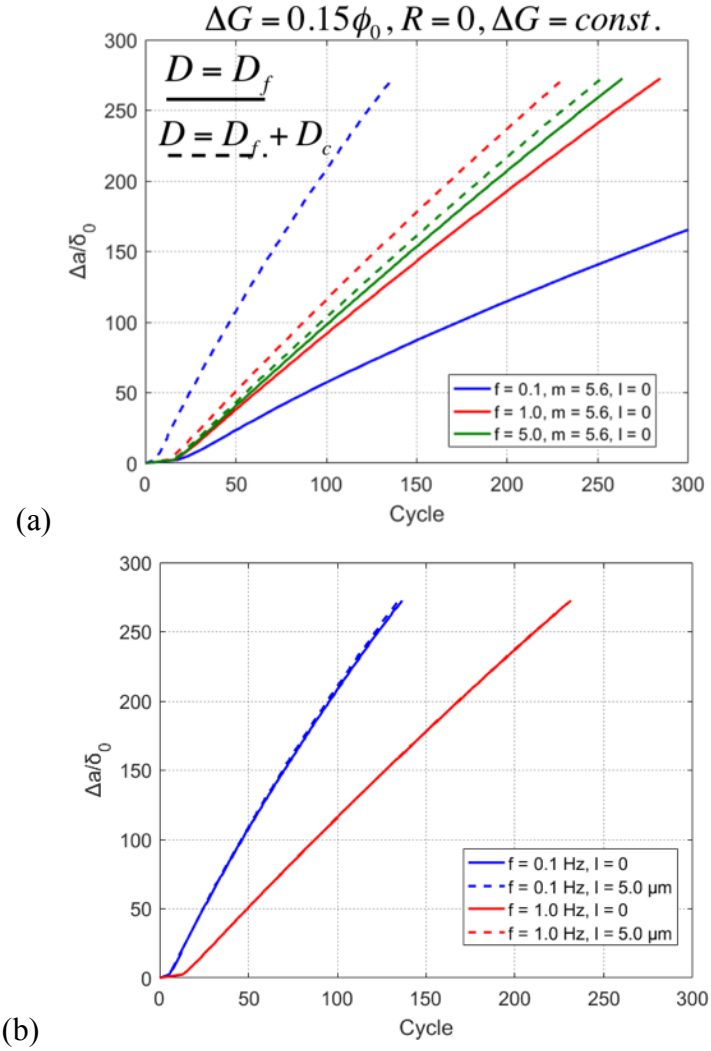

Fig. 99. Predicted fatigue crack growth rate for a MBL model with visco-plastic deformation (length independent (a) and length scale dependent (b)), and considering rate independent and rate dependent material separation processes, respectively.

The addition of the time dependent damage mechanisms into the crack growth model reverses the frequency dependence of crack growth rate. Now, the case of f=0.1 Hz leads to the highest crack growth rate with the crack growth rate declining with increasing frequency (f=1 Hz and and f=5 Hz, respectively). This outcome is in agreement with the frequency dependence of the crack growth rate found in experiments on Alloy 617. We find that the inclusion of strain gradients into the visco-plastic deformation had little effect on the predicted crack growth rates, Fig. 99(b). This

is especially true at high frequencies (here 1 Hz) since such a case the amount of plastic deformation is low and thus plastic strain gradients are small. For the frequency of 0.1 Hz the computation accounting for the plastic strain gradients lead to a crack growth rate only slightly higher than the one observed for l=0. At low frequencies the amount of visco-plastic strain increases but at the same time the domain over which plastic deformation occurs also increases and as such the gradient only increases marginally, thus again affecting the predicted crack growth only marginally. Fig. 100 depicts the active visco-plastic zones for l=0 (a) and l=5.0 μm (b), as well as the corresponding strain gradient rate domain (c). The active plastic zone is well confined and is located between the position of damage D=1.0 and maximum traction. The active plastic gradient zone is shifted towards D=1.0 and is of size similar to that of the active plastic zone.

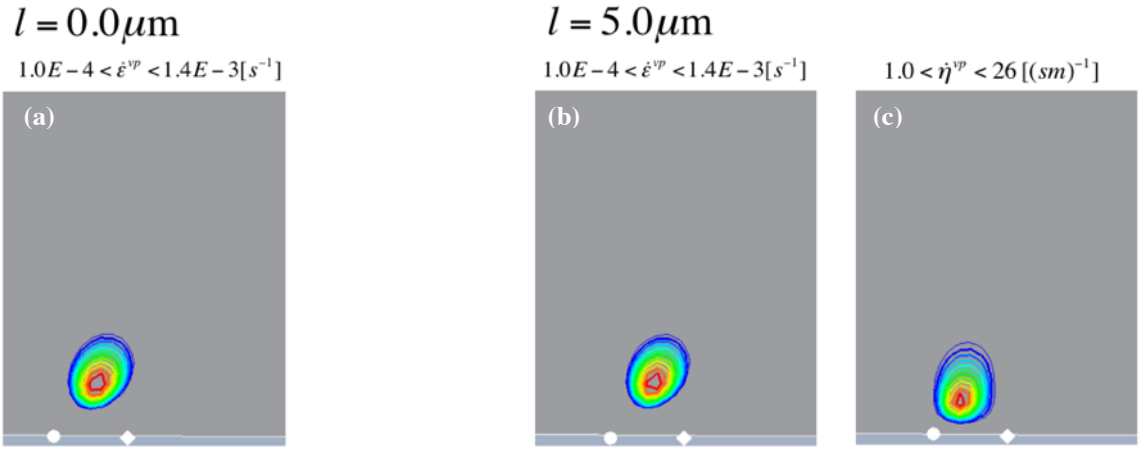

Fig. 100. Comparison of active plastic zones (a) and (b) for fatigue crack growth with length scale independent and length scale dependent visco-plasticity, respectively, and (c) the active strain gradient zone. Instances for which contour plots are shown correspond to the steady state growth condition in Fig. 76. Markers denote positions of D=1.0 (*circles*) and maximum normal traction (*diamonds*).

The next set of results obtained with the MBL model under cyclic loading refer to **overload conditions.** Experiments of this study have demonstrated that single fatigue crack growth overloads do not lead to the commonly observed crack growth retardation effect. In addition to the constant amplitude, a single overload (R=0, and the overload amplitude is taken as three times the steady state amplitude in the applied energy release rate range) is added to the load history. The results presented are examples of the computation and focus on simulations with f=1 Hz, both l=0.0 and 5.0 μm are considered, and crack growth occurs due to cyclic and time dependent damage. The computational results are shown in Fig. 101(a-c). In agreement with experimental data, it is found that single overloads do not lead to crack retardation at the overload. Instead the crack advance is accelerated during the overload cycle and returns to the initial steady state crack growth rate over subsequent load cycles, Fig. 101(a). While such a finding was not observed for a single overload, this is likely due to the resolution of the crack length monitoring system and the experiments with multiple overloads show such behavior. Fig. 101(b) depicts the active plastic zone at the overload maximum. While the amount of plastic strain rate and that of the plastic strain gradient rate is increased compared to the steady state, the increase is not substantial enough to cause crack closure in the subsequent cycle, Fig. 101(c). In all cases the cohesive tractions at the minimum load are barely compressive. This finding indicates that crack closure does not contribute substantially to the crack retardation at the OL, and this the damage processes dominate at the overload. Fig. 101(d) provides two diagrams that aid in the interpretation of this finding. Overload

experiments were conducted under a constant frequency. Thus, during the overload cycle the strain rate is actually increased, and this then leads to an increase in the effective yield strength. On the other hand, the magnitude of plastic deformation depends on the ratio between cohesive strength and yield strength. Now since the effective yield strength is increased during this cycle, the ratio of cohesive strength to effective yield strength drops. This causes the influence of plasticity on fatigue crack growth to reduce. Then the damage processes dominate the crack advance, leading to the acceleration of crack growth at the overload.

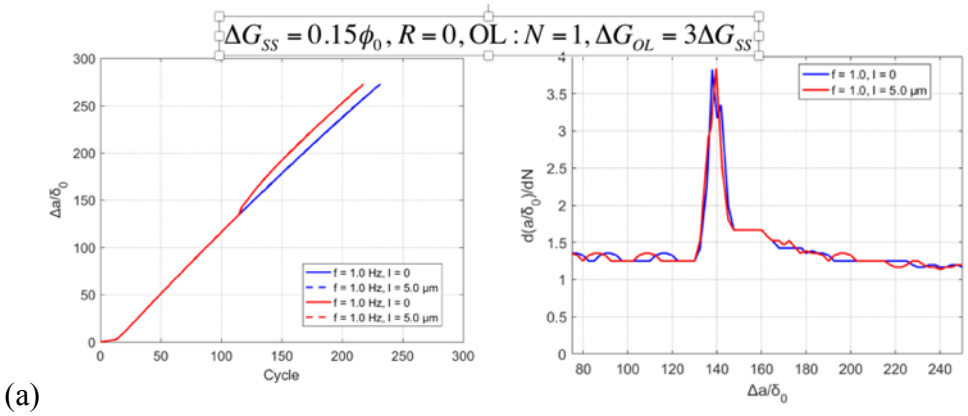

(a)

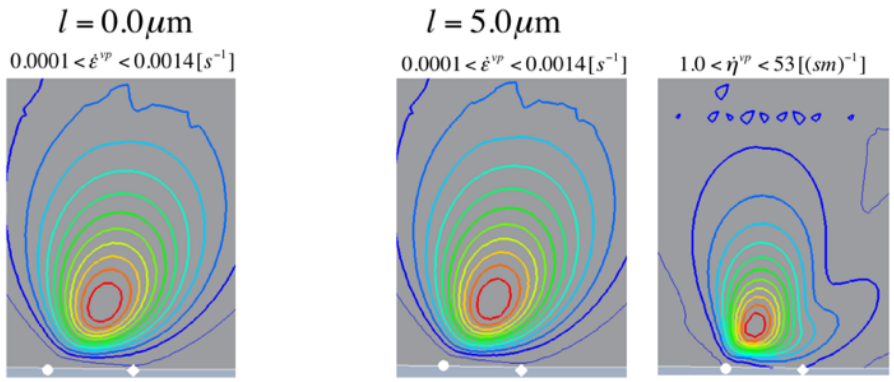

(b)

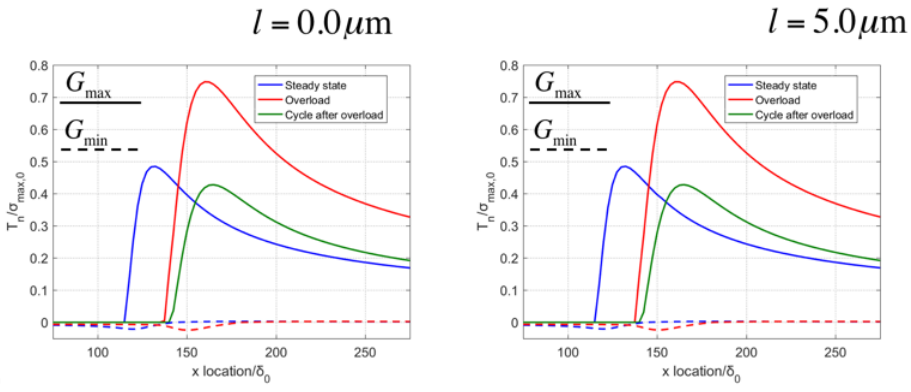

(c)

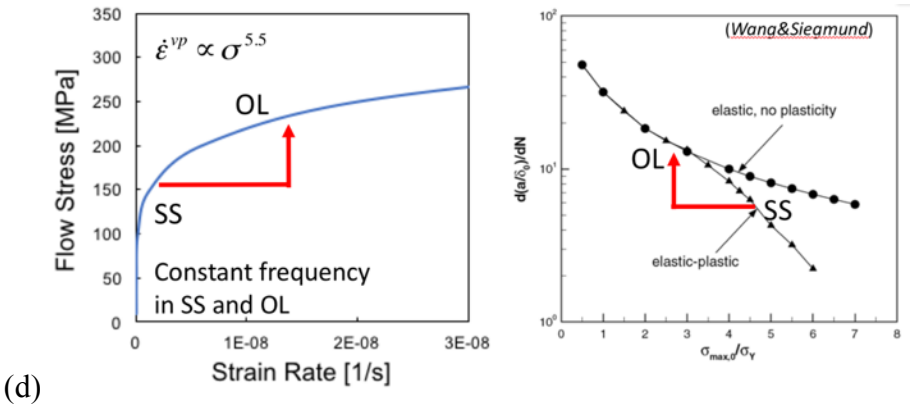

(d)

Fig. 101. Predicted crack extension for a single overload in a visco-plastic solid. (a) Crack extension and crack growth rate in dependence of applied cycle number and crack position, respectively. (b) Active plastic zones and gradient zone. (c) Cohesive tractions during steady state, at the overload and the cycle following the overload. (d) Explaining the overload effect in visco-plastic materials.

The prediction of the rate dependent model can be compared to those from a rate-independent version (both in the solid and in the cohesive zone) and results are displayed in Fig. 102. Now the computations predict a distinct crack retardation at the overload, Fig. 102(a). The magnitude of the crack retardation at the overload depends on the applied load magnitude (higher loads and higher respective overloads lead to more retardation) and also on the strain gradient magnitude (once strain gradients are accounted for the retardation is less pronounced). Fig. 102(b) depicts the active plastic zone sizes, and the magnitudes of plastic strain rates and gradient rates are substantially larger than those for the rate dependent case shown in Fig. 101(b). This leads to quite different traction profiles. During steady state crack growth crack closure is absent, but during the overload a substantial amount of crack closure develops, Fig. 102(c). Only once the crack tip leaves the zone influenced by crack closure is the steady state crack growth rate recovered. Such findings are in general agreement with observation in fatigue crack growth in rate independent plasticity, yet Alloy 617 at 800^{o}C did exhibit a very different response.

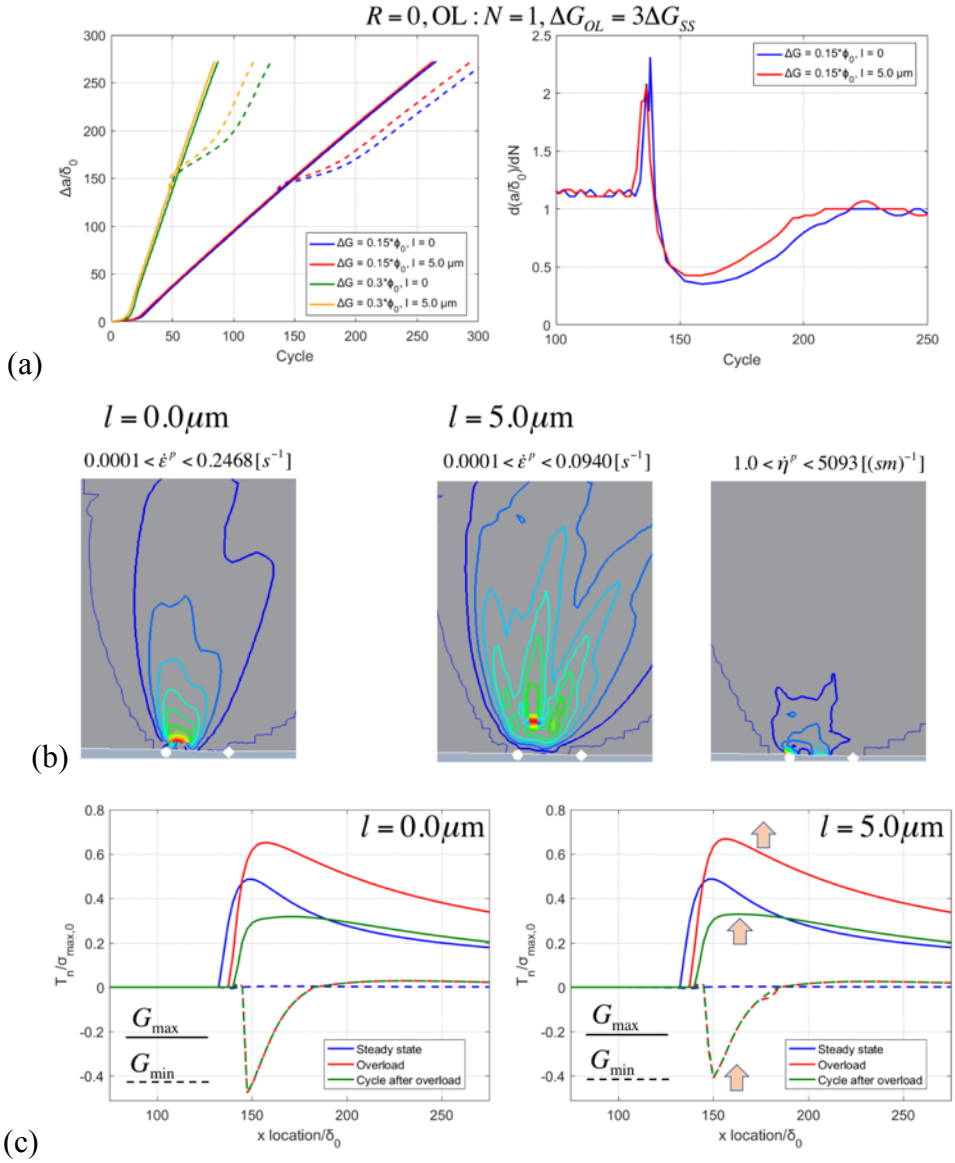

Fig. 102. Predicted crack extension for a single overload in an elastic-plastic solid (a) Crack extension and crack growth rate in dependence of applied cycle number and crack position, respectively. (b) Active plastic zones and gradient zone. (c) Cohesive tractions during steady state, at the overload and the cycle following the overload.

2.4.4.5. *Modified Boundary Layer Limitations*

There are potential limitations of the use of the modified boundary layer model. The displacement boundary conditions applied at the outer nodes of the modified boundary layer (MBL) model do not necessarily account for the visco-plastic behavior in a full compact tension specimen at elevated temperature. In the MBL, a constant K_I leads to a constant displacement of the outer boundary in the MBL model. This is a condition not necessarily met in a C(T) specimen. For this reason, a compact tension specimen was studied considering the visco-plastic behavior

during holding of the maximum load P_{max}. The geometry of the C(T)-specimen is according to ASTM standard E647 [28]. The geometry and details of the mesh of the CT-specimen including the mesh specific to the crack tip domain is shown in Fig. 103. The mesh for the crack tip domain is identical to that of a modified boundary layer model. Along the outer boundary of the crack tip mesh domain, displacement values are extracted from the FE computation and compared to those from the *K*-solutions. A contact interaction is defined between the pin and the hole of the C(T) specimen. Friction can be neglected because the pin is mounted inside a roller bearing during the test and therefore is rotating freely. Simulations with different values of the coefficient of friction further confirm that friction is not an influencing factor. To define the contact area, the pin was assumed to possess a diameter less than the hole, r_{pin}=3 mm vs. r_{hole}=3.125 mm. The pin is approximated as a rigid body. Contact is defined as frictionless surface-to-surface contact between the pin and the hole. The contact pressure-overclosure relationship is set to hard. The reference point A (characterizing the point of load) is restricted to move in the Y-axis only and all nodes along the crack face are restricted to move parallel to the *x*-axis. Imposing such symmetry conditions allows for computations with a half-model of the C(T) specimen. First, in a displacement controlled load step, the pin is brought into contact with the inner surface of the hole of the C(T) specimen. In order to minimize the influence of this initial load step, the pin is only moved 60µm over a time for 1s. This ensures that the subsequent visoplastic analysis in not influenced by the initial load step. A MATLAB script was developed to automate the mesh generation.

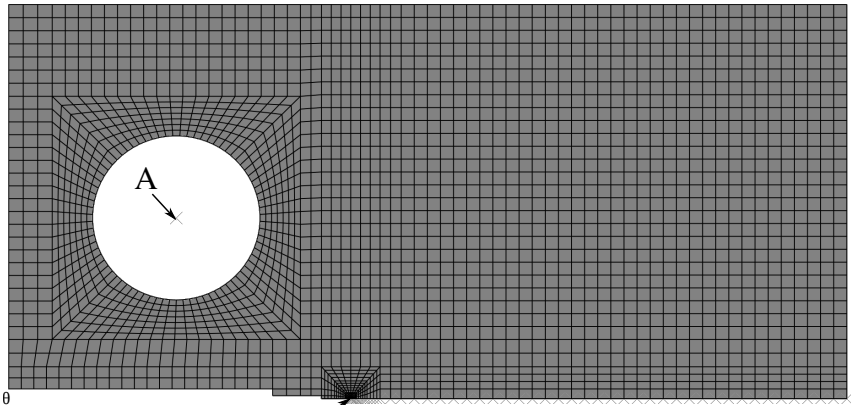

Fig. 103. Geometry and mesh of the CT specimen, including the embedded circular near tip mesh domain.

To validate the results of the simulation of the C(T)-specimen with the displacement equations for the MBL model, elastic material behavior is considered first (E=157 GPa, ν=0.3). The crack-length a was varied (6.6 mm, to 9.1 mm, 11.6 mm, 19.1 mm) by moving the embedded circular near-tip mesh domain. In ASTM standard E647 [28], the relationship between P and the stress intensity factor K_I is:

$$K_I = \frac{2P\left(2+\alpha\right)}{B\sqrt{b}\left(1-\alpha\right)^{3/2}}\left(0.433+2.23\alpha-6.66\alpha^2+7.36\alpha^3-2.8\alpha^4\right) \qquad \text{Eq. 54}$$

where b is the depth of the C(T)-specimen (length from point A to the right edge of the specimen in Fig. 103), B is the thickness of the C(T)-specimen (B=6.35 mm), and α is the crack length to depth ratio $\alpha=a/b$. For every crack-length the corresponding load P is calculated as shown in Table

7. Fig. 104 shows the computed displacement of the outer boundary of the circular boundary on the circular near-tip mesh domain over the angle θ ($0° \leq \theta \leq 180°$). The displacement in U_2 can be considered constant for every θ over a. However, the displacement in U_1-direction shows a small variance if a is increased as higher-order effects become relevant. The magnitude of higher-order terms (e.g. T-stresses) increases with the crack length. In addition to the displacement values, the J-integral was evaluated. J under plane strain can be calculated by the standard expression

$$J = \frac{K_I^2\left(1-\nu^2\right)}{E} \qquad \text{Eq. 55}$$

The calculated values of J of FE simulation deviates by 2 – 5% of the theoretical value.

Table 7. Calculated load and J for constant K_I=146.2 MPa$\sqrt{}$mm. The J-integral equals 0.124 kJ/m^2.

a [mm]	P [N]	J-integral [kJ/m^2]	Error between analytical and measured J [%]
6.6	924.0	0.126	1.6
9.1	715.7	0.118	4.8
11.6	549.8	0.118	4.8
19.1	159.7	0.122	1.6

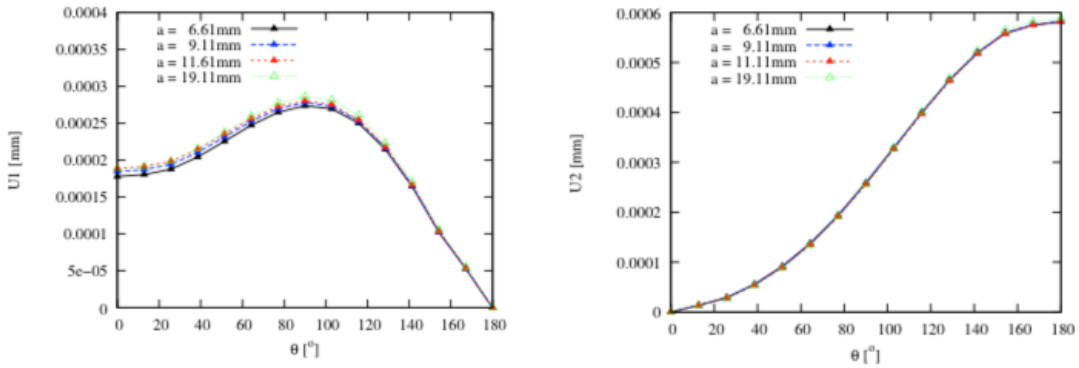

Fig. 104. Displacement values computed at the outer boundary of the embedded circular near-tip mesh domain. Constant stress intensity factor.

Fig. 105 and Fig. 106 show the displacement in comparison to the analytical solution. An analytical solution for the C(T)-specimen can be obtained by evaluating the so-called Williams-expansion for the displacement U_1 and U_2

$$u_x = \sum_{n=1}^{\infty} \frac{r^{n/2}}{2\mu} a_n \left[\left(\kappa + \frac{n}{2} + (-1)^n \right) cos\left(\frac{n}{2}\theta \right) - \frac{n}{2} cos\left(\left(\frac{n}{2} - 2 \right)\theta \right) \right]$$
$$u_x = \sum_{n=1}^{\infty} \frac{r^{n/2}}{2\mu} a_n \left[\left(\kappa - \frac{n}{2} - (-1)^n \right) sin\left(\frac{n}{2}\theta \right) + \frac{n}{2} sin\left(\left(\frac{n}{2} - 2 \right)\theta \right) \right] \qquad \text{Eq. 56}$$

The crack opening is considered under mode I. The general case of the Williams-expansion includes additional terms for shear and torsion, but these loading conditions do not appear in the C(T) specimen. The standard approach is to evaluate the first two terms in the Williams expansion with $a_1 = K_I / \sqrt{2\pi}$ and $\sigma_x = T = 4a_2$. The *T*-stress for the C(T) specimen is obtained as e.g. $T/\sigma = -2.616 + 8.019\alpha + 16.421\alpha^2$ where $\sigma = P/b$. Xiao and Karihaloo [73] evaluated the Williams-expansion by introducing unit-less coefficients. By using hybrid crack elements, they fitted coefficients up to the fifth order. Here we focus on the results up to the third order:

$$k(\alpha) = \frac{K_I Bb}{P\sqrt{2\pi b}} = \frac{a_1 B\sqrt{b}}{P} = 373.08\alpha^5 - 567.33\alpha^4 + 321.47\alpha^3 - 73.124\alpha^2 + 9.8345\alpha + 0.8436$$
$$t(\alpha) = \frac{TBb}{4P} = \frac{a_2 Bb}{P} = 294.23\alpha^5 - 520.3\alpha^4 + 320.88\alpha^3 - 71.418\alpha^2 + 2.3668\alpha + 0.9443$$
$$g_3(\alpha) = \frac{a_3 Bb}{P/\sqrt{b}} = -4774.1\alpha^6 + 9231.3\alpha^5 - 7083\alpha^4 + 2799.1\alpha^3 - 664.26\alpha^2 + 94.256\alpha - 7.6254 \qquad \text{Eq. 57}$$

such that $k(\alpha) = a_1/(\sigma\sqrt{b}), t(\alpha) = a_2/\sigma, g_3 = a_3/(\sigma\sqrt{b})$. These equations are used to calculate the displacement of the first up to the third order. The results and the comparison with the results of the elastic calculation can be found in Fig. 105 and Fig. 106. The present computational simulations are in overall good agreement with the results by Xiao and Karihaloo [73]. For the displacement component normal to the crack face, 1st, 2nd and 3rd order expression lead to virtually the same outcome. For the displacement parallel to the crack face, the error between the displacement calculated using the first order expression, $k(\alpha)$, and the FE simulation of the full C(T)-specimen is about 6 – 7%. If the *T*-stresses (second order) and third order effects are taken into account this error is reduced. The second order effect is strongest at $\theta \approx 0°$ while the 3rd order component, $g_3(\alpha)$, exhibits the strongest influence for $\theta \approx 90°$. We find that second and third order effects are in the same order of magnitude and should both be taken into account. Higher order terms (not shown in the figures) were evaluated but are two orders of magnitudes smaller than the *T*-stresses and therefore can be ignored for the given problem.

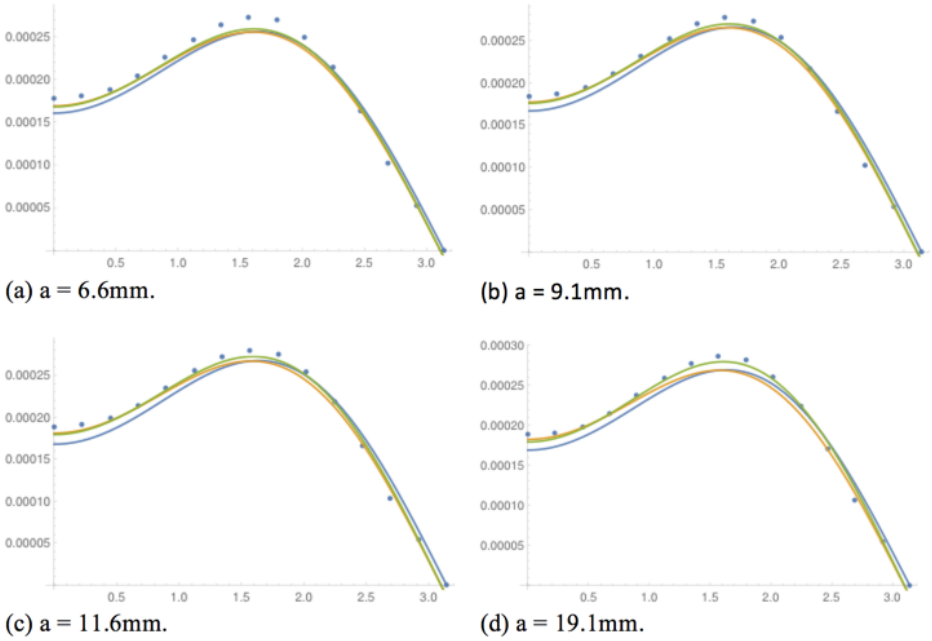

Fig. 105. Displacement u_x at the outer boundary of the embedded MBL-mesh domain in comparison to the analytical solution. Blue line: 1st order solution, green line: 2nd order solution, red line: 3rd order solution.

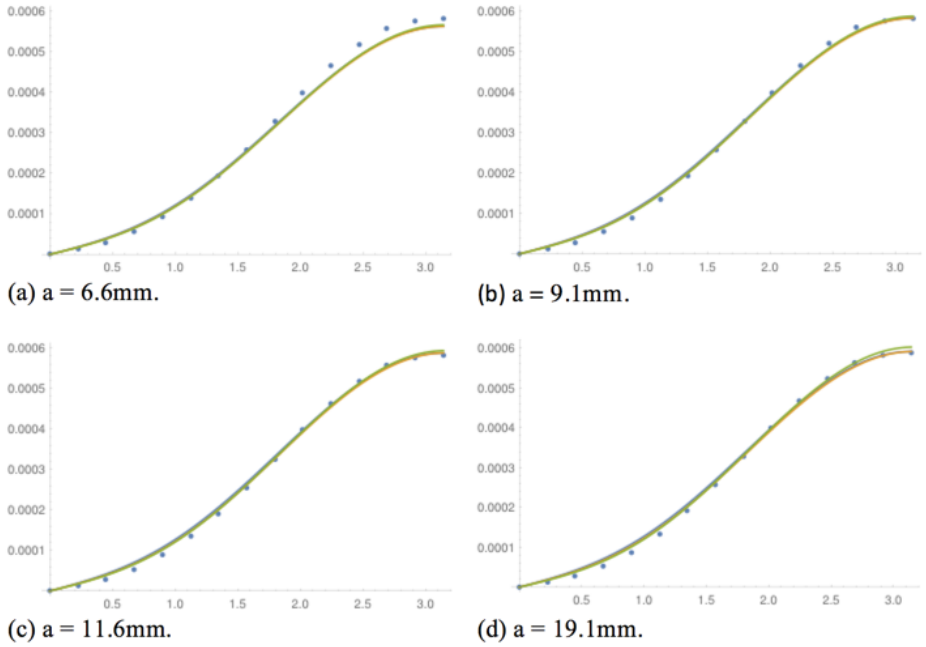

Fig. 106. Displacement u_y at the outer boundary of the embedded MBL-mesh domain in comparison to the analytical solution. Blue line: 1st order solution, green line: 2nd order solution, red line: 3rd order solution.

Visco-plastic behavior of the material was considered in the C(T)-specimen. In the MBL model, it

was assumed that a constant K_I value would be well represented by keeping the displacement on the MBL boundary constant. The accuracy of this assumption is investigated under the condition of visco-plastic deformation. The C(T) specimen was loaded as described in the previous section but holding step of 100 s was added, and a power-law creep law is used [2].

Fig. 107 and Fig. 108 show the time-dependent displacements at the boundary of the embedded circular near-tip mesh domain during the holding step. It was found that the displacements at the circular boundary of the embedded over circular near tip mesh domain do change with time. At the beginning of the holding step (t_{hold}=0 s) only small amounts of creep-strain are found and therefore the calculated displacement matches the analytical formulations for the displacements used for the boundary conditions with the MBL model. However, already for t_{hold}=50s and t_{hold}=100s time dependent deformation plays a role. For such instances, the additional creep-related displacement contributions at the outer boundary of the embedded circular near tip mesh domain are about 10% of the total displacement. It is shown that the displacement is decreasing in X-direction and increasing in Y-direction. This distortion leads to a superposition of an additional load state imposed on the embedded circular near tip mesh domain and consists of compression parallel to the crack and extension normal to the crack. This behavior cannot be modeled by adapting K_I over the holding time.

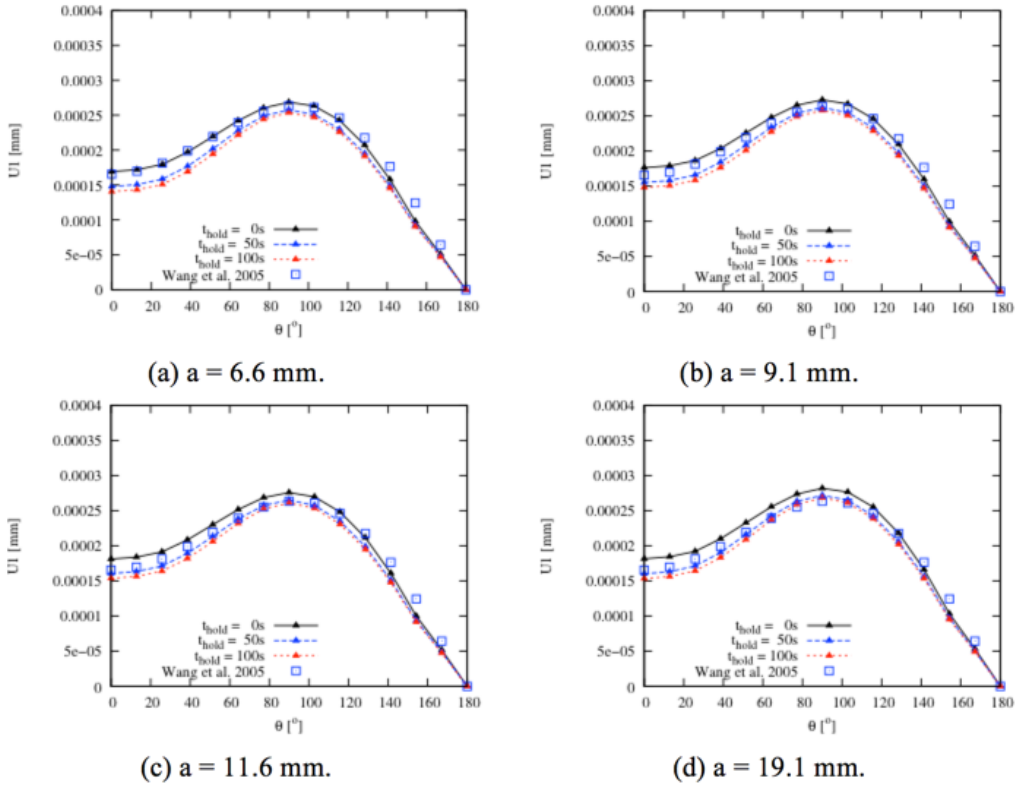

(a) a = 6.6 mm. (b) a = 9.1 mm.

(c) a = 11.6 mm. (d) a = 19.1 mm.

Fig. 107. Displacement u_x at the outer boundary of the embedded circular near tip mesh domain during holding, visco-plastic deformation.

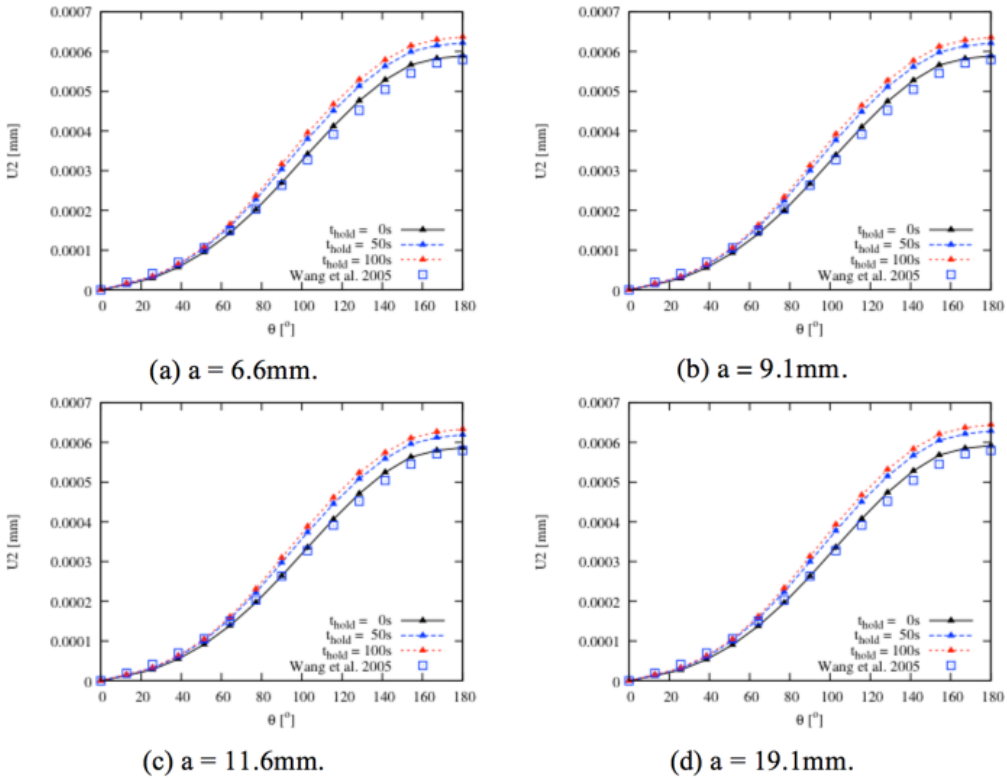

Fig. 108. Displacement u_y at the outer boundary of the embedded circular near tip mesh domain during mesh domain during holding, visco-plastic deformation.

Summary on Computational Modeling: Analysis with a Modified Boundary Layer Model

(a) Model description: A finite element model is considered which represents the near-crack tip conditions. Both stationary and growing cracks are considered. The visco-plastic strain gradient model is combined with cohesive zone models for material separation.

(b) Performance criteria: Implementation needs to be successful to key observations of crack growth rates observed in experiments.

(c) Test results demonstrating meeting model performance criteria: It has been demonstrated that the model predicts fundamental trends of crack growth in IN 617.

(d) Theory behind the model: The model is a novel combination of the theory of the rate dependent conventional mechanism strain gradient plasticity with irreversible cohesive zone models for damage accumulation in cyclic loading and creep. Specific load cases are executed with a standard nonlinear finite element model.

(e) Mathematics to be used, formulas and calculation methods: See Eq. 33-38 for the constitutive model of the visco-plastic strain gradient model. See Eq. 46-51 for the constitutive equations for the cohesive zone models. The implementation uses a nonlinear finite element formulation.

(f) Peer review of theory and algorithm, strength and weaknesses: The model on stationary crack and monotonic loading has been peer reviewed. The model for cyclic loading has not been peer reviewed. Strength: The model allows to predict fundamental fracture processes without

confounding effects of specimen geometry. Weakness: The model does not capture the conditions in the fracture mechanics specimen used in experiments.
(g) Hardware: Executable with a linux environment, requires the ABAQUS finite element code and fortran compiler.
(h) Documentation (user guide, model code): Available on request to PI Siegmund (siegmund@purdue.edu)

2.4.5. Crack Growth Simulations with a Model C(T) Geometry

The modified boundary layer model described in section 1.4.4 of this report and the associated computational results only consider creep-fatigue crack growth in a parametric space. While general experimental trends are predicted correctly, the predicted crack growth rates are not those in the experiments. Consequently, a model of the C(T) specimen as used in the experiments was employed for computations. Minor modifications to the cohesive zone constitutive equations were considered in these computations.

The specific model geometry with the global mesh and the local mesh at the crack tip are shown in Fig. 109. The mesh is created by a meshing script in MATLAB to create the near-tip mesh and the general ABAQUS CAE tool to create the global mesh. The mesh consists of linear plane strain elements while the loading pin is a rigid body. Further details are given in the previous section. The MATLAB script used a meshing strategy based on the modified boundary layer model. The structured mesh around the crack tip consists of equal-sized quadrilateral elements. The coarsening strategy shown in Fig. 109(b) allows for a transition from the structured crack-tip mesh to larger elements with minimal element distortion. Finally, the near tip mesh is linked to the global mesh through the semicircle of nodes marked in Fig. 109(b). Fig. 109(c) depicts the overall stress state.

(a)

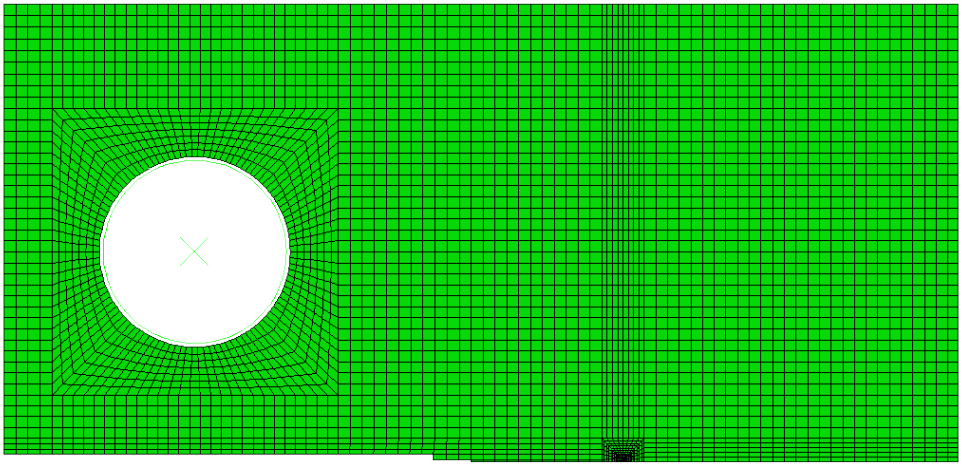

(b)

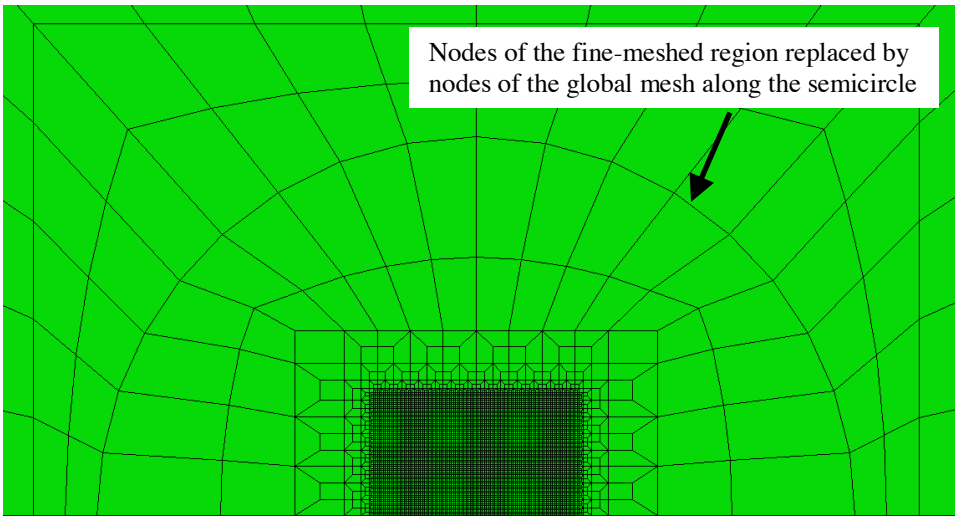

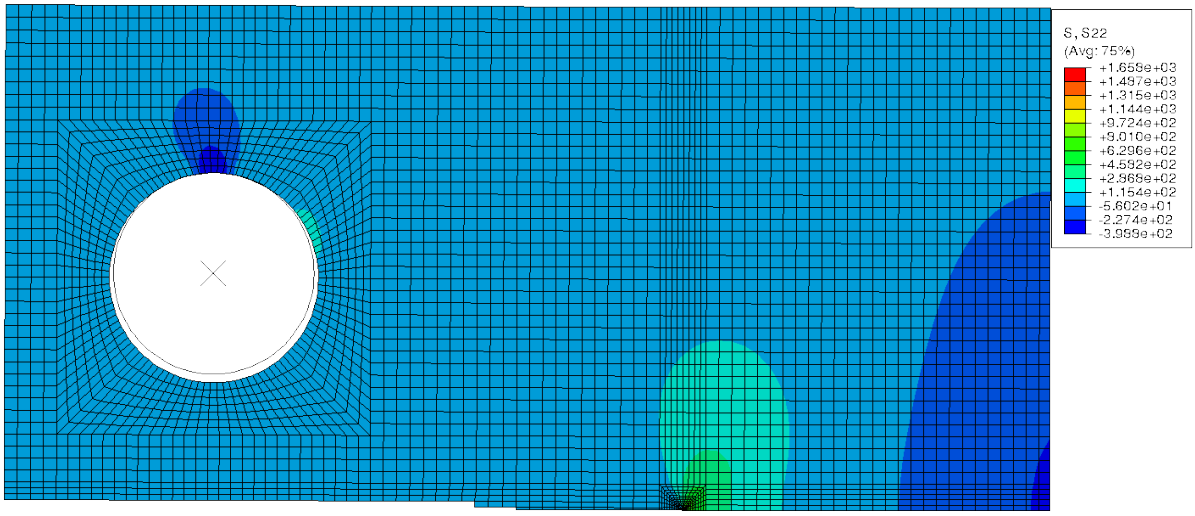

(c)

Fig. 109. FE model of the specimen geometry employed in experiments (a) half model with symmetry boundary conditions, (b) near tip mesh, (c) typical stress field at maximum load (crack opening stress S22).

We employ a modified version of the creep damage law in the cohesive zone based on several considerations. First, the creep law of Bouvard et al. [84], Eq. 53, uses the traction calculated from the traction-separation law using the current cohesive strength σ_{max}. However, the creep traction threshold, T_c, is constant. This means that, when damage causes σ_{max} to fall below T_c, no more creep damage will accumulate. Such a situation is deemed as non-physical. A more appropriate measure is the damage-effective traction T / (1 – D). The modified creep damage evolution equation is therefore:

$$D_{creep} = (1-D)^{-p}\left(\frac{\frac{T}{1-D}-T_c}{C_C}\right)^r \qquad \text{Eq. 58}$$

Furthermore, Zyczkowski [85] argued that, in the original Kachanov-Rabotnov damage evolution equation for continuum creep damage, only one model exponent is needed, which acts on the damage-effective stress. In the modified cohesive zone creep damage equation above, this corresponds to setting $p = 0$, giving the final creep damage evolution equation as:

$$D_{creep} = \left(\frac{\frac{T}{1-D}-T_c}{C_C}\right)^r \qquad \text{Eq. 59}$$

Sun et al. [86] used a similar approach for cohesive zone creep damage, with only the r exponent, although those authors used a damage-effective threshold $T_c(1 – D)$ rather than damage-effective traction. It is also worth noting that the creep damage evolution equation now takes a similar form as the fatigue damage evolution equation, Eq. 51. This equation can be rewritten as

$$D_{fatigue} = \frac{|\delta|}{\delta_\Sigma}\left[\frac{\frac{T}{1-D} - \sigma_f}{\sigma_{\max,0}}\right] \qquad \text{Eq. 60}$$

where $\sigma_f = C_f \sigma_{max,0}$. Now, both damage evolution equations are written in a similar form. A threshold term is subtracted from the damage-effective traction, which is then normalized by a strength. The fatigue damage is scaled by the rate of separation, while the creep damage includes the exponent *r*.

Using the creep data from Benz et al. [1-3], the threshold term T_c is approximated as 15 MPa. This value is based on the fit of strain rate to applied stress given in [2]. The stress at zero strain rate in such a fit can be considered as a threshold below which creep does not occur, which corresponds to T_c. This leaves C_C and *r* as creep parameters to be determined using the creep crack growth experiments. In addition, δ_Σ, $\sigma_{max,0}$, and σ_f must be determined for the fatigue damage evolution.

The continuum is modeled using the CMSG-vp formulation discussed in Section 2.4.2. In addition, the 15 MPa threshold stress identified above is incorporated in the viscoplastic flow rule, so that the effective stress used to calculate the viscoplastic strain rate in Eq. 38 becomes $\sigma_e - (15\,\text{MPa})$. The other continuum properties are identified from the nanoindentation experiments, the high strain rate low cycle fatigue data from INL, and the creep experiments in [2]. The viscoplastic exponent *m* is 5.6, viscoplastic prefactor *A* is 5E-18 $\text{MPa}^\text{m}/\text{s}$, the cyclic yield stress is 284 MPa, the material intrinsic length *l* is 4.5 μm, and the isotropic hardening exponent *N* is 0, which models a secondary creep regime. The tertiary creep damage is localized to the cohesive zone via Eq. 59. The elastic properties are a shear modulus *G* of 61 GPa and Poisson's ratio ν of 0.3. The continuum properties and fitted cohesive zone properties described in the following paragraphs are summarized in Table 8.
First, computations are reported on the two bounds, fatigue damage dominated and creep damage dominated. We subsequently apply the model – without any adjustment of model parameters – to the creep-fatigue regime under both steady state and variable amplitude loading conditions.

Fig. 110(a) depicts predicted and experimentally obtained crack growth data (da/dN) for the fatigue regime, i.e. load frequency of 5 Hz with a triangular waveform. The model considers the crack length data at a/W=0.485, a/W=0.560 with the maximum applied load F_{max} = 1500 N and load ratio *R* = 0.5. The computation with properties $\sigma_{max,0}$ = 3408 MPa, $\delta_\Sigma = 28\delta_0$, and $\sigma_f/\sigma_{max,0}$ = 0.1 gave the most reasonable fit. The model is able to describe the measured crack growth rate well, Fig. 110(a). Damage in the cohesive zone is virtually all from the fatigue damage evolution (independent of the exact parameter values for the creep damage model as long as its parameters are within a reasonable range) and is depicted in its spatial distribution in Fig. 110(b). The corresponding traction distribution is shown in Fig. 110(c).

Fig. 111(a) depicts predicted and experimentally obtained crack growth data (da/dt) for the creep regime, with trapezoidal loading using a ramp rate of 0.33 Hz and a hold time of 17 s per cycle. The model considers the crack length data at a/W=0.485, a/W=0.560. At both crack lengths, loading is considered with the maximum applied load F_{max}=1500 N. In addition, the experiment with maximum applied load F_{max}=1750 N is considered at a/W=0.485, although that experiment did not reach a/W=0.560. Therefore, three values of *K* can be considered (two at a/W=0.485 and

one at a/W=0.560). The computation with C=5500 MPa, r=4.6 and considering the underlying cohesive zone paremeters of $\sigma_{max,0}$ and δ_0 provides the best fit. The model is able to describe the measured crack growth rate well, Fig. 111(a). Damage in the cohesive zone is virtually all from the creep damage evolution and is depicted in its spatial distribution in Fig. 111(b), along with the traction distribution. Plastic zone contours are shown in Fig. 111(c).

Fig. 112(a) depicts predicted and experimentally obtained crack growth data (da/dt) for the creep-fatigue regime, with triangular loading at f=0.33 Hz, and compares the crack growth data to the fatigue and creep bounds. The model considers the crack length data at a/W=0.485, a/W=0.560, with maximum applied load F_{max}=1500 N and load ratio R=0.5. No further adjustment of the model parameters is undertaken and the damage superposition is linear. The model is not quite able to describe the measured crack growth rate at f=0.33 Hz, Fig. 112(a). While the predicted crack growth rate is between the fatigue and the creep bound, the predicted rate is too low compared to the experimental data. Damage in the cohesive zone is virtually equally attributed to all creep and to fatigue damage, and is depicted in its spatial distribution in Fig. 112(b). The traction distribution, also in Fig. 112(b) lies between the traction distributions for fatigue-dominated and creep-dominated conditions. Fig. 112(c) shows plastic zone contours.

Table 8. Summary of continuum and cohesive zone properties for the C(T) specimen simulations.

Continuum Properties		Cohesive Zone Properties	
A	5E-18 (MPa^m)/s	$\sigma_{max,0}$	3408 MPa
m	5.6	$C_f = \sigma_f / \sigma_{max,0}$	0.1
σ_y	284 MPa	δ_0	0.4 μm
N	0	δ_Σ / δ_0	28
l	4.5 μm	C	5500 MPa(s$^{1/r}$)
G	61000 MPa	T_C	15 MPa
v	0.3	r	4.6

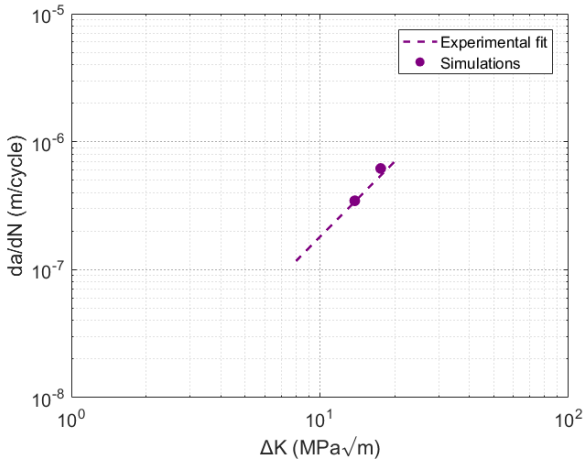

(a)

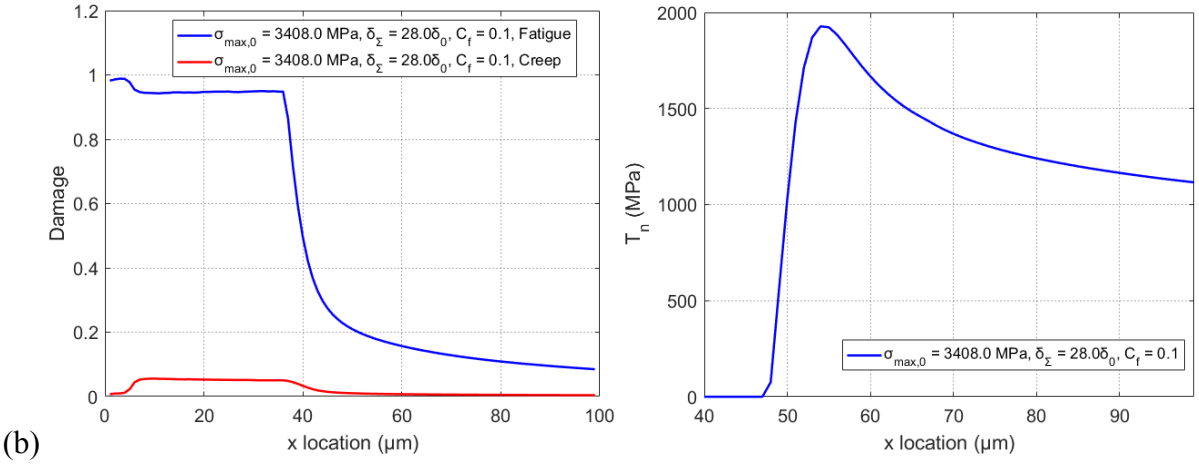

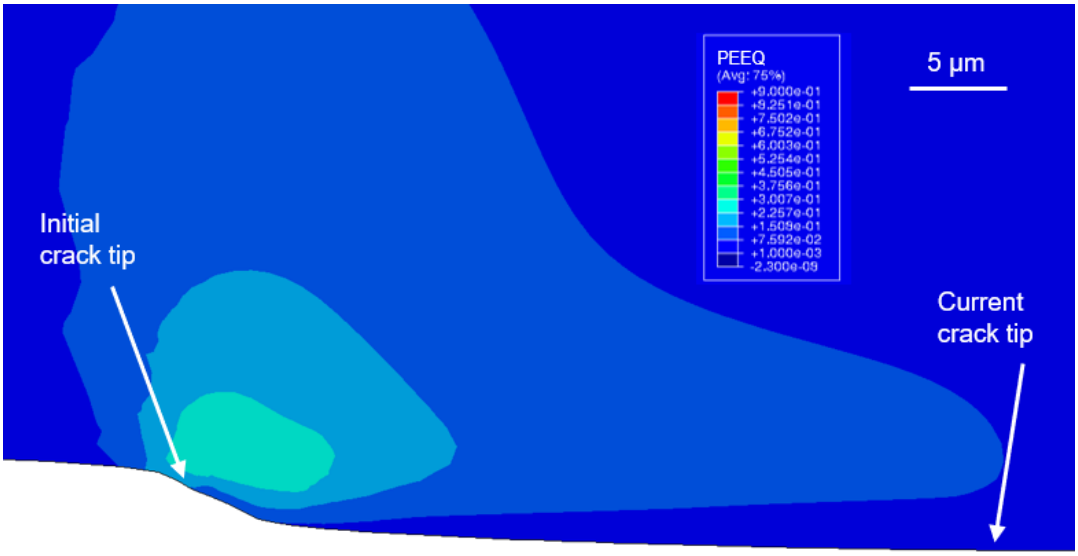

Fig. 110. Fatigue damage dominated crack growth in Alloy 617: (a) Simulated and experimentally determined crack growth rate under conditions of 5 Hz ramp loading. (b) Damage and traction distributions for a/W = 0.560. (c) Contour plot of plastic zone for a/W = 0.560.

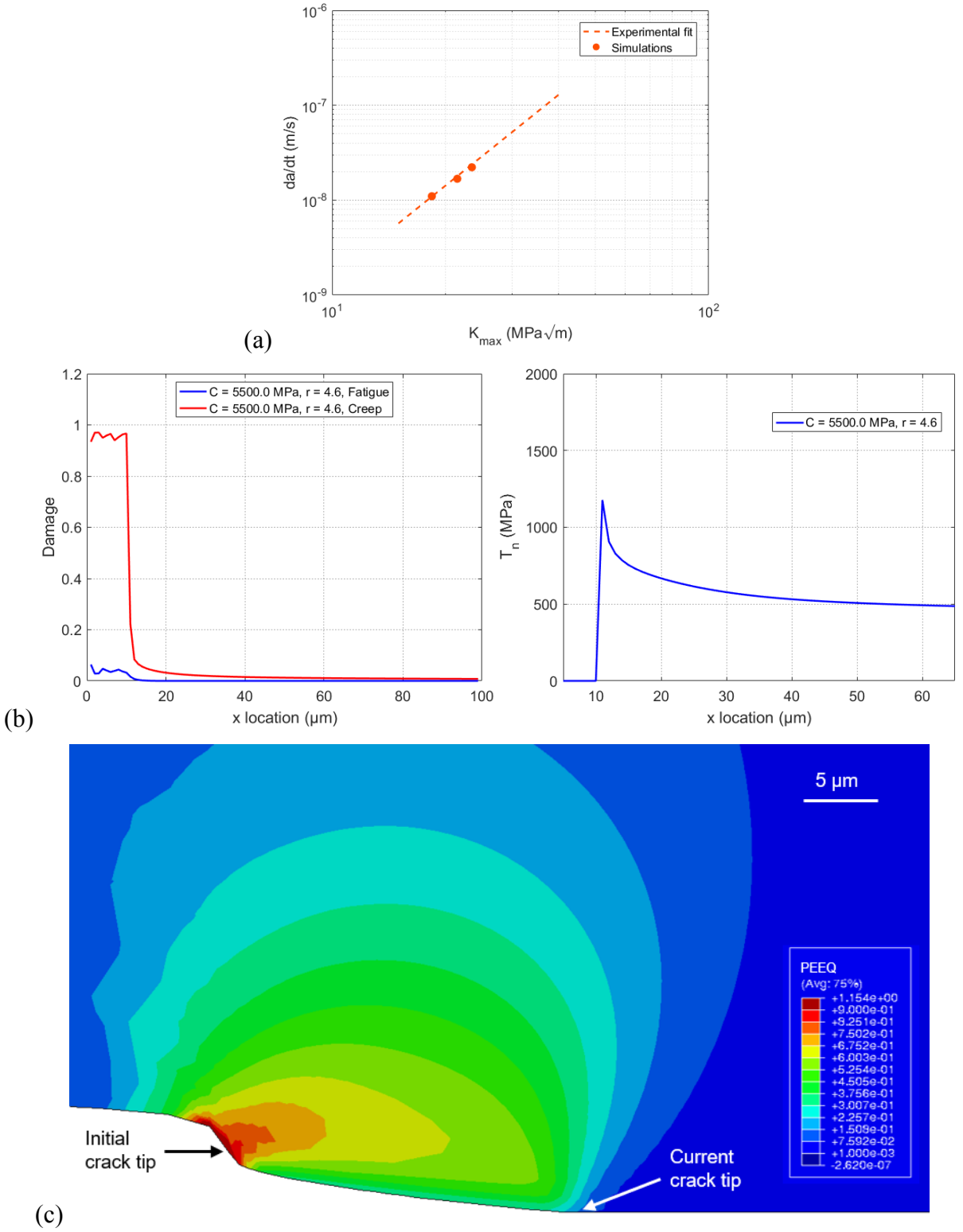

Fig. 111. Creep damage dominated crack growth in Alloy 617: (a) Simulated and experimentally observed crack growth rate under conditions of trapezoidal loading. (b) Damage distribution and traction distribution at the crack tip. (c) Contour of plastic zone for a/W = 0.560.

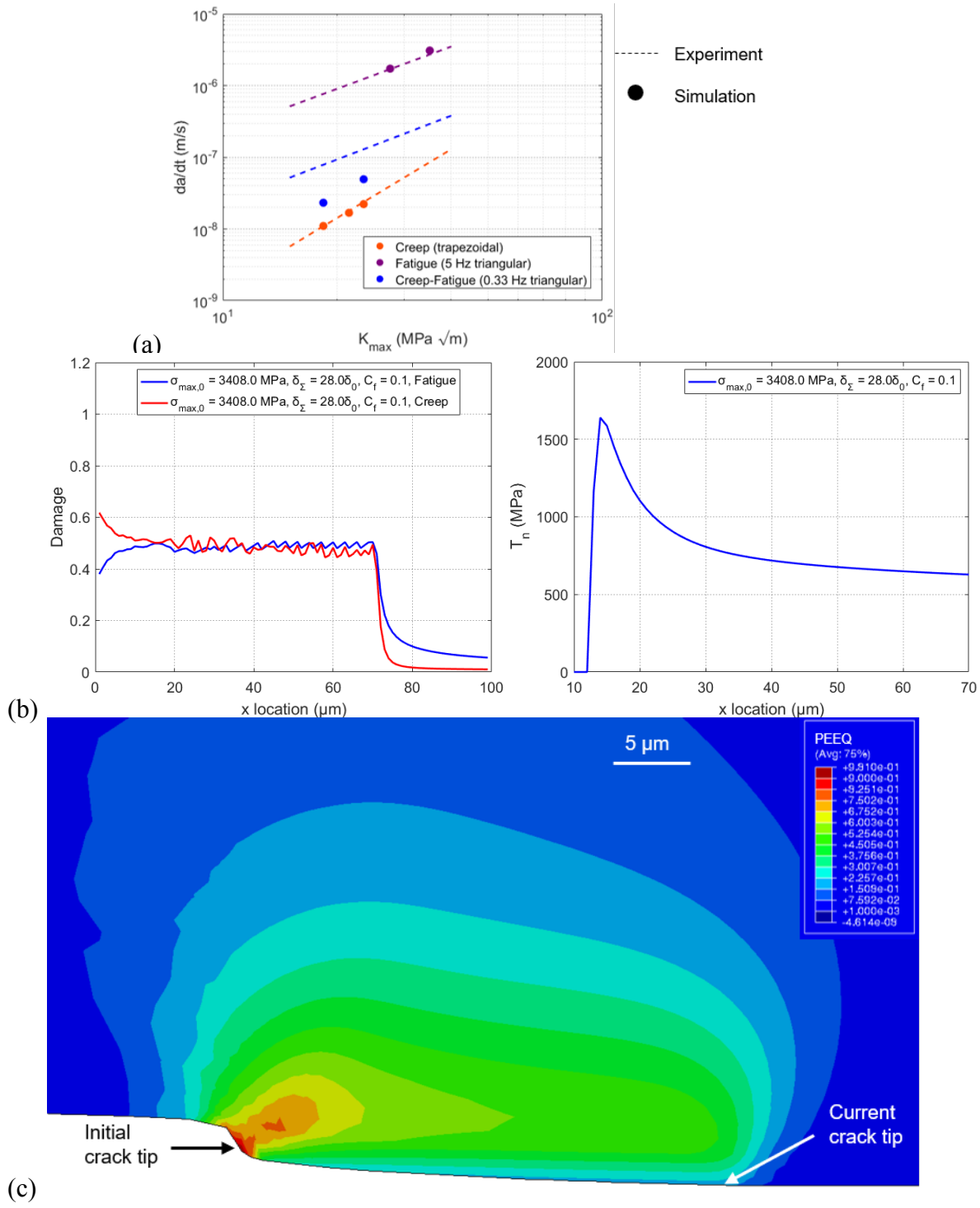

Fig. 112. Creep-fatigue crack growth in Alloy 617: (a) Simulated and experimentally observed crack growth rate under conditions of 0.33 Hz ramp loading. Crack growth rates under fatigue conditions (Fig. 110) and creep conditions (Fig. 111) are shown for reference. (b) Damage and traction distributions for a/W = 0.560. (c) Contour plot of plastic zone for a/W = 0.560

Fig. 113(a) depicts predicted crack growth data (a vs. N) for a block overload scenario in the creep-fatigue regime, ramp loading at f=0.33 Hz with 20 overload cycles at 1.5 overload factor. Corresponding experimental data are given in Fig. 69. Crack length vs cycle count surrounding the first 20 cycle 150% Kmax overload block applied to sample 617-28GO. ΔK measured just prior to the overload block was 8.3 MPa√m. The average ΔK during the overload block was 12.6 MPa√m.. The model considers the crack length data at a/W=0.485, a/W=0.560. No further adjustment of the model parameters is undertaken and the damage superposition is linear. The model is able to describe the measured crack growth response well, i.e. the model predicts the observed response that a block overload leads to acceleration of crack growth during the overload and a subsequent slow return to the steady state crack growth rate. Fig. 113(b) depicts corresponding crack growth rates vs. the crack tip position. The damage distributions are shown in Fig. 113(c), and the traction distributions before and after the overload block are shown in Fig. 113(d). Note that, for both crack lengths, the tractions at maximum load are diminished after the overload block. The plastic zone sizes are shown in Fig. 113(d).

Fig. 114(a) depicts predicted crack growth data (a vs. N) for a single overload scenario in the creep-fatigue regime, ramp loading at f=0.33 Hz at 1.5 overload factor. The model considers the crack length data at a/W=0.485, a/W=0.560. No further adjustment of the model parameters is undertaken and the damage superposition is linear. The model is able to capture the experimental finding that a single overload causes neither detectable crack growth acceleration nor crack growth rate retardation. Fig. 114(b) depicts corresponding crack growth rates vs. the crack tip position, and again shows the lack of acceleration and retardation provided by the overload. The damage distributions are shown in Fig. 114(c), and the traction distributions are shown in Fig. 114(d). The traction at maximum load after the single overload is comparable to the steady-state traction before the overload. The plastic zone sizes are shown in Fig. 114(e).

(a)

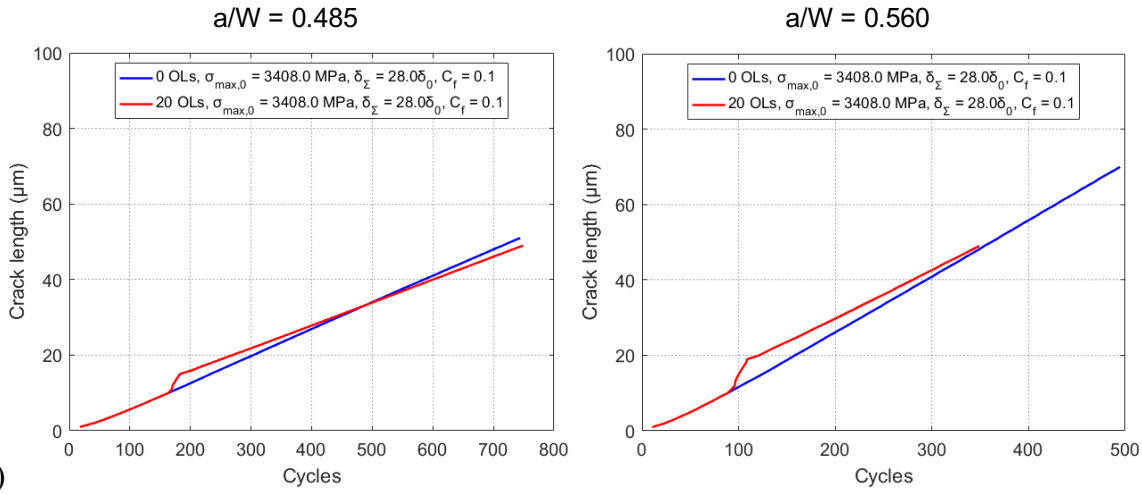

(b)

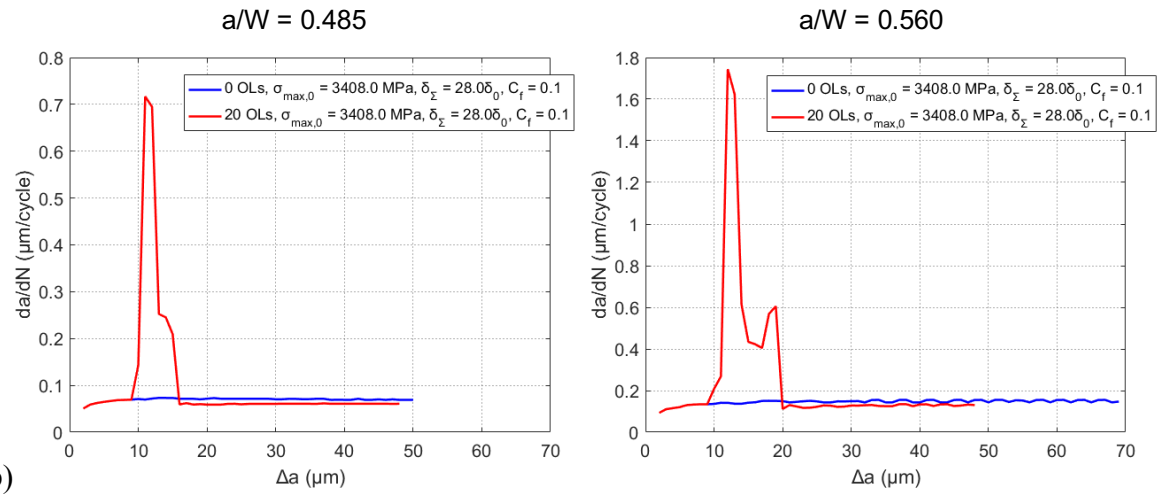
a/W = 0.485
a/W = 0.560
0 OLs, σmax,0 = 3408.0 MPa, δΣ = 28.0δ0, Cf = 0.1
20 OLs, σmax,0 = 3408.0 MPa, δΣ = 28.0δ0, Cf = 0.1
da/dN (μm/cycle)
Δa (μm)

(c)

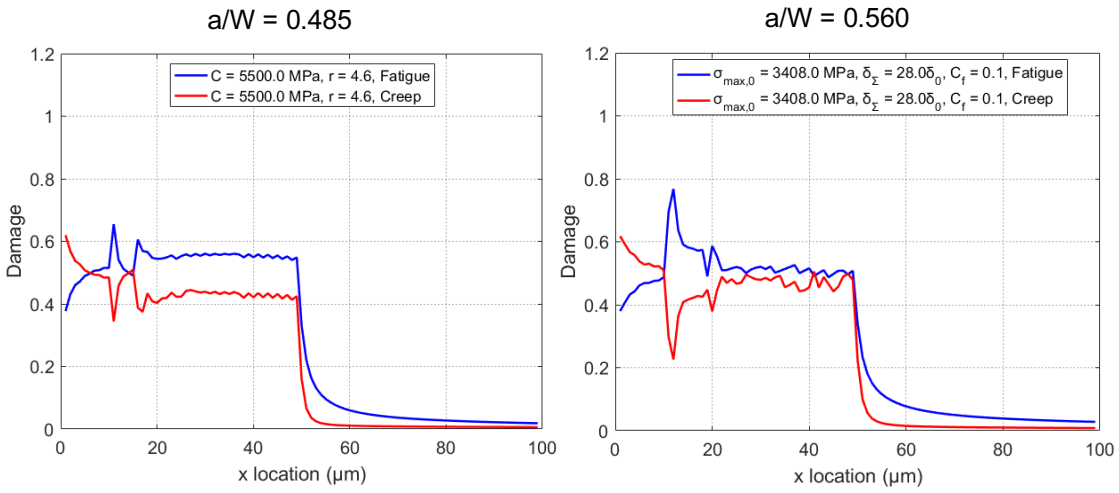
a/W = 0.485
a/W = 0.560
C = 5500.0 MPa, r = 4.6, Fatigue
C = 5500.0 MPa, r = 4.6, Creep
σmax,0 = 3408.0 MPa, δΣ = 28.0δ0, Cf = 0.1, Fatigue
σmax,0 = 3408.0 MPa, δΣ = 28.0δ0, Cf = 0.1, Creep
Damage
x location (μm)

(d)

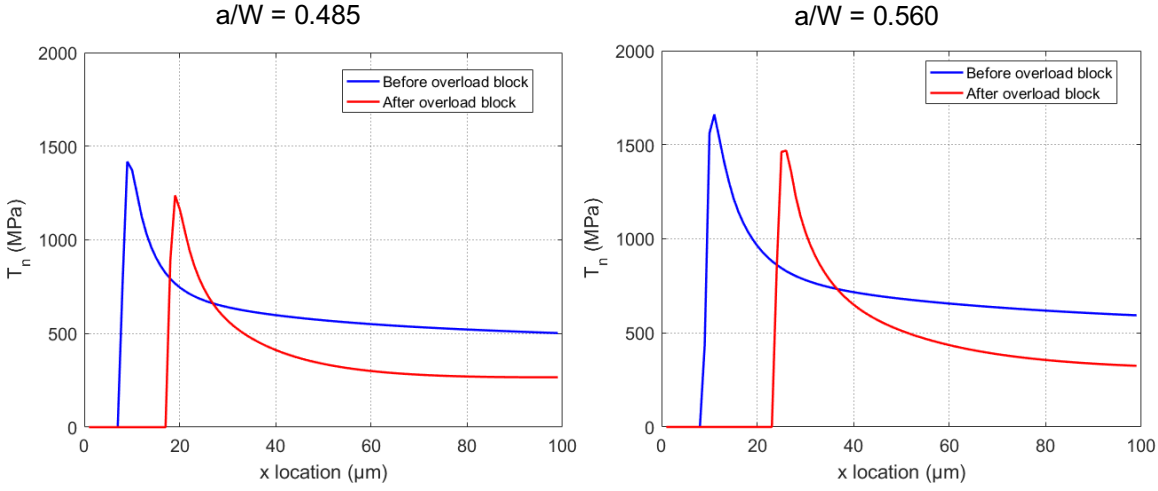
a/W = 0.485
a/W = 0.560
Before overload block
After overload block
Tn (MPa)
x location (μm)

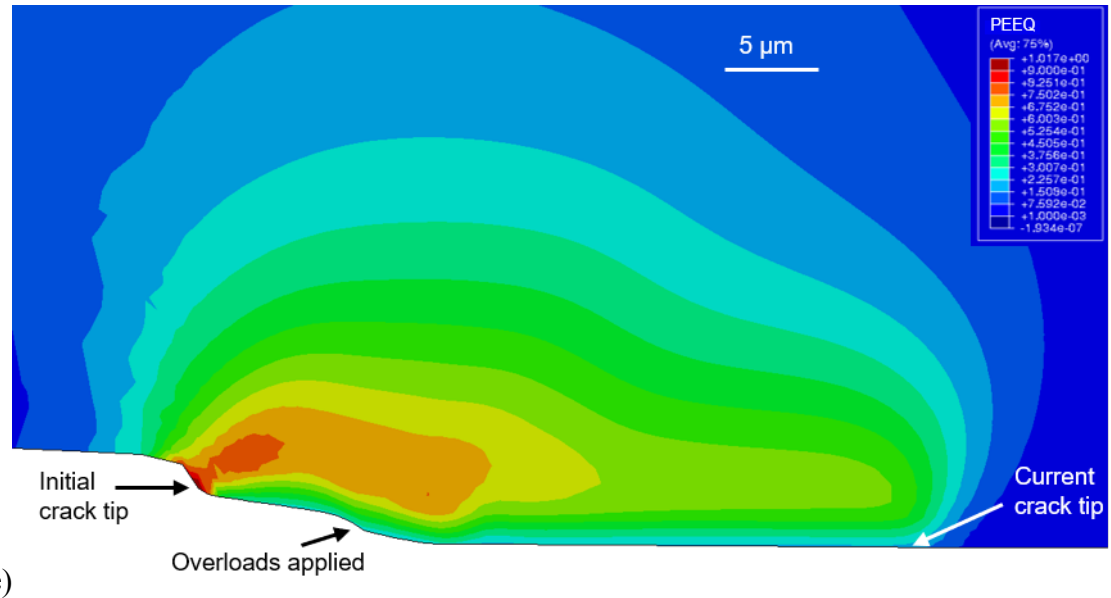

(e)

Fig. 113. Block overload response for creep-fatigue crack growth in IN 617: (a) Simulated crack extension. (b) Crack growth rate plotted against crack extension. (c) Fatigue and creep damage distributions. (d) Traction profiles before and after the overload block. (e) Plastic zone contour plot for a/W = 0.560.

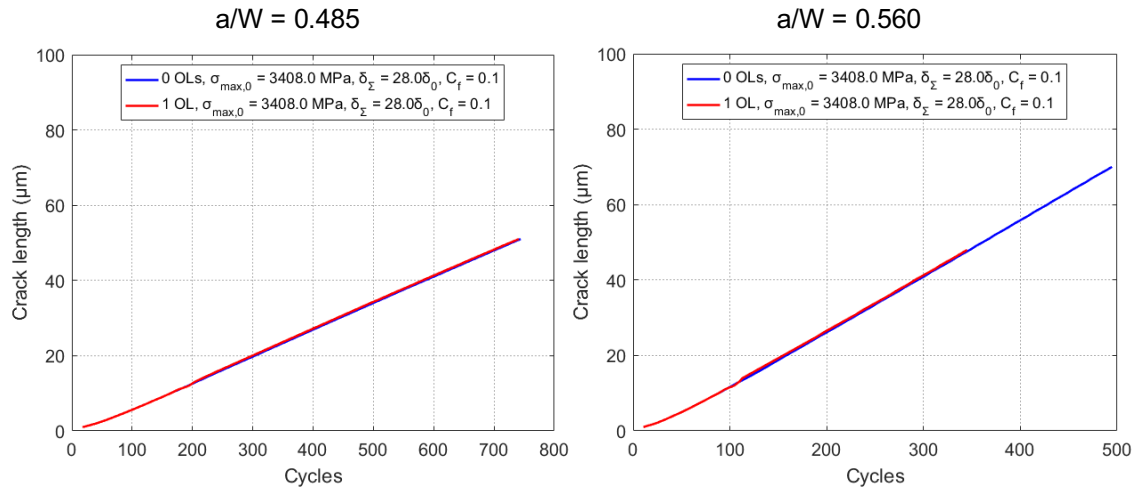

(a)

(b)

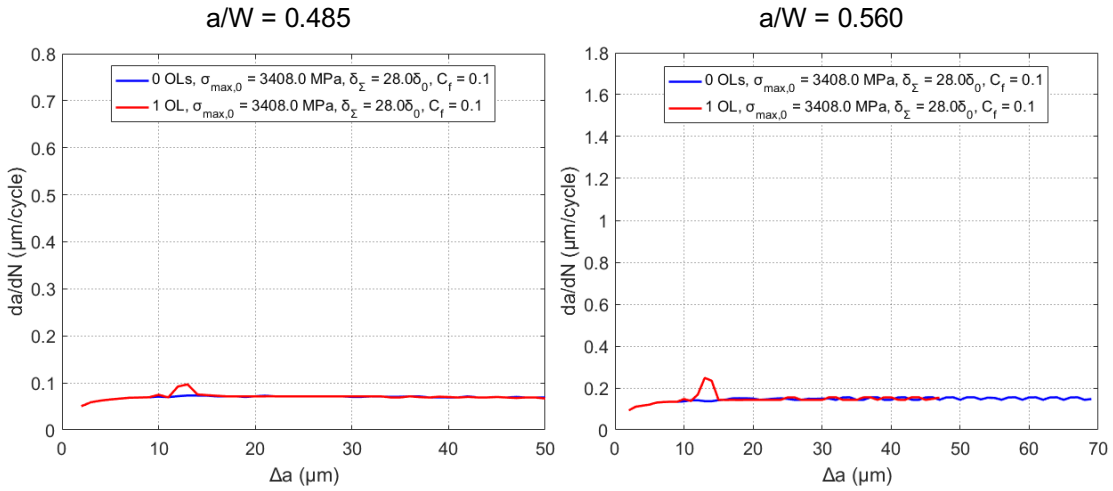
a/W = 0.485
a/W = 0.560
0 OLs, σmax,0 = 3408.0 MPa, δΣ = 28.0δ0, Cf = 0.1
1 OL, σmax,0 = 3408.0 MPa, δΣ = 28.0δ0, Cf = 0.1
da/dN (μm/cycle)
Δa (μm)

(c)

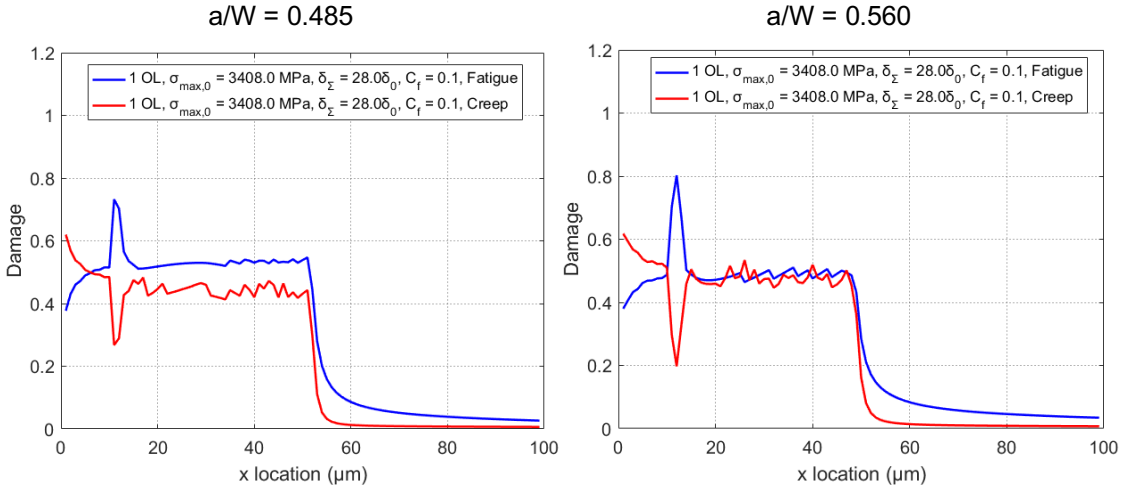
a/W = 0.485
a/W = 0.560
1 OL, σmax,0 = 3408.0 MPa, δΣ = 28.0δ0, Cf = 0.1, Fatigue
1 OL, σmax,0 = 3408.0 MPa, δΣ = 28.0δ0, Cf = 0.1, Creep
Damage
x location (μm)

(d)

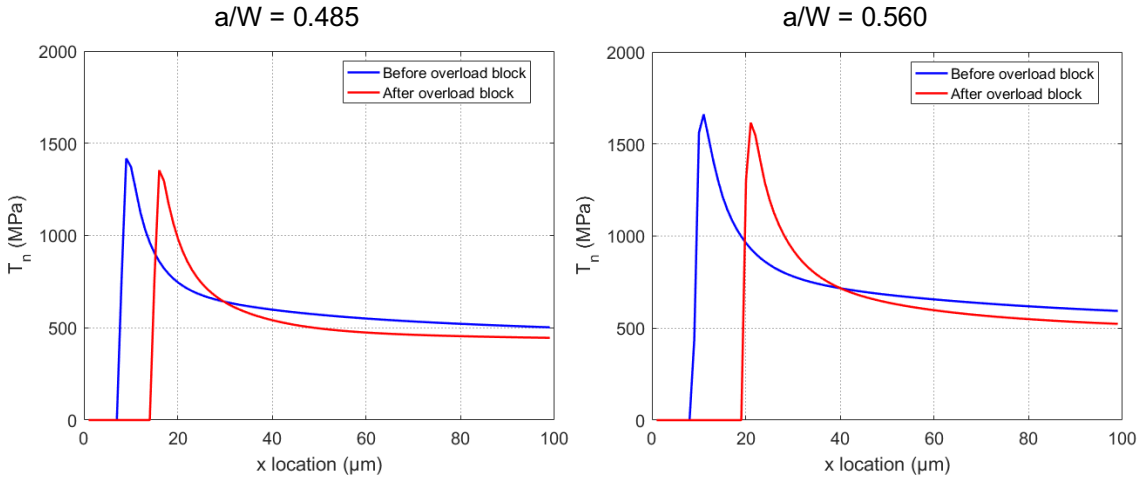
a/W = 0.485
a/W = 0.560
Before overload block
After overload block
Tn (MPa)
x location (μm)

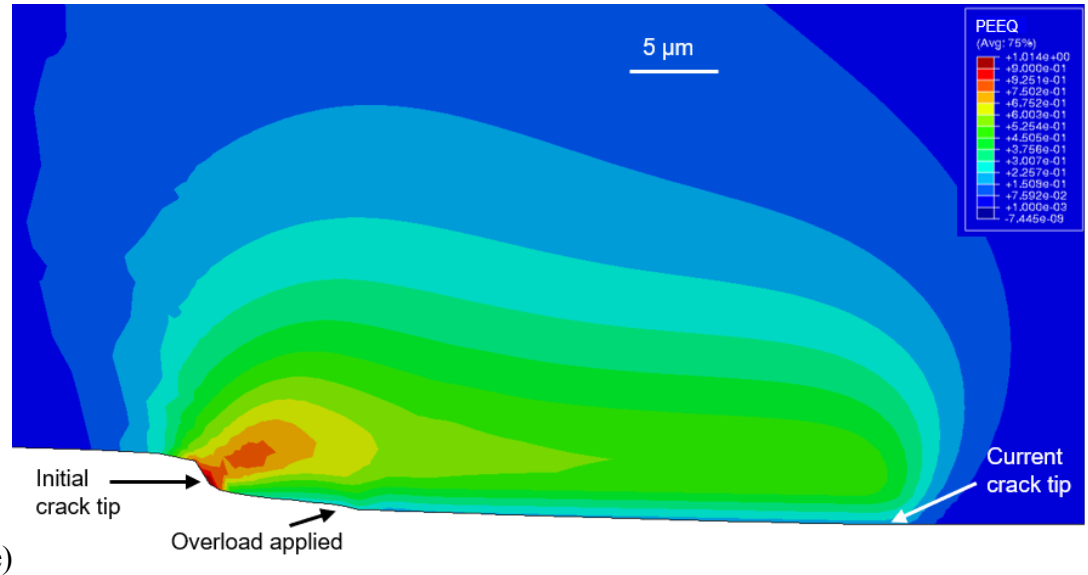

(e)

Fig. 114. Single overload response for creep-fatigue crack growth in IN 617: (a) Simulated crack extension. (b) Crack growth rate plotted against crack extension. (c) Damage distribution. (d) Traction distribution before and after the overload. (e) Plastic zone contour plot for a/W = 0.560.

Underpredicting the crack growth rates with combined creep-fatigue damage (i.e. 0.33 Hz ramp loading) could point towards the need for an additional damage interaction description in the cohesive zone. One approach that has been considered in this situation is recalibrating either the creep or fatigue damage law for creep-fatigue conditions [84], although this has the disadvantage of introducing additional parameters with unclear physical meaning to the model. Nonetheless, further consideration of creep-fatigue damage interaction effects could also provide insight into the experimental observation that there appeared to be a K, K, or a/W threshold beyond which even the block overloads did not cause a retardation.

Overall, the model is able to replicate several experimental trends, particularly the single and block overload responses for creep-fatigue loading. The model also has the advantage of maintaining a reasonably small parameter space: the continuum is modeled by power-law creep with a first-order strain gradient plasticity formulation while the fatigue and tertiary creep damage are localized to the cohesive zone with linear damage superposition. Finally, each set of parameters is associated with a particular set of experiments: nanoindentation and creep tests for the continuum parameters, fatigue-dominated high-frequency crack growth tests for the fatigue damage parameters, and creep-dominated trapezoidal loading crack growth tests for the creep damage parameters.

Summary on Computational Modeling: Analysis of Crack Growth in IN 617 at 800°C in the Compact Tension Specimen

(a) Model description: A finite element model is considered which represents the compact tension specimen. Crack growth simulations under conditions considered in experiments are considered. The visco-plastic strain gradient model is combined with cohesive zone models for material separation.

(b) Performance criteria: Implementation needs to be successful to quantitatively describe crack growth rates measured in experiments.

(c) Test results demonstrating meeting model performance criteria: It has been demonstrated that the model predicts crack growth rates in IN 617 at 5 Hz and for the trapezoidal load. The crack growth rate at 0.33 Hz is predicted as lower than observed. The model is however successful in predicting the observed overload response.
(d) Theory behind the model: The model is a novel combination of the theory of the rate dependent conventional mechanism strain gradient plasticity with irreversible cohesive zone models for damage accumulation in cyclic loading and creep. Specific load cases are executed with a standard nonlinear finite element model.
(e) Mathematics to be used, formulas and calculation methods: See Eq. 33-38 for the constitutive model of the visco-plastic strain gradient model. See Eq. 46-51 for the constitutive equations for the cohesive zone models. The implementation uses a nonlinear finite element formulation.
(f) Peer review of theory and algorithm, strength and weaknesses: The model has not been peer reviewed. Strength: The model predicts both the fatigue and the creep damage dominated experimental conditions. Weakness: While the model predicts the crack growth rate under creep-fatigue conditions to be between the pure fatigue and creep condition, the model underestimates the experimentally observed crack growth rate in the combined creep-fatigue regime
(g) Hardware: Executable with a linux environment, requires the ABAQUS finite element code and fortran compiler.
(h) Documentation (user guide, model code): Available on request to PI Siegmund (siegmund@purdue.edu)

2.5. Summary of Key Accomplishments

1. Experimental data were compiled to provide material parameter inputs for the crack growth model specific to Alloy 617. An initial set of material parameters for Alloy 617 has been determined for use in the model.
2. Nanoindentation studies were used to understand the strain gradient material length scale for Alloy 617 via the indentation size effect. Furthermore, a methodology for extracting a short time scale creep law from nanoindentation data was successfully implemented and validated by comparison to uniaxial data.
3. Crack growth experiments were used to understand cracking mechanisms and the roles of loading frequency, hold times, and overloads on crack growth rates in Alloy 617 at 800 °C.
4. A visco-plasticity strain gradient formulation was implemented and the explicit time integration is augmented with a creep tolerance parameter.
5. An inverse parameter identification approach was established such that the creep model parameters for Alloy 617 could be determined by a combination of high temperature nanoindentation and the inverse analysis model. The creep exponent found with this approach is identical to that from conventional creep experiments based on the minimum creep rate. Furthermore, using the mechanistic approach by Huang et al. [42] to the evaluation of nanoindentation data and size dependent plasticity, we determine that Alloy 617 exhibits strain gradient plasticity effects. The intrinsic length scale is of the order of several micrometers.
6. The visco-plastic strain gradient model has been applied in a modified boundary layer (MBL) model together with a rate independent and a rate dependent contribution to

material separation captured in a cohesive zone model. The MBL model was loaded using a mode I asymptotic crack tip solution, in which the stress intensity factor KI, relative to the reference stress intensity factor K_0 set by the cohesive zone properties was used to calculate the boundary displacement. Three loading scenarios were considered: (i) a stationary crack with no crack advance and a hold time, (ii) a crack advance using a cohesive-zone formulation under monotonic loading and no hold time, (iii) cyclic loading. The parameters of the constitutive visco-plastic model and the intrinsic material length were varied.

7. The visco-plastic strain gradient model has been applied in a compact tension C(T) specimen model together with a rate independent and a rate dependent contribution to material separation captured in a cohesive zone model. This model is able to describe experimentally observed crack growth rates in the fatigue regime and in the creep regime. The model predicts crack growth rate under creep-fatigue conditions to be within the bounds of the fatigue-only and creep-only experiments, however, predicted creep-fatigue crack growth rates are slightly too low. The model accurately predicts the overload response for Alloy 617 in the creep-fatigue regimes, i.e. that a single overload does not alter the crack growth rate, and that a sequence of multiple overloads leads to a crack acceleration followed by a slow return to the steady state crack growth rate.

2.6. Summary of Key Findings

1. Good agreement is found for creep parameters found by uniaxial creep experiments and nanoindentaion creep experiments. In the latter case, both an analytical analysis and an inverse numerical analysis gave similar results. Furthermore, it was concluded that alloy 617 demonstrates a plastic strain gradient affect and the length scale was quantified.
2. Crack growth results at 800°C show that Alloy 617 has relatively low sensitivity to frequency, hold times, and overloads in the low growth rate regime. An effect of frequency was observed between 5 Hz and 0.33 Hz, but slowing to 0.5 Hz or adding a hold time had little further effect in this regime. This is likely due to the stress levels being too low to trigger the intergranular cracking mechanisms that are observed at higher stress levels. Such results are significant since most of the lifetime will be spent in the low growth rate regime.
3. Adding a single overload at 0.33 Hz loading frequency had no noticeable effect, while blocks of 20 overloads showed an acceleration during the overload block followed by a period of retardation in crack growth rates.
4. Simulation results show that plastic strain gradient hardening is more prominent in cases of large visco-plastic power law exponents and with longer hold times.
5. Under monotonic loading simulations, plastic strain gradients reduce crack initiation toughness and crack growth resistance and that effect is more pronounced for large visco-plastic powers;
6. Simulation results show that the dependence of initiation toughness and tearing modulus on the ratio between intrinsic lengthscale and plastic zone size is most pronounced at small value of this ratio but saturates as the ratio increases. Furthermore, the influence of the intrinsic lengthscale on initial toughness and tearing modulus is found to decreases with an

increase in loading rate, and this rate dependence is more pronounced for smaller values of the intrinsic lengthscale

7. In reference to the crack growth direction, the spatial location of the maximum in the rate of the plastic strain gradient is always ahead of the location of the maximum plastic strain, but the position relative to the crack tip is found to depend on the magnitude of blunting accompanying the crack advance. The strong dependence of initiation toughness and tearing modulus on the ratio between intrinsic lengthscale and plastic zone size is an important finding of this study. It demonstrates that the influence of the intrinsic material length at the crack tip should be considered even for small measured values.
8. Under cyclic loading it is necessary to account for rate dependent material separation in the simulations to capture the rate dependence of fatigue crack growth in Alloy 617. This is accomplished by a combination of a rate independent fatigue component and a rate dependent Kachanov-Robotov model component.
9. Overload cycles in fatigue crack growth simulations for the visco-plastic solid only become relevant if multiple overloads are applied in an overload cycle block. The overload cycle block leads to a temporary acceleration of the crack growth followed by a pronounced retardation step. Such results are in good agreement with our overload experiments.
10. The accuracy of the MBL model is visco-plastic deformation is limited to short times and small creep deformation magnitudes. If these conditions are not fulfilled, it is necessary to use a full-scale specimen geometry corresponding the experimental conditions. The crack growth rates and plastic zone sizes compatible with experiments can be predicted.
11. The use of a plane strain model for the compact tension specimen demonstrates that a cohesive zone model approach for creep-fatigue crack growth can be successfully used to describe experimentally observed crack growth rates under steady state and under overload conditions.

3. Project Methodology Updates

Over the course of the project methodology has been updated based on concerns raised about various aspects of the proposed approach. Some concerns and questions have included:

1. Alloy 617 does not demonstrate steady state creep behavior.
2. Initial visco-plastic model may be too simplistic.
3. Modified boundary layer model formulation may not be appropriate.

Updates on addressing these concerns are as follows.

1. Alloy 617 does not demonstrate steady state creep behavior in uniaxial tension. After reviewing the uniaxial data for short time scales and high stresses, which is most relevant to a growing crack visco-plastic zone, the material shows power law behavior in tension that is easy to fit and use in model development. Furthermore, we observed similar creep behavior using indentation with the same creep exponent. Both indentation creep testing and uniaxial results were used to define the visco-plastic formulation for the model.
2. There was concern that the initial visco-plastic model may be too simplistic. Given the complexity of the overall model, we used a combination of uniaxial data and indentation creep

experiments to initially define the visco-plastic response. Furthermore, we used parametric studies to compare visco-plastic model approaches and find the best approach for our crack growth model. Our goal was to utilize the simplest model that achieves the needed material response.

3. Modified boundary layer formulation may not be appropriate. To address this, we have compared predictions from 2-D modified boundary field formulation (zero T-stress) with those from a 2-D, plane strain, C(T) specimen model.

4. Problems or Delays

Michelle Jennings (graduate student at OSU) left the project mid-2015, and Philipp Seiler (postdoc at Purdue) left the project mid-2016. We hired new graduate students, Dylan Addison at OSU in September 2015 and Joshua Pribe at Purdue in August 2016. This delay was managed by extending the project into the no-cost extension period to complete the experimental work at OSU and modeling development and validation at Purdue.

5. Products Produced and Technology Transfer

5.1. Journal Articles (several more are in preparation)

1. Y. Zhang, P. Seiler, T. Siegmund, J. J. Kruzic, V. Tomar, (2017) "High Temperature Indentation Based Property Measurements of Inconel IN-617," *International Journal of Plasticity*, **96**, 264-281.

2. Y. Zhang, D. P. Mohanty, V. Tomar, (2016), "Visualizing In Situ Microstructure Dependent Crack Tip Stress Distribution in IN-617 Using Nano-mechanical Raman Spectroscopy," *JOM*, **68** (11) 2742-2747.

3. P. Seiler, T. Siegmund, Y. Zhang, V. Tomar, and J. J. Kruzic, (2016), "Stationary and propagating cracks in a strain gradient visco-plastic solid," *International Journal of Fracture*, **202,** 111-125.

5.2. Conference Papers

1. Y. Zhang, D. P. Mohanty, V. Tomar, (2017), "Analyses of nanoscale to microscale strength and crack-tip stresses using nanomechanical Raman spectroscopy in IN-617", in: *Conference Proceedings of the Society for Experimental Mechanics Series, Volume 2*; Annual Conference and Exposition on Experimental and Applied Mechanics 2016, Orlando, FL, June 6-9, 2016, pp. 9-16.

2. Y. Zhang, P. Seiler, V. Tomar, (2015) "High temperature indentation experiments and size effect analyses in IN-617", in: *Proceedings of the American Nuclear Society 2015 Annual Meeting*, San Antonio, TX, June 7-11, 2015. (4 Pages, paper is part of electronic proceeding CD-ROM, no number assigned).

5.3. Dissertations/Theses

1. Dylan Addison, "Time-Dependent Crack Growth Mechanisms in Alloy 617 at 800°C in Air," M.S. Thesis, Oregon State University. Defense date: June 7, 2017
2. Yang Zhang, "Characterization of Crack Tip Plasticity and Size Effect in High Temperature Material Using Nano-mechanical Raman Spectroscopy and Indentation", PhD Dissertation, 2017, Purdue University.

5.4. Presentations (speaker underlined)

1. J. Pribe, T. Siegmund, "Strain gradient effects in fatigue crack growth". 2018 ASTM-E08 Committee Meeting, abstract submitted.
2. J. Pribe, T. Siegmund, "Creep-fatigue crack growth in a strain gradient viscoplastic solid," 3rd Midwest Mechanics Workshop, Purdue University, West Lafayette, IN, Aug. 11, 2017.
3. J. Pribe, T. Siegmund, "Fatigue crack growth during overloads: Influence of rate and strain gradients," 54th Technical Meeting of the Society for Engineering Science, Northeastern University, Boston, MA, July 25-27, 2017.
4. Y. Zhang, C. Prakash, V. Tomar, "Characterization of Crack Tip Plasticity and Size Effect in High Temperature Material Using Nano-mechanical Raman Spectroscopy and Indentation," SEM Annual Meeting, Indianapolis, IN, June 2017.
5. Y. Zhang, V. Tomar, "Visualizing In-situ Microstructure Dependent Crack Tip Stress Distribution in IN-617 Using Nano-mechanical Raman Spectroscopy," Oral Presentation, 2017 TMS Annual Meeting, San Diego, CA, February/March 2017.
6. V. Tomar, "Digital Stress Imaging in Mesoscale Microstructure Dependent Deformation Visualized Using Nano-mechanical Raman Spectroscopy: Role of Initial Manufacturing Originated Residual Stresses," Oral Presentation, 2017 TMS Annual Meeting, San Diego, CA, February/March 2017.
7. D. A. Addison, J. J. Kruzic, "Frequency, Hold Time and Overload Effects on Crack Growth Rates in Alloy 617 at 800°C in Air," Poster Presentation, 2017 TMS Annual Meeting, San Diego, CA, February/March 2017.
8. D. A. Addison, J. J. Kruzic, "Creep-fatigue Crack Growth Mechanisms for Alloy 617 at 800°C," Poster Presentation, Materials Science & Technology 2016, Salt Lake City, UT, October 2016.
9. T. Siegmund, V. Tomar, J. J. Kruzic, T. Ngyuen, P. Seiler, "Experiments and simulations in NI-based superalloy failure at high temperatures," Oral Presentation, 2016 ASME International Mechanical Engineering Congress and Exposition, Phoenix, AZ, November 2016.
10. J. J. Kruzic, D. A. Addison, P. Seiler, T. Siegmund, Y. Zhang, and V. Tomar, "Mechanistic Models of Creep-Fatigue Crack Growth Interactions for Advanced High Temperature Reactor Components," Poster presentation, ART Advanced Materials Program Review, Department of Energy Headquarters, Germantown, MD, June, 2016.
11. Zhang, Y., Mohanty, D., Seiler, P., Tomar, V., Characterization of high temperature crack tip plasticity and size effect in alloy 617 using high temperature indentation and nanomechanical

Raman spectroscopy, Oral presentation, 2016 TMS Annual Meeting, Nashville, TN, February, 2016.

12. Gan, M., Zhang, Y., and Tomar, V., Role of length scale and temperature in ultra-high temperature properties of materials examined using nanoindentation, Oral presentation, 2016 International Plasticity Conference, Kona, HI, January, 2016.
13. P. Seiler, J. J. Kruzic, Y. Zhang, V. Tomar, and T. Siegmund, High-temperature fatigue crack growth in a visco-plastic strain gradient material model, *52nd Anual SES (Society of Engineering Science) Technical Meeting*, Oral presentation, Texas A&M University, College Station, October, 2015.
14. Zhang, Y., Tomar, V., Characterization of high temperature crack tip plasticity and size effect in alloy 617 using high temperature indentation and nanomechanical Raman spectroscopy, 2015 SES Annual Meeting, Oral presentation, Texas A&M University, College Station, October, 2015.
15. P. Seiler, T. Siegmund, J. J. Kruzic, Y. Zhang, and, V. Tomar, High temperature crack growth in a visco-plastic strain gradient material model, *1st Midwest Workshop on Mechanics of Materials and Structures*, Poster presentation, University of Illinois, Urbana-Champaign, August, 2015.
16. J. J. Kruzic, P. Seiler, T. Siegmund, Y. Zhang, and V. Tomar, Mechanistic Models of Creep-Fatigue Crack Growth Interactions for Advanced High Temperature Reactor Components, *ART Advanced Materials Program Review*, Poster presentation, Idaho National Labs, Idaho Falls, ID, July, 2015.
17. P. Seiler, J. J. Kruzic, Y. Zhang, V. Tomar, and T. Siegmund, Simulation of rate-dependent fatigue crack growth in alloy 617, ASME 2015 Applied Mechanics and Materials Conference (McMAT), Oral presentation, Seattle, June 29 - July 1, 2015.
18. Zhang, Y., Seiler, P., and Tomar, V., High temperature indentation experiments and size effect analyses in IN-617, Oral presentation, American Nuclear Society, 2015 Annual Meeting, San Antonio, Texas, June 2015.
19. P. Seiler, T. Siegmund, V. Tomar, and J. J. Kruzic, Identification of creep parameters using microindentation, 15th Pan-American Congress of Applied Mechanics (PACAM), Oral presentation, University of Illinois, Urbana-Champaign, May, 2015.
20. Gan, M., Zhang, Y., and Tomar, V., Role of length scale and temperature in ultra-high temperature properties of materials examined using nanoindentation, Oral presentation, 2015 TMS Annual Meeting, Orlando, FL, March, 2015.

P. Seiler and T. Siegmund, Identification of creep parameters of nickel-based alloys by inverse analysis, *AmeriMech Symposium: Material Property Identification*, Oral presentation, University of Texas, Austin, December, 2014.

6. References

[1] J.K. Wright, L.J. Carroll, C. Cabet, T.M. Lillo, J.K. Benz, J.A. Simpson, W.R. Lloyd, J.A. Chapman, R.N. Wright, Characterization of elevated temperature properties of heat exchanger and steam generator alloys, *Nucl Eng Des*, 251 (2012) 252-260.

[2] J.K. Benz, L.J. Carroll, J.K. Wright, R.N. Wright, T.M. Lillo, Threshold Stress Creep Behavior of Alloy 617 at Intermediate Temperatures, *Metall. Mater. Trans. A*, 45a (2014) 3010-3022.

[3] J.K. Benz, T.M. Lillo, R.N. Wright, Aging of Alloy 617 at 650 and 750°C, in, Idaho National Laboratory, 2012.

[4] W.C. Oliver, G.M. Pharr, An improved technique for determining hardness and elastic modulus using load and displacement sensing indentation experiments, *Journal of materials research*, 7 (1992) 1564-1583.

[5] W.C. Oliver, G.M. Pharr, Measurement of hardness and elastic modulus by instrumented indentation: Advances in understanding and refinements to methodology, *Journal of materials research*, 19 (2004) 3-20.

[6] G. Pharr, Measurement of mechanical properties by ultra-low load indentation, *Materials Science and Engineering: A*, 253 (1998) 151-159.

[7] I.N. Sneddon, The relation between load and penetration in the axisymmetric Boussinesq problem for a punch of arbitrary profile, *International Journal of Engineering Science*, 3 (1965) 47-57.

[8] A. Bower, N. Fleck, A. Needleman, N. Ogbonna, Indentation of a power law creeping solid, *Proceedings of the Royal Society of London. Series A: Mathematical and Physical Sciences*, 441 (1993) 97-124.

[9] H. Li, A. Ngan, Size effects of nanoindentation creep, *Journal of materials research*, 19 (2004) 513-522.

[10] Z. Cao, P. Li, H. Lu, Y. Huang, Y. Zhou, X. Meng, Indentation size effects on the creep behavior of nanocrystalline tetragonal Ta films, *Scripta Materialia*, 60 (2009) 415-418.

[11] Z. Ma, S. Long, Y. Zhou, Y. Pan, Indentation scale dependence of tip-in creep behavior in Ni thin films, *Scripta Materialia*, 59 (2008) 195-198.

[12] M. Gan, V. Tomar, Role of length scale and temperature in indentation induced creep behavior of polymer derived Si–C–O ceramics, *Materials Science and Engineering: A*, 527 (2010) 7615-7623.

[13] V. Raman, R. Berriche, An investigation of the creep processes in tin and aluminum using a depth-sensing indentation technique, *Journal of materials research*, 7 (1992) 627-638.

[14] T. Weihs, J. Pethica, Monitoring time-dependent deformation in small volumes, in: MRS Proceedings, Cambridge Univ Press, 1991, pp. 325.

[15] B. Lucas, W. Oliver, Indentation power-law creep of high-purity indium, *Metallurgical and Materials Transactions A*, 30 (1999) 601-610.

[16] F. Alisafaei, C.-S. Han, N. Garg, On couple-stress elasto-plastic constitutive frameworks for glassy polymers, *International Journal of Plasticity*, 77 (2016) 30-53.

[17] E. Bittencourt, Dynamic explicit solution for higher-order crystal plasticity theories, *International Journal of Plasticity*, 53 (2014) 1-16.

[18] M.-Y. Seok, Y.-J. Kim, I.-C. Choi, Y. Zhao, J.-i. Jang, Predicting flow curves of two-phase steels from spherical nanoindentation data of constituent phases: Isostrain method vs. non-isostrain method, *International Journal of Plasticity*, 59 (2014) 108-118.

[19] W.D. Nix, H.J. Gao, Indentation size effects in crystalline materials: A law for strain gradient plasticity, *J. Mech. Phys. Solids*, 46 (1998) 411-425.

[20] K. Danas, V.S. Deshpande, N. Fleck, Size effects in the conical indentation of an elasto-plastic solid, *Journal of the Mechanics and Physics of Solids*, 60 (2012) 1605-1625.

[21] R.K.A. Al-Rub, G.Z. Voyiadjis, Analytical and experimental determination of the material intrinsic length scale of strain gradient plasticity theory from micro-and nano-indentation experiments, *International Journal of Plasticity*, 20 (2004) 1139-1182.

[22] M.R. Begley, J.W. Hutchinson, The mechanics of size-dependent indentation, *Journal of the Mechanics and Physics of Solids*, 46 (1998) 2049-2068.

[23] Y. Huang, F. Zhang, K. Hwang, W. Nix, G. Pharr, G. Feng, A model of size effects in nano-indentation, *Journal of the Mechanics and Physics of Solids*, 54 (2006) 1668-1686.

[24] C.F. Dahlberg, J. Faleskog, C.F. Niordson, B.N. Legarth, A deformation mechanism map for polycrystals modeled using strain gradient plasticity and interfaces that slide and separate, *International Journal of Plasticity*, 43 (2013) 177-195.

[25] E. Martínez-Pañeda, C. Niordson, On fracture in finite strain gradient plasticity, *International Journal of Plasticity*, (2015).

[26] B. Hansen, I. Beyerlein, C. Bronkhorst, E. Cerreta, D. Dennis-Koller, A dislocation-based multi-rate single crystal plasticity model, *International Journal of Plasticity*, 44 (2013) 129-146.

[27] K.A. Al-Hatab, M.A. Al-Bukhaiti, U. Krupp, Cyclic oxidation kinetics and oxide scale morphologies developed on alloy 617, *Appl Surf Sci*, 318 (2014) 275-279.

[28] ASTM Standard E647-15e1, Standard Test Method for Measurement of Fatigue Crack Growth Rates, in, ASTM International, West Conshohocken, Pennsylvania, USA, 2015, pp. DOI: 10.1520/E0647-1515E1501, www.astm.org.

[29] ASTM Standard E2760-16, Standard Test Method for Creep-Fatigue Crack Growth Testing, in, ASTM International, West Conshohocken, Pennsylvania, USA, 2016, pp. DOI: 10.1520/E2760-1516, www.astm.org.

[30] M. Rödig, H. Huthmann, W. Hartnagel, Fatigue and creep crack growth of Alloy 800 and Alloy 617 at high temperatures, *Materials at High Temperatures*, 10 (1992) 268-274.

[31] J.R. Rice, H. Riedel, Tensile cracks in creeping solids, in: Fracture Mechanics: 12th Conference, ASTM International, 1980, pp. 112.

[32] K.S. Chan, Time-Dependent Crack Growth Thresholds of Ni-Base Superalloys, *Metall. Mater. Trans. A*, 45a (2014) 3454-3466.

[33] P.S. Phani, W.C. Oliver, A direct comparison of high temperature nanoindentation creep and uniaxial creep measurements for commercial purity aluminum, *Acta Mater.*, 111 (2016) 31-38.

[34] N.A. Fleck, G.M. Muller, M.F. Ashby, J.W. Hutchinson, Strain Gradient Plasticity - Theory and Experiment, *Acta Metall. Mater.*, 42 (1994) 475-487.

[35] Q. Ma, D.R. Clarke, Size-Dependent Hardness of Silver Single-Crystals, *J Mater Res*, 10 (1995) 853-863.

[36] J.S. Stolken, A.G. Evans, A microbend test method for measuring the plasticity length scale, *Acta Mater.*, 46 (1998) 5109-5115.

[37] P. Shrotriya, S.M. Allameh, J. Lou, T. Buchheit, W.O. Soboyejo, On the measurement of the plasticity length scale parameter in LIGA nickel foils, *Mech. Mater.*, 35 (2003) 233-243.

[38] M. Gan, V. Tomar, Scale and Temperature Dependent Creep Modeling and Experiments in Materials, *Jom-Us*, 63 (2011) 27-34.

[39] M. Gan, V. Tomar, Role of length scale and temperature in indentation induced creep behavior of polymer derived Si-C-O ceramics, *Materials Science and Engineering a-Structural Materials Properties Microstructure and Processing*, 527 (2010) 7615-7623.

[40] N.A. Fleck, J.W. Hutchinson, A Phenomenological Theory for Strain Gradient Effects in Plasticity, *J. Mech. Phys. Solids*, 41 (1993) 1825-1857.

[41] H. Gao, Y. Huang, W.D. Nix, J.W. Hutchinson, Mechanism-based strain gradient plasticity - I. Theory, *J. Mech. Phys. Solids*, 47 (1999) 1239-1263.

[42] Y. Huang, H. Gao, W.D. Nix, J.W. Hutchinson, Mechanism-based strain gradient plasticity - II. Analysis, *J. Mech. Phys. Solids*, 48 (2000) 99-128.

[43] Y. Huang, S. Qu, K.C. Hwang, M. Li, H. Gao, A conventional theory of mechanism-based strain gradient plasticity, *Int. J. Plast.*, 20 (2004) 753-782.

[44] Y.G. Wei, J.W. Hutchinson, Steady-state crack growth and work of fracture for solids characterized by strain gradient plasticity, *J. Mech. Phys. Solids*, 45 (1997) 1253-1273.

[45] J.G. Sevillano, The effective threshold for fatigue crack propagation: A plastic size effect?, *Scripta Mater.*, 44 (2001) 2661-2665.

[46] S. Qu, Y. Huang, H. Jiang, C. Liu, P.D. Wu, K.C. Hwang, Fracture analysis in the conventional theory of mechanism-based strain gradient (CMSG) plasticity, *Int. J. Fract.*, 129 (2004) 199-220.

[47] J.Y. Chen, Y. Wei, Y. Huang, J.W. Hutchinson, K.C. Hwang, The crack tip fields in strain gradient plasticity: the asymptotic and numerical analyses, *Eng. Fract. Mech.*, 64 (1999) 625-648.

[48] Y. Huang, J.Y. Chen, T.F. Guo, L. Zhang, K.C. Huang, Analytic and numerical studies on mode I and mode II fracture in elastic-plastic materials with strain gradient effects, *Int. J. Fract.*, 100 (1999) 1-27.

[49] E. Martinez-Paneda, C. Betegon, Modeling damage and fracture within strain-gradient plasticity, *International Journal of Solids and Structures*, 59 (2015) 208-215.

[50] E. Martinez-Paneda, C.F. Niordson, On fracture in finite strain gradient plasticity, *Int. J. Plast.*, 80 (2016) 154-167.

[51] V. Tvergaard, J.W. Hutchinson, Effect of strain-dependent cohesive zone model on predictions of crack growth resistance, *International Journal of Solids and Structures*, 33 (1996) 3297-3308.

[52] Y. Wei, X. Qiu, K.C. Hwang, Steady-state crack growth and fracture work based on the theory of mechanism-based strain gradient plasticity, *Eng. Fract. Mech.*, 71 (2004) 107-125.

[53] M.E. Gurtin, A gradient theory of single-crystal viscoplasticity that accounts for geometrically necessary dislocations, *J. Mech. Phys. Solids*, 50 (2002) 5-32.

[54] M.E. Gurtin, On a framework for small-deformation viscoplasticity: free energy, microforces, strain gradients, *Int. J. Plast.*, 19 (2003) 47-90.

[55] P. Gudmundson, A unified treatment of strain gradient plasticity, *J. Mech. Phys. Solids*, 52 (2004) 1379-1406.

[56] P. Fredriksson, P. Gudmundson, Size-dependent yield strength and surface energies of thin films, *Materials Science and Engineering a-Structural Materials Properties Microstructure and Processing*, 400 (2005) 448-450.

[57] U. Borg, C.F. Niordson, N.A. Fleck, V. Tvergaard, A viscoplastic strain gradient analysis of materials with voids or inclusions, *International Journal of Solids and Structures*, 43 (2006) 4906-4916.

[58] N.A. Fleck, J.W. Hutchinson, A reformulation of strain gradient plasticity, *J. Mech. Phys. Solids*, 49 (2001) 2245-2271.

[59] C.F. Niordson, P. Redanz, Size-effects in plane strain sheet-necking, *J. Mech. Phys. Solids*, 52 (2004) 2431-2454.

[60] S.P. Lele, L. Anand, A small-deformation strain-gradient theory for isotropic viscoplastic materials, *Philosophical Magazine*, 88 (2008).

[61] S.P. Lele, L. Anand, A large-deformation strain-gradient theory for isotropic viscoplastic materials, *Int. J. Plast.*, 25 (2009) 420-453.

[62] K.L. Nielsen, C.F. Niordson, A numerical basis for strain-gradient plasticity theory: Rate-independent and rate-dependent formulations, *J. Mech. Phys. Solids*, 63 (2014) 113-127.

[63] N.A. Fleck, J.R. Willis, A mathematical basis for strain-gradient plasticity theory-Part I: Scalar plastic multiplier, *J. Mech. Phys. Solids*, 57 (2009) 161-177.

[64] K.L. Nielsen, C.F. Niordson, J.W. Hutchinson, Strain gradient effects on steady state crack growth in rate-sensitive materials, *Eng. Fract. Mech.*, 96 (2012) 61-71.

[65] K.L. Nielsen, C.F. Niordson, Rate sensitivity of mixed mode interface toughness of dissimilar metallic materials: Studied at steady state, *International Journal of Solids and Structures*, 49 (2012) 576-583.

[66] Z. Suo, C.F. Shih, A.G. Varias, A Theory for Cleavage Cracking in the Presence of Plastic-Flow, *Acta Metall. Mater.*, 41 (1993) 1551-1557.

[67] J. Rösler, H. Harders, M. Bäker, *Mechanical Behaviour of Engineering Materials: Metals, Ceramics, Polymers, and Composites*, Springer, 2007.

[68] R.C. Reed, *The superalloys: fundamentals and applications*, Cambridge university press, 2008.

[69] Z. Shi, X. Feng, Y. Huang, J. Xiao, K.C. Hwang, The equivalent axisymmetric model for Berkovich indenters in power-law hardening materials, *Int. J. Plast.*, 26 (2010) 141-148.

[70] B. Wang, T. Siegmund, Numerical simulation of constraint effects in fatigue crack growth, *Int. J. Fatigue*, 27 (2005) 1328-1334.

[71] X.B. Ren, Z.L. Zhang, B. Nyhus, Effect of residual stress on cleavage fracture toughness by using cohesive zone model, *Fatigue & Fracture of Engineering Materials & Structures*, 34 (2011) 592-603.

[72] M.L. Williams, On the Stress Distribution at the Base of a Stationary Crack, *J. App. Mech.*, 24 (1957) 109-114.

[73] Q.Z. Xiao, B.L. Karihaloo, Coefficients of the crack tip asymptotic field for a standard compact tension specimen, *Int. J. Fract.*, 118 (2002) 1-15.

[74] V. Tvergaard, J.W. Hutchinson, Effect of T-Stress on Mode-I Crack-Growth Resistance in a Ductile Solid, *International Journal of Solids and Structures*, 31 (1994) 823-833.

[75] A. Needleman, An Analysis of Decohesion Along an Imperfect Interface, *Int. J. Fract.*, 42 (1990) 21-40.

[76] A. Needleman, Micromechanical Modeling of Interfacial Decohesion, *Ultramicroscopy*, 40 (1992) 203-214.

[77] K.L. Roe, T. Siegmund, An irreversible cohesive zone model for interface fatigue crack growth simulation, *Eng. Fract. Mech.*, 70 (2003) 209-232.

[78] C.M. Landis, T. Pardoen, J.W. Hutchinson, Crack velocity dependent toughness in rate dependent materials, *Mech. Mater.*, 32 (2000) 663-678.

[79] T.L. Anderson, *Fracture Mechanics: Fundamentals and Applications*, 3rd ed., Taylor and Francis Group, Boca Raton, FL, 2005.

[80] J.L. Bassani, D.E. Hawk, Influence of Damage on Crack-Tip Fields under Small-Scale-Creep Conditions, *Int. J. Fract.*, 42 (1990) 157-172.

[81] R.M. McMeeking, D.M. Parks, On criteria for J-dominance of crack-tip fields in large-scale yielding, in: J.D. Landes, J.A. Begley, G.A. Clarke (Eds.) *Elastic-Plastic Fracture, ASTM STP 668*, American Society for Testing and Materials, 1979, pp. 175-194.

[82] D. François, A. Pineau, A. Zaoui, *Mechanical Behaviour of Materials: Volume II: Fracture Mechanics and Damage*, Springer Netherlands, 2012.